UNIVERSITÀ DEGLI STUDI DI PADOVA

UNIVERSITÀ DEGLI STUDI DI PADOVA

DIPARTIMENTO DI FISICA E ASTRONOMIA "GALILEO GALILEI"

CORSO DI DOTTORATO DI RICERCA IN ASTRONOMIA
Ciclo XXXV

BAR ROTATION RATE: A TOOL TO PROBE THE FORMATION AND DYNAMICS OF BARRED GALAXIES

Coordinatore: Ch.mo Prof. Giovanni Carraro
Supervisore: Ch.mo Prof. Enrico Maria Corsini
Co-Supervisore: Ch.mo Prof. Victor Debattista

Dottoranda: Chiara Buttitta

Abstract

Galaxies are the fundamental bricks of the hierarchical structure of the Universe. They are complex systems composed of stars, gas, and dust, and present a large variety of structures, sizes and shapes. More than two-thirds of disc galaxies in the Local Universe host an elliptical structure tumbling at the centre of the disc that is commonly known as a bar. The bar radius $R_{\rm bar}$, strength $S_{\rm bar}$, and angular frequency $\Omega_{\rm bar}$ change in time through secular evolution, affecting the morphological and kinematic properties of the host galaxy. The angular frequency or *bar pattern speed* is one of the most important parameters that characterise a bar. It controls the position of the resonances, affects the stellar dynamics, and depends on the dark matter (DM) content. The bar pattern speed is usually parameterised by the *rotation rate* $\mathcal{R}$ a dimensionless and distance-independent parameter that separates bars in slow, fast, and ultrafast.

Dynamical studies and simulations-based works had allowed to shed the light on the formation of barred galaxies and to track the evolution of the bar properties, while observational studies based on wide and deep surveys had permitted to draw a picture of the properties of barred galaxies in the present day. Fast bars can form naturally in disc galaxies due to internal instabilities which force stars to move into more elongated orbits. The bar formation can also occur in galaxies with a nearby companion, due to tidal interaction. These bars are typically slower with respect to those naturally formed. Moreover, theoretical works and cosmological simulations show that bars slow down after the interaction with a centrally concentrated DM halo through dynamical friction. According to orbital theory, ultrafast bars are not expected to exist since the stellar orbits cannot efficiently support the bar structure.

Many observational studies found that bars in the Local Universe are compatible with the fast regime, a fraction of them lie in the ultrafast regime, and the few slow bars detected so far have too large uncertainties to be considered genuinely slow. In this thesis, we aim at investigating the nature and dynamics of barred galaxies by studying ultrafast, fast, and slow bars and analysing the internal structure of their host galaxies using dynamical models and N-body simulations.

In Chapter 2 we discuss the case of ultrafast bars. These objects challenge our understanding of the orbital structure of barred galaxies. We analysed the properties of the ultrafast bars detected in the Calar Alto Legacy Integral Field Area Survey (CALIFA) survey to investigate whether they are an artefact resulting from an overestimation of $R_{\rm bar}$ or a new class of bars, whose orbital structure has not yet been understood. We revised the available measurements of $R_{\rm bar}$ based on ellipse fitting and Fourier analysis and of $\Omega_{\rm bar}$ from the Tremaine & Weinberg (TW) method. In addition, we measured $R_{\rm bar}$ from the analysis of the maps tracing the transverse-to-radial force ratio, which we obtained from the deprojected i-band images of the galaxies retrieved from the Sloan Digital Sky Survey (SDSS). We found that nearly all the sample galaxies are spirals with an inner ring or pseudo-ring circling the bar and/or strong spiral arms, which hamper the measurement of $R_{\rm bar}$ from the ellipse fitting and Fourier analysis. According to these methods, the bar ends overlap the ring or the spiral arms making the adopted $R_{\rm bar}$ unreliable. We conclude that ultrafast bars are no longer observed when the correct measurement of $R_{\rm bar}$ is adopted. Deriving $R_{\rm bar}$ in galaxies with rings and strong spiral arms is not straightforward and a solid measurement method based on both photometric and kinematic data is still missing.

In Chapter 3 we present the first case of a slow stellar bar hosted in the lenticular barred galaxy NGC 4277. We measured $R_{\rm bar}$ and $S_{\rm bar}$ from the surface photometry obtained from the broad-band imaging of the SDSS and we derived $\Omega_{\rm bar}$ from the stellar kinematics obtained from the integral-field spectroscopy performed with the Multi Unit Spectroscopic Explorer (MUSE) at the Very Large Telescope (VLT). We found that NGC 4277 hosts a short, weak, and slow bar and its pattern speed is amongst the best-constrained ones ever obtained with the TW method. NGC 4277 is the first clear-cut case of a galaxy hosting a slow stellar bar measured with the TW method. A possible interaction with the neighbour galaxy NGC 4273 could have triggered the formation of such a slow bar and/or the bar could be slowed down due to the dynamical friction with a significant amount of DM within the bar region.

In Chapter 4 we present the photometric and kinematic analysis of the lopsided bar hosted in the dwarf galaxy IC 3167. We measured $R_{\rm bar}$ and $S_{\rm bar}$ from the surface photometry obtained from the broad-band imaging of the SDSS and we derived $\Omega_{\rm bar}$ from the stellar kinematics obtained from the integral-field spectroscopy performed with MUSE at VLT. We found that IC 3167 hosts a short, weak, and slow bar. The probability that the bar is rotating slowly is twice more likely to be slow (68%) rather than fast (32%). This allows us to infer that the formation of this bar was triggered by the ongoing interaction.

In Chapter 5 we investigate the link between $\mathcal{R}$ and the DM content in barred galaxies by concentrating on the cases of the lenticular galaxies NGC 4264 and NGC 4277. These two gas-poor galaxies have similar morphologies, sizes, and luminosities. But, NGC 4264 hosts a fast bar, which extends to nearly the corotation, while the bar embedded in NGC 4277 is slow and falls short of corotation. We derive the fraction of DM $f_{\rm DM,bar}$ within the bar region from Jeans axisymmetric dynamical models by matching the stellar kinematics obtained with MUSE and using SDSS images to recover the stellar mass distribution. We build mass-follows-light models as well as mass models with a DM spherical halo, which is not tied to the stars. We find that the inner regions of NGC 4277 host a larger fraction of DM ($f_{\rm DM,bar} = 0.53 \pm 0.02$) with respect to NGC 4264 ($f_{\rm DM,bar} = 0.33 \pm 0.04$) in agreement with the predictions of theoretical works and the findings of numerical simulations, which have found that fast bars live in baryon-dominated discs, whereas slow bars experienced a strong drag from the dynamical friction due to a dense DM halo. This is the first time that $\mathcal{R}$ is coupled to $f_{\rm DM,bar}$ derived from dynamical modelling.

In Chapter 6 we build N-body simulations to mimic the photometric and kinematic properties of the lenticular barred galaxy NGC 4277. Our galaxy models are pure collisionless models with a bulge, disc, and DM halo. The models are evolved in isolation, therefore it is not possible to test whether the formation of the slow bar hosted in NGC 4277 was triggered by the tidal interaction with the companion NGC 4273. The galaxy model that best reproduces both the photometry and the kinematics of NGC 4277 is characterised by a massive DM halo. Our results agree with the prediction obtained by dynamical modelling, which found a considerable fraction of DM in the innermost region of NGC 4277. Thus, we confirmed that the bar hosted in NGC 4277 experienced a strong drag as a consequence of the interaction with a dense DM halo.

Finally, in Chapter 7 we summarise the main conclusions of the thesis and present some future perspectives.

Contents

Chapter 1

Introduction

In this chapter, we present the global properties, the dynamics and the formation and evolution of barred galaxies. In Section 1.1 we introduce the morphology, the light distribution of bars and the fraction of barred galaxies. In Section 1.2 we describe the main properties which characterised the bar structure. In Section 1.3 we describe the stellar and gaseous dynamics inside a barred potential and in Section 1.4 we present the formation and evolution of bars.

1.1 General properties

Morphology of barred galaxies

Bars are triaxial structures that tumble around the centre of the disc galaxies. Curtis (1918) first identified the presence of a bar structure in spiral galaxies and he defined a new class of objects named *ϕ-type galaxies* due to their similarity to the Greek letter ϕ. Hubble (1926) coined the term of *barred galaxies* suggesting instead the use of the Greek letter θ because the extension of the bar never exceeds the internal spiral structure of the galactic disc. He considered them in his morphological classification, disposing the barred galaxies along one of the two arms of the tuning fork diagram, the other being assigned to the normal galaxies (Fig. 1.1).

A more detailed classification of the barred galaxies was introduced by de Vaucouleurs et al. (1964), which introduced *families* and *varieties* to distinguish the contribution of the bar and its relation with the spiral structure (Fig. 1.2). In his fuse diagram, he recognised normal galaxies (SA), barred galaxies (SB) and an intermediate class of objects which are defined as *weakly barred galaxies* (SAB). He separated them into galaxies with a spiral structure that emerges from an inner ring encompassing the bar (r), galaxies with spiral arms that emerge from the bar ends (s) or with an intermediate condition (rs).

Later, van den Bergh (1976) classified disc galaxies taking also into account the prominence of the bar. He disposed elliptical galaxies on the handle of a trident diagram, and gas-free lenticulars (S0), poor-gas anaemic (A) and gas-rich spirals (S) on the three prongs, respectively. He placed barred galaxies along three parallel sequences sorting them into unbarred (S), weakly barred (S(B)) and barred galaxies (SB). Finally, the Morgan (1958) classification divided galaxies according to the light concentration (from k to a for more to less concentrated systems), families (E for ellipticals, S for spirals, B for barred spirals, I for irregulars, L for low-surface brightness systems, N for galaxies with bright nucleus, R for system with rotational symmetry but no evidence of spiral or elliptical structure), and axial ratio (1 represents the circular shape and 6 represents the most flattened structure).

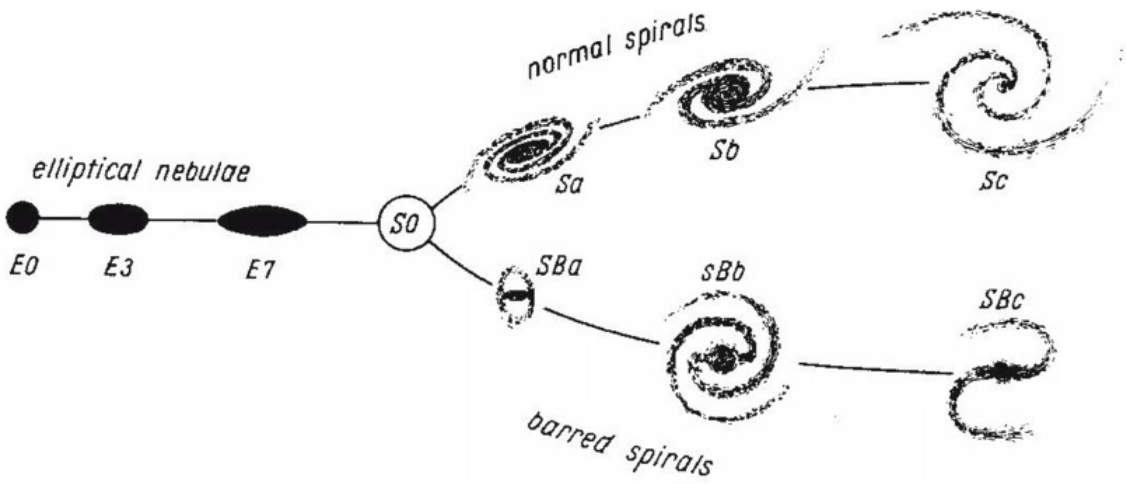

Figure 1.1: Tuning fork diagram. From Hubble (1926).

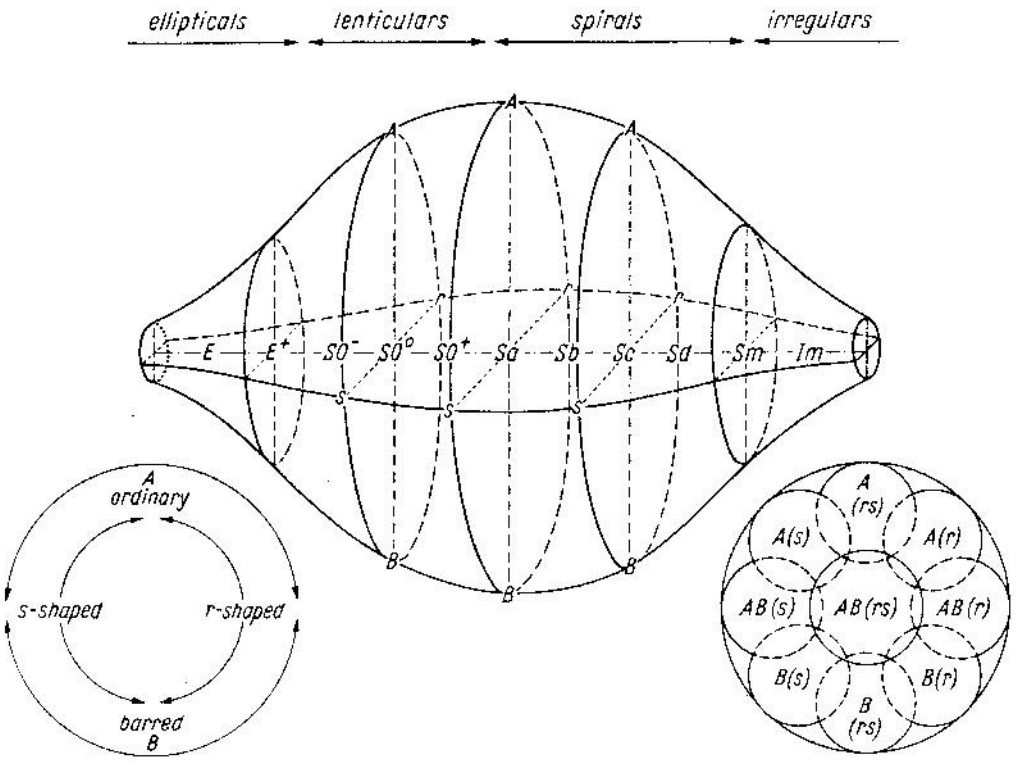

Figure 1.2: *Top*: Fuse diagram. *Bottom left*: Schematic representation of families and varieties. *Bottom right*: Schematic representation of a section of the fuse diagram containing the mixed families and varieties. From de Vaucouleurs et al. (1964).

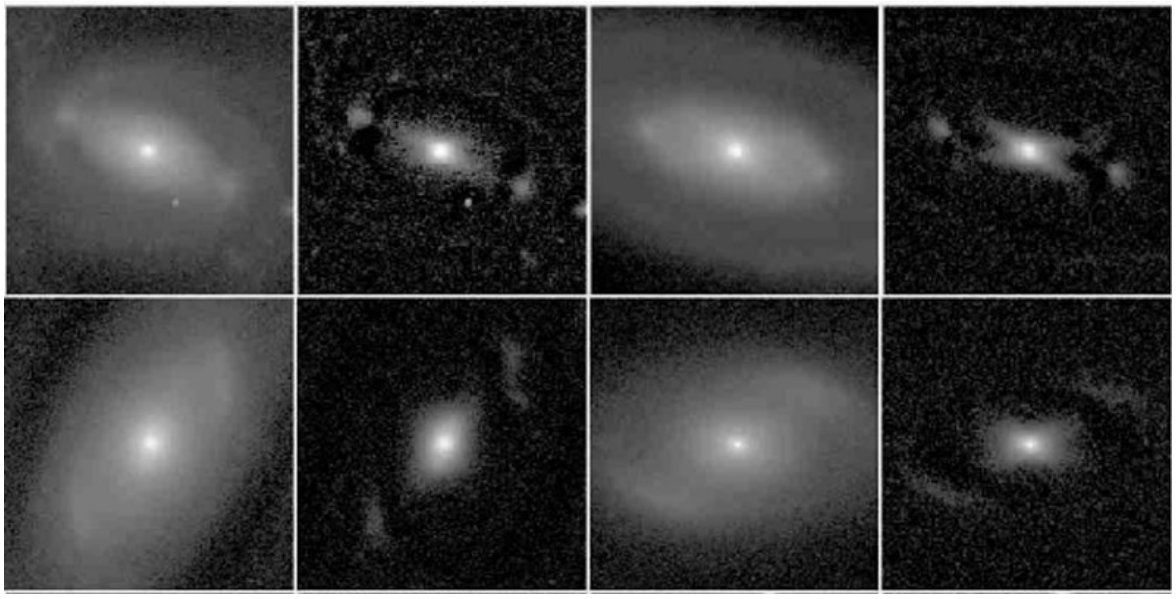

Figure 1.3: Examples of ansae-type bars. For each galaxy, the left panel is the observed image while the right panel is the unsharp masked image. *Top panels, from left to right*: NGC 5375 and NGC 7020, with round ansae. *Bottom panels, from left to right*: NGC 7098 with partly wavy ansae and NGC 1079 with curved ansae. From Martinez-Valpuesta et al. (2007).

Barred galaxies may have more complex features. Some galaxies host *ansae*-type bars: symmetrical and bright enhancements at the ends of the bar that can resemble "handles". These structures can be round, linear or resemble an arch (Fig 1.3) and are seen in images. But they become more evident in unsharp masked images. Martinez-Valpuesta et al. (2007) used N-body simulations to study the frequency of ansae in barred galaxies. They found that ansae-type bars are common in early-type disc galaxies ($\sim 40\%$ in S0-Sb) and rare in late-type galaxies. They are composed of old stellar populations, but their origin is still unclear.

Ovals are elongated structures that produce in the inner disc a global deviation from the axisymmetric shape. They play a bar-like role in galaxies, affecting the structure and dynamics of the disc and can be identified by photometric and kinematic signatures (Kormendy & Kennicutt, 2004). Lenses are structures associated with the bar and have a round or slightly elliptical shape with sharp edges. Ovals and lenses are very common in early-type barred galaxies, they seem to be the product of a bar weakening due to the growth of a mass concentration at centre (Laurikainen et al., 2009).

Rings (or pseudorings if partially completed) are common structures in barred galaxies too. They are classified into nuclear, inner and outer rings. Nuclear rings are located in the very centre of the galaxy. They are characterised by an intense star-forming activity and are associated to the inner Lindblad resonances. Inner rings envelop the bar, have circular or elliptical shapes, and are usually related to the corotation. Outer rings are large and diffuse structures typically seen in early-type galaxies with a radius twice the radius of the bar, usually associated with the outer Lindblad resonance. Type 1 outer rings (R_1) are perpendicular to the bar while type 2 (R_2) rings are aligned with the bar (Buta, 1996).

Bar shape and light profile

Barred galaxies are a combination of multiple components with different sizes and shapes. Separating the contribution of each element is not a straightforward task, since the overlapping of the several components produces isophotes with a composite shape that clearly deviates from the perfect ellipse. The procedure that allows to separate each galactic component and derives its light contribution is defined as photometric decomposition. The photometric decomposition can be parametric - when the light profile is described by analytical functions with some face parameters - or non parametric. In the last decades, many algorithms were developed to perform photometric decomposition on barred galaxies, such as Galaxy Fitting (GALFIT, Peng et al., 2002), Galaxy Automatic Surface Photometry (GASPHOT, Pignatelli et al., 2006), Galaxy Surface Photometry 2 Dimensional decomposition (GASP2D, Méndez-Abreu et al., 2008), Bulge/Disk Decomposition Analysis (BUDDA, de Souza et al., 2004; Gadotti, 2008), and Image Fitting (IMFIT, Erwin, 2015).

Bar isophotes can be described as generalised ellipsis with ellipticity $\epsilon_{\rm bar} = 1 - q_{\rm bar}$, axial ratio $q_{\rm bar}$ and position angle $\mathrm{PA}_{\rm bar}$ (Athanassoula et al., 1990). The shape of the isophote can be described through the c parameter (Fig. 1.4, left panel) with radial distance $r_{\rm bar}$ defined as:

$$r_{\rm bar} = [(-(x-x_0)\sin\mathrm{PA}_{\rm bar} + (y-y_0)\cos\mathrm{PA}_{\rm bar})^c + \\ -((x-x_0)\cos\mathrm{PA}_{\rm bar} + (y-y_0)\sin\mathrm{PA}_{\rm bar})^c/q_{\rm bar}^c]^{1/c}.$$

Isophotes with $c = 2$ are perfect ellipses, whereas the isophotes with $c < 2$ ($c > 2$) have sharper (rounder) edges and are defined as *disky* (*boxy*). Athanassoula et al. (1990) first found that bar isophotes are more rectangular-like, and have on average a shape parameter of $c \sim 3.5$ as measured in 11 early-type barred galaxies.

Méndez-Abreu et al. (2018b) performed a detailed analysis of the intrinsic shape of the bar in a sample of barred galaxies extracted from the Calar Alto Legacy Integral Field Area Survey (CALIFA, Sánchez et al., 2012). They described the bar as a triaxial ellipsoid embedded in an axisymmetric disc parameterised as an oblate ellipsoid. They derived the intrinsic bar axial ratios (B/A, C/A) using the projected bar and disc geometric parameters obtained from the photometric decomposition. They found that the 68% of the sample hosts a bar modelled as a prolate-triaxial ellipsoid, and 14% hosts a bar described as an oblate-triaxial ellipsoid with average intrinsic ratios of $B/A \sim 0.31$ and $C/A \sim 0.34$. Moreover, Méndez-Abreu et al. (2018b) found that massive early-type barred galaxies with a prominent and concentrated bulge, host thicker and rounder bars with respect to their less massive late-type counterparts.

The light radial profile of the bar is brighter along the major axis and fainter along the minor one (Sellwood & Wilkinson, 1993). The surface brightness radial profile of the bar can be described through different parametric laws:

Ferrers profile (Laurikainen et al., 2005)

$$I_{\rm bar}^{\rm Ferrers}(x,y) = I_{0,\rm bar}\left[1 - \left(\frac{r_{\rm bar}}{a_{\rm bar}}\right)^2\right]^{n_{\rm bar}+0.5} \qquad r_{\rm bar} \leqslant a_{\rm bar}$$

where $I_{0,\rm bar}$ and $a_{\rm bar}$ represent the central surface brightness and bar radius, respectively. The parameter $n_{\rm bar}$ defines the shape of the radial profile, and usually in literature it is adopted the value of $n_{\rm bar} = 2$ (Aguerri et al., 2009). The radial distance $r_{\rm bar}$ is defined as before.

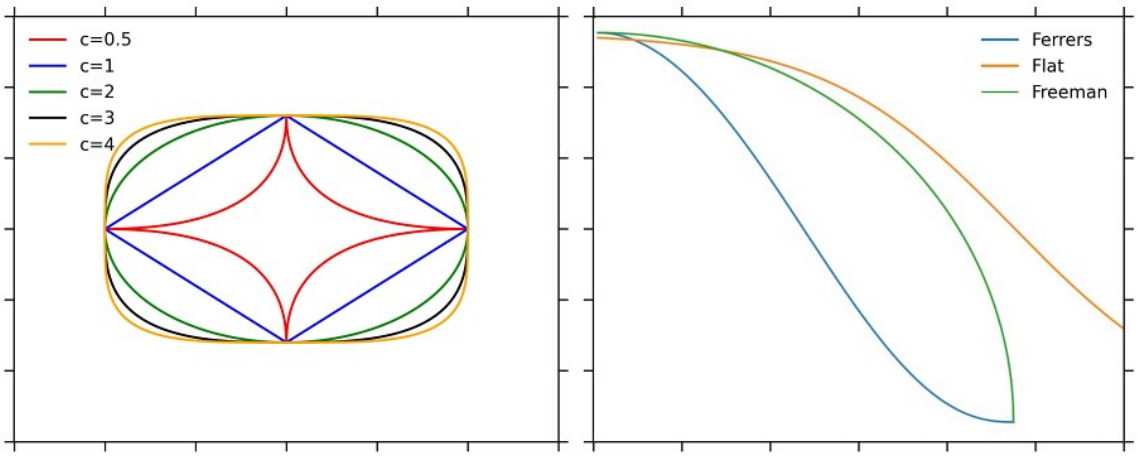

Figure 1.4: *Left panel*: The shape of the bar isophotes as a function of the c parameter. For values $c > 2$ isophotes are *boxy*, for $c < 2$ isophotes are *disky*, while $c = 2$ corresponds to a perfect ellipse. *Right panel*: Surface brightness radial profiles of a Ferrers (blue line), flat (orange line), and Freeman (green line) bar.

Flat profile (Prieto et al., 2001)

$$I_{\rm bar}^{\rm Flat}(x,y) = I_{0,\rm bar}\left[\frac{1}{1+e^{(r_{\rm bar}-a_{\rm bar})/r_{\rm s}}}\right]$$

where $I_{0,\rm bar}$ and $a_{\rm bar}$ are the central surface brightness and bar radius, respectively. The radial profile decreases with a scalelength $r_{\rm s}$ for $r_{\rm bar} > a_{\rm bar}$. The radial distance $r_{\rm bar}$ is defined as before.

Freeman profile (Freeman, 1966)

$$I_{\rm bar}^{\rm Freeman}(x,y) = I_{0,\rm bar}\sqrt{1-\left(\frac{r_{\rm bar}}{a_{\rm bar}}\right)^2} \qquad r_{\rm bar} \leqslant a_{\rm bar}$$

where $I_{0,\rm bar}$ and $a_{\rm bar}$ represent the central surface brightness and bar radius, respectively. The radial distance $r_{\rm bar}$ is defined as before.

The radial profiles of Ferrers, flat, and Freeman bars are shown in Fig. 1.4, the scalelengths are equal to the unity ($a_{\rm bar} = 1$, $r_{\rm s} = 1$) while the $I_{0,\rm bar}$ is defined in order to satisfy $I_{\rm bar}(r = 0) = 1$.

Elmegreen & Elmegreen (1985) found a correlation between the surface brightness radial profiles of bars and galaxy morphological type. Early-type galaxies host bars with more flat profiles, while late-type galaxies have bars with a more exponential radial profile. Moreover, they found that early-type galaxies host in general longer and stronger bars with respect to their late-type counterparts, which host shorter and weaker bars.

Kim et al. (2015) studied the structural properties of a sample of barred galaxies observed in the Spitzer Survey of Stellar Structure in Galaxies (S^4G, Sheth et al., 2010). They found that more massive galaxies with classical bulges host a bar with a flat profile, whereas less massive bulgeless galaxies have a bar with a more exponential profile.

Fraction of barred galaxies

Barred galaxies represent the majority of disc galaxies in the Local Universe, but the fraction of barred galaxies strongly depends on the wavelength range and method adopted to identify bars. Observations at short wavelength ranges underestimate the bar fraction since bars are mainly composed of old stellar populations, and so the majority of the light is emitted at redder bands. Longer wavelengths are less affected by dust contamination, so the fraction of barred increases. Many works had explored the fraction of barred galaxies in different wavelength ranges by adopting different techniques.

de Vaucouleurs et al. (1991) first performed a visual inspection of barred galaxies on B-band plates and found a fraction of barred galaxies of $\sim 30\%$, that increases up to $\sim 60\%$ if also weekly barred galaxies and oval distortions are included.

Barazza et al. (2008) studied the distribution of barred galaxies in the Local Universe ($0.01 < z < 0.03$) using a sample of ~ 3700 barred galaxies extracted from Sloan Digitized Sky Survey (SDSS, York et al., 2000). They used a more quantitative approach to identify bars in galaxies, performing an isophotal analysis on g-band images. They found an average bar fraction of $\sim 52\%$. Moreover, they reported that bluer galaxies have a higher bar fraction (58% at $g - r = 0.3$) with respect to redder objects (32% at $g - r = 0.65$).

Aguerri et al. (2009) analysed a sample of ~ 2100 disc galaxies extracted from the SDSS survey in the redshift range between $0.01 < z < 0.04$ and with an absolute magnitude of $M_r < -20$ mag. The galaxies in the sample are divided into four subsamples according to their morphology and light concentration: elliptical galaxies have an average concentration of $C = 3.18$ (26% of the sample), lenticulars have $C = 3.10$ (29% of the sample), early-type spirals (S0/a - Sb) have $C = 2.53$ (20% of the sample) and late-type spirals (Sc-Sm) have $C = 2.10$ (25% of the sample). They used two different methods to detect the bar: the isophotal and Fourier analysis (see Sec. 1.2). The isophotal analysis showed that 45% of disc galaxies host a bar, while the Fourier analysis identified a bar fraction of 26%. The Fourier method is less efficient in the detection of the bar, especially in late-type spiral galaxies, since strong spiral arms or lenses make the bar edges less evident. They confirmed the relation between the bar fraction and light concentration discussed by Barazza et al. (2008). Indeed the fraction of barred galaxies is higher in more concentrated galaxies.

More recently, Masters et al. (2011) have carried out a massive analysis of ~ 14.000 galaxies located in the redshift range $0.01 < z < 0.06$ belonging to the Galaxy Zoo project. This project permits citizens to identify and classify galaxies through a series of questions and a visual inspection of the images. Galaxies images are a combination of the SDSS g, r, and i bands and have an absolute magnitude of $M_r < -19.38$ mag. They found an average bar fraction of $\sim 29\%$ for disc galaxies, but a more detailed analysis shows that the fraction of barred galaxies does not have a monotonic trend: it reaches a maximum (60%) for S0/a galaxies, decreases at a value of $\sim 30\%$ for Sc galaxies and then increases again for the extremely-late spirals. Moreover, they found that redder galaxies host large bulges and have a higher fraction of bars, whereas bluer systems have smaller or no bulges and a lower bar fraction.

Méndez-Abreu et al. (2017) performed the photometric decomposition of a sample of ~ 400 galaxies extracted from the CALIFA survey. They found on average a fraction of barred galaxies of $\sim 57\%$ and no significant trend with the Hubble type. On the other hand, they found a dependence from the mass of the host galaxy: the bar fraction is higher in galaxies with a stellar mass of $M_\star = 10^{9.5}\,\mathrm{M}_\odot$ ($\sim 75\%$) and decreases to a value of $\sim 25\%$ in systems with $M_\star = 10^{11}\,\mathrm{M}_\odot$ (Fig. 1.5).

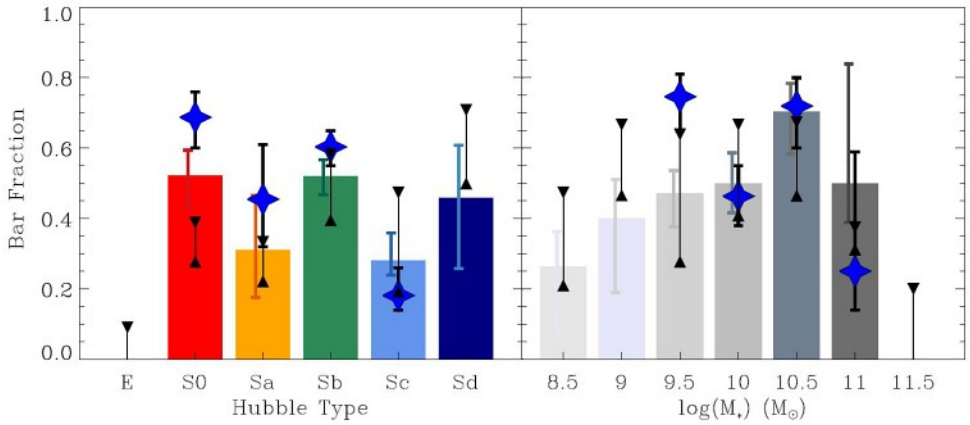

Figure 1.5: *Left panel*: Bar fraction as a function of Hubble type. *Right panel*: Bar fraction as a function of stellar mass. From Méndez-Abreu et al. (2017).

Eskridge et al. (2000) studied the morphology of ∼ 180 disc galaxies extracted from the Ohio State University Bright Spiral Galaxy Survey (OSUBSGS, Eskridge et al., 2002). The sample has a total magnitude of $M_B < 12$ mag. They analysed both optical and near-infrared wavelength observations (H-band) and divided the sample into strongly barred (56%), mildly barred (16%), and unbarred galaxies (27%). However, they did not detect any correlation between the bar fraction and morphological types.

Marinova & Jogee (2007) analysed the same sample of disc galaxies extracted from the OSUBSGS survey using B and H-band images. They identified and classified bars before and after the deprojection to face-on view finding a bar fraction of 44% and 60% in optical and near-infrared wavelength ranges, respectively. The fraction of barred galaxies remains nearly the same after the deprojection. This means that the fraction of barred galaxies could be estimated without necessarily performing the deprojection, which on the other hand does not work very well for too high inclinations.

Buta et al. (2015) investigated the morphology of a large sample of disc galaxies extracted from the S^{4}G survey. The survey imaged more than ∼ 2400 galaxies in mid-infrared bands (3.6, 4.5, 5.8, and 8.0 μm). Buta et al. (2015) divided the sample into low-inclined ($i < 60°$) and high-inclined ($i > 60°$) systems and carefully analysed the morphological structures like bars, spiral arms, lenses and rings. They found the late-type galaxies have a higher bar fraction (Scd-Sm: ∼ 81%) with respect to the early-type ones (S0: ∼ 55%) with a significant drop for the intermediate-type galaxies (Sb-Sc: ∼ 35%).

As already shown, many works investigated the correlations between the bar fraction and properties of the host galaxies, such as the morphological type, colours, and stellar mass. Erwin (2018) has recently explored these relationships in a sample of ∼ 650 spiral galaxies from the S^{4}G survey. They belong to a complete distance and mass-limited sample ($D < 25$ Mpc, $M_\star > 10^8$ M$_\odot$) of low inclined systems ($i < 65°$). The fraction of barred galaxies reaches a peak of 70% at stellar masses $\log(M_\star/\mathrm{M}_\odot) \sim 9.7$ and decreases at lower and higher masses, is almost constant with the colour and with the gas fraction (Fig. 1.6). These findings are not in agreement with previous results based on SDSS observations, which show a clear dependence on the galaxy mass and colours. Erwin (2018) argued that this discrepancy is due to a difference in the angular resolution. S^{4}G an SDSS have a spatial resolution of ∼ 0.17 kpc and ∼ 1.3 kpc, respectively. This means that long bars hosted in more massive and red galaxies can be detected more easily.

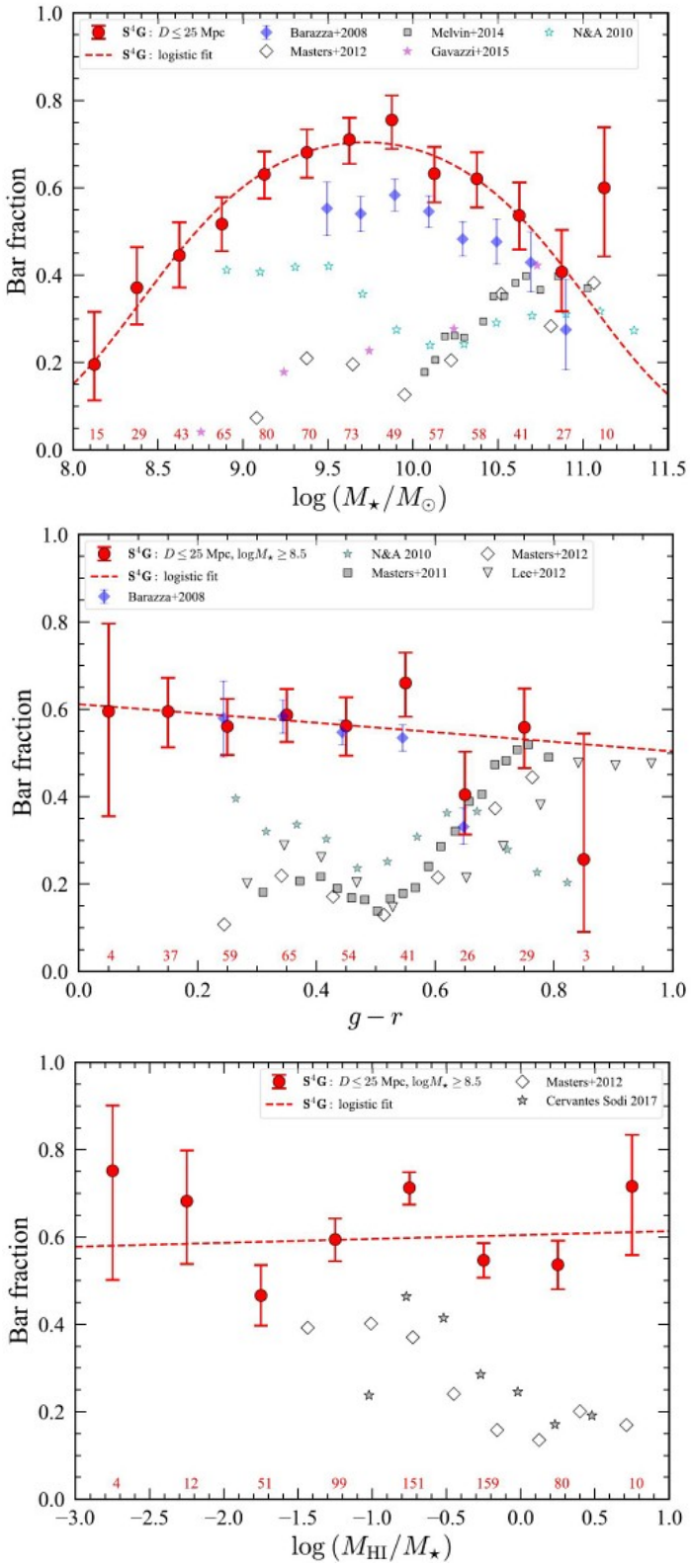

Figure 1.6: Bar fraction as a function of stellar mass (*top panel*), $g - r$ colour (*central panel*), and gas fraction (*bottom panel*). From Erwin (2018).

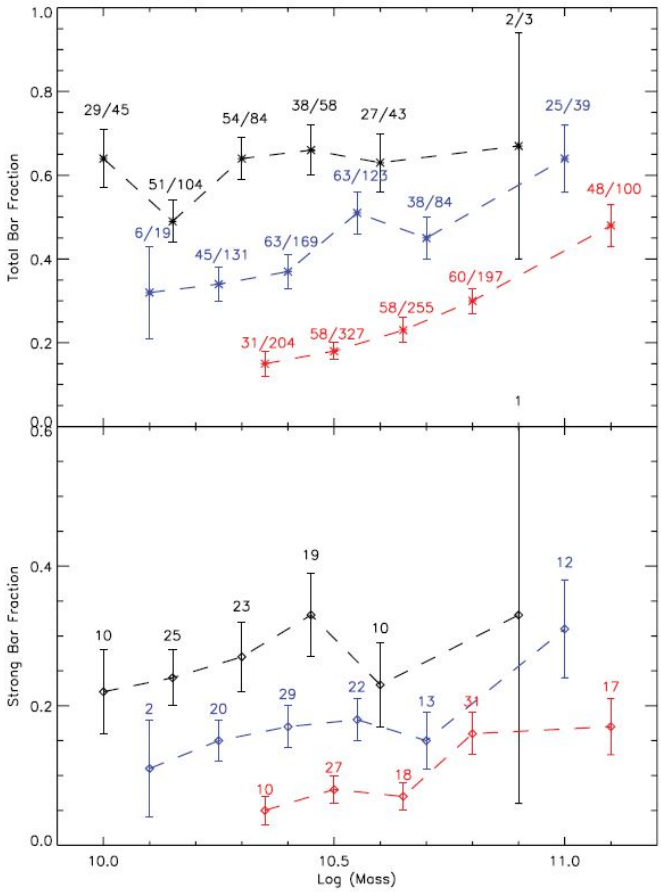

Figure 1.7: Total bar fraction (*top panel*) and strong bar fraction (*bottom panel*) as a function of Hubble type in three redshift bins: $0.14 \leqslant z \leqslant 0.37$ (black line), $0.37 \leqslant z \leqslant 0.60$ (blue line), and $0.60 \leqslant z \leqslant 0.84$ (red line). From Sheth et al. (2008).

The study of the properties of barred galaxies at high redshift suffers from some limitations. Due to the cosmological redshift, it becomes necessary to observe even longer passbands to identify a bar structure. In addition, the surface brightness is fainter and the spatial resolution is lower.

Jogee et al. (2004) analysed a sample of $\sim$ 1500 galaxies extracted from the Galaxy Evolution from Morphologies and Spectral Energy Distribution Survey (GEMS, Rix et al., 2004) in the redshift range $0.2 \leqslant z \leqslant 1$. Applying an isophotal analysis on the F606W and F850LP images observed with the HST/ACS, (Rix et al., 2004) found that the fraction of barred galaxies remains almost constant ($\sim$ 30%) till redshift $z \sim 0.7$.

Sheth et al. (2008) investigated the bar fraction in a sample $\sim$ 2100 face-on spiral galaxies extracted from the Cosmic Evolution Survey (COSMOS, Koekemoer et al., 2007)) located in a redshift range $0.14 \leqslant z \leqslant 0.84$. The fraction of barred spirals decreases rapidly with the redshift. In the Local Universe, the bar fraction (SB+SAB) in bright spiral galaxies is $\sim$ 65%, and it rapidly decreases to 20% at redshift $z \sim 0.84$. The fraction of strong bars decreases from 30% to $<$ 10%0. In addition, the fraction of bars has a dependence on the mass and colours of the host galaxies: the more massive, bright and redder galaxies host a higher fraction of bars with respect to the low massive galaxies (Fig. 1.7).

The study of the fraction of barred galaxies in different environments allows to explore the mechanisms that trigger the bar formation and the role of the environment in reshaping the properties of disc galaxies. Many works examined the possible correlation between the environment and barred galaxies, but the results did not agree (Thompson, 1981; Eskridge et al., 2000; Varela et al., 2004).

Méndez-Abreu et al. (2012) derived the bar fraction in different galaxy environments. The first sample they selected is composed by ∼2400 field galaxies extracted from the SDSS survey with absolute r-band magnitude in $-24 \lesssim M_r \lesssim -20$ mag range. A second sample, with fainter galaxies with respect to the first one, is composed of ∼ 350 disc galaxies with $-21 \lesssim M_r \lesssim -13$ mag, located in low-density environments. The third and fourth samples are composed by ∼590 and ∼170 disc galaxies located in the Virgo and Come clusters, respectively. They have $-22 \lesssim M_r \lesssim -13$ mag and $-23 \lesssim M_r \lesssim -14$ mag, respectively. Méndez-Abreu et al. (2012) visually inspected the galaxy images and derived the bar fraction as a function of the luminosity and galaxy environment. They found that the fraction of barred galaxies reaches a maximum value of ∼ 50% at $M_r = -20.5$ mag in clusters, whereas the peak of the bar fraction occurs at $M_r = -19$ mag in low-density environments. They argued that more massive, and thus brighter, disc galaxies are more robust against the galaxy interactions that can trigger the bar formation. On the contrary, fainter or less massive disc galaxies are fragile and prone to develop a bar. Their results showed that the fraction of barred galaxies depend on the properties of the host galaxies and not on the environment.

These results were later confirmed by Sarkar et al. (2021), who studied the bar fraction in a large sample of spiral galaxies extracted from the SDSS. Their sample consists in ∼ 11300 spiral galaxies whose morphological classification is provided through the Galaxy Zoo 2 project (Willett et al., 2013). The galaxies belong to a volume-limited sample with $z \lesssim 0.087$ and SDSS r-band absolute magnitude $M_r \leqslant -21$ mag. They performed multiple tests on the morphological classification of the galaxies to discard possible biases and verify statistical differences. They found no correlation between the barred/unbarred fraction of spiral galaxies and small and large-scale environments, confirming again that the formation and properties of bar mainly depend on the properties of host galaxies rather than the environment.

Recently, Tawfeek et al. (2022) have studied the bar fraction in 32 clusters of galaxies extracted from the OmegaWINGS survey (Gullieuszik et al., 2015). Their sample is composed of ∼ 3500 disc galaxies with a surface brightness in V-band $\mu_V \lesssim 21.5$ mag arcsec^{-2}. They performed both a visual inspection and an isophotal analysis of the galaxy images to identify the bar. They explored possible dependences of the bar fraction from the properties of the host galaxy, such as the total stellar mass, colour, morphological type, and its cluster environment. They found that the bar fraction increases with the mass of the galaxy, in agreement with previous studies, and a negative correlation with the colour, i.e. blue galaxies host a larger fraction of bars with respect to their red counterparts. The bar fraction also increases from early to late-type galaxies, but when the morphological type is fixed, the correlation with the colour disappears, indicating that the relation between the bar fraction and colour is driven by the morphological type. Moreover, Tawfeek et al. (2022) found that the bar fraction is maximum in the outermost regions of clusters. Since galaxies are morphologically transformed when infalling toward the centre of the cluster, they argued that the tidal forces may be responsible for a weakening or a dissolution of a bar.

1.2 Properties of bars

Bars are ellipsoidal structures that can be generally described by three parameters: the radius $R_{\rm bar}$, strength $S_{\rm bar}$, and pattern speed $\Omega_{\rm bar}$. In the following sections, we describe the bar properties and the various methods used to measure them.

Bar radius $R_{\rm bar}$

The bar radius $R_{\rm bar}$ represents the maximum radial extension of the stellar orbits which support the bar structure and it corresponds to the semi-major axis of the bar (Contopoulos, 1981). The determination of $R_{\rm bar}$ is not an easy task, since bar edges are not always well-defined. In addition, the bar is usually associated with other structures such as rings or spiral arms, which may affect and complicate the measure of $R_{\rm bar}$. In literature, many methods were proposed to estimate $R_{\rm bar}$, but each of them suffers from some limitations, therefore, the most reasonable choice is to use a combination of several methods.

- **Visual inspection/radial profile**: $R_{\rm bar}$ can be directly estimated on the image of a barred galaxy by visual inspection (Kormendy, 1979; Herrera-Endoqui et al., 2015). This technique is subjective and cannot be applied to high-redshift barred galaxies, since the resolution of the images drastically decreases. Alternatively, $R_{\rm bar}$ can be measured from the radial surface brightness profile (Gerssen et al., 1999). The light profile along the bar major axis shows a typical flat region, especially in early-type barred galaxies. This feature can be used to recover a qualitative measure of $R_{\rm bar}$.

- **Isophotal analysis**: the analysis of the radial profiles of ellipticity ϵ and position angle PA of the interpolated ellipses permits to measure $R_{\rm bar}$. Barred galaxies typically show a local maximum in the ϵ radial profile that corresponds to the bar region, while the radial profile of PA remains constant The measure of $R_{\rm bar}$ is defined as the radial distance at which the maximum of ϵ occurs, or alternatively, it could be defined as the radius at which the PA changes by an angle ΔPA=5° with respect to the PA of the isophote with the maximum ellipticity (Erwin & Sparke, 2003; Gadotti et al., 2007; Guo et al., 2019).

- **Fourier analysis**: the deprojected surface brightness $I(R,\phi)$ of a galaxy can be described with a Fourier series (Ohta et al., 1990; Aguerri et al., 2000):

$$I(R,\phi) = \frac{A_0(R)}{2} + \sum_{m=1}^{\infty} [A_m(R)\cos(m\phi) + B_m(R)\sin(m\phi)],$$

  where R is the galactocentric radius on the galaxy plane and ϕ is the azimuthal angle measured anticlockwise from the line of nodes. The Fourier coefficients are defined as follows:

$$A_m(R) = \frac{1}{\pi}\int_0^{2\pi} I(R,\phi)\cos(m\phi)\,{\rm d}\phi \qquad , \qquad B_m(R) = \frac{1}{\pi}\int_0^{2\pi} I(R,\phi)\sin(m\phi)\,{\rm d}\phi$$

  while the m-th Fourier amplitude is defined as:

$$I_m(R) = \begin{cases} A_0(R)/2 & \text{if } m = 0 \\ \sqrt{A_m^2(R) + B_m^2(R)} & \text{if } m \neq 0. \end{cases}$$

Since the $m = 2$ phase angle $\phi_2(R) = \arctan\left[A_2(R)/B_2(R)\right]$ remains almost constant in the bar region, it can be used to estimate $R_{\rm bar}$ (Debattista & Sellwood, 2000; Debattista et al., 2002). The bar radius can be defined as the radius at which the bar phase angle changes of $\Delta\phi_2 = 5^\circ$. Aguerri et al. (2003) proposed an independent measure of $R_{\rm bar}$ from the luminosity contrast between the bar and interbar region. In barred galaxies, the even Fourier components are more prominent with respect to the odd ones. In particular, the $m = 2$ is the predominant one. The intensity of the bar region is defined as $I_{\rm bar} = I_0 + I_2 + I_4 + I_6$, while the interbar region is defined as $I_{\rm interbar} = I_0 - I_2 + I_4 - I_6$. The bar radius is defined as the radial distance corresponding to the FWHM of the radial profile of the bar-interbar ratio $I_{\rm bar}/I_{\rm interbar}$:

$$\frac{I_{\rm bar}}{I_{\rm ibar}} > \frac{1}{2}\left[\max\left(\frac{I_{\rm bar}}{I_{\rm ibar}}\right) - \min\left(\frac{I_{\rm bar}}{I_{\rm ibar}}\right)\right] + \min\left(\frac{I_{\rm bar}}{I_{\rm ibar}}\right).$$

- **Photometric decomposition**: another way to estimate $R_{\rm bar}$ is by performing a photometric decomposition. The surface brightness of a galaxy is a combination of several galactic components with a specific light distribution. The bar radius is a free parameter in various parametric laws (see Sec. 1.1). It can be recovered by performing a photometric decomposition along the bar major and minor axes (Prieto et al., 2001) or on the entire image of the galaxy (Laurikainen et al., 2005; Gadotti, 2011; Méndez-Abreu et al., 2018b).

- **Tangential-to-radial force ratio**: an alternative method to measure $R_{\rm bar}$ employs the calculation of the gravitational potential of a barred galaxy. Originally, it was proposed by Buta et al. (2001) to perform a morphological classification of barred and unbarred systems. Only recently it has been applied by Lee et al. (2020) to measure $R_{\rm bar}$. Given a gravitational potential $\Phi(R,\theta)$ in a disc plane in polar coordinates (R,θ), the mean asymmetric radial force $\langle F_R(R)\rangle$ and transverse force $F_T(R,\theta)$ are defined as:

$$\langle F_R(R)\rangle \equiv R\frac{d\Phi_0}{dR} \quad , \quad F_T(R,\theta) \equiv \left|\frac{\partial\Phi(R,\theta)}{\partial\theta}\right|$$

where Φ_0 is the $m = 0$ Fourier component of the gravitational potential. The tangential-to-radial force map is defined as:

$$Q_T(R,\theta) = \frac{F_T(R,\theta)}{\langle F_R(R)\rangle}.$$

The map presents four thick slabs corresponding to the four edges of the bar, while in Cartesian coordinate, it presents a typical butterfly-shaped pattern. The azimuthally-averaged radial profile of the transverse-to-radial force ratio $\langle Q_T\rangle$ (R) is defined as:

$$\langle Q_T(R)\rangle = \frac{1}{2\pi}\int_0^{2\pi} Q_T(R,\theta)d\theta.$$

Bar radius is defined as the radial distance at which $\langle Q_T(R)\rangle$ reaches a maximum value.

Bar strength $S_{\rm bar}$

The bar strength $S_{\rm bar}$ represents the bar contribution to the total gravitational potential of the galaxy (Buta et al., 2001). It can be interpreted as the fraction of stars in the bar region that one has to rearrange to transform the structure into an axisymmetric one. As for $R_{\rm bar}$, many methods were proposed to measure $S_{\rm bar}$:

- **Bar axial ratio**: bar strength can be measured using the bar shape (Abraham & Merrifield, 2000; Aguerri et al., 2009) through the formula:

$$S_{\rm bar} = \frac{2}{\pi}\Big[\arctan\left(q_{\rm bar}\right)^{-0.5} - \arctan\left(q_{\rm bar}\right)^{0.5}\Big],$$

  where $q_{\rm bar}$ is the bar axial ratio. It can be recovered by performing an isophotal analysis and measuring the bar ellipticity $\epsilon_{\rm bar} = 1 - q_{\rm bar}$ at the bar radius, or alternatively, it can be estimated by modelling the shape of the bar with a photometric decomposition. $S_{\rm bar}$ varies from 0 for an unbarred system to 1 for a strongly barred system.

- **Fourier analysis**: an alternative method to estimate $S_{\rm bar}$ is using the Fourier analysis. Since in a barred galaxy the even Fourier components are larger than the odd ones, they can be used to measure $S_{\rm bar}$. It is defined as the mean value of the $m = 2$ Fourier relative amplitude I_2/I_0 calculated in the bar region (Aguerri et al., 2000):

$$S_{\rm bar} = \frac{1}{R_{\rm bar}}\int_0^{R_{\rm bar}} \frac{I_2(R)}{I_0(R)} dR.$$

  Alternatively, $S_{\rm bar}$ can be estimated by measuring the maximum value of the $m = 2$ Fourier relative amplitude (Athanassoula & Misiriotis, 2002; Guo et al., 2019):

$$S_{\rm bar} = \left(\frac{I_2(R)}{I_0(R)}\right)_{\rm max}.$$

- **Tangential-to-radial force ratio**: an alternative measure of $S_{\rm bar}$ can be obtained from the tangential-to-radial force ratio map $Q_T(R,\theta)$ (Buta et al., 2001; Lee et al., 2020):

$$S_{\rm bar} = Q_b \equiv \frac{1}{m}\sum_{i=1}^{m} Q_{T,i},$$

  where $Q_{T,i}$ is the maximum value of each i-th peak of $Q_T(R_{\rm bar},\theta)$ azimuthal profile, and m is equal to four for a bar structure.

Aguerri et al. (2009) analysed the bar properties in a sample of galaxies of the CALIFA survey. They applied an isophotal analysis on the galaxy images to measure $R_{\rm bar}$ by using the ϵ and PA radial profiles. According to the PA radial profile method, early-type barred galaxies host longer bars (S0: $\langle R_{\rm bar}\rangle^{\rm PA}$=5.6 kpc, S0/a: $\langle R_{\rm bar}\rangle^{\rm PA}$=5.4 kpc, Sbc-Sm: $\langle R_{\rm bar}\rangle^{\rm PA}$=4.9 kpc). The measure of $R_{\rm bar}$ obtained from the ϵ radial profile method is systematically smaller (S0: $\langle R_{\rm bar}\rangle^{\epsilon}$=3.5 kpc, S0/a: $\langle R_{\rm bar}\rangle^{\epsilon}$=4.0 kpc, Sbc-Sm: $\langle R_{\rm bar}\rangle^{\epsilon}$=3.8 kpc). Moreover, $R_{\rm bar}$ correlates with the galaxy size since larger galaxies host longer bars. They also found that early-type barred galaxies have a lower value of $S_{\rm bar}$ (S0: $\langle S_{\rm bar}\rangle = 0.16$) with respect to their late-type counterparts (S0/a: $\langle S_{\rm bar}\rangle = 0.19$, Sbc-Sm: $\langle S_{\rm bar}\rangle = 0.20$).

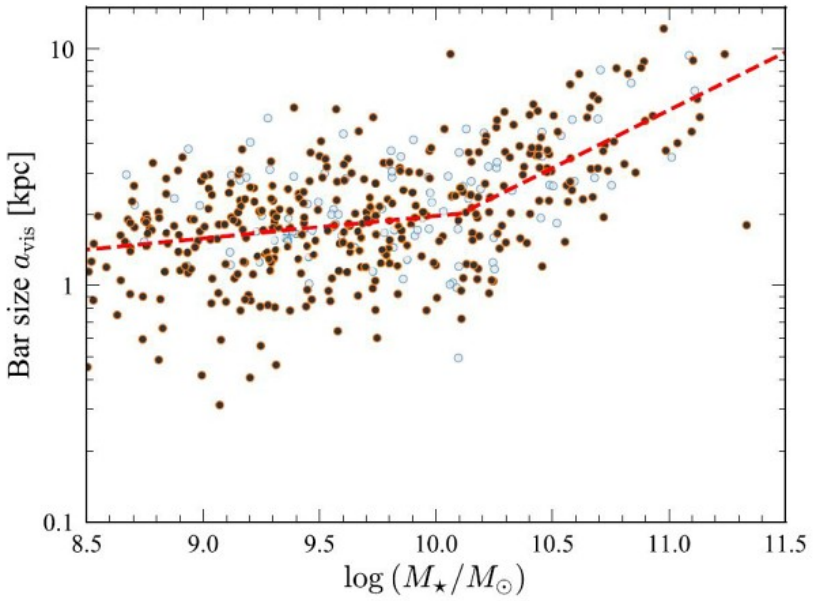

Figure 1.8: Bar radius as a function of stellar mass for galaxies with distance $D < 25$ Mpc (filled circles) and with a distance between $25 \leqslant D \leqslant 30$ Mpc (open circles). The dashed red line represents a broken linear fit to all the galaxies with mass $\log(M_\star/\mathrm{M}_\odot) = 9 - 11$. From Erwin (2018).

Erwin (2018) studied possible dependencies of $R_{\rm bar}$ from galaxies properties in a sample of ∼650 spiral galaxies from the S^{4}G survey. He found a correlation between the bar size and mass of the host galaxy, finding that long bars are frequent in massive galaxies and this relation becomes steeper at even larger stellar masses (Fig. 1.8).

Cuomo et al. (2019b) studied a sample of ∼ 50 galaxies classified as weakly and strongly barred galaxies according to the classification provided by the CALIFA survey. They found that weakly barred galaxies do not host a genuine bar component or the central structure is not in rigid rotation. Both the weakly and strongly barred galaxies have similar bulge properties. They finally proposed a quantitative way to separate bars into weak and strong using $S_{\rm bar}$=0.4 as the dividing value.

Kim et al. (2021) explored the evolution of the bar parameters with the redshift in a sample of ∼ 380 galaxies extracted from the COSMOS survey in redshift range $0.2 \leqslant z \leqslant 0.84$ and with stellar mass $10.0 \leqslant \log(M_\star/\mathrm{M}_\odot) \leqslant 11.4$. They found that the median value of $R_{\rm bar}$ remains nearly constant with the redshift, independently from the stellar mass (Fig. 1.9, left panel). The normalised bar radii show the same trend, suggesting that the bar evolves in proportion to the disc growth. The relation between the bar size and stellar mass of the host galaxies is still valid at higher redshift (Fig. 1.9, right panel). The bar strength does not evolve with the redshift both in low and high-massive systems. (Fig. 1.10).

More recently, Guo et al. (2022) have recovered the properties of bars hosted in high redshift galaxies ($1 \leqslant z \leqslant 3$) by analysing the James Webb Space Telescope (JWST, Gardner et al., 2006) near-infrared images. The excellent sensitivity and resolution of JWST (FWHM∼ 0.16 arcsec) permitted to identify and measure the bar properties in 6 galaxies with a stellar mass of $M_\star \sim 2 \times 10^{11}\,\mathrm{M}_\odot$. The values of $R_{\rm bar}$ and $S_{\rm bar}$ were measured by performing an isophotal analysis on the deprojected images of the galaxies.

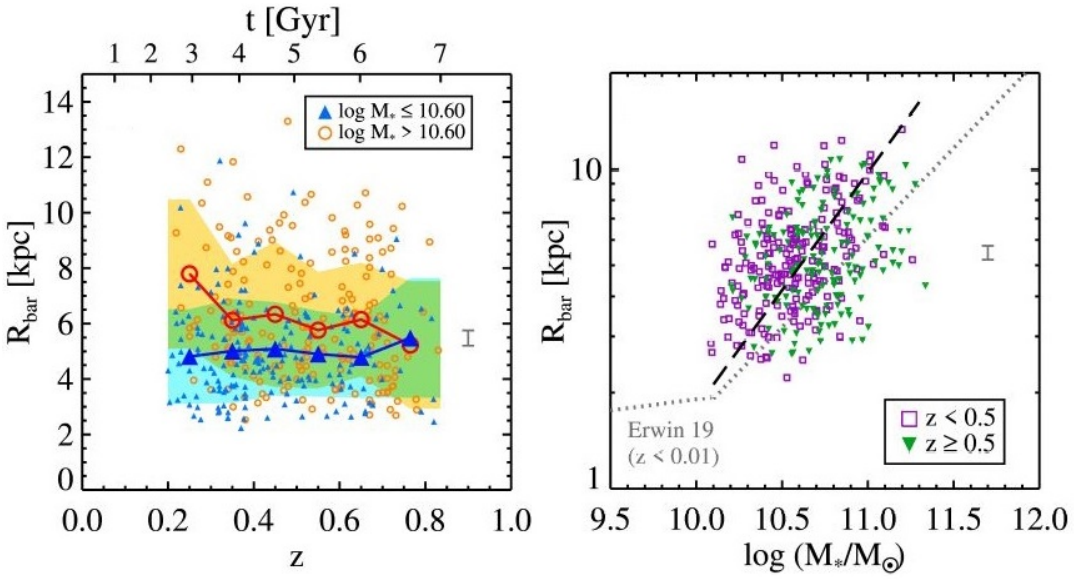

Figure 1.9: *Left panel*: Bar radius as a function of redshift for low-mass (triangles) and high-mass (circles) systems. Larger triangles (circles) connected with a solid line and a blue (orange) shaded area represent the mean value at each redshift bin for low (high) mass systems with the associated uncertainty, respectively. *Right panel*: Bar radius as a function of stellar mass. The black dashed line represents the least-square fit to all the data. The dotted broken line marks the weighted regression fit for nearby ($D < 30$ Mpc) galaxies from Erwin (2018). From Kim et al. (2021).

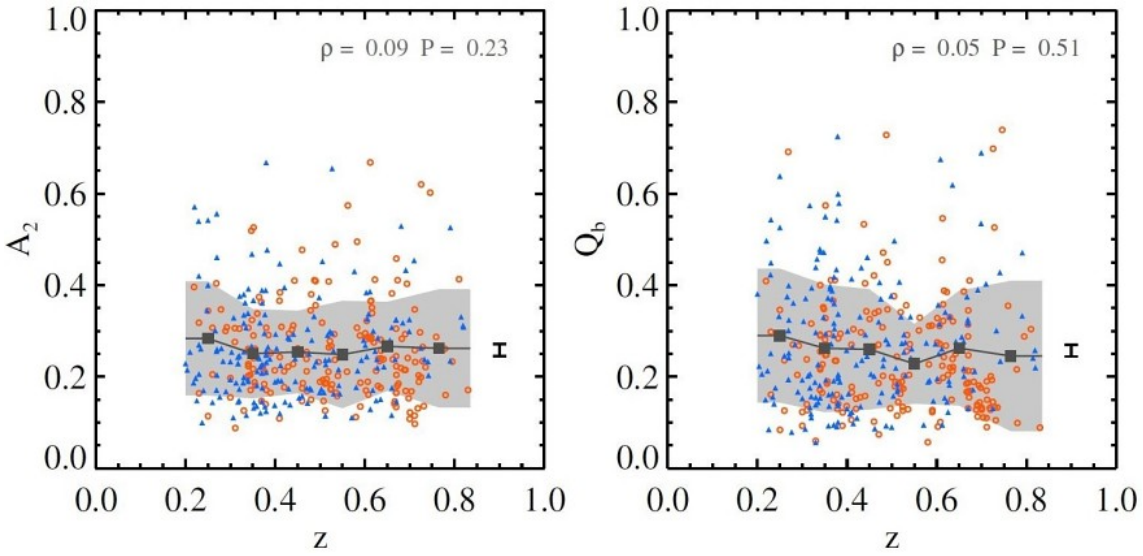

Figure 1.10: Bar strength as a function of redshift. Bar strength is measured as the maximum of relative $m = 2$ Fourier amplitude (*left panel*) and as the maximum of the tangential-to-radial force ratio (*right panel*). The black squares represent the mean value at each redshift bin while the grey-shaded area is the standard deviation. Orange circles and blue triangles represent high and low-mass galaxies. From Kim et al. (2021).

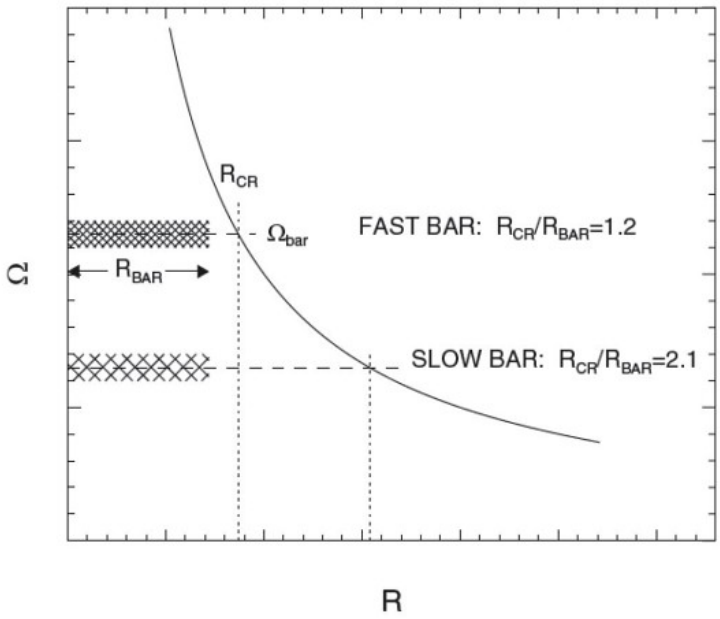

Figure 1.11: Schematic representation of fast and slow bars. The shaded region represents the bar radius, the horizontal dashed lines identify the value of the bar pattern speed for a slow ($\mathcal{R}$=2.1) and fast bar ($\mathcal{R}$=1.2) and corresponding values of the corotation radius are marked by the vertical dotted lines. From Rautiainen et al. (2008).

Bar pattern speed $\Omega_{\rm bar}$

The bar pattern speed $\Omega_{\rm bar}$ is the angular frequency with which the bar rotates around the galactic centre. It is a dynamical parameter so it requires the measurement of the stellar kinematics. It is usually parameterised with the rotation rate $\mathcal{R}$ defined as:

$$\mathcal{R} \equiv \frac{R_{\rm cor}}{R_{\rm bar}},$$

where $R_{\rm cor}$ is the corotation radius and represents the galactocentric distance at which the centrifugal and gravitational forces balance each other in the bar rest-frame. The corotation radius can be obtained from the bar pattern speed and stellar circular velocity $V_{\rm circ}$ assuming a flat rotation curve:

$$R_{\rm cor} = \frac{V_{\rm circ}}{\Omega_{\rm bar}}.$$

The rotation rate $\mathcal{R}$ is a dimensionless parameter that does not depend on the distance of the galaxy and allow to classify bars into fast ($1 \leqslant \mathcal{R} \leqslant 1.4$) and slow ($\mathcal{R} > 1.4$) (Athanassoula, 1992; Debattista & Sellwood, 2000). The value of 1.4 does not correspond to a specific value of $\Omega_{\rm bar}$, it was chosen by general consensus in the literature. If the bar ends close to the corotation radius, it is rotating as fast as it can, whereas it is defined as slow if the corotation radius exceeds the bar radius (Fig. 1.11). Bars with $\mathcal{R} < 1$ are termed ultrafast but are considered unphysical objects since in this regime, stellar orbits align perpendicularly to the bar major axis and do not support the bar structure anymore (Contopoulos, 1981). Many methods were proposed in the literature to directly or indirectly measure $\Omega_{\rm bar}$.

- **Analysis of dust lanes**: the study of the shape and offset of dust lanes reveals the location of Lindblad resonances (Athanassoula, 1992; Sánchez-Menguiano et al., 2015). Dust lanes are the locations where the gas accumulates and can extend from the nuclear to the spiral arm region. They can be straight or curved and their curvature depends on the bar strength. Athanassoula (1992) first visually analysed the shape of dust lanes using hydro-dynamical simulations of gas. She concluded that a strong fast bar has straighter dust lanes, whereas a fast weak bar has curved dust lanes. Fast bar dust lanes show an *offset* from the bar major axis, while slow bars have *centred* dust lanes. The position of the dust lanes is linked with $\Omega_{\rm bar}$ since it regulates the location of the resonances and $R_{\rm cor}$.

- **Puerari & Dottori method**: an alternative way to recover the position of $R_{\rm cor}$ is studying the location of the shock-induced regions (Puerari & Dottori, 1997). The star-forming activity produces an azimuthal gradient of age that assumes the opposite sign across the corotation radius. Young and old stellar populations azimuthally invert across the spiral arms. Performing a Fourier analysis on red and blue images of the galaxy allows to study the stellar populations in the disc. The intersection of the phase angles of density waves of these stellar populations marks the location of $R_{\rm cor}$.

- **Comparison with N-body simulations**: $\Omega_{\rm bar}$ can be estimated by comparing the photometric and kinematic properties of barred galaxies with simulations. Weiner et al. (2001) used fluid-dynamical models of gas flow to study the gas kinematics in barred galaxies. Rautiainen et al. (2008), instead, used simulations composed by both stellar and gaseous particles to compare the morphology of simulated barred galaxy with the observations. The gravitational potential can be directly estimated from the light distribution assuming a constant mass-to-light ratio M/L, but models strongly depend on the adopted $\Omega_{\rm bar}$.

- **Identification of Lindblad resonances with rings**: rings are circular or elliptical structures usually associated with resonances. The inner rings are located closer to the inner Lindblad resonance, while the outer rings are usually associated with the presence of an outer Lindblad resonance. The correct identification of rings with resonances allows to recover the location of $R_{\rm cor}$ (Jeong et al., 2007).

- **Zhang & Buta method**: an alternative way to estimate $R_{\rm cor}$ is studying the azimuthal phase-shift between the bar potential and density waves (Zhang & Buta, 2007). While density waves rigidly rotate around the galactic centre, stars located in different regions of the disc have differential rotation. Stars are faster than density waves in the innermost region of the galaxy, and slower in the outermost region. The positive-to-negative phase shift between the density waves and stars occurs at the $R_{\rm cor}$. The gravitational potential can be estimated from the light distribution assuming a constant M/L ratio.

- **Font & Beckman method**: recently, Font et al. (2011) have developed an independent method to identify the location of $R_{\rm cor}$ in disc galaxies by using 2D stellar or gaseous kinematic data. The kinematic fields are used to estimate a 2D model of the circular velocity of the galaxy that is subtracted from the observed velocity map. The residual map only contains the non-circular velocity component, and the zero points correspond to the locations where a phase change of 180° in the flow vector of the streaming motions occurs. These points correspond to the location of resonances. It is possible to identify the position of $R_{\rm cor}$ by comparing the reconstructed histogram of the zero points with the image of the galaxy.

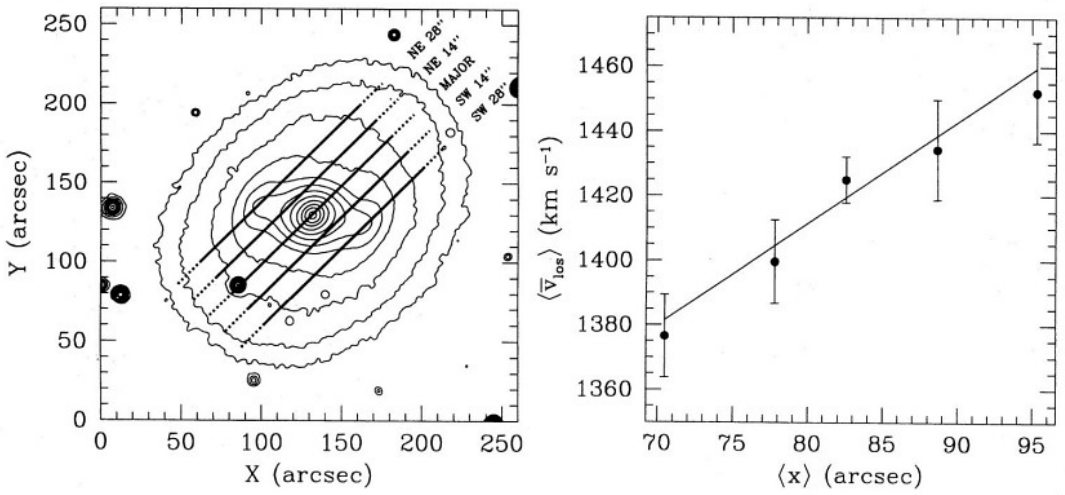

Figure 1.12: *Left panel*: Contour plot of I-band image of galaxy NGC 936 superimposed with the position of the apertures. *Right panel*: Photometric and kinematic integrals measured along the apertures with the best linear fit to the data (black line). From Merrifield & Kuijken (1995).

- **Tremaine & Weinberg method**: the only direct method to measure $\Omega_{\rm bar}$ is the one proposed by Tremaine & Weinberg (1984) (hereafter TW) which correlates the bar pattern speed with observable quantities. This method is based on three main assumptions: 1) the disc is flat and axisymmetric, 2) the bar rotates as a rigid body, which means the bar has a well-defined $\Omega_{\rm bar}$, and 3) the tracer satisfies the following continuity equation:

$$\langle V \rangle = \langle X \rangle \sin(i)\, \Omega_{\rm bar}$$

where i is the disc inclination, and $\langle X \rangle$ and $\langle V \rangle$ represent the luminosity-weighted position and line-of-sight (LOS) velocity of the tracer, respectively (Merrifield & Kuijken, 1995; Merrifield et al., 2006). The quantities $\langle X \rangle$ and $\langle V \rangle$ are known as photometric and kinematic integrals and are defined as:

$$\langle X \rangle = \frac{\int X \Sigma \, d\Sigma}{\int \Sigma \, d\Sigma} \quad , \quad \langle V \rangle = \frac{\int V_{\rm LOS} \Sigma \, d\Sigma}{\int \Sigma \, d\Sigma}$$

where Σ is the surface brightness of the tracer that has to be proportional to the surface mass density of the tracer itself. These quantities have to be measured along apertures perfectly centred on the disc minor axis, parallel to the disc major axis, crossing the bar region (Fig. 1.12, left panel). The integration of photometric and kinematic integrals has to be in principle performed in the range $(-\infty, +\infty)$, however, it is sufficient to measure them in apertures long enough to map the entire disc region. In this way, the contribution of the disc contained in the half-length of the aperture will be balanced by the contribution in the other half, and it will remain only the signature of the bar component. The value of $\langle X \rangle$ is measured by calculating the weighted average of the total flux profile of each aperture, while $\langle V \rangle$ can be measured by collapsing along its spatial direction a long-slit spectrum or co-adding all the integral-field spectra contained in an aperture and measuring the average velocity of the stars from a one-dimensional spectrum.

Photometric and kinematic integrals dispose along a line (Fig. 1.12, right panel) the slope of the best-fitting line is proportional to the disc inclination and $\Omega_{\rm bar}$. The most suitable tracer for the application of the TW method are old stars, with no star formation activity and patchy dust lanes. Several works applied the TW method with a gaseous tracer (Bureau et al., 1999; Banerjee et al., 2013; Patra & Jog, 2019), however, its reliability is unclear since gas could presents shocks or phase transition and thus it does not satisfy the continuity equation.

Rautiainen et al. (2008) recovered $\Omega_{\rm bar}$ in 38 barred galaxies extracted from the OSUBSG survey. They modelled and compared the morphology of observed and simulated barred galaxies and found that $\mathcal{R}$ depends on the morphological type. Early-type barred galaxies (S0/Sab) have on average $\langle\mathcal{R}\rangle$=1.15±0.25, intermediate morphological types (Sb) have $\langle\mathcal{R}\rangle$=1.44±0.29 whereas late-type galaxies (Sbc-Sc) have $\langle\mathcal{R}\rangle$=1.82±0.63. In addition, slow bars are usually shorter. A similar correlation was found by Buta & Zhang (2009), that recovered $\Omega_{\rm bar}$ in a sample of $\sim$ 150 barred galaxies recovering the location of $R_{\rm cor}$ by calculating the phase-shift between the density wave and bar potential. They found that early-type barred galaxies have on average a lower value of $\mathcal{R}$ ($\mathcal{R}$=1.03±0.37) with respect to that of late-type barred galaxies ($\mathcal{R}$=1.50±0.63). Many of these measures of $\Omega_{\rm bar}$ obtained by indirect methods do not have a solid estimation of the uncertainty, it remains unclear if the resulting $\mathcal{R}$ is fully reliable.

The TW method is the only model-independent method that allows the measure of $\Omega_{\rm bar}$, but despite its simple application, it presents many sources of errors (Corsini, 2011). The measure of $\Omega_{\rm bar}$ is affected by the correct identification of the galactic centre coordinates and systemic velocity of the galaxy $V_{\rm syst}$. To deal with this issue with long-slit spectroscopic data, it is necessary to fix an arbitrary reference position and velocity frame common for all the pseudoslits. Integral-field data permits instead to correctly estimate the centre of the galaxy, defining the pseudo-slits *a posteriori* on the reconstructed image, and thus minimising the error associated with the correct centring. The values of $\langle X\rangle$ and $\langle V\rangle$ are sensible to the noise of the data. To increase the signal-to-noise (S/N), it is possible to collapse along the spatial direction a long-slit spectrum (Merrifield & Kuijken, 1995) or to sum all the integral-field spectra within a pseudo-slit (Debattista & Williams, 2004). The main source of uncertainty in the TW method is the correct identification of the disc position angle. Since the apertures have to be parallel to the disc major axis, it is mandatory to accurately measure the disc orientation. Debattista (2003) explored the sensitivity of the TW method to the uncertainty in disc PA using simulated galaxies with different inclinations, finding that an error of ΔPA$\sim 2^\circ - 4^\circ$ results in a relative uncertainty of $\Delta\Omega_{\rm bar}/\Omega_{\rm bar}$=0.3. The presence of rings or spiral arms can also affect the correct estimate of the disc PA. Galaxies with inclination in the range $50^\circ \leqslant i \leqslant 60^\circ$ and with a bar oriented with an angle of 20° with respect to the line-of-node (LON) are less sensitive to misalignment. The dust obscuration and star formation activity represent an additional source of error in the TW method. (Gerssen & Debattista, 2007) explored the effect of the dust and star formation rate in the TW method using simulated galaxies. They found that a diffuse disc of dust with a mean value of the extinction $A_V \sim 3$ results in uncertainty on bar pattern speed of $\Delta\Omega_{\rm bar}/\Omega_{\rm bar}$=0.05. Dust lanes with a mean value of the extinction $A_V \sim 3$, instead, lead to a relative error of $0.08 \leqslant \Delta\Omega_{\rm bar}/\Omega_{\rm bar} \leqslant 0.25$. Finally, the number of adopted pseudo-slits may affect the final estimate of $\Omega_{\rm bar}$. Since the $\Omega_{\rm bar}$ is determined by fitting $\langle X\rangle$ and $\langle V\rangle$ with a straight line, the accuracy in the measure of $\Omega_{\rm bar}$ depends on the number of pseudoslits. The number of slits is limited when long-slit spectroscopy is employed, integral-field spectroscopy, instead, permits to define *a posteriori* a larger number of pseudoslits.

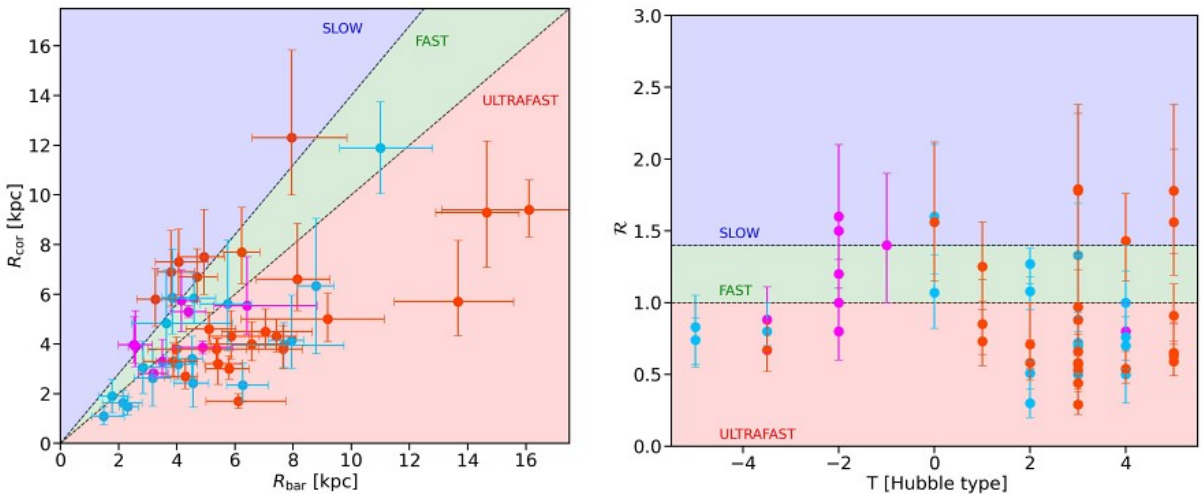

Figure 1.13: Corotation radius as a function of bar radius (*left panel*) and rotation rate as a function of the Hubble type (*right panel*) for galaxies with a relative error $\Delta\Omega_{\rm bar}/\Omega_{\rm bar}<50\%$ on bar pattern speed. Blue circles represent data from the CALIFA survey (Aguerri et al., 2015; Cuomo et al., 2019b), red circles show data from the MANGA survey (Guo et al., 2019; Garma-Oehmichen et al., 2020), and magenta circles mark long-slit data (Corsini, 2011) and integral-field spectroscopic MUSE data (Cuomo et al., 2019a). Red, green, and blue shaded areas represent the ultrafast, fast, and slow regimes, respectively.

Zou et al. (2019) has recently explored possible limitations and uncertainties in the application of the TW method with integral-field data using simulated barred galaxies. Their mock galaxies span a large variety of disc inclination and PA, bar orientation, and spatial resolution. They concluded that to obtain an accurate measure of $\Omega_{\rm bar}$ it is necessary to use pseudo-slits located in the bar region, avoiding apertures that contain the bar edges. In addition, they suggested constructing perfect rectangular pseudo-slits instead of defining irregularly-shaped apertures. They pointed out the importance of checking the convergence of photometric and kinematic integrals, evaluating that the value of $\langle X\rangle$ and $\langle V\rangle$ in pseudo-slits with different lengths remains almost constant. This allows to define of a minimum length for the adopted pseudoslits, avoiding spurious sources that can affect the accuracy of the measures.

The TW method has been extensively applied by using both long-slit data (Corsini, 2011) and integral-field data on samples of galaxies extracted from CALIFA survey (Sánchez et al., 2012), Mapping Nearby Galaxies at APO survey (MANGA, Bundy et al., 2015), and Physics at High Angular resolution in Nearby GalaxieS with MUSE survey (PHANGS, Emsellem et al., 2022). In Fig. 1.13 we show all the measures of $\Omega_{\rm bar}$ obtained from the application of the TW method and with a relative error lower than $\Delta\Omega_{\rm bar}/\Omega_{\rm bar}<0.5$. The whole sample is composed of more than 100 barred galaxies that span a large variety of morphological types, from lenticular to very late-type spiral galaxies. Blue circles represent galaxies extracted from the CALIFA survey (Aguerri et al., 2015; Cuomo et al., 2019b), red circles are those extracted from the MANGA survey (Guo et al., 2019; Garma-Oehmichen et al., 2020), and magenta circles are galaxies studied with long-slit (Corsini, 2011) and integral-field spectroscopic data (Cuomo et al., 2019a). The majority of bars result to be consistent with the fast regime (Corsini, 2011; Aguerri et al., 2015; Cuomo et al., 2019b,a; Guo et al., 2019; Garma-Oehmichen et al., 2020, 2022) with a mean value of $\langle\mathcal{R}\rangle\sim1.1$. Moreover, there is no clear dependence of $\mathcal{R}$ with the galaxy morphological types.

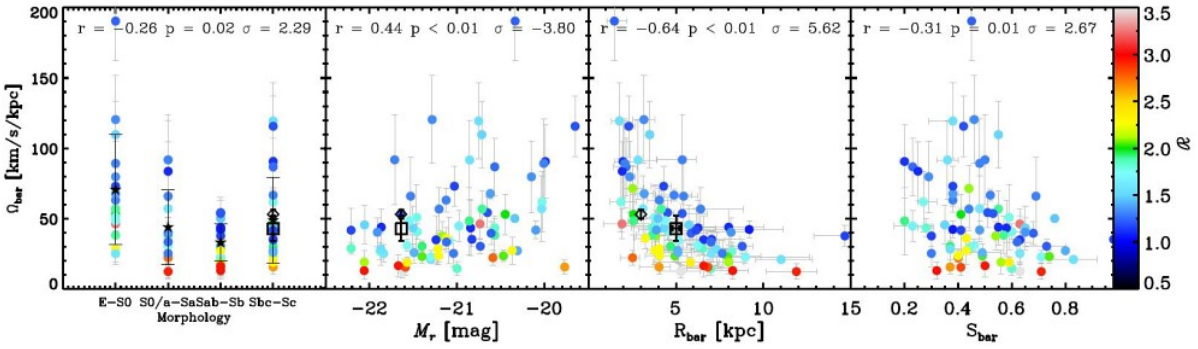

Figure 1.14: Bar pattern speed as a function of morphological type, total absolute r-band magnitude, bar radius, and bar strength. Points are colour-coded by the value of $\mathcal{R}$. The black-filled stars represent the mean value of $\Omega_{\rm bar}$ for each bin of Hubble type. The black open diamond (square) represents the result of the Milky Way for the short (long) bar case. From Cuomo et al. (2020).

Cuomo et al. (2020) collected all the available data of barred galaxies for which $\Omega_{\rm bar}$ was accurately estimated with the TW method and explored possible relations between the bar properties and the structural parameters of the host galaxy (Fig. 1.14). They found that longer bars are stronger and rotate with slower angular frequency. This is in agreement with theoretical predictions on the secular evolution of bars, according to which bars evolve in time exchanging angular momentum with disc and halo, growing in size and strength while $\Omega_{\rm bar}$ is slowly decreasing (Debattista & Sellwood, 1998, 2000; Athanassoula, 2003). In addition, they found that longer bars are more frequent in bright galaxies that have larger corotation radii (e.g. larger value of $\mathcal{R}$).

A large fraction of barred galaxies analysed so far with the TW method locates in the ultrafast regime ($\mathcal{R}$<1) with more than 90% of confidence level (Fig. 1.13, left panel). Theoretical works on the orbital structure of barred galaxies showed that these ultrafast bars should not exist since the x_1 family of stellar orbits that sustain the bar structure never exceed $R_{\rm cor}$ (Contopoulos, 1981; Athanassoula, 1992). Stellar orbits with radial extension longer than $R_{\rm cor}$ are aligned perpendicular to the bar major axis and tend to weaken the bar structure that will dissolve in a few rotations around the galactic centre. A large number of ultrafast bars were found by the application of other methods to recover $\Omega_{\rm bar}$. Buta & Zhang (2009) first found a non-negligible fraction of ultrafast bars arguing that the $R_{\rm cor}$ can locate inside the bar region. Recently, (Zou et al., 2019) have found that ultrafast bars could be the result of a wrong estimation of the angle between the bar and disc. They used N-body simulations to show that a misalignment of the disc PA results in an overestimation of $\Omega_{\rm bar}$ and thus an underestimation of $\mathcal{R}$. Further investigation is required to assess if ultrafast bars are a special type of bars or if they are due to a wrong estimation of $R_{\rm bar}$ and $R_{\rm cor}$ (Buta, 2017).

On the contrary, slow bars are rare objects. In Fig. 1.15 we reported all the slow bars avaiable in literature for which the $\Omega_{\rm bar}$ was obtained using both direct and indirect methods and with a face value of $\mathcal{R}\geqslant$1.4. Many slow bars from TW-based works with a stellar tracer have large uncertainties and are not fully consistent with the slow regime (Gerssen et al., 2003; Aguerri et al., 2003, 2015; Guo et al., 2019). Few slow bars are gaseous bars and were observed by applying the TW method on H I (Bureau et al., 1999; Banerjee et al., 2013) or H II (Chemin & Hernandez, 2009; Fathi et al., 2009; Patra & Jog, 2019). The reliability of these latter results is still unclear since a gaseous tracer could not fully satisfy the continuity equation. Many slow bars were detected by applying indirect methods to recover $\Omega_{\rm bar}$ (Buta et al., 1998; Rautiainen et al., 2008; Buta & Zhang, 2009; Font et al., 2014).

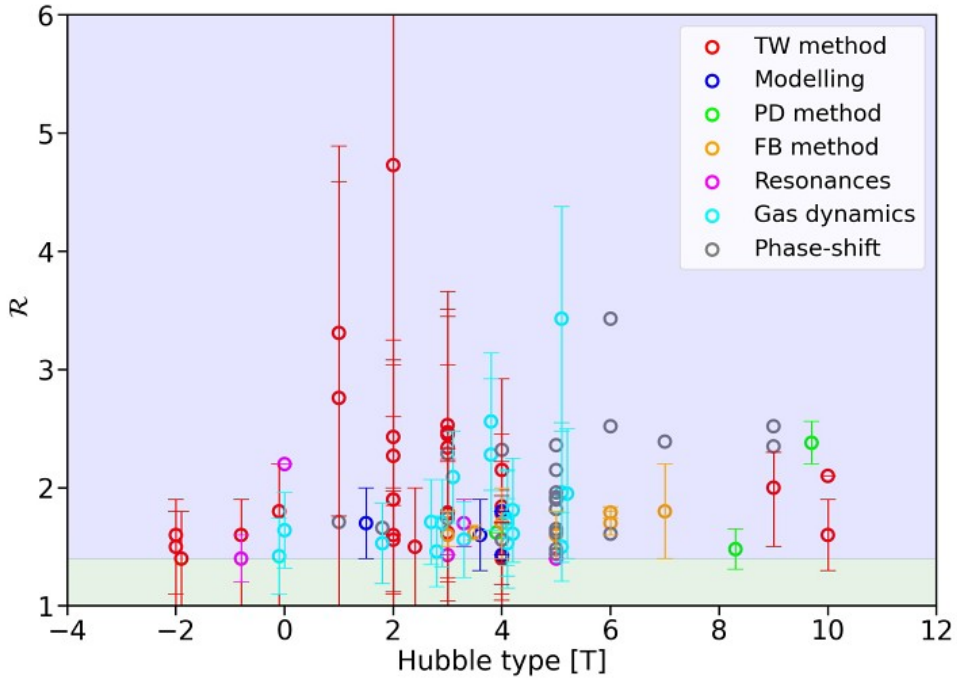

Figure 1.15: Rotation rate as a function of morphological type for all the slow bars with a face value of $\mathcal{R}\geqslant 1.4$. Different colours represent different methods adopted to recover $\Omega_{\rm bar}$ TW method (red), comparison with the N-body simulations (blue), Puerari & Dottori method (green), Font & Beckman method (yellow), identification of $R_{\rm cor}$ with rings (pink), modelling of gas dynamics (cyan), and Zhang & Buta method (grey).

All these methods are model-dependent and suffer from some limitations. Buta et al. (1998) used the locations of the rings to identify $R_{\rm cor}$ and gas kinematics to recover $V_{\rm circ}$. The correct identification of resonances is not a straightforward task, especially in late-type galaxies that can present multiple structures as pseudo-rings and spiral arms. Gas dynamical models and N-body simulations provide a non-unique solution when compared to the actual morphology of a barred galaxy (Rautiainen et al., 2008). Finally, results provided by indirect methods do not always have a solid estimate of the uncertainty. Further analysis is needed to investigate the paucity of slow bars.

1.3 Dynamics of barred galaxies

Bars play an important role in stellar dynamics and in the exchange of the angular momentum among the several components of a galaxy (Sellwood & Wilkinson, 1993). Stars in an unperturbed disc orbit onto nearly circular orbits. The presence of an ellipsoidal structure, like a bar, introduces a non-axisymmetric component in the total gravitational potential of the galaxy, which modifies the original path of the stars. Planar orbits in a barred galaxy can be described with the epicyclic approximation as a composition of a retrograde elliptical orbit with *angular epicyclic frequency* k superimposed to a circular orbit with *angular frequency* Ω. The changes in stellar orbits depend on the amount of angular momentum that stars absorb or emit in the proximity of a *resonance*.

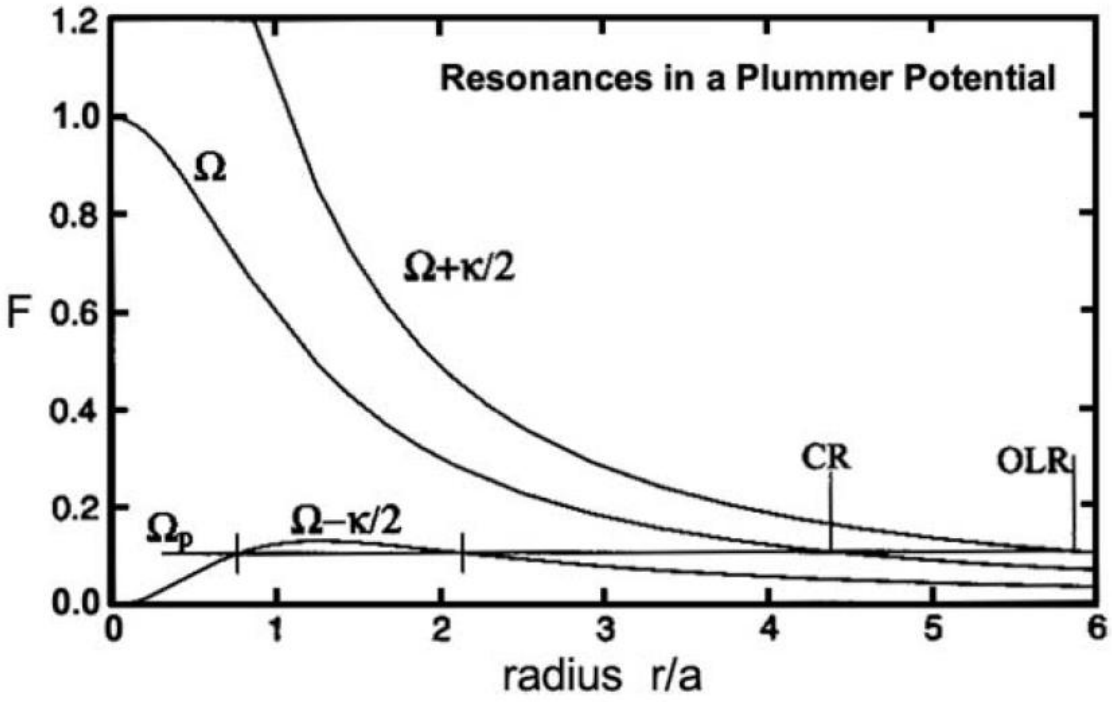

Figure 1.16: Angular velocity (Ω) and resonances in a Plummer potential. For a given value of Ω_p, the corotation (CR) occurs at $\Omega_p = \Omega$, two ILRs occur at $\Omega_p = \Omega - k/2$, and OLR occurs at $\Omega_p = \Omega + k/2$. From Sparke & Gallagher (2000).

A resonance occurs when a star performs a fixed number of radial oscillations each time the star goes around the bar:

$$lk + m\Omega = m\Omega_p,$$

where Ω_p and Ω are the angular frequency of the bar and star, and l and m are integer numbers, respectively. The most important resonances are:

- the *corotation* (CR), where $\Omega_p = \Omega$ ($l = 0$, $m = 1$);
- the *inner Lindblad resonance* (ILR) where $\Omega_p = \Omega - k/2$ ($l = -1$, $m = 2$) ;
- the *outer Lindblad resonance* (OLR) where $\Omega_p = \Omega + k/2$ ($l = 1$, $m = 2$).

An example is shown in Fig. 1.16. At the CR, the star has the same angular frequency as the bar, instead, at the ILR and OLR, the star performs two radial oscillations during a revolution around the galactic centre in the direct and retrograde sense, respectively. Disc stars near the ILR emit a certain quantity of angular momentum which depends on the stellar density in the proximity of the resonance. In this way stars in the bar region can be more easily trapped by the bar gravitational potential and the bar becomes stronger (Athanassoula, 2003).

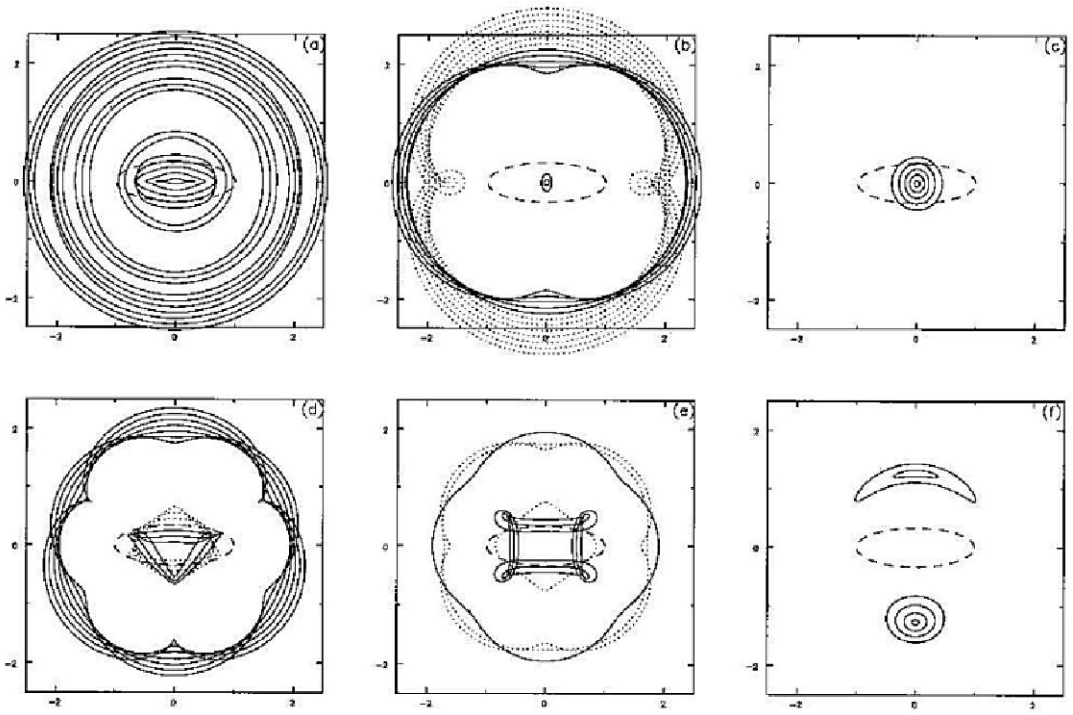

Figure 1.17: Examples of periodic orbits in a barred potential. The solid (dotted) curves represent the stable (unstable) orbits. The dashed ellipse marks the bar. *Panel a*: x_1 resonant periodic orbits. *Panel b*: Orbits near the bar centre are x_2 orbits, instead the external orbits are members of 2:1 family. *Panel c*: x_4 retrograde periodic orbits. *Panels d* and *e*: Inner and outer orbits are the 3:1 and 4:1 family orbits, respectively. *Panel f*: Banana-like long and short-period orbits near the Lagrangian points. From Sellwood & Wilkinson (1993).

In a frame corotating with the bar, the total gravitational potential Φ of the galaxy can be expressed in cylindrical coordinates in the following way:

$$\Phi_{\text{eff}} = \Phi(r, \theta, z) - \frac{\Omega_p^2 r^2}{2},$$

where Φ_{eff} is the *effective potential* and r is the radial distance from the rotating centre. There exist five points where the gradient of the effective potential is null, and they are called *Lagrangian points*. In these points, the gravitational and centrifugal forces balance each other. The two saddle points L_1 and L_2 lie along the major axis of the bar, L_3 is a minimum point located at the centre, and L_4 and L_5 are two maxima points opposite to each other with respect to the centre along the bar minor axis. A star located in one of these points is stable and appears as a fixed particle in the rotating frame or performs a circular orbit with angular frequency Ω_p in an external inertial frame.

A star performs a *periodic* orbit when it identically traces the same path at each passage around the galactic centre. These orbits are closed if the ratio between the angular frequency Ω and epicyclic frequency k is an integer or rational number. When the value of Ω/k is equal to a non-rational number, the stellar orbits trace *non-periodic* orbits. This type of orbit is trapped to oscillate around a parent periodic orbit and fill a torus. Finally, *chaotic* orbits are open orbits with an unpredictable trajectory: a star moving onto a chaotic orbit fills an entire volume (Pfenniger & Norman, 1990).

The stellar orbits between the ILR and CR are elongated along the bar major axis. This family of orbits is named x_1 and it is the most important family of stellar orbits which supports the bar. The x_1 orbits are ILR resonant orbits, so they close after two radial oscillations. They have a typical elliptical shape or present cusps at the edges (Fig. 1.17, panel a). They are also responsible for the trapping of non-periodic orbits between the ILR and CR. Outside the CR, the orbits align parallel to the bar minor axis and perpendicularly to the x_1 family. This type of orbit is named x_2 if they are prograde and stable, or x_3 if they are retrograde and unstable (Fig. 1.17, panel b). The x_2 orbits, which are present at the centre of the galaxy, are nearly circular but perpendicular to the bar major axis. These are the orbits that support the nuclear stellar discs. Finally, the x_4 orbits are nearly circular resonant orbits and slightly elongated perpendicular to the bar major axis (Fig. 1.17, panel c). All the x_i orbits are $2:1$ resonant orbits, but there exist many other families of periodic orbits with different shapes and orientations (Fig. 1.17, panels d-f) Contopoulos & Grosbol (1989); Sellwood & Wilkinson (1993).

Gas dynamics in barred galaxies

In a barred potential, the behaviour of the gas is different from that of the stars. Gas tends to follow the path of stars along their periodic orbits. As the star approaches a resonance, the eccentricity of the orbits increases and the major axis switches orientation across the resonance (Sellwood & Wilkinson, 1993). Since orbits cross each other at the resonance, the trajectory of the gas is inevitably perturbed due to its collisional and dissipative nature. Gaseous clouds accelerate (decelerate) as they approach (leave) the bar and tend to accumulate on the bar ends. The locations where gas piles up are characterised by shock, responsible for the gas infall and are usually associated with dust lanes Athanassoula (1992); Sánchez-Menguiano et al. (2015).

Athanassoula (1992) studied the response of gas to a bar potential by focusing on gas shocks and their relations with the dust lanes. These structures can extend from the nuclear region and reach the spiral arms. From the visual inspection of hydrodynamical simulations of gas, she found that strong fast bars have straight and offset dust lanes with respect to the bar major axis. On the contrary, weak bars are characterised by curved dust lanes. These structures are the photometric signature of the bar secular evolution (Kormendy & Kennicutt, 2004; Kormendy, 2013).

The shocks are nearly radial, the gas impacts at a steep angle and thus it inevitably falls towards the centre. Within the CR, the accumulation of the gas is responsible for the formation of a nuclear ring, an enhancement of the star formation activity, or a starburst (Kormendy & Kennicutt, 2004; Fisher, 2006; Scannapieco & Athanassoula, 2012). Spinoso et al. (2017) explored how bar formation and evolution affect the gas distribution and star formation by analysing high-resolution hydrodynamical cosmological simulations constructed with the aim of reproducing the properties of Milky Way-like galaxies. The gas distribution is strongly affected and perturbed by the bar gravitational forces. The torque effect of the bar drives the gas toward the centre and it is promptly transformed into stars. They found that as soon as the bar starts to form, the gas infalls toward the centre and as a consequence, the star formation is strongly enhanced. When the bar is formed and emerges in the disc as a well-defined non-axisymmetric structure, the star formation is nearly quenched. They argued that the lack of a strong nuclear star formation activity can be explained by the impossibility to easily detect bars in the early phases of formation (Fanali et al., 2015).

The accumulation of a large amount of gas in the central region can be responsible for a deceleration in the evolution of the bar through exchanging angular momentum in favour of the bar, or alternatively, can refuel the formation of a new bar (Bournaud & Combes, 2002; Bournaud et al., 2005; Villa-Vargas et al., 2010).

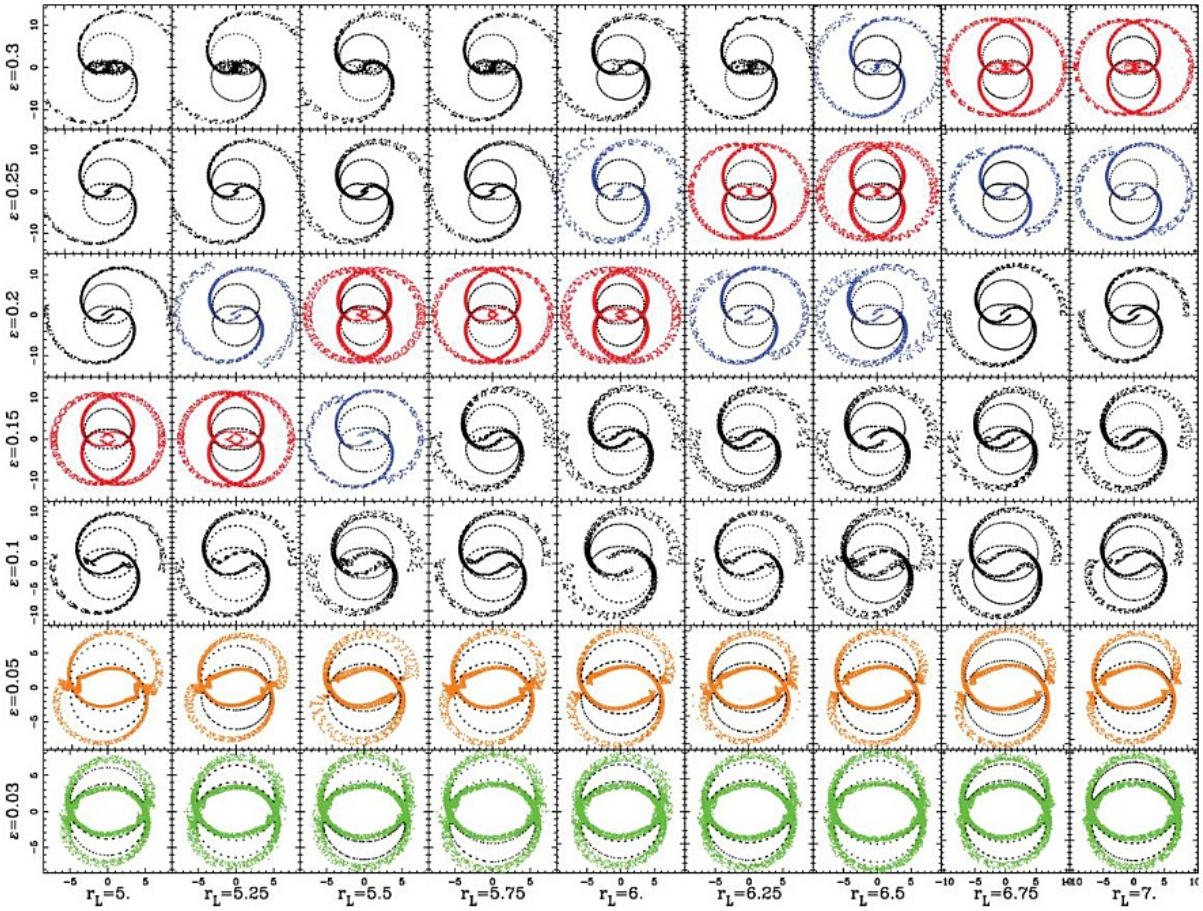

Figure 1.18: Manifold loci for different values of the Langrangian radius and bar strength. The colours represent different manifold morphologies: green for R_1, orange for R_1', blue for R_2, red for $R_1\,R_2$, and black for spirals. The black dotted lines represent the zero-velocity curves. From Athanassoula et al. (2009).

The gravitational torque exerted by the bar is responsible for the redistribution of the gas. Gas located between the CR and OLR acquires angular momentum and drifts outwards. The CR is slowly depopulated and gas accumulated in the proximity of the OLR forming a two-armed long-lasting spiral structure or an outer ring (Sellwood, 1981; Combes, 1991; Buta & Combes, 1996; Athanassoula, 2000; Kormendy & Kennicutt, 2004; Athanassoula et al., 2009). The formation of rings can be explained through the dynamics of invariant manifolds around the Lagrangian points L_1 and L_2 (Romero-Gómez et al., 2006, 2007; Athanassoula et al., 2009; Romero-Gómez, 2012). These points are unstable saddle points, they are unable to trap quasi-periodic orbits around them and therefore stars tend to escape from them following specific directions called *invariant manifolds*. These structures are associated with periodic orbits and can be imagined as tubes that guide and delimit the chaotic orbits. From each of these periodic orbits, manifolds are separated into four branches: two stable and two unstable. The shape and configurations of the orbits inside the branches produce spiral arms and different types of rings and they depend on the bar strength and the radial distance between the Lagrangian point and the centre, defined as the *Lagrangian radius* $r_{\rm L}$ (Fig. 1.18).

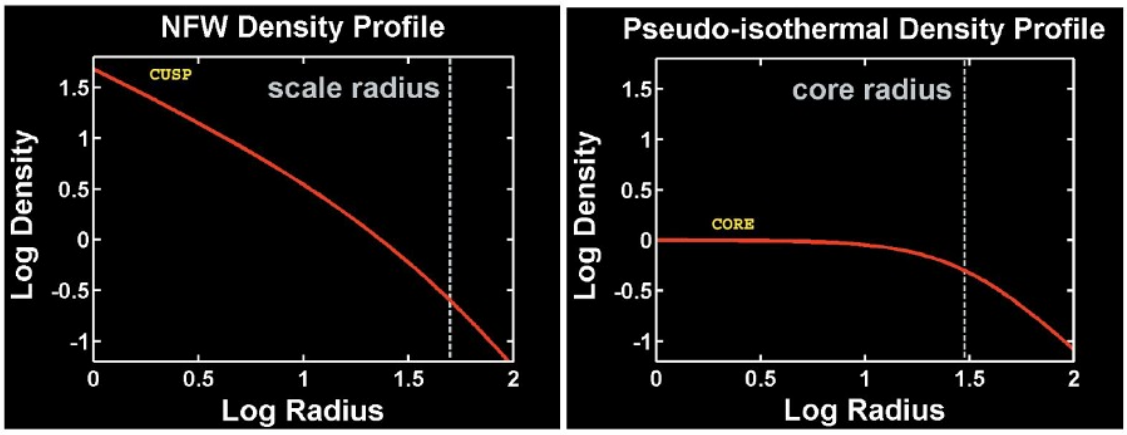

Figure 1.19: Illustration of the cusp-core problem. The Navarro-Frenk-White (*left panel*) and cored (*right panel*) warm density profiles are shown. The vertical lines represent the scale radius (*left panel*) and the core radius (*right panel*). From Del Popolo & Le Delliou (2021).

Athanassoula et al. (2011) showed that similar conclusions hold also for simulations with the gaseous component parameterised as sticky particles. Gas particles follow the stellar behaviour except when they loose kinetic energy due to the collisions and end up forming rings and thinner spiral arms with respect to the stellar arms. Rings (pseudorings) can be closed (unclosed) and have a circular or elliptical shape with a size that is roughly twice the bar extension. But they may present a more complicated morphology if considering the presence, position and shape of the spiral arms or a lens (Buta et al., 2004; Comerón et al., 2014). Rings can be aligned perpendicular to the bar (R_1 type) or parallel to it (R_2 type), and sometimes both of them co-exist ($R_1\,R_2$ type). Pseudorings are marked with the $'$ symbol.

Mass distribution in barred galaxies

The analysis of the mass distribution in galaxies allow to investigate their dynamic structure and assembly history. Early observational studies already pointed out the need to introduce the contribution of a dark matter (DM) halo to reproduce the rotation curves of spiral galaxies (Kent, 1987; Flores & Primack, 1994). In fact, the flatness of the rotation curves obtained from H I data whose extension typically reaches 2-3 times the optical radius, requires a DM halo with a warm density profile with a decline of $\rho \sim r^{-2}$. The innermost regions of a galaxy are instead dominated by the stellar component. The mass density profile can be estimated starting from a measure of the surface brightness distribution and assuming a constant M/L. Fine tuning the contribution of the disc and eventually of the bulge, it is possible to predict the mass density of the DM, for which the analytical form is not known *a priori*. It is defined as *maximum disc* hypothesis when M/L is chosen as high as possible without exceeding the observational rotation curve, on the contrary, the *minimum disc* hypothesis occurs when the disc has a null contribution. Alternatively, the mass profile of the DM halo was parameterised with a non-singular isothermal (Athanassoula et al., 1987) or a pseudo-isothermal sphere (Begeman et al., 1991), characterised by a central mass density plateau (Fig. 1.19, right panel). High-resolution observations of H I in late-type spiral galaxies confirmed that mass density distribution of the DM halo in innermost regions is well reproduced by a flattened or mildly steep power-law profile $\rho \sim r^{\alpha}$, with $\alpha \sim 0.2 - 0$ (Blais-Ouellette et al., 2001).

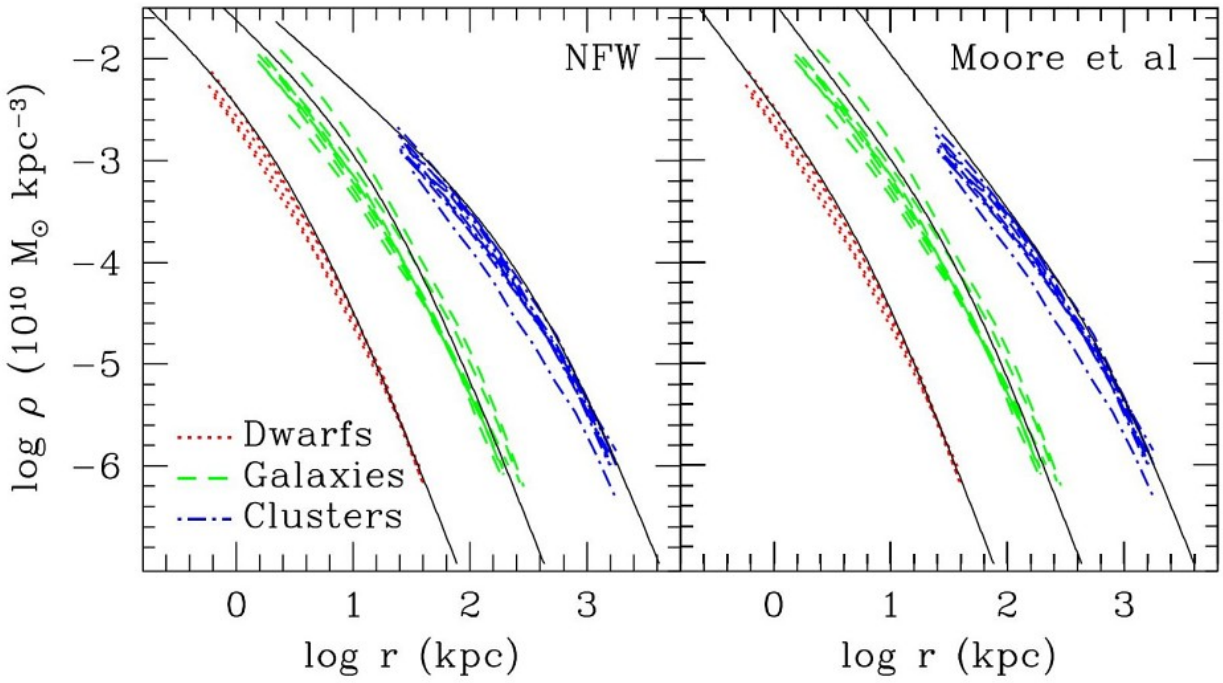

Figure 1.20: Comparisons of observed warm density profiles with simulations. The solid line represents the theoretical prediction for a Navarro et al. (1995) (*left panel*) and Moore et al. (1999) (*right panel*) profile. Coloured lines show three different classes of mass systems: dotted red lines correspond to dwarf galaxies, dashed green lines to medium-sized galaxies, and dash-dotted blue to clusters of galaxies. From Navarro et al. (2004).

However, the relative contribution of the stellar and DM components in the inner regions still represents a critical point when compared with the predictions derived in a cosmological framework. The ΛCDM cosmological model provides a successful description of the Universe on large scale, but some issues still remain under debate at smaller scales. Navarro et al. (1995) used dissipationless cold DM N-body simulations to derive the mass distribution of the DM in galaxies. They found a universal warm density profile for the DM halo, independently on the cosmological scale and characterised by a steep power-law $\rho \sim r^{\alpha}$ with $\alpha = -1$ that produces a central *cusp*.

However, other works based on high-resolution cosmological simulations found inner steeper ($\alpha = -1.5$, Moore et al. 1999, $\alpha = -1.2$, Diemand et al. 2005) or shallower slope ($\alpha = -0.75$, Taylor & Navarro 2001). Moreover, the slope of the density dark matter profile depends on the mass of the halo, in the sense that the largest systems as clusters of galaxies have a slightly steeper slope with respect to the smallest systems, like the dwarf spheroidal galaxies (Fig. 1.20, Ricotti, 2003, Navarro et al., 2004). Both the Navarro et al. (1995) and Moore et al. (1999) profiles seem well reproduce the predictions obtained from high-resolution cosmological simulations with no evidence of a core profile. The discrepancy between the cosmological predictions and the observations has led to the so-called *cusp-core problem*. Many astrophysical and cosmological solutions were proposed to resolve this issue.

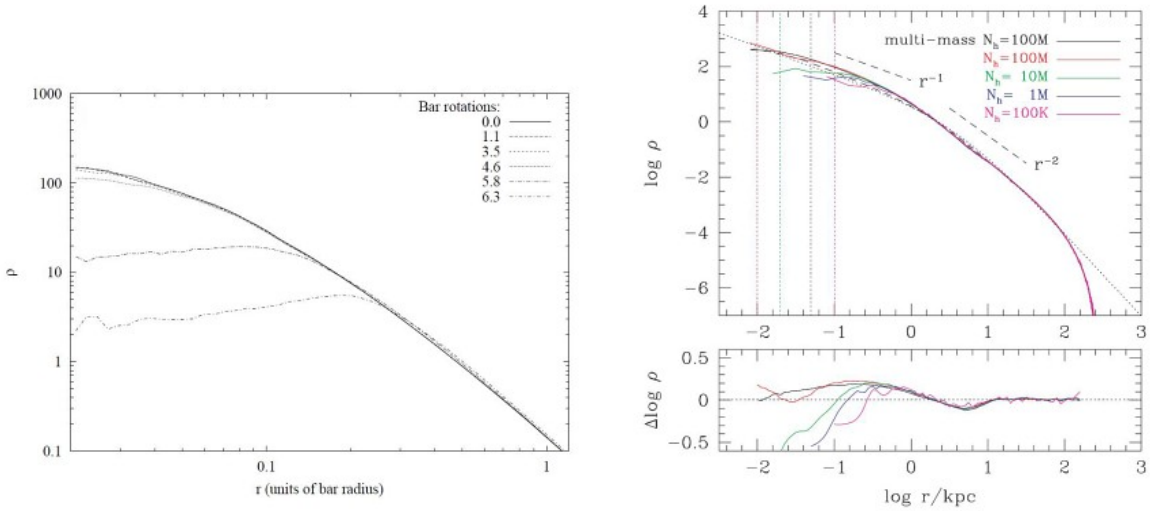

Figure 1.21: *Left panel*: Evolution of a DM halo with Navarro-Frenk-White (NFW) profile due to a rigid rotating bar. From Weinberg & Katz (2002). *Right panel*: Comparison of DM density profiles for a different number of halo particles (*top panel*) and relative residuals (*bottom panel*). The dashed line is the initial mass density, the dotted coloured lines show the best-fitting NFW profiles, and the dotted vertical lines mark the corresponding softening length. From Dubinski et al. (2009).

The first attempts pointed out that the systematic effects and low spatial resolution of observational data could produce a core warm density profile, masking the actual cuspy distribution. de Blok & McGaugh (1997) found that the low resolution is indeed responsible for a smearing effect in the central regions, but it is not sufficient to erase the cusp.

Some interesting solutions proposed the dynamical friction and interaction between baryonic and DM as responsible for the central flattening of the mass density distribution.

Weinberg & Katz (2002) used the linear perturbation theory and idealised N-body simulations to show that the different galactic components interplay with each other exchanging angular momentum. In their simulations, the bar is represented by a rigid ellipsoidal structure embedded in a cuspy DM halo. The interaction between the bar and DM halo is responsible for bar slowdown and for erasing of the central peak of DM mass density (Fig. 1.21, left panel). These results were later confirmed by Holley-Bockelmann et al. (2005), who used high-resolution and self-consistent simulations. They found that bars lose angular momentum in favour of the DM halo. While the bar becomes stronger, longer, and slower, the central cusp of the DM halo becomes smoother. Moreover, they showed that bars formed due to an external perturbation produce the same effect on the DM central mass distribution.

Dubinski et al. (2009) used high-resolution simulations of self-consistent barred galaxies to study the time evolution of the DM halo density profile. Their self-consistent models are composed of an exponential disc unstable to bar formation and a NFW DM halo. The bars in these models form and evolve undergoing buckling instability, a phase during which the bar vertically bends and becomes thicker. During the bar evolution, a large amount of mass concentrates at the very centre of the galaxy, inducing the halo to adiabatically contract and thus steepening its density (Fig. 1.21, right panel). Their results are in contrast with those obtained by Weinberg & Katz (2002). They argued that rigid thin bars modelled by Weinberg & Katz (2002) are not realistic. They are robust to instability and more efficient in destabilising the DM particles in the central region.

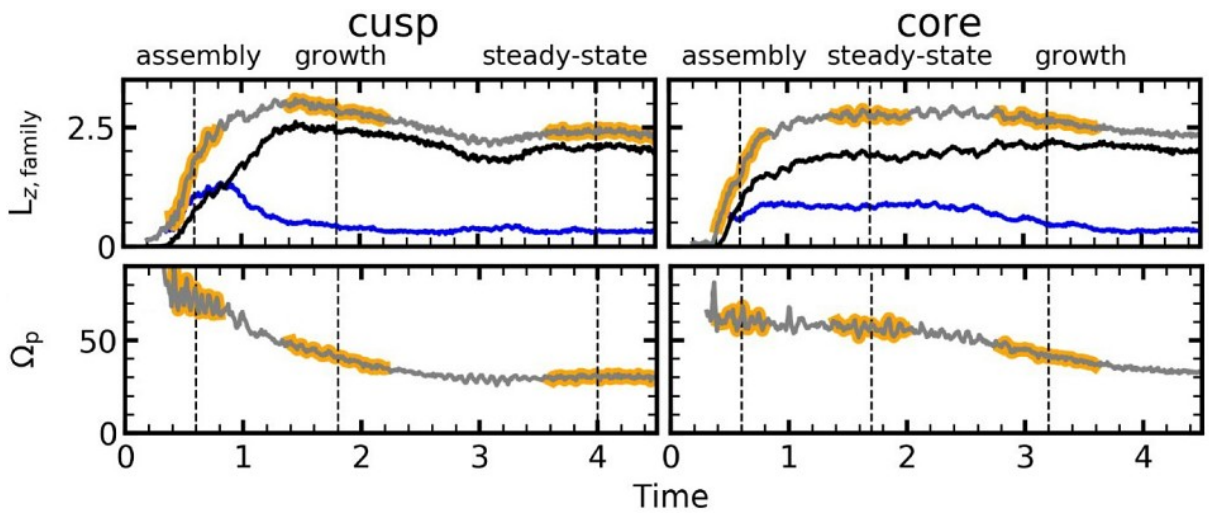

Figure 1.22: Total angular momentum (*top panels*) and bar pattern speed evolution (*bottom panels*) in the cusp (*left panels*) and core simulations (*right panels*). The grey lines represent the evolution of the total bar component, the black lines represent the x_1 family orbits, and the blue lines represent the other family orbits supporting the bar. From Petersen et al. (2019).

Recently, Petersen et al. (2019) have studied the secular evolution in simulated barred galaxies with a different central DM distribution. They constructed two simulations, one with a central cusp and the other with a core in the mass density profile of the DM halo. By analysing the evolution of the stellar orbits and the exchange of angular momentum among the different galactic components, they distinguished three main phases in the bar evolution: assembly, growth, and steady state. During the assembly phase, local instabilities force the disc material to rearrange and match the same bar pattern speed. Disc stars lose angular momentum in favour of the bar, which grows in mass by trapping stellar orbits. The bar keeps increasing its mass during the growth phase, even if it loses angular momentum in favour of the DM halo and outer disc. In the steady-state phase, the bar reaches a stationary condition during which there are no significant changes.

During the same phases, the cusp and core simulations show similar physical and dynamical processes, but the order in which the growth and steady state phases occur differs. The growth phase is followed by the steady state phase for the cusp simulation. On the contrary, the steady state occurs before the growth phase in the core simulation (Fig. 1.22). Indeed, the steady-state phase can be either a transient or a long-lasting process. The bar assembly phase modifies the inner distribution of the DM halo: the effects are more remarkable in cusp simulation, whereas they are less pronounced in core simulation. The formation of the bar appears more violent in the cusp simulation with respect to that formed in the core one. The main difference between the two simulations resides in the different channels through which the angular momentum is exchanged. In the cusp simulation, the DM halo is the main source of torque on the bar. It can more efficiently couple with the inner disc and is more prone to absorb angular momentum in proximity of the ILR. In the core simulation, the DM halo is not able to accept angular momentum that is promptly absorbed by the outer disc. Observed bars mainly appear in the steady state phase. The assembly phase lasts too short to be easily detected, but the steady state phase may not be the final configuration. The duration of this phase depends on the central DM distribution. A robust observational diagnostic able to distinguish the two different bar formation scenarios is still missing.

1.4 Formation and evolution of barred galaxies

Life cycle of bars

Observational studies provide a description of the properties of nearby barred galaxies but only theoretical predictions and simulation-based works allow to investigate the formation scenarios, the evolution of the bar properties, and the processes responsible for the bar dissolution. Bars are not rigid and static structures, they form and grow actively participating in the evolution of the morphological, photometric, and dynamical properties of the host galaxy.

Bars can form spontaneously in unstable and isolated stellar discs due to internal instability (Sellwood, 1981; Athanassoula et al., 2013). These spontaneous perturbations occur when the *Toomre stability parameter* $Q_\star$ reaches a value of $Q_\star \leqslant 2.0 - 2.5$ (Toomre, 1981; Binney & Tremaine, 2008). These stabilities grow through the *swing amplification* mechanism (Goldreich & Lynden-Bell, 1965; Fujii et al., 2018), according to which the disc acts like a resonant cavity for the density waves that reflect when propagating through the centre and switch from leading to trailing mode (or viceversa) as they reach a resonance (Binney & Tremaine, 2008; Sellwood & Wilkinson, 1993). Bar formation can be eventually triggered by close interaction with a companion (Noguchi, 1987; Martinez-Valpuesta et al., 2017). The induced formation requires a less severe condition ($Q_\star \leqslant 2.5 - 3.0$) that can occur in both cool and hot discs (Friedli, 1999; Łokas, 2018). The initial growth of the bar lasts few Gyrs, at the end of this phase, the disc presents a distinctive elongated structure.

Young bars are usually thin ($c/a \sim 0.1$) but rapidly grow and become thicker ($c/a \sim 0.3$) undergoing the so-called *buckling instability* phase (Binney & Tremaine, 2008; Friedli, 1999; Athanassoula, 2016; Łokas, 2019). Along the bar major axis, the streaming motion is more rapid and this makes the bar more susceptible to buckling instability with respect to the disc where it is embedded (Sellwood & Wilkinson, 1993). During this phase that typically lasts $\sim 1\,\mathrm{Gyr}$, disc stars are diffused along the vertical direction and stellar orbits in the bar region become more eccentric. The bar asymmetrically bends and heats the disc stars producing an increase in the vertical dispersion of the stellar orbits responsible for the thickening of the bar. A buckled bar can be identified through both photometric and kinematic diagnostics by looking for characteristic *boxy-peanut-X* shape (Martinez-Valpuesta et al., 2006; Athanassoula et al., 2013; Erwin & Debattista, 2013; Kruk et al., 2019).

After the buckling instability, the bar keeps slowly evolving during the so-called *secular evolution*, the longest phase of its life cycle (Sellwood & Wilkinson, 1993; Debattista et al., 2006; Athanassoula, 2013; Kormendy, 2013; Sellwood, 2014; Kim et al., 2016; Fragkoudi et al., 2016). During this phase, the bar exchanges angular momentum, mass, and energy among the other galactic components. At the ILR, the bar acquires angular momentum from the inner disc forcing stars to match its pattern. At the OLR, the bar transfers angular momentum to the bulge and halo. The evolution of the bulge is strongly influenced by the presence of the bar, which can contribute to the formation of a *pseudobulge*, a spheroidal structure with photometric and kinematic properties similar to a disc, and characterised by an enhanced star-formation activity (Debattista & Williams, 2004; Gadotti, 2009; Kormendy & Kennicutt, 2004; Kruk et al., 2018). The bar is also responsible for the redistribution of gaseous and stellar material within the whole galaxy, which results in the formation of long-termed or short-lived structures, such as spiral arms and rings.

As well as they form, bars can also die. Bars can be weakened and eventually dissolved by the growth of a central mass concentration, such as a massive black hole, a nuclear star cluster or a large condensation of gas (Kormendy & Kennicutt, 2004; Debattista et al., 2006). The accumulation of a central concentration of mass reduces the space volume populated by the x_1 periodic orbits and other family orbits that provide the main support for the bar structure.

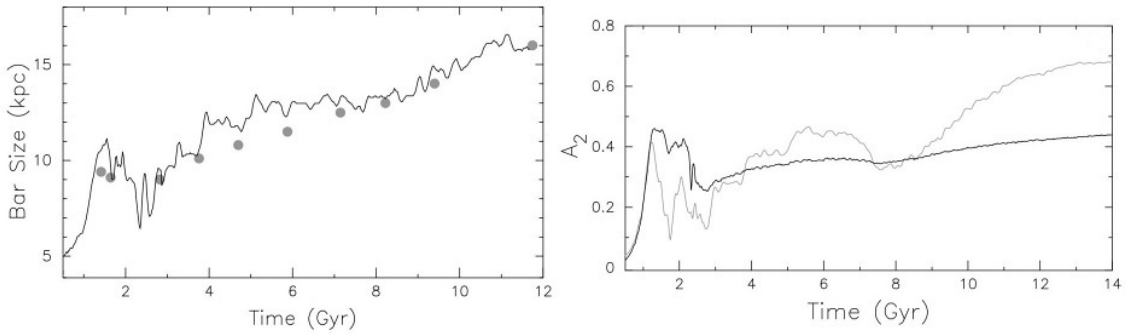

Figure 1.23: *Left panel*: Time evolution of the bar radius. The solid line represents the bar radius obtained from the ellipse fitting method, while the filled circles correspond to the bar radius obtained from the semi-major axis of the last stable x_1 periodic orbit. *Right panel*: Time evolution of the bar strength. The thick and thin line represent the bar strength obtained from the $m = 2$ amplitude of the density distribution in the radial region $r = 0 - 11\,\mathrm{kpc}$ and $r = 7 - 11\,\mathrm{kpc}$, respectively. From Martinez-Valpuesta et al. (2006).

The gravitational torque exerted by the gas on the bar produces a misalignment of the stellar orbits in the bar region that can weaken the bar and eventually destroy it (Bournaud & Combes, 2002; Bournaud et al., 2005). However, it was demonstrated that destroying a bar is quite hard. The mass of the central concentration has to be $\sim 10\%$ of the mass of the disc to be able to completely destroy the bar structure (Shen & Sellwood, 2004). Extremely violent encounters can be responsible for the dissolution of the bar (Friedli, 1999; Ghosh et al., 2021), but it still remains unclear the typical bar annihilation timescale, which spans a wide temporal range (0.2-10 Gyr). Lenses or oval distortions can be the final product of a bar dissolution (Kormendy, 1979; Debattista et al., 2004, 2006; Kruk et al., 2018). On the other hand, a considerable amount of gas may be responsible for a reformation of new bar instabilities (Bournaud & Combes, 2002).

Evolution of bar parameters and the role of dark matter halo

During the whole bar life, its parameters are not constant, they evolve according to the exchange of mass, energy, and angular momentum with the disc and halo (Sellwood, 1981; Debattista & Sellwood, 1998, 2000; Athanassoula & Misiriotis, 2002; Martinez-Valpuesta et al., 2006; Athanassoula, 2013; Martinez-Valpuesta et al., 2017; Petersen et al., 2019). The bar gravitational potential perturbs the orbital structure of the disc forcing the stars to move on more elongated orbits. The bar radius rapidly grows until a clear bar structure is formed (Fig. 1.23, left panel). As R_{bar} also S_{bar} evolves over time. During the initial growth, S_{bar} quickly increases and reaches a peak corresponding to the maximum development of the bar amplitudes in the disc (Fig. 1.23, right panel). The buckling instability phase modifies the stellar orbital structure of the bar, resulting in a mild increase of R_{bar}, an abrupt decrease of S_{bar} followed by another rise in strength.

As the bar starts to form, it loses angular momentum becoming longer, thinner, and stronger. The capability of the halo to absorb angular momentum strongly affects the evolution of the bar. Athanassoula & Misiriotis (2002) showed that a live and responsive DM halo efficiently absorbs the angular momentum from the disc permitting the formation of a thin and long bar (Fig 1.24, central panels). A non-rotating DM halo inhibits the angular momentum loss and produces a weak oval distortion in the disc (Fig 1.24, right panels). A less massive DM halo is responsible for the formation of a shorter and rounder bar (Fig 1.24, left panels).

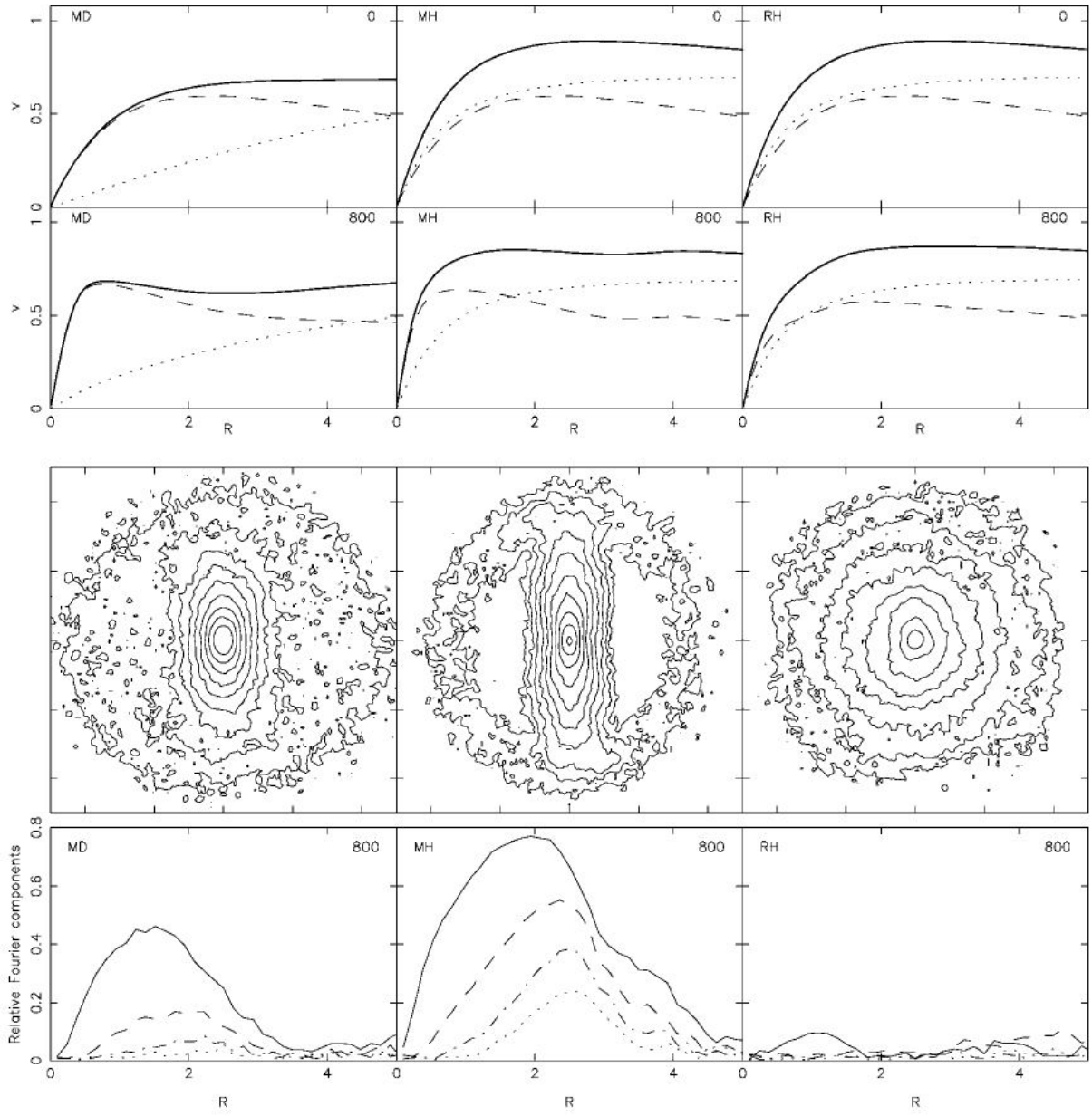

Figure 1.24: *Top panels*: Circular velocity curves at $t = 0$ (first row) and $t = 800$ (second row) for a simulation with a massive disc (MD, *left panels*), massive halo (MH, *central panels*)), and rigid halo (RH, *right panels*). The contribution of the disc and halo components are marked by dashed and dotted lines, respectively, while their sum is represented by the solid line. *Central panel*: Isocontours of the disc surface density at $t = 800$ for a simulation with a massive disc (MD), massive halo (MH), and rigid halo (RH). *Bottom panel*: Fourier analysis at $t = 800$ for a simulation with a massive disc (MD), massive halo (MH), and rigid halo (RH). The solid ($m = 2$), dashed ($m = 4$), dot-dashed ($m = 6$), and dotted lines ($m = 8$) represent the different Fourier amplitudes. From Athanassoula & Misiriotis (2002).

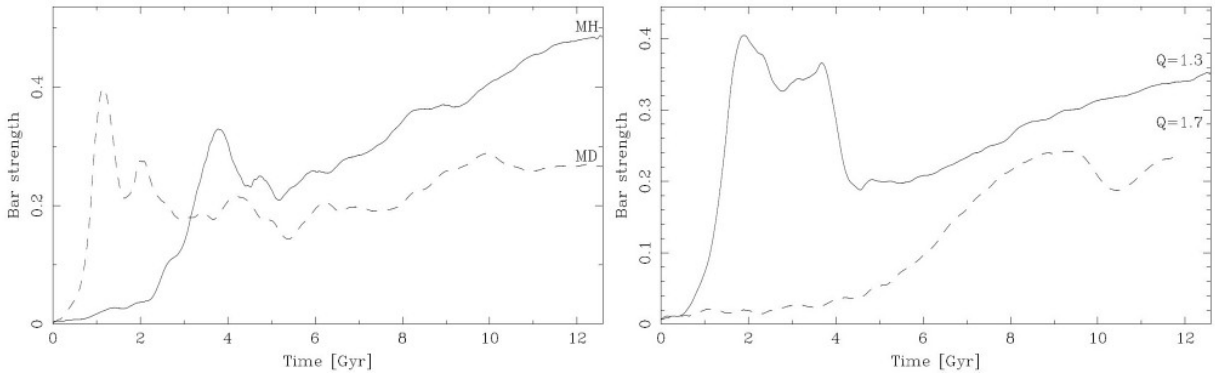

Figure 1.25: *Left panel*: Time evolution of bar strength for a simulation with a massive halo (solid line) and a massive disc (dashed line). *Right panel*: Time evolution of bar strength for a simulation with a cool disc (solid line) and a hot disc (dashed line). From Athanassoula & Misiriotis (2002).

The left panel of Fig. 1.25 shows the time evolution of the bar strength in two different simulations, one with a massive halo (MH), and the other with a massive disc (MD) (Athanassoula & Misiriotis, 2002). Bar forms in less than Gyr in the MD simulation, while it takes $\sim 2\,\mathrm{Gyr}$ in the MH model. As for the formation, the growth phase lasts shorter in the MD simulation and longer in the MH model. Athanassoula & Misiriotis (2002) demonstrated that the presence of a massive responsive spheroidal component not only produces a delay in the bar formation process, but also is responsible for a slowdown in the evolution. The bar growth phase ends when the bar reaches a peak in S_{bar}. After the peak, the bar strength in both the MH and MD models abruptly decreases during the buckling instability phase. After this short phase, the bars in both the models undergo the secular evolution phase, which occurs after $\sim 3\,\mathrm{Gyr}$ and $\sim 5\,\mathrm{Gyr}$ for the MD and MH simulations, respectively. At the end of the simulation, the bar in MH is stronger with respect to the bar in the MD simulation. This happens because the redistribution of the angular momentum is more efficient in presence of a spherical component, such as a bulge or a DM halo. This consideration still holds in the case of a rigid halo (RH).

The right panel of Fig. 1.25 shows the time evolution of the bar strength in two different simulations, one with a cool disc ($Q = 1.3$) and the other with a hot disc ($Q = 1.7$) (Athanassoula & Misiriotis, 2002). The bar in the simulation with a cooler disc forms early and grows a lot in the first $\sim 1.5\,\mathrm{Gyr}$. Bar strength decreases after the bucking instability and then continues to increase till the end of the simulation, during the secular evolution phase. In the model with a hotter disc, it is unclear to distinguish the beginning and end of the several evolutionary phases. The bar formation is delayed, the growth of the instabilities is less prominent and at the end of the simulation, the bar is weaker with respect to the bar born in the cooler disc.

In general, bar formation is delayed in galaxies with large values of the spheroid-to-disc mass ratio. Once formed, during the last stages of the evolution, bars grow stronger in galaxies with large values of the spheroid-to-disc mass ratio.

The efficiency in the exchange of angular momentum among the different galactic components depends not only on the relative contribution between the disc and halo but also on the shape of the DM halo and on the gas fraction (Athanassoula et al., 2013; Kumar et al., 2022). Athanassoula et al. (2013) built a set of N-body simulations composed of a disc and a DM halo, and explored the evolution of the bar parameters in models with different shapes of the DM halo and gas fraction.

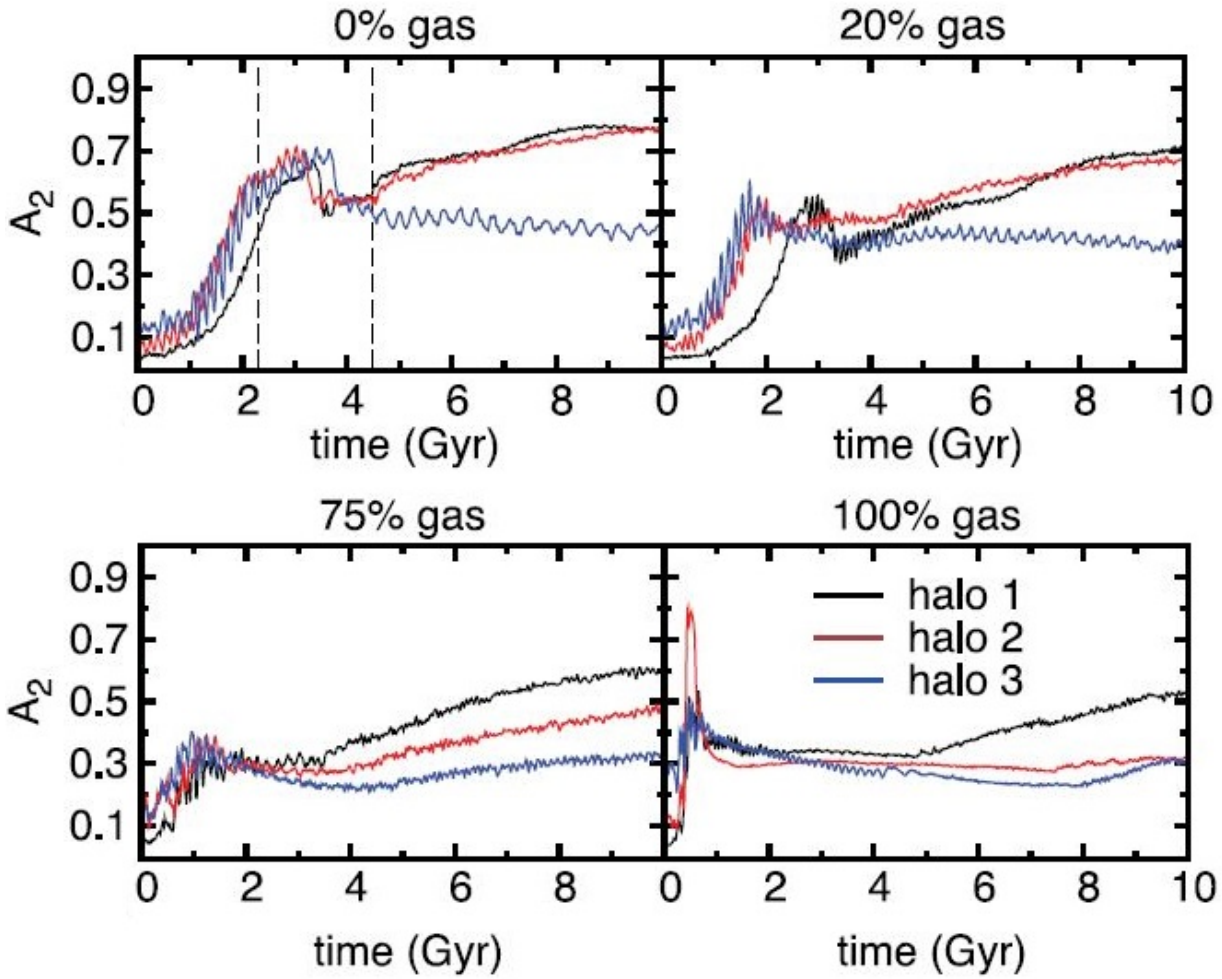

Figure 1.26: Time evolution of bar strength in simulations with different triaxial DM haloes and gas fractions. The gas fraction is given in each panel. Different colour represents halo with different triaxiality. Black lines represent an axisymmetric halo, while red (b/a, c/a)=(0.8, 0.6) and blue lines (b/a, c/a)=(0.6, 0.4) represent two different triaxial haloes. From Athanassoula et al. (2013).

The evolution of the bar strength looks similar in models with a gas content lower than 20%, independently of the shape of the halo. It is characterised by an initial growth, a short phase in which $S_{\rm bar}$ decreases, and a long phase during which $S_{\rm bar}$ remains nearly constant or keeps growing (Fig. 1.26, *top panels*). The strongest bars form in models with a spherical halo and no gas content. Bar formation occurs earlier in galaxies with a triaxial halo, but the growth of the $S_{\rm bar}$ is hampered by the non-linear interaction between the two non-axisymmetries, those of the bar and of the halo.

The evolution of $S_{\rm bar}$ in gas-rich models is more complicated. The initial phases of the bar amplitudes are noisy and characterised by the formation of transient spiral arms or rings. At the end of this phase, a short bar starts to form, and as the bar amplitudes sufficiently increase, a longer bar appears in the disc. The transition from the short to a longer bar is characterised by rapid growth of $S_{\rm bar}$, which occurs later in the models with a large gas fraction and with more triaxial haloes (Fig. 1.26, *bottom panels*). For all the gas-rich models, the bar undergoes a slow secular evolution that ends up with the formation of weak bars.

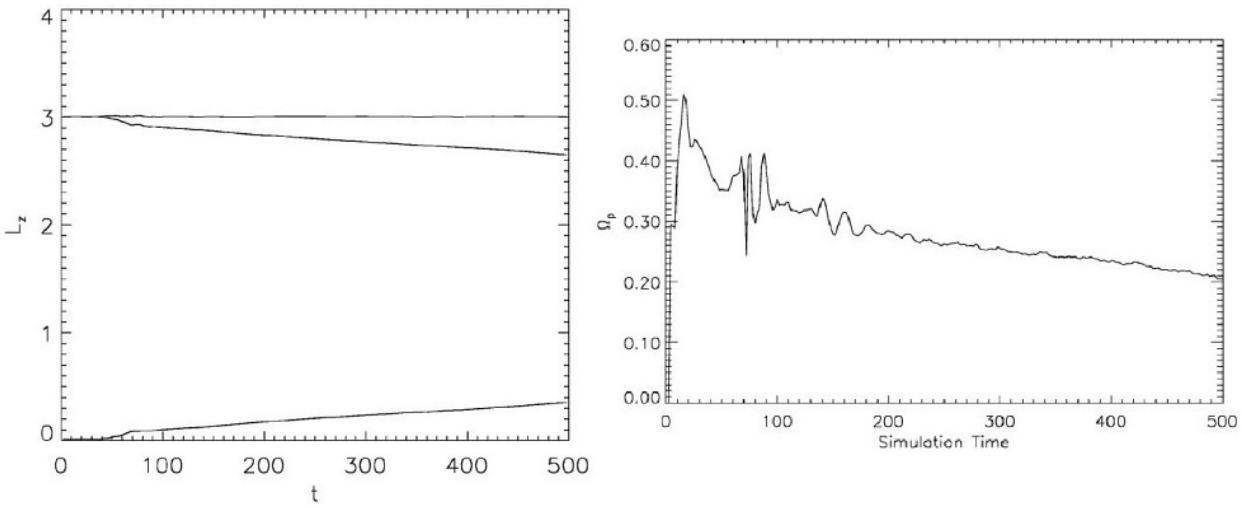

Figure 1.27: *Left panel*: Time evolution of the angular momentum. The top, middle, and bottom lines represent the total, disc, and halo components, respectively. *Right panel*: Time evolution of the bar pattern speed. From O'Neill & Dubinski (2003).

The bar pattern speed is the most important among the bar properties. It controls the location of the resonances and stellar orbits, affects the gas dynamics, and is linked to the DM content within the central regions of the galaxy. Bars formed spontaneously in unstable stellar discs have a larger value of $\Omega_{\rm bar}$ with respect to the bars whose formation was triggered by the tidal interaction of a neighbour galaxy. Martinez-Valpuesta et al. (2017) found that the bars formed after coplanar flybys with massive companions typically have a rotation rate $\mathcal{R} > 1.8$. Similarly, large rotation rates characterise the bars formed in the numerical experiments of Łokas (2018), which explored the case of retrograde encounters of two galaxies with comparable mass.

During its evolution, the bar transfers angular momentum to the halo, and as a consequence, it slows down (Fig. 1.27). With the decrease of $\Omega_{\rm bar}$, the location of resonances shifts towards larger distances, yielding $R_{\rm cor}$ to increase. The value of $R_{\rm bar}$ increases with time, therefore, the overall effect is that $\mathcal{R}$ increases too. Furthermore, a bar can be braked by a dense DM halo through the dynamical friction mechanism (Weinberg, 1985; Debattista & Sellwood, 1998, 2000; Athanassoula & Misiriotis, 2002; Athanassoula, 2003; O'Neill & Dubinski, 2003; Martinez-Valpuesta et al., 2006; Villa-Vargas et al., 2010; Athanassoula et al., 2013; Martinez-Valpuesta et al., 2017; Petersen et al., 2019). In the innermost region, the frictional torque exerted by a massive DM halo causes a massive loss of angular momentum. The transfer of angular momentum from the disc to the halo produces an abrupt slowdown, shifting the bar towards an even slower regime.

Debattista & Sellwood (1998) built a set of N-body galaxy models composed of a disc and a DM halo with different masses and studied how the evolution of the bar pattern speed is linked with the exchange of angular momentum between the disc and halo. All the galaxy models have the same total mass, but different disc mass fraction that spans from 0.3 to 0.6 in models with the most and least massive DM haloes, respectively. The left and central panels of Fig. 1.28 show the rotation curves of the models that host the most and least massive DM halo. In the simulation with the most massive halo, the disc transfers $\sim 40\%$ of the initial angular momentum to the halo, the bar consequently slowdown and the value of $\Omega_{\rm bar}$ decreases a factor of 5 in 50 bar rotations (Fig. 1.28).

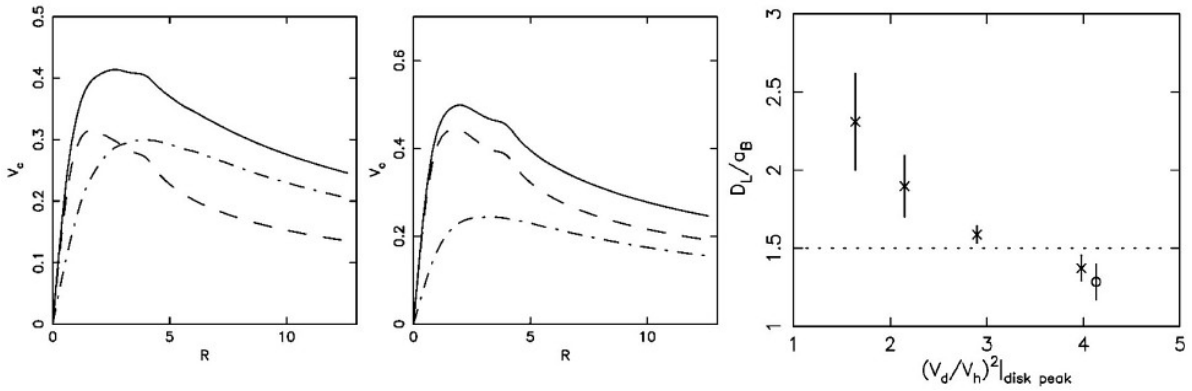

Figure 1.28: Rotation curves of simulations with the most massive (*left panel*) and least massive (*central panel*) halo, and bar rotation rate as a function of the square of the initial ratio disc-to-halo circular velocities estimated at the peak of the disc rotation curve (*right panel*). The solid, dashed, and dot-dashed lines in the left and central panels represent the total, disc, and halo components. The crosses in the right panel represent the bar rotation rate in simulations without an extended halo, while the circle represents the value in a more realistic simulation. The horizontal dashed line marks the value of $\mathcal{R}$=1.5. From Debattista & Sellwood (1998).

In the simulation with the least massive halo, instead, the bar keeps rotating fast. The frictional torque exerted by the halo is weaker because the disc, and thus the bar, is more massive, therefore the effect of the dynamical friction on the bar pattern speed is weaker. In addition, Debattista & Sellwood (1998) built a model with a more realistic DM halo represented by a circle in the right panel of Fig. 1.28.

The bar evolution in both the simulation with a realistic and a less extended DM halo is similar: the bar appears in the disc as a strong non-axisymmetric structure that evolves slowing down its bar pattern speed. Since the final value of $\mathcal{R}$ is nearly equal for both models ($\mathcal{R}\sim$1.3), they stressed the possibility that the dynamical friction depends not only on the total mass of DM but also on its distribution within the galaxy. Their results agreed with the predictions previously found by Weinberg (1985), who used the linear perturbation theory.

Valenzuela & Klypin (2003) built high-resolution N-body simulations of stellar discs embedded in cosmologically-motivated DM haloes that naturally develop a bar in order to study the bar evolution in relation to the exchange of angular momentum between the disc and DM halo. They found that the friction between the DM halo and bar translates into an exchange of angular momentum, as previously found in other works. But, their bars do not slowdown and remain nearly fast ($\mathcal{R} \sim 1.2-1.7$). Sellwood & Debattista (2006) reanalysed in detail these simulations and found opposite results. The simulations have an anomalous gradient of particle density in proximity of the resonances, which reduces the amount of exchanged angular momentum. This phenomenon, combined with other specific numerical ingredients, is responsible for a metastable condition suppressing the dynamical friction. Thus, the bars of Valenzuela & Klypin (2003) remain artificially fast for a long time. After correcting these artefacts, the bars experience a strong drag and slowdown as expected ($\mathcal{R} \sim 2.4$, Sellwood & Debattista 2006).

Many other factors may affect the evolution of $\Omega_{\rm bar}$ and the exchange of angular momentum, such as the numerical resolution, the gas amount, the shape and spin of the DM halo. Using galaxy models composed of stellar and gaseous discs embedded in DM halo, Villa-Vargas et al. (2010) found that both the gas fraction and numerical resolution may modify the transfer of angular momentum.

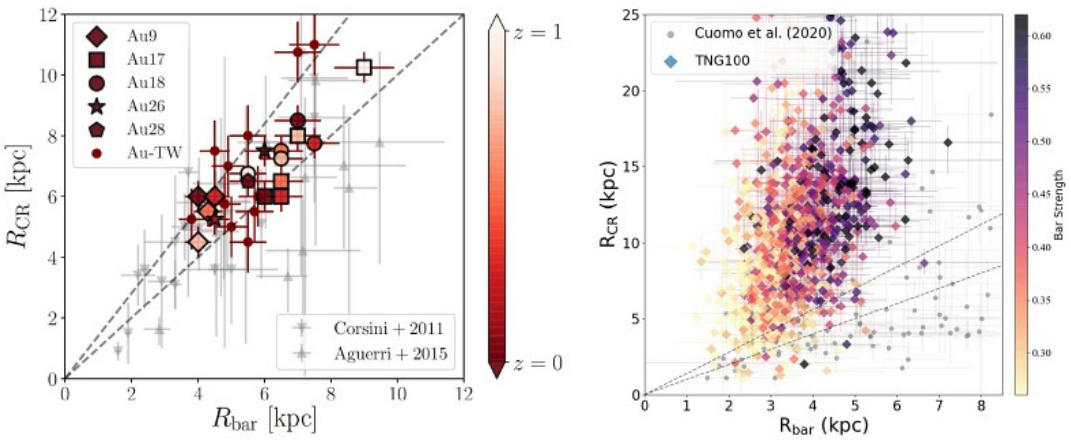

Figure 1.29: *Left panel*: Bar rotation rates for Auriga galaxies. Grey symbols represent data from Corsini (2011) and Aguerri et al. (2015). Symbols are colour-coded according to the redshift. From Fragkoudi et al. (2021). *Right panel*: Bar rotation rates for TNG100 galaxies. Grey circles represent data from Cuomo et al. (2020). The diamonds are colour coded by the value of the bar strength calculated as the maximum of the $m = 2$ Fourier component. From Roshan et al. (2021). In both panels, the grey dashed lines mark the slow, fast, and ultrafast regimes.

They found that pure stellar discs lose a larger quantity of angular momentum with respect to gas-rich systems. Therefore, bars in systems with a small gas content rapidly decrease, whereas bars in gas-rich discs slowly evolve or maintain a nearly constant $\Omega_{\rm bar}$. The effect of the resolution becomes important in models with a high gas content. As the bar evolves, $\mathcal{R}$ increases to larger values. In gas-rich models, it slowly increases and rarely exceeds the unity, and at high numerical resolutions its rise is further damped. Athanassoula et al. (2013) explored a set of N-body models with different shapes of DM haloes and found that galaxy models with a triaxial DM halo exchange a larger amount of angular momentum with respect to the case of mildly-triaxial or axisymmetric DM halo. Collier et al. (2018) extended the analysis on the shape of the haloes by studying the evolution of stellar bars in models with oblate and prolate spinning DM haloes. During the initial phase, the set-up of the bar instabilities occurs early. During the secular evolution, instead, both the growth of the bar amplitudes and transfer of angular momentum are reduced in more spinning haloes. The value of $\Omega_{\rm bar}$ abruptly decreases in galaxies with low-spin haloes, while it remains flat or mildly increases in high-spin haloes. Later, Collier et al. (2019) explored the bar evolution in galaxy models with retrograde spin haloes too. Initially, the bar instabilities are slowed down in more counter-rotating haloes, but the subsequent secular evolution remains nearly unaltered.

According to theoretical predictions and studies based on simulations, we expect to observe slow bars in DM-dominated systems and fast bars in galaxies with less dense DM haloes. However, observational studies showed that the vast majority of bars are fast (Corsini, 2011; Aguerri et al., 2015; Guo et al., 2019; Garma-Oehmichen et al., 2020; Cuomo et al., 2020). Some slow bars were detected through an indirect measure of $\Omega_{\rm bar}$ (Buta et al., 1998; Rautiainen et al., 2008; Buta & Zhang, 2009; Font et al., 2014). Nevertheless, since the estimate of the uncertainty is not solid or absent, it is impossible to accurately establish if these bars are genuine slow bars. These results have important implications for the density distribution of the baryonic and DM components. The large abundance of fast bars implies that barred galaxies contain a low amount of DM in the very central regions, enforcing the scenario of the maximum-disc hypothesis.

In the last decade, significant progress has been achieved in the development of more complex large simulations that permitted to investigate the evolutionary history of barred galaxies in a cosmological framework. Many works based on high-resolution hydrodynamical simulations traced the formation and evolution of barred galaxies in different environments, and compare properties of simulated bars with nowadays real observations (Algorry et al., 2017; Łokas, 2018; Peschken & Łokas, 2019; Fragkoudi et al., 2021; Roshan et al., 2021; Marioni et al., 2022). However, the results obtained by studies based on cosmological simulations are controversial. Recently, Fragkoudi et al. (2021) used the Auriga (Grand et al., 2017) simulations to study the evolution of the bar parameters. Auriga simulations consist of 30 magneto-hydrodynamical cosmological simulations with mass range $1 - 2 \cdot 10^{12}\,\mathrm{M}_{\odot}$. In order to better compare the measure of $R_{\rm bar}$ and $R_{\rm cor}$ with the observational sample, they used the ellipse fitting method and the TW method, respectively. Finally, they estimated $\mathcal{R}$ and they found that simulated bars are fast at $z \sim 1$ and remain fast till the present day (Fig 1.29, left panel), in agreement with the observations. They also found that Auriga-simulated barred galaxies are baryonic-dominated systems. This means that bars suffer from lower dynamical friction that permits them to remain fast.

Roshan et al. (2021) studied the bar properties and the fraction of barred galaxies at redshift $z = 0$ using IllustrisTNG (Marinacci et al., 2018) and EAGLE (Schaye et al., 2015) simulations. TNG and EAGLE simulations are cosmological simulations with a different mass resolution, implemented in order to reproduce properties of the nowadays galaxies. Roshan et al. (2021) applied an isophotal and Fourier analysis to the simulated barred galaxies to recover the value of $R_{\rm bar}$. The value of $\Omega_{\rm bar}$ was estimated by applying the TW method. They calculated $\mathcal{R}$ and found that the vast majority of simulated bars are slow (Fig 1.29, right panel).

The disagreement between the theoretical predictions, observations, and studies based on simulations has led to the so-called ΛCDM *tension*. On one hand, theoretical works had permitted to build of reasonable predictions on the properties of barred galaxies, confirmed later by extensive studies on large samples of disc galaxies, and enforced by a detailed and realistic representation of simulated barred galaxies. On the other hand, barred galaxies present a complicated description of the dynamics, whose implications reflect on the understanding of cosmology, that need to be further investigated in detail.

1.5 Aim and outline of the thesis

In this thesis, we aim at investigating the nature and the dynamics of barred galaxies by studying ultrafast, fast, and slow bars and analysing the internal structure of their host galaxies using dynamical models and N-body simulations. The chapters are organised as follows.

- **Chapter 2** (based on Cuomo, V., Lee, Y. H., Buttitta, C., et al. 2021, A&A, 649, A30) More than 10% of the barred galaxies with a direct measurement of $\Omega_{\rm bar}$ host an ultrafast bar. These bars extend well beyond $R_{\rm cor}$ and challenge our understanding of the orbital structure of barred galaxies. Most of them are found in spiral galaxies, rather than in lenticular ones. We analysed the properties of the ultrafast bars detected in the CALIFA survey to investigate whether they are an artefact resulting from an overestimation of $R_{\rm bar}$ and/or an underestimation of $R_{\rm cor}$ or a new class of bars, whose orbital structure has not yet been understood. We revised the available measurements of $R_{\rm bar}$ based on ellipse fitting and Fourier analysis and of $\Omega_{\rm bar}$ from the TW method. In addition, we measured $R_{\rm bar}$ from the analysis of the maps tracing the transverse-to-radial force ratio, which we obtained from the deprojected i-band images of the galaxies retrieved from the SDSS. We found that nearly all the sample galaxies are spirals

with an inner ring or pseudo-ring circling the bar and/or strong spiral arms, which hamper the measurement of $R_{\rm bar}$ from the ellipse fitting and Fourier analysis. According to these methods, the bar ends overlap the ring or the spiral arms making the adopted $R_{\rm bar}$ unreliable. On the contrary, the value of $R_{\rm bar}$ from the ratio maps is shorter than the corotation radius. This is in agreement with the theoretical predictions and findings of numerical simulations about the extension and stability of the stellar orbits supporting the bars. We conclude that ultrafast bars are no longer observed when the correct measurement of $R_{\rm bar}$ is adopted. Deriving $R_{\rm bar}$ in galaxies with rings and strong spiral arms is not straightforward and a solid measurement method based on both photometric and kinematic data is still missing.

I extensively contributed to the analysis of the photometric data, discussion of the results, and paper writing.

Chapter 3 (based on Buttitta, C., Corsini, E. M., Cuomo, V., et al. 2022, A&A, 664, L10) We characterised the properties of the bar hosted in lenticular galaxy NGC 4277. We measured $R_{\rm bar}$ and $S_{\rm bar}$ from the surface photometry obtained from the broad-band imaging of the SDSS and we derived $\Omega_{\rm bar}$ from the stellar kinematics obtained from the integral-field spectroscopy performed with the Multi Unit Spectroscopic Explorer (MUSE) at the Very Large Telescope (VLT). We estimated $V_{\rm circ}$ by correcting the stellar streaming motions for asymmetric drift and we derived $\mathcal{R}$. We found that NGC 4277 hosts a short ($R_{\rm bar}$= $3.2^{+0.9}_{-0.6}$ kpc), weak ($S_{\rm bar}$= 0.21 ± 0.02), and slow ($\mathcal{R}$= $1.8^{+0.5}_{-0.3}$) bar and its pattern speed is amongst the best-constrained ones ever obtained with the TW method. NGC 4277 is the first clear-cut case of a galaxy hosting a slow stellar bar measured with the TW method. A possible interaction with the neighbour galaxy NGC 4273 could have triggered the formation of such a slow bar and/or the bar could be slowed down due to the dynamical friction with a significant amount of DM within the bar region.

I analysed the photometric and kinematic data, interpreted and discussed the results, and took care of the paper writing.

Chapter 4 (based on Cuomo, V., Corsini, E. M., Morelli, L., et al. 2022, MNRAS, 516, L24) We characterised the properties of the bar hosted in dwarf galaxy IC 3167. We measured $R_{\rm bar}$ and $S_{\rm bar}$ from the surface photometry obtained from the broad-band imaging of the SDSS and we derived $\Omega_{\rm bar}$ from the stellar kinematics obtained from the integral-field spectroscopy performed with the MUSE spectrograph at the VLT. We estimated $V_{\rm circ}$ by correcting the stellar streaming motions for asymmetric drift and we derived $\mathcal{R}$. We found that IC 3167 hosts a short ($R_{\rm bar}$=$1.1^{+0.4}_{-0.2}$ kpc), weak ($S_{\rm bar}$=0.27 ± 0.04), and slow ($\mathcal{R}$= $1.7^{+0.5}_{-0.3}$) bar. The probability that the bar is rotating slowly (68%) is twice more likely to be slow (probability of 68%) rather than fast (32%). This allows us to infer that the formation of this bar was triggered by the ongoing interaction rather than to internal processes.

I extensively contributed to the analysis of the photometric data and discussion of the results.

Chapter 5 (based on Buttitta, C., Corsini, E. M., Aguerri, J. A. L., et al. 2022, MNRAS, submitted) We investigate the link between $\mathcal{R}$ and DM content in barred galaxies by concentrating on the cases of the lenticular galaxies NGC 4264 and NGC 4277. These two gas-poor galaxies have similar morphologies, sizes, and luminosities. But, NGC 4264 hosts a fast bar, which extends to nearly the corotation, while the bar embedded in NGC 4277 is slow and falls short of corotation. We derive the DM fraction $f_{\rm DM,bar}$ within the bar region from Jeans axisymmetric dynamical models by matching the stellar kinematics obtained with the MUSE integral-field spectrograph and using SDSS images to recover the stellar mass distribution. We

build mass-follows-light models as well as mass models with a spherical DM halo, which is not tied to the stars. We find that the inner regions of NGC 4277 host a larger DM fraction ($f_{\rm DM,bar} = 0.53 \pm 0.02$) with respect to NGC 4264 ($f_{\rm DM,bar} = 0.33 \pm 0.04$) in agreement with the predictions of theoretical works and the findings of numerical simulations, which have found that fast bars live in baryon-dominated discs, whereas slow bars experienced a strong drag from the dynamical friction due to a dense DM halo. This is the first time that $\mathcal{R}$ is coupled to $f_{\rm DM,bar}$ derived from dynamical modelling.

I built the dynamical models, interpreted and discussed the results, and took care of the paper writing.

Chapter 6 (based on Buttitta, C., Corsini, E. M., Debattista, V. P., et al., in preparation) We built N-body simulations to mimic the photometric and kinematic properties of the lenticular barred galaxy NGC 4277. Our galaxy models are pure collisionless models comprised of a bulge, a disc, and a DM halo. The models were evolved in isolation, therefore it is not possible to test whether the formation of the slow bar hosted in NGC 4277 was triggered by the tidal interaction with the companion NGC 4273. The galaxy model that best reproduces both the photometry and stellar kinematics of NGC 4277 is characterised by a massive DM halo. Our results agree with the prediction obtained by dynamical modelling, which found a considerable DM fraction in the innermost region of NGC 4277. Thus, we confirmed that the bar hosted in NGC 4277 had experienced a strong drag as a consequence of the interaction with a dense DM halo.

I run the numerical simulations, interpreted and discussed the results, and took care of the paper writing.

Chapter 7 We report our conclusions and some future perspectives.

Chapter 2

Solving the puzzle of ultrafast bars[§]

Abstract

More than 10% of the barred galaxies with a direct measurement of $\Omega_{\rm bar}$ host an ultrafast bar. These bars extend well beyond $R_{\rm cor}$ and challenge our understanding of the orbital structure of barred galaxies. Most of them are found in spiral galaxies, rather than in lenticular ones. We analysed the properties of the ultrafast bars detected in the CALIFA survey to investigate whether they are an artefact resulting from an overestimation of $R_{\rm bar}$ and/or an underestimation of $R_{\rm cor}$ or a new class of bars, whose orbital structure has not yet been understood. We revised the available measurements of $R_{\rm bar}$ based on ellipse fitting and Fourier analysis and of $\Omega_{\rm bar}$ from the TW method. In addition, we measured $R_{\rm bar}$ from the analysis of the maps tracing the transverse-to-radial force ratio, which we obtained from the deprojected i-band images of the galaxies retrieved from the SDSS. We found that nearly all the sample galaxies are spirals with an inner ring or pseudo-ring circling the bar and/or strong spiral arms, which hamper the measurement of $R_{\rm bar}$ from the ellipse fitting and Fourier analysis. According to these methods, the bar ends overlap the ring or the spiral arms making the adopted $R_{\rm bar}$ unreliable. On the contrary, the value of $R_{\rm bar}$ from the ratio maps is shorter than the corotation radius. This is in agreement with the theoretical predictions and findings of numerical simulations about the extension and stability of the stellar orbits supporting the bars. We conclude that ultrafast bars are no longer observed when the correct measurement of $R_{\rm bar}$ is adopted. Deriving $R_{\rm bar}$ in galaxies with rings and strong spiral arms is not straightforward and a solid measurement method based on both photometric and kinematic data is still missing.

2.1 Introduction

More than 100 galaxies have been analysed so far with the TW method, the only model-independent method to recover $\Omega_{\rm bar}$ (see Cuomo et al., 2020, for a review). The bar pattern speed can be parameterised with $\mathcal{R}$, a distance-independent parameter that permits to divide bars into fast and slow (Athanassoula, 1992; Debattista & Sellwood, 2000). Bars are mainly supported by elongated stellar orbits called x_1 orbits, which are stable within $R_{\rm cor}$. In contrast, x_1 orbits outside $R_{\rm cor}$ are arranged perpendicular to the bar major axis and do not sustain the bar structure (Contopoulos & Papayannopoulos, 1980; Contopoulos, 1981; Vasiliev & Athanassoula, 2015). Current dynamical arguments show that bars can not have $\mathcal{R} < 1.0$. Despite theoretical predictions, $\sim 10\%$ of the galaxies with $\Omega_{\rm bar}$ measured with the TW method shows $\mathcal{R} < 1.0$ at 95% confident level: these bars are termed as 'ultrafast' (Buta & Zhang, 2009).

[§] *Based on Cuomo, V., Lee, Y. H., Buttitta, C., et al. 2021, A&A, 649, A30.*

According to the morphological classification provided in Cuomo et al. (2020), all of them are found in late-type barred galaxies with Hubble type T between 2 and 7, except for the lenticular galaxy NGC 2880. It is not clear whether ultrafast bars are the consequence of an erroneous application of the TW method or a special class of bars, which do not obey to the predictions of theory and numerical simulations (see Aguerri et al. 2015 and Guo et al. 2019, for a discussion). However, a non-negligible fraction of ultrafast bars was also observed while applying other methods (Buta & Zhang, 2009; Buta, 2017). Garma-Oehmichen et al. (2020) analysed the different sources of error in the TW method and quantified how much they are affecting the final measurement of $\Omega_{\rm bar}$ in a sample of 15 galaxies. The dominant sources of error are the identification of the disc position angle PA and the length of the apertures along which to measure the position and velocity of the tracer, while centring errors and a degraded PSF result in a small or negligible effect. Garma-Oehmichen et al. (2020) did not observe a significant correlation between the error sources, but they stressed the importance of the correct error treatment. In fact, they claimed that a large fraction of ultrafast bars may be the result of an erroneous treatment of the errors together with low spatial resolution data. New studies are needed to eventually exclude that these results are flawed because of an improper application of the TW method and/or to investigate if some information about the nature of ultrafast bars is still missing.

Recent studies pointed out that spiral arms may affect the measurement of $R_{\rm bar}$ (Petersen et al., 2019; Hilmi et al., 2020). In particular, Hilmi et al. (2020) showed with their simulations that the measurement of $R_{\rm bar}$ dramatically fluctuates on a dynamical timescale depending on the strength of the spiral structure and on the measurement threshold. In this chapter, we aim to test whether the measurements of $R_{\rm bar}$ adopted in literature may be biased by the presence of the spiral arms or other components, which caused the extremely low values of $\mathcal{R}$.
We organise the chapter as follows. We report the general properties of the galaxy sample in Sect. 2.2. We present our analysis in Sect. 2.3. We discuss our results in Sect. 2.4, and report our conclusions in Sect. 2.5. We adopt as cosmological parameters, $\Omega_{\rm M} = 0.286$, $\Omega_{\Lambda} = 0.714$, and $H_0 = 69.3$ km s^{-1} Mpc^{-1} (Hinshaw et al., 2013).

2.2 Sample selection and available data

We considered the 31 barred galaxies studied by Aguerri et al. (2015) and Cuomo et al. (2019b) for which a direct TW measurement of $\Omega_{\rm bar}$ was obtained by analysing the stellar kinematics from CALIFA (Sánchez et al., 2012). Aguerri et al. (2015) selected 15 strongly-barred galaxies, while Cuomo et al. (2019b) focused their attention onto 16 weakly-barred galaxies. The resulting sample spans a wide range of morphological types (SB0 − SBd), redshifts (0.005 − 0.02), and absolute SDSS r-band magnitudes ($-18.5 - -22.0$ mag). Twelve galaxies measured by Aguerri et al. (2015) and Cuomo et al. (2019b) turned out to host an ultrafast bar, according to their values of $\mathcal{R}$ and corresponding errors. Fig.2.1 shows the distributions of morphological types, absolute SDSS r-band magnitudes, circular velocities, and bar radii of the initial sample of 31 galaxies compared to those of the sub-sample of 12 galaxies hosting an ultrafast bar. These distributions are similar to those of the total sample of bright barred galaxies targeted by the CALIFA survey. We ran a Kolmogorov–Smirnov test with the IDL procedure KSTWO and verified there are no statistical differences at a very high confidence level ($> 95\%$) between the distributions of properties of the two samples. All the ultrafast bars except for one are found in SBab − SBc spiral galaxies.

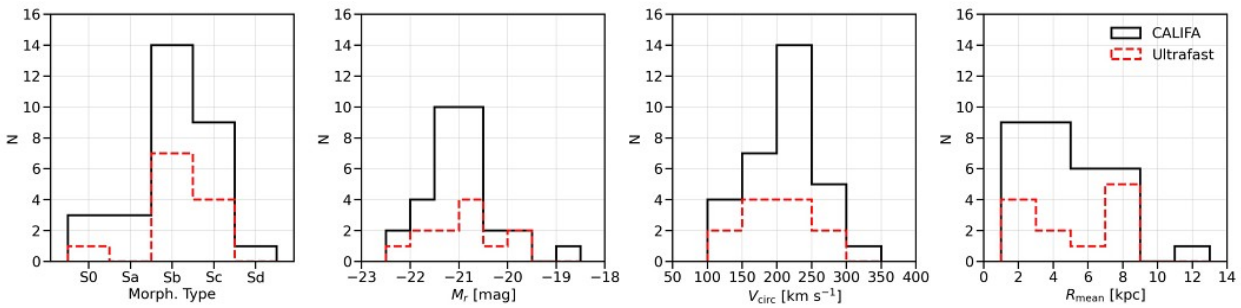

Figure 2.1: Distribution of the morphological types, absolute SDSS r-band magnitudes, circular velocities, and bar radii of the initial sample of 31 CALIFA galaxies analysed with the TW method by Aguerri et al. (2015) and Cuomo et al. (2019b) (black solid line) and of the sub-sample of 12 galaxies hosting an ultrafast bar discussed in this chapter (red dotted line).

For the sample galaxies, we adopted the values of $\Omega_{\rm bar}$ obtained by fitting with a straight line the luminosity-weighted photometric $\langle X \rangle$ and kinematic $\langle V \rangle$ integrals (Aguerri et al. 2015, Col. 4 in Table 3 and Cuomo et al. 2019b, Col. 3 in Table 2). As an alternative, the kinematic integrals can be directly obtained from the stellar velocity field. Moreover, either a map of the stellar surface brightness (Aguerri et al., 2015; Guo et al., 2019; Garma-Oehmichen et al., 2020) or stellar surface mass density (Aguerri et al., 2015; Guo et al., 2019; Williams et al., 2021) can be used as a weight in the definition of the integrals. However, the mass and light distributions often do not match well, particularly in the presence of ongoing star formation, as is usually the case in spiral galaxies.

The radius of $R_{\rm bar}$ is usually obtained as the mean value of various measurements retrieved using several methods (Corsini et al., 2003). Indeed, three different methods were adopted in Aguerri et al. (2015) and Cuomo et al. (2019b) to recover $R_{\rm bar}$ based on the photometric analysis of SDSS images (Abazajian et al., 2009). Hereafter, we refer to this estimate as $R_{\rm mean}$. The first two methods are based on the study of the radial profile of ϵ and PA of the ellipses which best fit the galaxy isophotes (Menéndez-Delmestre et al., 2007; Aguerri et al., 2009). The bar radius corresponds to the position of the peak in the ellipticity profile, $R_{\epsilon,\rm peak}$, or to the position where the PA changes by $\Delta{\rm PA} = 5^\circ$ from the PA of the ellipse with the maximum ϵ value, $R_{\rm PA}$. Undisturbed barred galaxies usually show a local peak and a sudden outward decrease of ϵ to a minimum value ($\Delta\epsilon \geqslant 0.08$), which corresponds to the region of the disc where the isophotes become circular in the face-on case (Wozniak & Pierce, 1991; Aguerri et al., 2000). On the other hand, the radial profile of PA is constant in the bar region ($\Delta{\rm PA} \leqslant 20^\circ$) (Wozniak & Pierce, 1991; Aguerri et al., 2000). These peculiarities are due to the shape and orientation of the stellar orbits of the bar (Contopoulos & Grosbol, 1989; Athanassoula, 1992). The third adopted approach to measure $R_{\rm bar}$ consists in the Fourier decomposition of the galaxy light and in the analysis of the bar/interbar intensity ratio and provides $R_{\rm Fourier}$ (Ohta et al., 1990; Aguerri et al., 2000) (see Sec. 1.2 for details).

The bar rotation rate $\mathcal{R}$ is obtained as the ratio between $R_{\rm cor}$ and $R_{\rm bar}$. In turn, $R_{\rm cor}$ is given by the ratio between $\Omega_{\rm bar}$ and $V_{\rm circ}$, which is usually estimated with an asymmetric drift correction of the observed stellar streaming velocities (Merrifield & Kuijken, 1995; Aguerri et al., 2015). In our analysis, the bar is considered to be ultrafast not only if the corresponding $\mathcal{R}$ is lower that 1.0 at 95% confident level (as done in Cuomo et al. 2020), but when the sum between $\mathcal{R}$ and its upper error is lower than 1.0. This choice allows us to build a better defined sample of possible ultrafast bars. The corresponding sample consists of 12 galaxies with properties presented in Table 2.1 and corresponding SDSS colour images given in Fig. 2.2.

Table 2.1: Properties of the sample barred galaxies hosting an ultrafast bar.

Galaxy	Morph. Type	Hubble Type	z	M_r [mag]	i [°]	PA [°]	$R_{\rm mean}$ [arcsec]	$\Omega_{\rm bar}$ [km s^{-1} arcsec^{-1}]	$R_{\rm cor}$ [arcsec]	$\mathcal{R}$	Ref.
(1)	(2)	(3)	(4)	(5)	(6)	(7)	(8)	(9)	(10)	(11)	(12)
IC 1528	SABbc	SAB(rs)b	0.013	-20.57	66.7	72.7	$8.89^{+2.73}_{-2.93}$	21.0 ± 3.8	6.74 ± 2.11	$0.76^{+0.14}_{-0.22}$	2
IC 1683	SABb	S?	0.016	-20.73	54.3	13.0	$27.39^{+1.93}_{-2.03}$	9.7 ± 0.4	19.72 ± 8.47	0.72 ± 0.21	2
IC 5309	SABc	Sb	0.014	-19.99	60.0	26.7	$7.39^{+3.32}_{-1.87}$	24.3 ± 7.5	4.67 ± 3.77	$0.63^{+0.35}_{-0.45}$	2
NGC 36	SBb	SAB(rs)b	0.020	-21.86	57.2	23.4	$20.19^{+5.09}_{-4.51}$	17.4 ± 5.2	$12.60^{+5.39}_{-3.91}$	$0.6^{+0.3}_{-0.2}$	1
NGC 2553	SABab	S?	0.016	-21.23	54.6	67.0	$22.16^{+5.97}_{-5.22}$	23.6 ± 1.7	11.40 ± 2.63	$0.51^{+0.08}_{-0.11}$	2
NGC 2880	EAB7	SB0$^-$	0.005	-20.34	56.7	144.6	$12.77^{+6.09}_{-3.60}$	22.2 ± 1.3	9.43 ± 3.09	$0.74^{+0.15}_{-0.19}$	2
NGC 5205	SBbc	S?	0.006	-19.65	50.0	170.1	$17.69^{+2.83}_{-2.07}$	15.1 ± 2.8	$11.34^{+2.99}_{-2.53}$	$0.7^{+0.2}_{-0.1}$	1
NGC 5406	SBb	SAB(rs)bc	0.018	-22.25	44.9	111.8	$21.00^{+1.09}_{-2.10}$	22.8 ± 8.0	$11.01^{+4.80}_{-3.00}$	$0.5^{+0.2}_{-0.1}$	1
NGC 5947	SBbc	SBbc	0.020	-21.28	44.6	72.5	$10.91^{+1.29}_{-1.60}$	31.7 ± 4.2	$5.79^{+2.39}_{-2.30}$	0.5 ± 0.2	1
NGC 5971	SABb	Sa	0.011	-20.57	69.0	132.0	$23.85^{+20.10}_{-10.91}$	16.9 ± 4.3	13.37 ± 6.44	$0.56^{+0.15}_{-0.32}$	2
NGC 6497	SBab	SB(r)b	0.010	-21.72	60.9	112.0	$14.70^{+2.09}_{-1.29}$	42.7 ± 7.4	$5.49^{+2.09}_{-1.60}$	0.3 ± 0.1	1
UGC 3253	SBb	SB(r)b	0.014	-20.65	56.8	92.0	$15.81^{+1.29}_{-2.20}$	15.5 ± 3.1	$11.89^{+3.18}_{-2.69}$	$0.7^{+0.2}_{-0.2}$	1

Notes: (1) Galaxy name. (2) Morphological classification from CALIFA (Walcher et al., 2014). (3) Hubble type (de Vaucouleurs et al., 1991, hereafter RC3). (4) Redshift from SDSS-DR14 (Abolfathi et al., 2018). (5) Absolute SDSS r-band magnitude obtained from the model r-band apparent magnitude m_r provided by the SDSS-DR14 and the galaxy distance from NED as obtained from the radial velocity with respect to the cosmic microwave background reference frame. (6) Disc inclination. (7) Disc position angle. (8) Deprojected bar radius. (9) Bar pattern speed. (10) Bar corotation radius. (11) Bar rotation rate. (12) Source of disc and bar properties: 1 = Aguerri et al. (2015), 2 = Cuomo et al. (2019b).

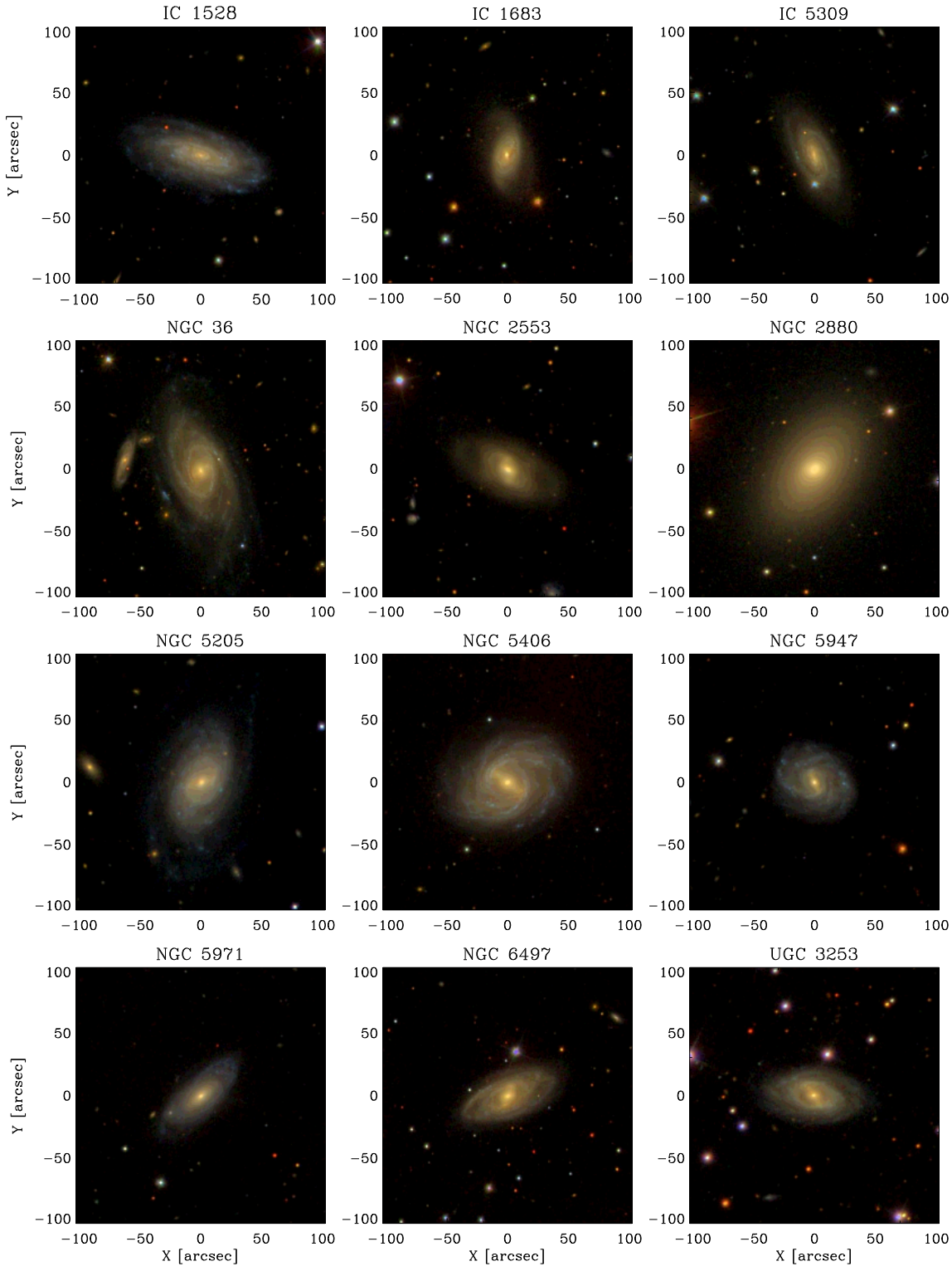

Figure 2.2: SDSS colour images of the sample galaxies hosting an ultrafast bar. Each FOV is 200×200 arcsec^2 and it is oriented with north up and east left.

2.3 Revising the determination of the bar rotation rate

The determination of $\mathcal{R}$ involves two different quantities which characterise the bar: its length and corotation radius. For our sample, the determination of $R_{\rm cor}$ was obtained with the TW method, so the corresponding sources of error have to be considered. On the other hand, $R_{\rm bar}$ was calculated using different methods based on photometry, which may be affected by their own limitations.

Sources of error for the TW analysis

The successful application of the TW method requires the disc to have an intermediate i and the bar to be located at an intermediate PA with respect to the disc major and minor axes (Corsini, 2011). Moreover, recovering bar PA and ϵ from ellipse fitting can be very difficult when the galaxy is very inclined (Comerón et al., 2014). All the sample galaxies were selected to have an inclination $20^\circ \lesssim i \lesssim 70^\circ$ and a PA difference between bar and disc major axis $10^\circ \lesssim \Delta{\rm PA} \lesssim 80^\circ$.

Cuomo et al. (2020) explored the relative errors on $\Omega_{\rm bar}$, $R_{\rm bar}$, and $R_{\rm cor}$ for all the galaxies with available TW measurements as a function of the disc i and bar ΔPA, respectively (see their Figs. 2 and 3). They did not observe any significant trend and excluded any selection bias on the entire galaxy sample. This result is true for the sub-sample of galaxies hosting an ultrafast bar as well.

Moreover, the right identification of the disc parameters (especially the PA along which to locate the pseudo-slits) is crucial for the TW method (Debattista, 2003; Zou et al., 2019). All the galaxies were carefully selected to be suitable for the TW analysis, because they present a constant behaviour of the PA radial profile in the disc region. Moreover, the sources of error associated to the TW method, i.e., uncertainties in the identification of the disc PA and galaxy centre, and in the choice of the length of the pseudo-slits (Corsini, 2011; Garma-Oehmichen et al., 2020), were fully taken into account in the application of the TW method and propagated in the error estimate of $\Omega_{\rm bar}$.

Considerations about galaxy morphology

In the early application of the TW method, mainly lenticular galaxies were targeted. This was done to face the strict requests of the method, the limitations due to the long-slit spectroscopy, and to avoid morphological peculiarities or multiple pattern speeds which may be associated to spiral arms (Merrifield et al., 2006). After integral-field spectroscopy became largely used and more theoretical studies about the impact of multiple spiral arms on the TW analysis were available (Debattista et al., 2002; Meidt et al., 2008), spiral galaxies were measured and a non-negligible fraction of ultrafast bars were found in these galaxies. Indeed, in the initial sample of 31 CALIFA galaxies, 11 out of 27 SBa − SBd galaxies (41%) host an ultrafast bar, while this is the case only for one out of 4 SB0s (25%). In fact, the presence of spiral arms and other structures makes it more difficult to correctly determine the disc parameters and TW integrals (Corsini, 2011; Cuomo et al., 2020). Nevertheless, the applicability of the TW method to spiral galaxies was tested and demonstrated by both theoretical (Gerssen & Debattista, 2007; Zou et al., 2019) and observational studies involving high quality integral-field data (Aguerri et al., 2015; Guo et al., 2019; Garma-Oehmichen et al., 2020; Williams et al., 2021). In particular, Gerssen & Debattista (2007) explored the possible influence of the presence of dust on the reliable application of the TW method. In addition, Aguerri et al. (2015) used the distribution of the mass as weight for the integrals, and they found that the results are compatible with the case of light as weight. In particular, they discussed the cases of NGC 36, NGC 5205, and NGC 6947, excluding that the presence of dust may lead to a value of $\mathcal{R} < 1.0$.

We carefully performed a visual inspection of the colour images of the galaxies showed in Fig. 2.2 and inspected the SDSS $g-i$ colour images before and after their deprojection. We concluded that most of the galaxy in our sample (7 out of 12, corresponding to $\sim 60\%$) host inner rings or pseudo-rings around the bar. Three of them present an outer ring or pseudo-ring too. These structures are often associated with a pronounced light deficit around the bar inside the inner ring, giving rise to a typical 'θ' shape, called 'dark gap' (Kim et al., 2016; James & Percival, 2016; Buta, 2017). This is the case for the galaxies: NGC 36, NGC 2553, NGC 5205, NGC 5406, NGC 5947, NGC 6497, and UGC 3253 (Fig. 2.2). We carefully analysed those features using the prescriptions of Buta et al. (2015), Buta (2017), and Bittner & et al. (2020). Multiple spiral arms are clearly visible in most of the sample galaxies except for IC 1683 and NGC 2553, which host a two-armed structure and NGC 2880 which does not host any spiral arm and it is a lenticular galaxy. Flocculent spiral arms are clearly visible in IC 1528, NGC 5406 and NGC 5947 while grand-design ones are visible in IC 5309 and NGC 36. We concluded that our sample galaxies host spiral arms with various geometrical properties, level of symmetry and amplitude, spanning from flocculent to multi-armed and grand-design morphologies.

Considerations about the bar radius

The adopted value of $R_{\rm bar}$ for the sample galaxies, $R_{\rm mean}$, corresponds to the mean result obtained using three different methods based on photometry. However, several issues may lead to the wrong determination of $R_{\rm bar}$. In particular, a late type morphology which includes the presence of strong spiral arms or other structures may hamper the right determination of $R_{\rm bar}$ (Petersen et al., 2019; Hilmi et al., 2020). In order to obtain an independent measure of $R_{\rm bar}$, we applied the method proposed by Lee et al. (2020) based on the analysis of the maps tracing the transverse-to-radial force ratio $Q_T(r,\phi)$ of the galaxy (Sanders & Tubbs, 1980; Combes & Sanders, 1981). While all the other methods discussed in Sect. 2.2 are based on the study of the light distribution in galaxies, the approach proposed by Lee et al. (2020) involves the calculation of the gravitational potential of the galaxy expected from the light distribution. Despite this method is based on photometry too, it allows to obtain an independent $R_{\rm bar}$ estimate, which we call $R_{\rm Qb}$ hereafter. In particular, it allows to disentangle the radius corresponding to the maximum strength of the bar from that of the spiral arms and/or rings by investigating the azimuthal profile according to the radius and to test whether $R_{\rm mean}$ truly matches the bar region. At the same time, it is obtained an alternative estimate of $S_{\rm bar}$, hereafter called $Q_{\rm b}$.

After deprojecting the SDSS i-band image of the galaxy, the Poisson equation is solved assuming a constant M/L ratio. The gravitational potential is obtained from the Poisson equation by the convolution of the three-dimensional mass density $\rho(\mathbf{x}')$ and $1/|\mathbf{x}-\mathbf{x}'|$ (Quillen et al., 1994; Buta et al., 2001):

$$\Psi(\mathbf{x}) = -G \int \frac{\rho(\mathbf{x}')\mathrm{d}^3\mathbf{x}'}{|\mathbf{x}-\mathbf{x}'|}.$$

The three-dimensional mass density can be written as $\rho(\mathbf{x}') = \Sigma(x,y)\rho_z(z)$, where $\Sigma(x,y)$ is the mass surface density in the plane of the galaxy and $\rho_z(z)$ is the normalised vertical density distribution assumed to follow an exponential profile. In the galaxy plane $z=0$, the two-dimensional potential can be defined in polar coordinates $\Phi(r,\phi) \equiv \Psi(x,y,z=0)$.

The mean radial force $\langle F_{\rm R}(r)\rangle$ and transverse force $F_{\rm T}(r,\phi)$ can be defined as:

$$\langle F_{\rm R}(r)\rangle \equiv \frac{{\rm d}\Phi_0(r)}{{\rm d}r}, \quad \text{and} \quad F_{\rm T}(r,\phi) \equiv \left|\frac{1}{r}\frac{\partial\Phi(r,\phi)}{\partial\phi}\right|$$

where Φ_0 is the $m = 0$ Fourier component of the gravitational potential (Buta et al., 2001). The maximum transverse force to the mean radial force is defined as:

$$Q_{\rm T}(r) \equiv \frac{F_{\rm T}^{\rm max}(r)}{\langle F_{\rm R}(r)\rangle}$$

where the maximum tangential force $F_{\rm T}^{\rm max}(r)$ is the maximum of $F_{\rm T}(r,\phi)$ along ϕ. The ratio map $Q_{\rm T}(r,\phi)$ of a barred galaxy typically presents four thick slabs and the four peaks along these slabs are observed near the four corners of the bar in the deprojected image of the galaxy (see Fig. 1 in Lee et al. 2020). The ratio map can be expressed in Cartesian coordinates $Q_{\rm T}(x,y)$ too, where a butterfly-shaped pattern is the typical signature of the presence of a bar. The radial profile of $Q_{\rm T}$ is calculated to be averaged over the azimuthal angle ϕ (Buta et al., 2001). The analysis of the shape of the $\langle Q_{\rm T}\rangle$ radial profile allows to constrain $R_{\rm bar}$. The location of a peak or a plateau in the $\langle Q_{\rm T}\rangle$ radial profile is adopted as a solid estimate of the bar radius, $R_{\rm Qb}$. At this radius, four peaks appear in the $Q_{\rm T}(R_{\rm Qb})$ azimuthal profile confirming the correct identification of the bar.

The method was originally proposed to perform a morphological classification, because the specific characteristics of both the $\langle Q_{\rm T}\rangle$ radial and $Q_{\rm T}(r_{\rm Qb})$ azimuthal profiles allow distinguishing between barred and unbarred galaxies. In particular, Lee et al. (2020) identify a barred galaxy when the $Q_{\rm T}(R_{\rm Qb})$ azimuthal profile presents four peaks corresponding to the four wings of the butterfly-shaped pattern shown in Buta et al. (2001), together with a global bar strength $Q_{\rm b} > 0.15$, defined as the bar force ratio in the polar coordinates:

$$Q_{\rm b} \equiv \frac{1}{n}\sum_{i=1}^{n} Q_{{\rm T},i}$$

where $Q_{{\rm T},i}$ is the maximum value at each peak on the $Q_{\rm T}(R_{\rm Qb})$ azimuthal profile, and n is the number of the peaks which is equal to four for a bar.

First of all, we considered the SDSS i-band images after measuring and subtracting the residual sky level, as done in Morelli et al. (2016). We deprojected the SDSS i-band images using the disc parameters provided by Aguerri et al. (2015) and Cuomo et al. (2019b) and reported in Table 2.1. To double check if these disc parameters were carefully identified and are suitable for the deprojection of the images, we repeated the image deprojection using the disc parameters obtained at the half of the radius of the isophote at a surface brightness level of $\mu_{\rm B} = 25$ mag arcsec^{-2} ($R_{25}/2$, RC3). This corresponds to the maximum extension of the residual sky-subtracted SDSS images. The two deprojected images provide consistent results in the resulting analysis. We adopted and present in the following the results corresponding to the deprojection based on the data from Aguerri et al. (2015) and Cuomo et al. (2019b).

In Fig. 2.3 we showed the analysis of the ratio map of the whole galaxy sample. The top panels show the original SDSS i-band image (left panel), the deprojected one obtained from the disc parameters tabulated in Table 2.1 (central panel), and the ratio map as a function of the polar coordinates (r,ϕ) (right panel). In the lower panels of the figure are presented the azimuthally-averaged radial profile of $\langle Q_{\rm T}\rangle$ (left panel), the azimuthal profile of the ratio map $Q_{\rm T}(R_{\rm Qb})$ at radius $R_{\rm Qb}$ (central panel), and the azimuthal profile of the ratio map $Q_{\rm T}(R_{\rm mean})$ at radius $R_{\rm mean}$ (right panel).

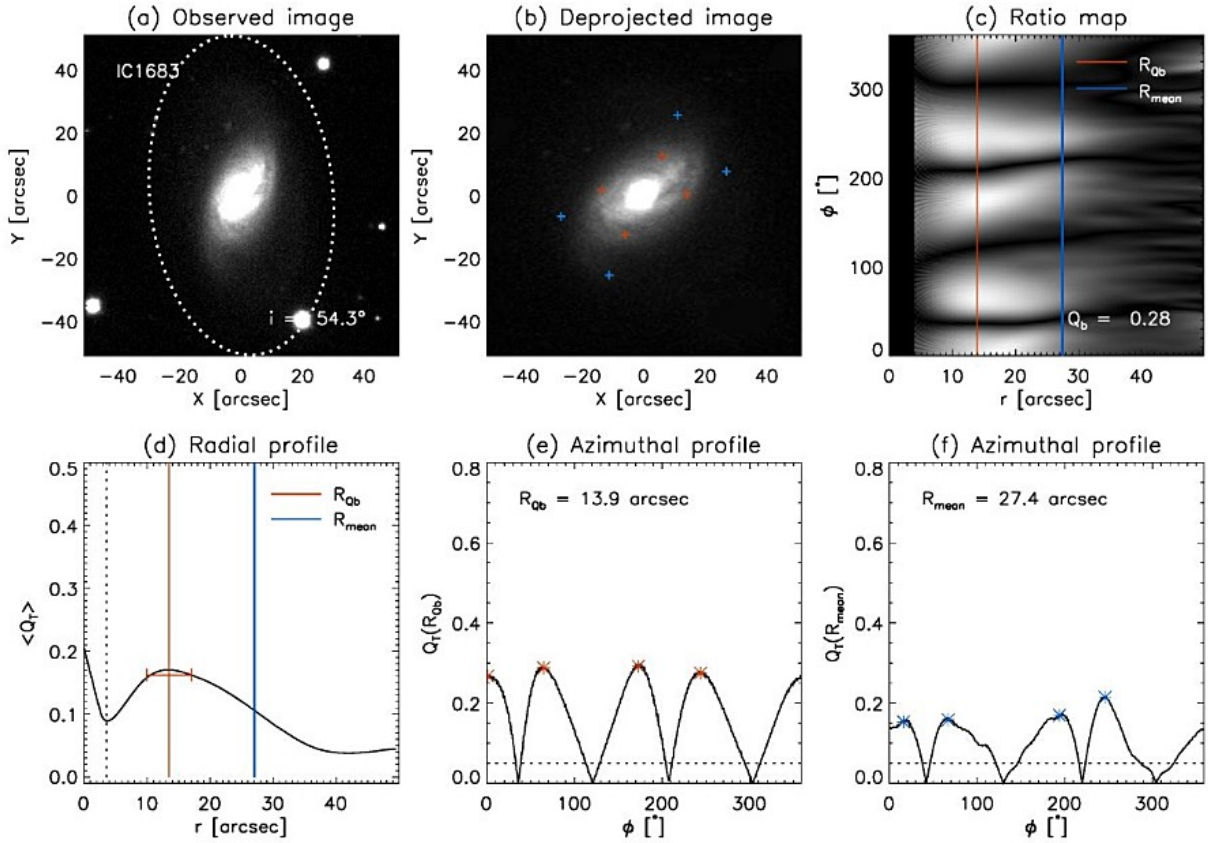

Figure 2.3: Analysis of the ratio map of IC 1683. *Panel (a)*: Observed i-band SDSS image of the galaxy with north up and east left. The dotted ellipse marks the region of the galaxy considered for the deprojection. The galaxy inclination is given in the bottom right corner. *Panel (b)*: Deprojected image of the galaxy. The red and blue crosses correspond to the peaks measured in the $Q_T(R_{\rm Qb})$ and $Q_T(R_{\rm mean})$ azimuthal profiles, respectively. *Panel (c)*: Map of the transverse-to-radial force ratio $Q_T(r, \phi)$. The vertical blue and red lines mark the location of $R_{\rm Qb}$ and $R_{\rm mean}$, respectively. The bar strength is given in the bottom right corner. *Panel (d)*: Radial profile of $\langle Q_T \rangle$. The vertical dotted line corresponds to the boundary of the bulge-dominated region, identified as the range from the centre to the minimum (or a change in the slope) in the $\langle Q_T \rangle$ radial profile. The vertical blue and red lines mark the location of $R_{\rm Qb}$ and $R_{\rm mean}$, respectively. The horizontal red segment is the error associated to $R_{\rm Qb}$. *Panel (e)*: Azimuthal profile of $Q_T(R_{\rm Qb})$. The local maxima of the profile are highlighted by red asterisks. The horizontal dotted line corresponds to the threshold value at $Q_{\rm T} = 0.05$, adopted to count the number of peaks associated to the bar. The value of $R_{\rm Qb}$ from this paper is given in top left corner. *Panel (f)*: Azimuthal profile of $Q_T(R_{\rm mean})$. The local maxima of the profile are highlighted by blue asterisks. The horizontal dotted line corresponds to the threshold value at $Q_{\rm T} = 0.05$, adopted to count the number of peaks associated to the bar. The value of $R_{\rm mean}$ from literature is given in top left corner.

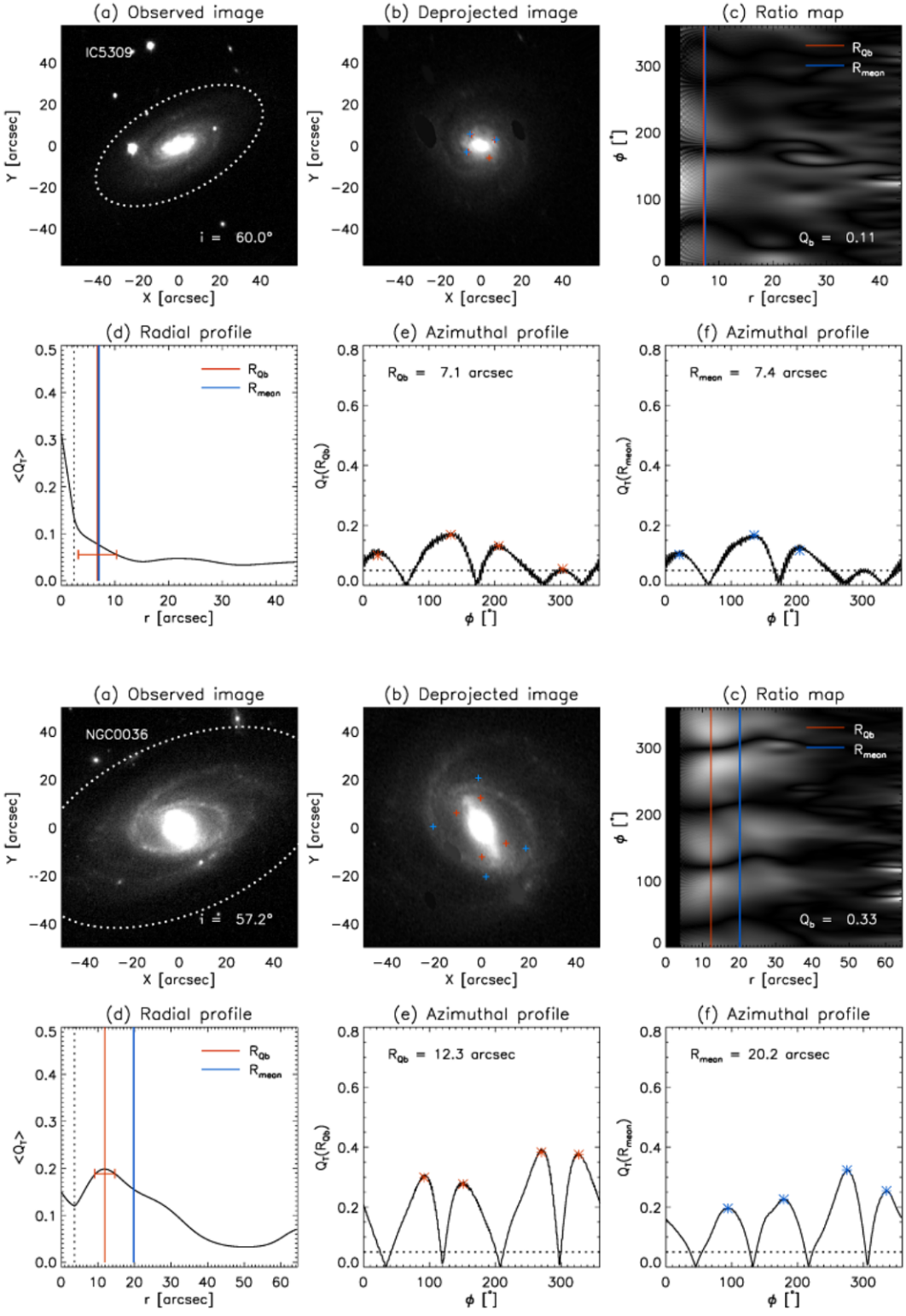

Figure 2.3: (continued).

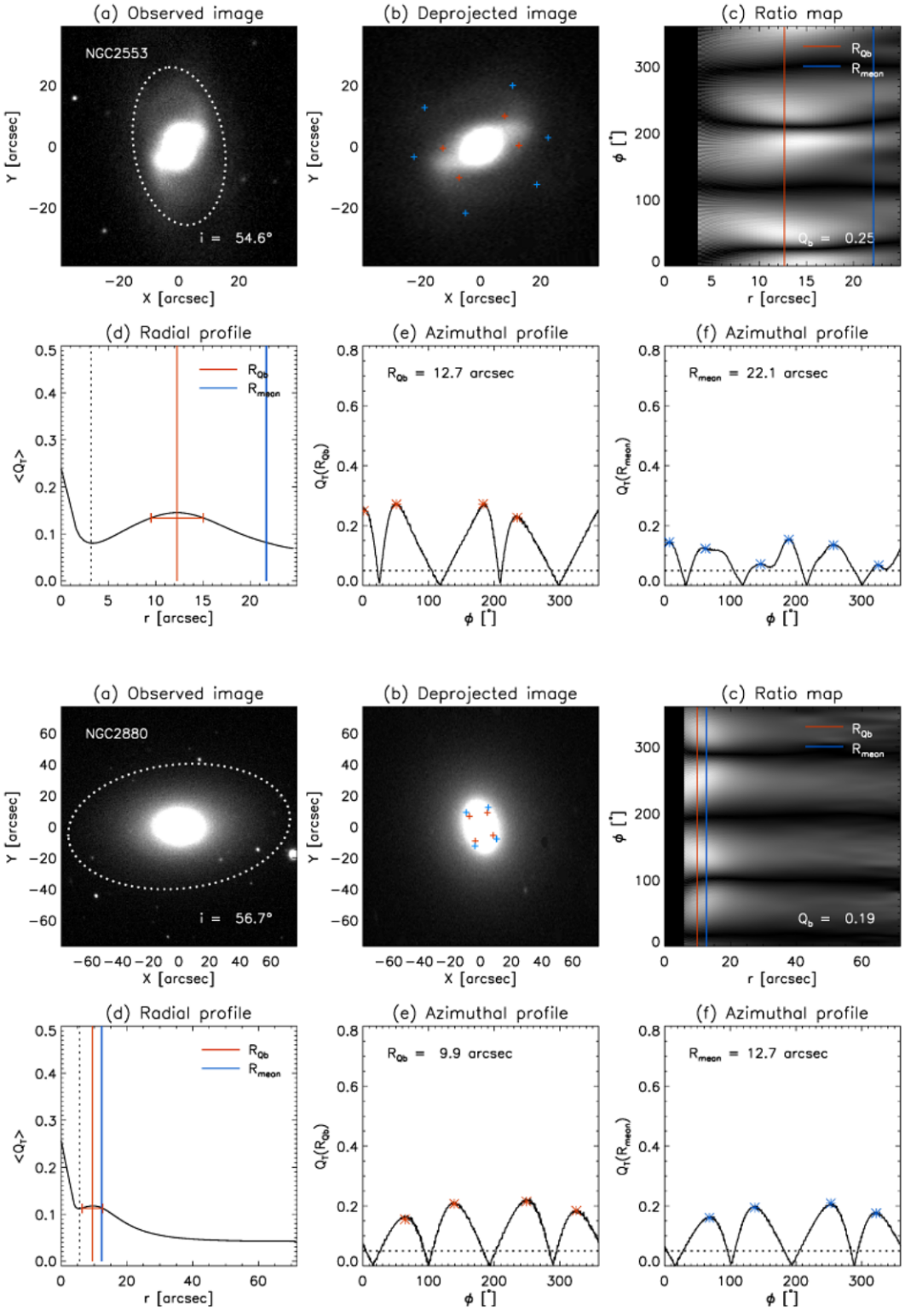

Figure 2.3: (continued).

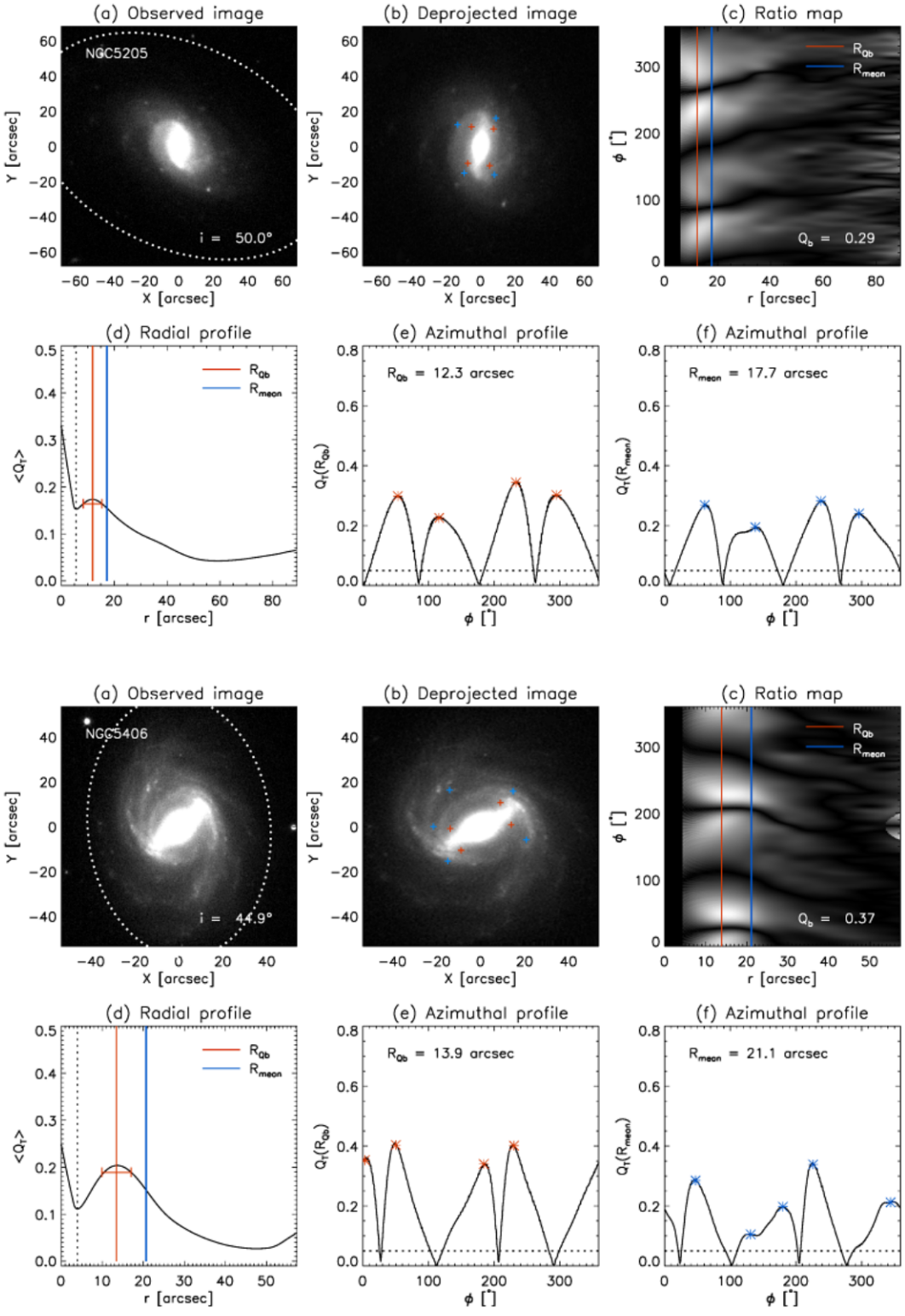

Figure 2.3: (continued).

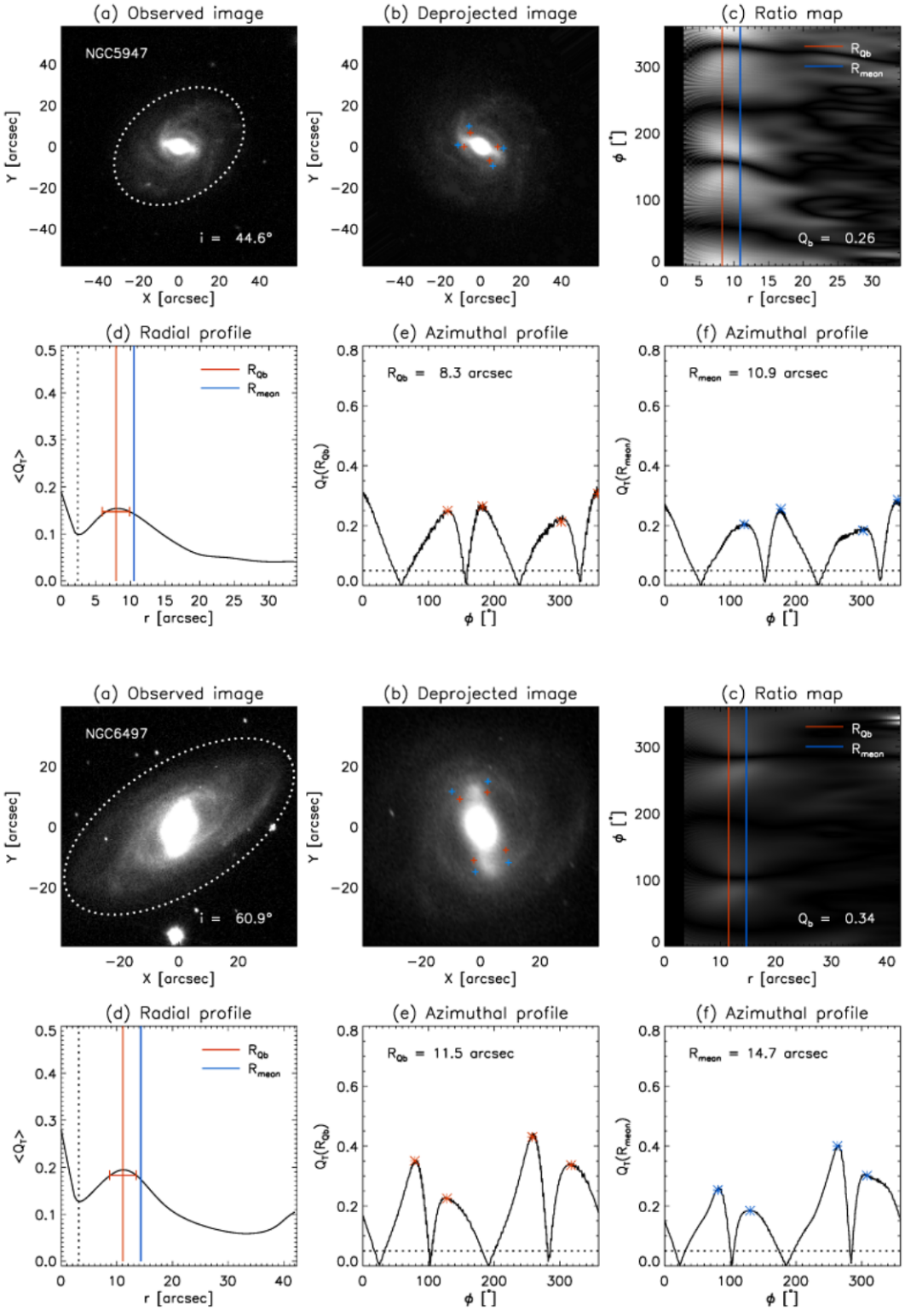

Figure 2.3: (continued).

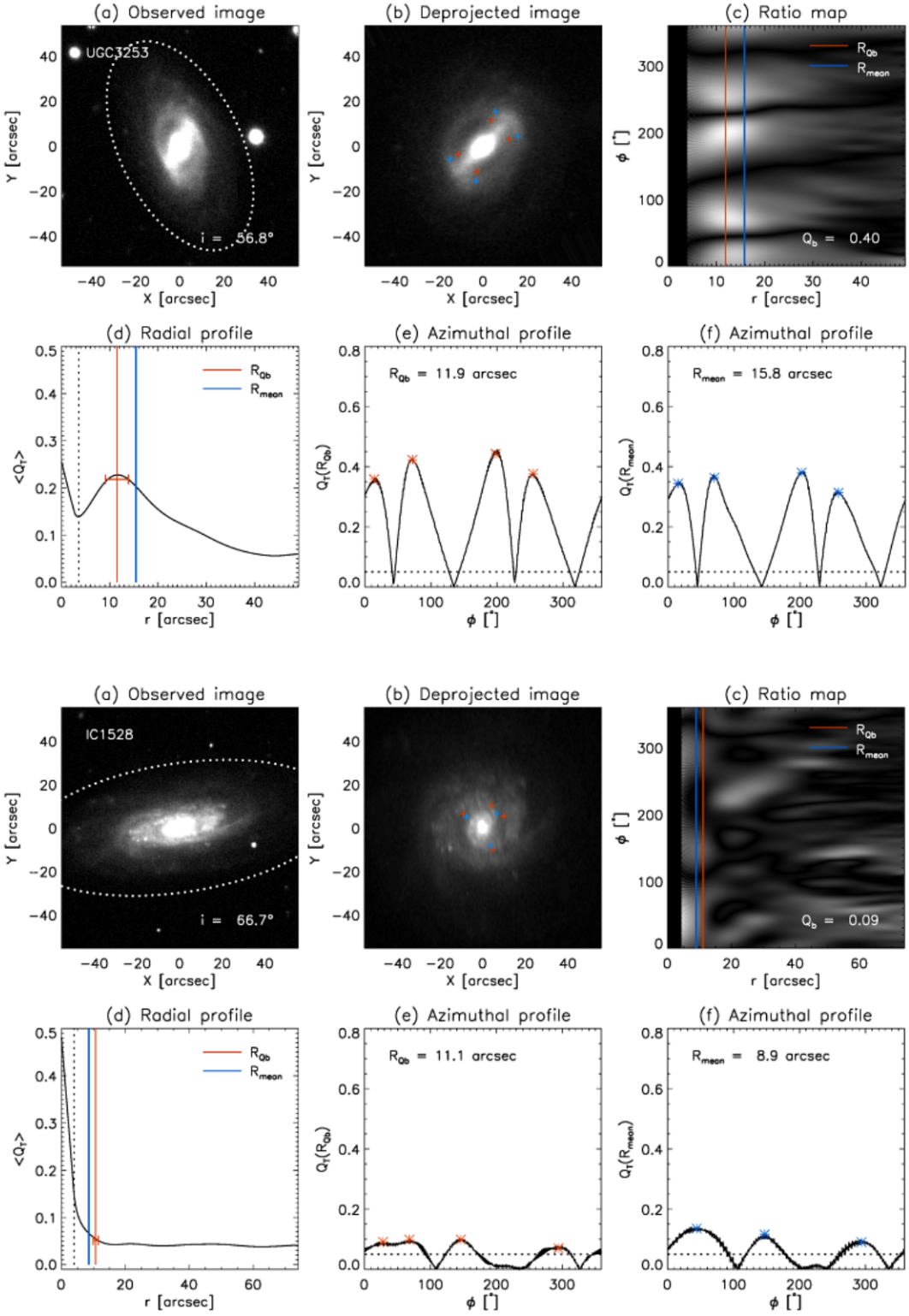

Figure 2.3: (continued).

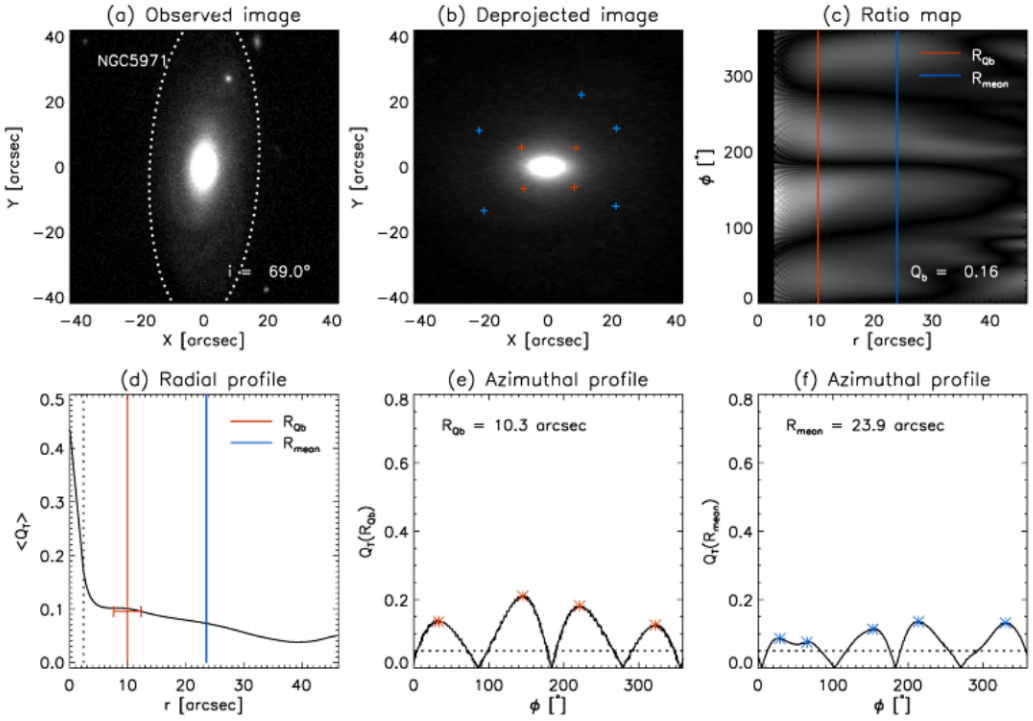

Figure 2.3: (continued).

We tested the value of $R_{\rm mean}$ tabulated in Table 2.1 to recover $\mathcal{R}$ by analysing the $Q_{\rm T}(R_{\rm mean})$ azimuthal profile to look for the typical four peaks expected for the bar. We checked where the resulting peaks are located on the galaxy image (see panel (b) of Fig. 2.3). The corresponding error on $R_{\rm Qb}$ was obtained as the width of the peak in the $\langle Q_{\rm T} \rangle$ radial profile, calculated where $\langle Q_{\rm T} \rangle$ reaches 95% of the peak value and using only the right side of the profile, since the peak is not always well defined. Here we summarised the results of our morphological analysis and the comparison between $R_{\rm Qb}$ and $R_{\rm mean}$ for the entire galaxy sample.

IC 1683 is a two-armed spiral galaxy without rings, which we classified to belong to the (s) variety with arms breaking out directly from the bar. The ratio map presents four slabs for $r \lesssim 35$ arcsec and an outer complex pattern corresponding to the spiral arms. The $\langle Q_{\rm T} \rangle$ radial profile decreases till a local minimum at $r = 4.0$ arcsec in the bulge region, then it increases to a maximum value at $R_{\rm Qb}$. The corresponding $Q_{\rm T}(R_{\rm Qb})$ azimuthal profile presents four peaks with $Q_{\rm b} = 0.28$. The $Q_{\rm T}(R_{\rm mean})$ azimuthal profile shows four weaker peaks. The value of $R_{\rm mean}$ is larger than $R_{\rm Qb}$ and they are not consistent with each other.

IC 5309 is an inclined spiral galaxy with strong grand-design spiral arms but no rings. The ratio map presents four slabs for $r \lesssim 10$ arcsec and an outer complex pattern corresponding to the spiral arms. The $\langle Q_{\rm T} \rangle$ radial profile is dominated by the bulge till $r = 2.8$ arcsec and then decreases to a kind of a plateau, corresponding to the four peaks in the $Q_{\rm T}(R_{\rm Qb})$ azimuthal profile. We classified the galaxy as weakly barred for its low bar strength $Q_b = 0.11$. The $Q_{\rm T}(R_{\rm mean})$ azimuthal profile presents only three peaks. The values of $R_{\rm mean}$ and $R_{\rm Qb}$ are consistent within the errors.

NGC 36 is a grand-design spiral galaxy with an inner ring and an outer pseudo-ring which we highlighted by adopting the (r) and (R'_2) varieties for the morphological classification. The ratio map presents four slabs extending to the outer regions of the galaxy and corresponding to both the bar and inner ring. The $\langle Q_T \rangle$ radial profile decreases to a local minimum at $r = 4.0$ arcsec in the bulge region, then it increases to a maximum value at R_{Qb}. The corresponding $Q_T(R_{Qb})$ azimuthal profile presents four peaks with $Q_b = 0.33$. The $Q_T(R_{mean})$ azimuthal profile shows four peaks, even if they are less prominent. The size of the inner ring corresponds to R_{mean}, which is not consistent with R_{Qb}.

NGC 2553 is a two-armed spiral which we recognise to have an inner (r) and an outer ($R_1R'_2$) morphology. The ratio maps present four well-defined slabs extending to the outer regions of the galaxy. The $\langle Q_T \rangle$ radial profile decreases to a local minimum at $r = 3.6$ arcsec in the bulge region, then it increases till a maximum value at R_{Qb}. The corresponding $Q_T(R_{Qb})$ azimuthal profile presents four peaks with $Q_b = 0.26$. The $Q_T(R_{mean})$ azimuthal profile shows six weak peaks. The size of the inner ring corresponds to R_{mean}, which is consistent with R_{Qb} within the errors.

NGC 2880 is the only lenticular galaxy of the sample. It hosts a large bulge and a bar almost aligned with the disc minor axis. The ratio map presents four well-defined slabs extending to the outer regions of the galaxy. The $\langle Q_T \rangle$ radial profile decreases to a local minimum at $r = 6.0$ arcsec in the bulge region. Then, it increases to a plateau corresponding to the four peaks in the $Q_T(R_{Qb})$ azimuthal profile with $Q_b = 0.19$. The $Q_T(R_{mean})$ azimuthal profile shows the same four peaks. The values of R_{mean} and R_{Qb} are consistent within the errors.

NGC 5205 is a multiple-armed spiral galaxy with an inner broken ring which we translated into an (rs) classification. The ratio map presents four slabs for $r \lesssim 30$ arcsec and an outer complex pattern corresponding to the spiral arms. The $\langle Q_T \rangle$ radial profile decreases to a local minimum at $r = 5.9$ arcsec in the bulge region, then it increases to a maximum value at R_{Qb}. The corresponding $Q_T(R_{Qb})$ azimuthal profile presents four peaks with $Q_b = 0.29$. The peaks are nearly the same in the $Q_T(R_{mean})$ azimuthal profile. The size of the inner broken ring corresponds to R_{mean}, which is consistent with R_{Qb} within the errors.

NGC 5406 is a multiple-armed spiral galaxy with an inner broken ring and an (rs) morphology. The ratio map presents four slabs for $r \lesssim 25$ arcsec and an outer complex pattern corresponding to the spiral arms. The $\langle Q_T \rangle$ radial profile decreases to a local minimum at $r = 4.4$ arcsec in the bulge region, then it increases till a maximum value at R_{Qb}. The corresponding $Q_T(R_{Qb})$ azimuthal profile presents four peaks with $Q_b = 0.37$. The value of R_{mean} corresponds to the ring size and the presence of a spiral arm in the ring region gives rise to the fifth peak observed in the $Q_T(R_{Qb})$ azimuthal profile. The values of R_{mean} and R_{Qb} are consistent within the errors.

NGC 5947 is a multiple-armed spiral galaxy. We noticed the presence of an inner ring, which translates into an (r) classification. The ratio map presents four slabs for $r \lesssim 20$ arcsec and an outer complex pattern corresponding to the spiral arms. The $\langle Q_T \rangle$ radial profile decreases to a local minimum at $r = 2.8$ arcsec in the bulge region, then it increases to a maximum value at R_{Qb}. The corresponding $Q_T(R_{Qb})$ azimuthal profile presents four peaks with $Q_b = 0.26$. The $Q_T(R_{mean})$ azimuthal profile is characterised by four peaks too. The size of the ring corresponds to R_{mean}, which is consistent with R_{Qb} within the errors.

NGC 6497 is a multiple-armed spiral galaxy with flocculent spiral arms. We translated the presence of outer rings into an ($R_1R'_2$) morphology. The ratio map presents four slabs for $r \lesssim 15$ arcsec. The $\langle Q_T \rangle$ radial profile decreases to a local minimum at $r = 3.6$ arcsec in the bulge region, then it increases to a maximum value at R_{Qb}. The corresponding $Q_T(R_{Qb})$ azimuthal profile presents four peaks with $Q_b = 0.34$. The same peaks are shown by the $Q_T(R_{mean})$ azimuthal profile. The ring size is consistent with R_{mean}, which agrees with R_{Qb} within the errors.

UGC 3253 is a multiple-armed spiral galaxy. The presence of an inner ring translates into an (r) classification. The ratio map presents four slabs for $r \lesssim 20$ arcsec and an outer complex pattern corresponding to the spiral arms. The $\langle Q_T \rangle$ radial profile decreases to a local minimum at $r = 4.0$ arcsec in the bulge region, then it increases to a maximum value at R_{Qb}. The corresponding $Q_T(R_{Qb})$ azimuthal profile presents four peaks with $Q_b = 0.40$. The $Q_T(R_{mean})$ azimuthal profile shows the same peaks. The size of the inner ring corresponds to R_{mean}, which is consistent with R_{Qb} within the errors.

IC 1528 is a flocculent galaxy with strong spiral arms and no rings. Due to its high inclination ($i \sim 70°$), we can not understand whether it is an unbarred galaxy, where the bar is mimicked by the winding spiral arms, or a genuine weakly barred galaxy, as suggested by the weak four peaks in the $Q_T(R_{Qb})$ azimuthal profile. The ratio map does not present the typical four slabs for barred galaxies and there is no peak or plateau in the $\langle Q_T \rangle$ radial profile. Therefore, we excluded IC 1528 from the discussion related to the analysis of the ratio maps.

NGC 5971 is an highly-inclined spiral galaxy ($i \sim 70°$) with multiple arms. Its deprojection produces an artifact bar structure along the disc minor axis hampering the analysis of the ratio map, which nevertheless shows the typical four slabs associated to a bar. We excluded NGC 5971 from the discussion related to the analysis of the ratio maps.

The galaxies IC 1528 and NGC 5971 are very inclined so the $Q_T(r, \phi)$ map analysis is not conclusive. In particular, IC 1528 does not present the typical features of a barred galaxy after deprojection, while the bar of NGC 5971 appears as an artefact structure elongated along the disc minor axis due to deprojection. We decided to discard these galaxies from further analysis of the ratio map and our final sample reduces to 10 objects.

2.4 Results

The new measurement of bar radius R_{Qb} and bar strength Q_b are tabulated in Table 2.2. We confirmed that all these galaxies host a strong bar, according to the criteria proposed by (Lee et al., 2020), except for IC 5309. This galaxy presents the typical four peaks in the $Q_T(R_{Qb})$ azimuthal profile but a lower value of Q_b than the threshold adopted to define a barred galaxy. This allowed us to confirm that it is a weakly barred galaxy, as already pointed out by the visual classification from CALIFA (Sánchez et al., 2012) and the analysis from Cuomo et al. (2019b). We found that $R_{mean} > R_{Qb}$ by $\sim 45\%$ on average and in three galaxies the two values are not even consistent with each other within their errors. In fact, R_{mean} is always larger than R_{Qb} at face values, but the large errors associated with R_{mean} make the two values consistent in many cases. Only for IC 1683, IC 5309, and NGC 2880, R_{mean} corresponds to the bar radius, but it remains larger than R_{Qb} at face values. On the contrary, we realised that R_{mean} for NGC 2553 and NGC 5406 is actually the radius of the ring circling the bar.

Table 2.2: Bar radius $R_{\rm Qb}$ and strength $Q_{\rm b}$ from the analysis of the transverse-to-radial force ratio map of the sample galaxies.

Galaxy	$R_{\rm Qb}$ [arcsec]	$Q_{\rm b}$	Class	$\mathcal{R}_{\rm new}$
(1)	(2)	(3)	(4)	(5)
IC 1683	13.86 ± 3.56	0.28	B	$1.42^{+0.62}_{-0.83}$
IC 5309	7.13 ± 3.56	0.11	NB	$0.65^{+0.47}_{-0.83}$
NGC 36	12.28 ± 2.77	0.33	B	$1.03^{+0.37}_{-0.41}$
NGC 2553	12.68 ± 2.77	0.25	B	$0.90^{+0.18}_{-0.22}$
NGC 2880	9.90 ± 3.17	0.19	B	$0.95^{+0.27}_{-0.39}$
NGC 5205	12.28 ± 3.56	0.29	B	$0.92^{+0.22}_{-0.28}$
NGC 5406	13.86 ± 3.56	0.37	B	$0.79^{+0.29}_{-0.24}$
NGC 5947	8.32 ± 1.98	0.26	B	$0.70^{+0.26}_{-0.30}$
NGC 6497	11.49 ± 2.38	0.34	B	$0.48^{+0.16}_{-0.17}$
UGC 3253	11.88 ± 1.89	0.40	B	$1.00^{+0.27}_{-0.24}$

Notes: (1) Galaxy name. (2) Deprojected bar radius. (3) Bar strength. (4) Barred (B) or unbarred (NB) classification according to Lee et al. (2020) criteria. (5) Bar rotation rate estimated as the ratio between $R_{\rm cor}$ tabulated in Table 2.1 and $R_{\rm Qb}$ from col. (2).

The corresponding $Q_{\rm T}(R_{\rm mean})$ azimuthal profile shows more than the four peaks we expect to have for a bar. For NGC 36, NGC 5205, NGC 5947, NGC 6497, and UGC 3253, the $Q_{\rm T}(R_{\rm mean})$ azimuthal profile shows four peaks but the value of $R_{\rm mean}$ corresponds to a galactocentric distance where a ring or spiral arms are clearly visible in the galaxy image.

Comparison of bar radius estimates

We measured $R_{\rm bar}$ in the sample galaxies with three more methods based on the ellipse fitting and Fourier analysis of the deprojected images, as done by Lee et al. (2019, 2020). In particular, we calculated R_ϵ and $R_{\rm tran}$ from the ellipticity and PA radial profiles of the deprojected SDSS i-band images, as the radius where the maximum of ϵ occurs and where the PA varies by 2° with respect to the location of the peak in ϵ, respectively and $R_{\rm A_2}$ as the radius corresponding to the maximum value of the amplitude A_2 of the Fourier $m = 2$ component, in the region where the phase angle ϕ_2 remains constant. We compare the new $R_{\rm bar}$ estimates with those obtained with similar methods by Aguerri et al. (2015) and Cuomo et al. (2019b) in Fig. 2.4. In particular, we put R_ϵ together with $R_{\epsilon,\rm peak}$, $R_{\rm tran}$ with $R_{\rm PA}$, and $R_{\rm A_2}$ with $R_{\rm Fourier}$. While $R_{\epsilon,\rm peak} \sim R_\epsilon$ and $R_{\rm PA} \sim R_{\rm tran}$ although with some scatter, it results that systematically $R_{\rm Fourier} > R_{\rm A_2}$. This discrepancy is due to the slightly different definition of $R_{\rm bar}$ in the two Fourier-based methods. In fact, $R_{\rm A_2}$ considers the peak of the $m = 2$ component of the Fourier series in the region where ϕ_2 remains constant to exclude the range with higher peaks in the Fourier $m = 2$ component caused by spiral arms. On the other, hand, $R_{\rm Fourier}$ requires the higher orders of the Fourier series and do not include the behaviour of the corresponding phase angles. The even components of the Fourier series, together with the corresponding phase angles and in particular the $m = 2$ one, can be strongly affected by the prominence of the bulge (Debattista et al., 2002; Lee et al., 2020).

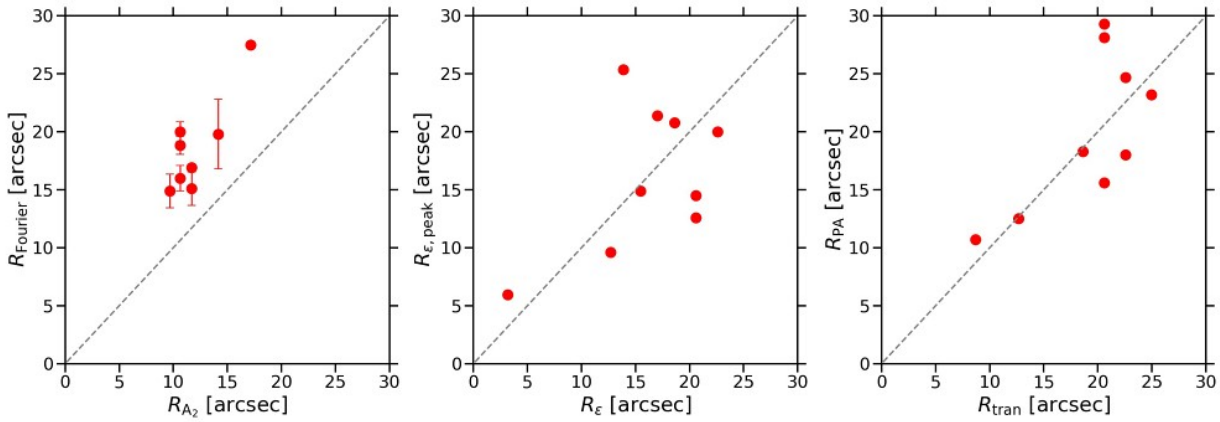

Figure 2.4: Comparison between the bar radius of the sample galaxies obtained with similar methods based on Fourier analysis (*left panel*), ellipticity (*central panel*) and PA (*right panel*) radial profiles.

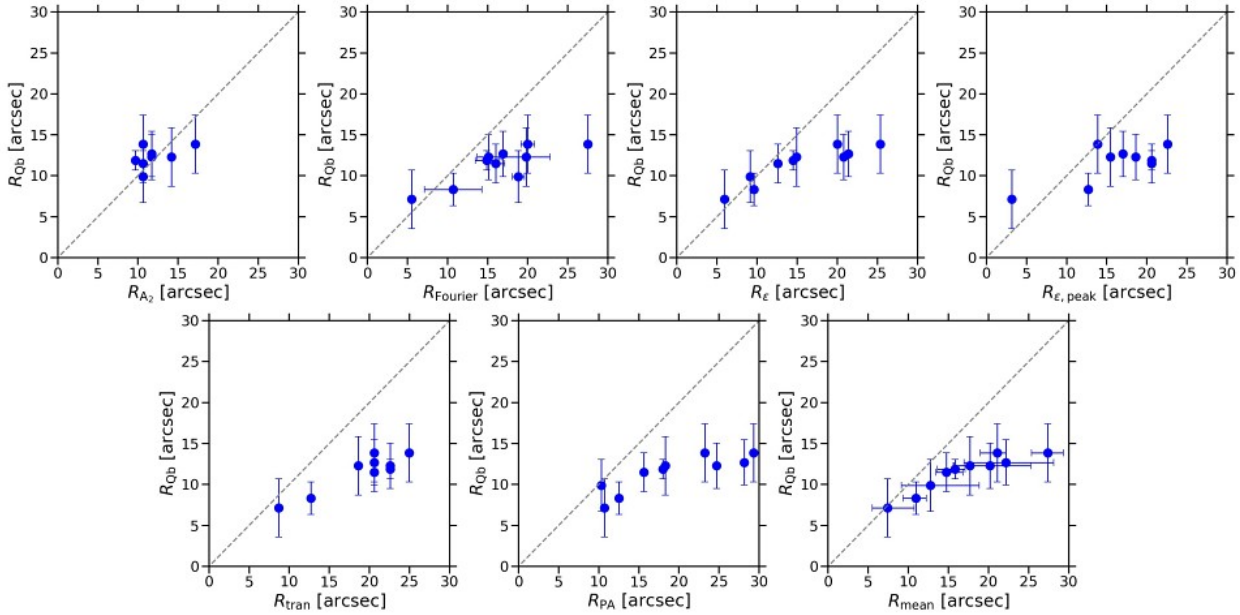

Figure 2.5: Comparison between the bar radius of the sample galaxies obtained with several methods and the analysis of the ratio maps. The last panel shows the comparison between $R_{\rm mean}$ and $R_{\rm Qb}$ given in Tables 2.1 and 2.2, respectively.

In Fig. 2.5 we compare all the different $R_{\rm bar}$ estimates of the sample galaxies to $R_{\rm Qb}$ as well as their mean value $R_{\rm mean}$ given in Table 2.1. We notice that $R_{\rm Qb}$ is systematically shorter than $R_{\rm mean}$ and the other available measurements of $R_{\rm bar}$. In particular, $R_{\rm Qb}$ is always shorter than $R_{\rm mean}$ at face values, but for three galaxies the two $R_{\rm bar}$ estimates are consistent within the errors. This is due to the large errors associated to $R_{\rm mean}$. The difference between $R_{\rm mean}$ and $R_{\rm Qb}$ increases for the longer bars of the sample, like those residing in IC 1683, NGC 36, NGC 2553, and NGC 5406. Our findings are in agreement with those of Lee et al. (2020) who compared their measurements of $R_{\rm bar}$ in sample of about 400 spiral galaxies with those available in literature (Laurikainen & Salo, 2002; Díaz-García et al., 2016) and found a strong correlation between $R_{\rm A_2}$ and $R_{\rm Qb}$.

Table 2.3: Bar rotation rates obtained with different bar radii.

Galaxy	$\mathcal{R}_1$	$\mathcal{R}_2$	$\mathcal{R}_3$	$\mathcal{R}_4$	$\mathcal{R}_5$	$\mathcal{R}_6$
(1)	(2)	(3)	(4)	(5)	(6)	(7)
IC 1528	1.13	0.74	$0.58^{+0.17}_{-0.20}$	-	-	-
IC 1683	0.78	0.67	$0.72^{+0.35}_{-0.32}$	1.42	0.96	1.15
IC 5309	0.79	0.44	$0.85^{+0.73}_{-0.34}$	1.47	0.54	-
NGC 36	0.61	0.51	$0.83^{+0.33}_{-0.27}$	0.68	0.56	1.08
NGC 2553	0.53	0.41	$0.67^{+0.14}_{-0.14}$	0.67	0.55	0.97
NGC 2880	1.04	0.92	$0.50^{+0.16}_{-0.15}$	-	-	0.89
NGC 5205	0.76	0.61	$0.57^{+0.14}_{-0.13}$	0.73	0.61	0.80
NGC 5406	0.55	0.47	$0.55^{+0.21}_{-0.13}$	0.49	0.44	1.03
NGC 5947	0.60	0.46	$0.54^{+0.20}_{-0.26}$	0.46	0.46	-
NGC 5971	0.91	0.30	$1.03^{+0.50}_{-0.46}$	-	-	-
NGC 6497	0.44	0.35	$0.34^{+0.13}_{-0.11}$	0.27	0.27	0.52
UGC 3253	0.82	0.66	$0.80^{+0.21}_{-0.19}$	0.58	0.53	1.23

Notes: (1) Galaxy name. (2) Bar rotation rate obtained using $R_{\epsilon,\mathrm{peak}}$ as bar radius estimate. (3) Bar rotation rate obtained using R_{PA} as bar radius estimate. (4) Bar rotation rate obtained using R_{Fourier} as bar radius estimate. (5) Bar rotation rate obtained using R_{ϵ} as bar radius estimate. (6) Bar rotation rate obtained using R_{trann} as bar radius estimate. (7) Bar rotation rate obtained using $R_{\mathrm{A_2}}$ as bar radius estimate.

The values of $\mathcal{R}$ derived for R_{mean} and R_{Qb} are given in Table 2.1 and 2.2, respectively, while the values of $\mathcal{R}$ obtained with all the available estimates of R_{bar} ($R_{\epsilon,\mathrm{peak}}$, R_{PA}, R_{Fourier}, R_{ϵ}, R_{tran}, and $R_{\mathrm{A_2}}$) are reported in Table 2.3. As a consequence of the trends shown in Fig. 2.5, we can conclude that the various estimates of R_{bar} generally lead to smaller values of $\mathcal{R}$ with respect to R_{Qb}, although a solid estimate of the errors on R_{bar} is not available so far for all the measurement methods.

Discussion

The bars of a number of disc galaxies of the CALIFA survey with direct and accurate measurements of Ω_{bar} are characterised by $\mathcal{R} < 1$ (Aguerri et al., 2015; Cuomo et al., 2019b). These unexpected observational findings are dynamically incompatible with the theoretical predictions about the stability of stellar orbits supporting the bar (Contopoulos, 1981). Therefore, we decided to test whether these ultrafast bars are actually an artefact due to an overestimated value of R_{bar} and/or an underestimated value of R_{cor} rather than a new class of non-axisymmetric stellar components, whose orbital structure has not been yet understood.

For all the sample galaxies, we found that the R_{bar} measurement based on the analysis of the ratio maps is shorter than that obtained with other methods based on ellipse fitting and Fourier analysis of the deprojected galaxy image. These methods turned out to be quite sensible to the presence of rings, pseudo-rings, and spiral arms which are very common in the galaxies we analysed and lead to systematically larger values of R_{bar}. All the sample galaxies present a rather complex spiral morphology, except for NGC 2880. This is a lenticular galaxy, which does not show any additional component to the bulge, bar, and disc and its R_{Qb} is consistent (although smaller) with R_{bar} derived from other methods.

When adopting $R_{\rm Qb}$ to calculate $\mathcal{R}$, all the galaxies turned out to host a fast bar at 95% confidence level with the only exception represented by NGC 6497. This galaxy was previously discussed in detail by Aguerri et al. (2015) and Garma-Oehmichen et al. (2020). Aguerri et al. (2015) analysed the galaxy extinction map to rule out problems in measuring $R_{\rm bar}$ due to dust and considered the gas kinematics to check $V_{\rm circ}$ and hence $R_{\rm cor}$ obtained from stellar dynamics. Garma-Oehmichen et al. (2020) reassessed the error budget of $\Omega_{\rm bar}$ by considering a broader set of error sources affecting the TW method. They remeasured $\Omega_{\rm bar}$ and recalculated $R_{\rm cor}$ obtaining $\mathcal{R} = 1.08^{+0.31}_{-0.25}$ which makes NGC 6497 fully consistent with the fast-bar regime.

Our results on the problems in measuring $R_{\rm bar}$ in barred galaxies confirm previous findings based on the analysis of mock images and numerical simulations. In fact, Michel-Dansac & Wozniak (2006) showed that $\mathcal{R}$ can increase from 1.0 to 1.4 just by changing of the method adopted to recover $R_{\rm bar}$. Using simulated images, they showed that $R_{\rm bar}$ obtained from the location of the maximum in the ϵ radial profile is closer to $R_{\rm cor}$, whereas $R_{\rm bar}$ estimated from the location of the constant PA or from the Fourier analysis correlates with the ultra-harmonic 4:1 resonance well within $R_{\rm cor}$. Different $R_{\rm bar}$ values translates into different $\mathcal{R}$ estimates. More recently, Petersen et al. (2019) have shown with N-body simulations that $R_{\rm bar}$ measured from ellipse fitting overestimates by a factor 1.5–2 the radial extent of the bar recovered from the maximum excursion of x_1 stellar orbits. This is because many entrapped stellar orbits reside in the physical regions of the x_1 family and are considered part of the bar by the ellipse fitting.

Using the images of mock galaxies, Lee et al. (2020) showed that the measurement of $R_{\rm bar}$ based on the ratio map are overestimated when the bulge-to-total ratio B/T increases from 0 to 0.8, but the same effect was pointed out for the ellipse fitting and Fourier analysis methods as well. This means that if there is a substantial contribution of the bulge, the corresponding rotation rate is more effectively driven out the ultrafast regime into the fast one. The bulges in our galaxies give a relatively low contribution to the total luminosity, with a mean value of $\langle B/T \rangle = 0.15$ (Méndez-Abreu et al., 2017), when excluding the SB0 NGC 2880 which hosts a large bulge ($B/T = 0.46$). Moreover, the ratio map allows to disentangle the radius corresponding to the maximum strength of the bar from that of the spiral arms and/or of rings by comparing the $Q_{\rm T}(R_{\rm Qb})$ and $Q_{\rm T}(R_{\rm mean})$ azimuthal profiles and looking where the local maxima of the azimuthal profiles are located in the image of the galaxy. As a future perspective, it is worth checking whether bars located in the safe fast regime are in turn affected by a wrong estimate of bar radius, especially when the host galaxies present spiral arms and/or rings. If this is the case, some of those bars may indeed belong to the slow regime, challenging the conclusions drawn so far in the framework of bar rotation regimes. Unfortunately, all the most widely adopted methods to recover $R_{\rm bar}$ are based only on photometry without considering kinematic information, which may help to successfully constrain the bar extension.

Hilmi et al. (2020) used hydro-dynamical simulations of Milky Way-like galaxies to assess the variation of the bar parameters on a dynamical timescale due to the interaction with the spiral structure. Using different approaches based on photometry, they recovered $R_{\rm bar}$, $S_{\rm bar}$, and $\Omega_{\rm bar}$ and traced their evolution with time. All the adopted methods overestimate $R_{\rm bar}$. The bar rotates faster than the spiral pattern and sometimes bar and spiral arms overlap. When the bar is connected to spiral arms, it seems to increase its radius. These bar pulsations are due to the coupling with the modes of the spiral pattern. Since the spiral modes can be odd, the two bar ends typically do not connect at exactly the same time to a spiral arm, so the two bar radii (one per each half) may be different at some given time. According to Hilmi et al. (2020), in $\sim$ 50% of Milky Way-like galaxies, the $R_{\rm bar}$ measurements of SBab and SBbc galaxies are overestimated by $\sim$ 15% and $\sim$ 55%, respectively with the stronger bars driving larger errors. Considering the sample analysed by Cuomo et al. (2020), we point out that ultrafast bars seem to be associated to stronger bars when

only galaxies with TW measurements are considered. We found that $R_{\rm Qb}$ values are on average $\sim 45\%$ shorter than other $R_{\rm bar}$ estimates for our sample galaxies and that this difference decreases from SBab to SBc galaxies. Moreover, Hilmi et al. (2020) showed that while the bar is increasing its radius due to the interaction with the spiral structure, the corresponding $\Omega_{\rm bar}$ decreases, but at a lower rate. Therefore, the two effects do not cancel out: intrinsically fast bars may appear as ultrafast. Given that $\Omega_{\rm bar}$ is well determined in our sample galaxies with the TW method, finding ultrafast bars need to be associated to an erroneous determination of $R_{\rm bar}$.

It should be noticed that it is mandatory to adopt the same approach in measuring $R_{\rm bar}$ when the theoretical predictions (Weinberg, 1985; Hernquist & Weinberg, 1992) and numerical simulations (Debattista & Sellwood, 2000; Zou et al., 2019) are compared to observational results to avoid misinterpreting the data. On the other hand, $\mathcal{R}$ also depends on $R_{\rm cor}$ and hence on $\Omega_{\rm bar}$ and $V_{\rm circ}$. Aguerri et al. (2015) and Cuomo et al. (2019b) derived $V_{\rm circ}$ from the asymmetric drift-corrected stellar kinematics in the disc region (Binney & Tremaine, 2008) and verified that their values agree with the Tully-Fisher relation predictions (Tully & Fisher, 1977; Reyes et al., 2011). Moreover, Aguerri et al. (2015) recovered $V_{\rm circ}$ for NGC 36, NGC 5205, and NGC 6497 using available gas kinematics (Theureau et al., 1998; García-Lorenzo et al., 2015) and excluded in these cases the determination of $V_{\rm circ}$ can explain the observed ultrafast regime. On the other hand, Garma-Oehmichen et al. (2020) directly estimated the value of $R_{\rm cor}$ as the intersection between $\Omega_{\rm bar}$ and the modelled angular rotation curve, which is useful for galaxies where the rotation curve rises slowly and $R_{\rm cor}$ can be overestimated when measured using $V_{\rm circ}$, but they did not infer any conclusion about the ultrafast regime.

We already discussed the sources of error of the TW method in Sect. 2.3 but some further considerations are worth bearing in mind. Using N-body simulations, Zou et al. (2019) suggested that $\mathcal{R} < 1$ can occur when ΔPA between bar and disc major axes is overestimated, the bar is too close to the disc minor axis, and the field-of-view (FOV) is too small to guarantee the convergence of the TW integrals. In addition, Cuomo et al. (2019a) showed that $\mathcal{R} < 1$ could be also the result of a wrong estimate of the disc PA from ellipse fitting when the PA radial profile is not constant as for warped discs. All the findings imply that ultrafast bars could be due to a wrong application of the TW method. However, we exclude this is the case for our sample galaxies which were carefully selected to be perfectly suitable for the correct application of the TW technique. As detailed by Aguerri et al. (2015) and Cuomo et al. (2019b) in performing their TW measurements, the PA of the bar and disc major axes were carefully measured with an ellipse fitting analysis, the constant portion of the PA profile corresponding to the disc region where the bar is located was identified, no correlation was found between the relative errors of $R_{\rm cor}$ and $R_{\rm bar}$ and the values of the disc i and bar ΔPA with respect to the disc major axis, and the radial extent of the photometric and kinematic data was chosen to allow the convergence of the TW integrals.

The existence of distinct pattern speeds corresponding to different galaxy structures was extensively discussed (Rautiainen et al., 2008; Cuomo et al., 2019b). The assumption of a well-defined rigidly rotating pattern speed in a barred galaxy can be questioned in the case of rings and/or spiral arms. The bar and spiral arms possibly share the same pattern speed when the arms are driven by the bar (Sanders & Huntley, 1976), or the bar and spiral arms can have different pattern speeds even if they are connected (Sellwood & Sparke, 1988; Beckman et al., 2018; Hilmi et al., 2020). Moreover, these pattern speeds may vary in space and/or time (Toomre, 1981; Bertin & Lin, 1996). The TW method provides an average pattern speed, if multiple pattern speeds are present. Since the length of the pseudo-slits must reach the axisymmetric disc, crossing both the bar and the spiral arms is unavoidable. As already pointed out by Tremaine & Weinberg (1984), Debattista et al. (2002) showed that small perturbations in the disc density do not contribute significantly to

$\Omega_{\rm bar}$. Low amplitudes correspond to a rapidly growing structure, which corresponds to spiral arms. Meidt et al. (2008) adapted the TW method to measure different pattern speeds from independent radial regions. They argued that also for spiral galaxies, the bar contribution to the measured pattern speed is maximal when only the photometric and kinematic integrals taken across the bar are considered in the analysis. This is commonly done in the application of the TW method to spiral galaxies (Aguerri et al., 2015; Cuomo et al., 2019b; Guo et al., 2019; Garma-Oehmichen et al., 2020; Williams et al., 2021). In this case, the measured pattern speed is reliable (Meidt et al., 2008). Moreover, deviations from the bar pattern speed are small when the spiral arms are dim (Williams et al., 2021). A slope change of the straight-line fitting the TW integrals was also interpreted as the signature of a nuclear bar rotating with a different pattern speed with respect to the main bar (Corsini et al., 2003; Maciejewski, 2006; Meidt et al., 2009). A slight slope change is observed in some of the galaxies of our sample, but also in other galaxies not hosting an ultrafast bar (Aguerri et al., 2015; Cuomo et al., 2019b), so we can conclude there is no clear link between the originally observed ultrafast regime and the slope change.

Dark gaps are commonly seen in early to intermediate-type barred galaxies having inner and outer rings or related features: the radial zone between an inner and outer ring appears dark, either continuously or in 2 – 4 distinct sections (Kim et al., 2016; James & Percival, 2016; Buta, 2017). Buta (2017) suggested that the dark gaps between inner and outer rings are associated with the L_4 and L_5 Lagrangian points in the gravitational potential of a bar or an oval. In turn, these points are theoretically expected to lie very close to the corotation resonance of the bar pattern, so the gaps may provide the location of $R_{\rm cor}$. According to Kim et al. (2016), the inner disc stars are swept by the bar and thus sparse regions are thought to be produced by the bar driven secular evolution. Pronounced light deficits are expected to be observed as the bar evolves becoming more extended and stronger. Indeed, during the evolution of a barred galaxy, the bar loses angular momentum by trapping nearby disc stars onto elongated orbits. This results into an increase of the bar radius and strength (Athanassoula & Misiriotis, 2002; Athanassoula et al., 2013; Kim et al., 2016). Buta (2017) found a mean bar rotation rate $\langle\mathcal{R}\rangle = 1.58 \pm 0.04$ for a sample of 50 galaxies with dark gaps and this means that they host slow-rotating bars. Measuring $\mathcal{R} < 1$ in galaxies with dark gaps reinforce the idea that ultrafast bars are due to an artefact in the determination of the rotation rate. Our analysis moved ultrafast bars in the fast (and even in the slow) regimes, in agreement with the expected results for evolved galaxies with dark gaps.

However, Buta (2017) identified a sub-class of dark gaps, where the interior of an inner ring appears darker than outside. He found a redder colour in the dark gaps with respect to the bars and no recent star formation. This is in agreement with the scenario of a bar depleting nearby regions from stars, while evolving. On the other hand, the rotation rates seem to locate these bars in the ultrafast regime. Buta (2017) claimed that if the dark spaces in these galaxies are interpreted in the same way as for the inner/outer ring gap galaxies, then either the existence of ultrafast bars would have to be acknowledged or another mechanism for forming dark gaps that has nothing to do with Lagrangian points would have to be hypothesised. This specific morphology can be recognised in two of our galaxies, NGC 5406 and NGC 5947. Since we excluded that the analysed bars are rotating extremely fast, we stress a different mechanism is need to explain at least this sub-class of galaxies with dark gaps. We calculated $\mathcal{R}$ by dividing the value of $R_{\rm cor}$ tabulated in Table 2.1 by $R_{\rm Qb}$ and present the results in Table 2.2. The value of $\mathcal{R}$ increases since $R_{\rm Qb}$ is shorter than $R_{\rm mean}$. All the galaxies move to the fast regime, except for NGC 6497. We discuss this galaxy later and conclude it does not host an ultrafast bar. In addition, the bars of IC 1683 and NGC 36 are consistent with being slow.

2.5 Conclusions

In this paper we considered the case of ultrafast bars, which are observed in more than 10% of barred galaxies with a direct measurement of the bar pattern speed. These bars end beyond the corotation radius and therefore challenge our understanding of stellar dynamics in barred galaxies. We aimed at investigating whether ultrafast bars are actually an artefact due to an overestimated value of $R_{\rm bar}$ and/or an underestimated value of $R_{\rm cor}$ rather than a new class of non-axisymmetric stellar components, whose orbital structure has not been yet understood.

We took into account the 12 barred galaxies, for which $\Omega_{\rm bar}$ was carefully measured by applying the TW method to the integral-field spectroscopic data obtained by the CALIFA survey and turned out to host an ultrafast bar according to its $\mathcal{R} < 1$ (Aguerri et al., 2015; Cuomo et al., 2019b). We checked that the galaxies were selected to be suitable for the application of the TW method and confirmed the values obtained for their $R_{\rm cor}$. Then, we analysed the issues related to the available $R_{\rm bar}$ measurements by Aguerri et al. (2015) and Cuomo et al. (2019b) based on the ellipse fitting and Fourier analysis of the deprojected SDSS i-band images of the sample galaxies. We also derived new estimates of $R_{\rm bar}$ from the analysis of the ϵ and PA radial profiles and of the Fourier $m = 2$ mode following the prescriptions of Lee et al. (2019, 2020). We realised that nearly all the sample galaxies are spiral galaxies with an inner ring or pseudo-ring circling the bar and/or strong spiral arms, which hamper the $R_{\rm bar}$ measurements based on the ellipse fitting and Fourier analysis of the deprojected galaxy images. According to these methods, the ends of the ultrafast bars overlap the inner ring and/or the spiral arms making the adopted $R_{\rm bar}$ unreliable.

Hence, we performed a further estimate of $R_{\rm bar}$ using the method proposed by Lee et al. (2020) and based on the analysis of the ratio maps, which we successfully applied to 10 galaxies. These values of $R_{\rm bar}$ are systematically smaller than $R_{\rm mean}$ and become smaller (or similar) to the corresponding $R_{\rm cor}$. This implies that the corresponding $\mathcal{R}$ are larger than those obtained before. All the galaxies turned out host a fast bar at 95% confidence level with the only exception represented by NGC 6497. However, Garma-Oehmichen et al. (2020) have recently recalculated $R_{\rm cor}$ for this galaxy and found it is consistent with the fast-bar regime too.

We can confidently conclude that ultrafast bars are no longer observed when a correct measurement of $R_{\rm bar}$ is adopted. However, we still miss a solid estimate of $R_{\rm bar}$ based on both photometric and kinematic data unveiling the extension of the stellar orbits which support the bar and helping the comparison with theoretical prescriptions and numerical simulations. This task requires further investigation.

Chapter 3

A slow bar in the lenticular barred galaxy NGC 4277[§]

Abstract

We characterised the properties of the bar hosted in lenticular galaxy NGC 4277. We measured $R_{\rm bar}$ and $S_{\rm bar}$ from the surface photometry obtained from the broad-band imaging of the SDSS and we derived $\Omega_{\rm bar}$ from the stellar kinematics obtained from the integral-field spectroscopy performed with the MUSE at the VLT. We estimated $V_{\rm circ}$ by correcting the stellar streaming motions for asymmetric drift and we derived the bar rotation rate $\mathcal{R}$. We found that NGC 4277 hosts a short ($R_{\rm bar}= 3.2^{+0.9}_{-0.6}$ kpc), weak ($S_{\rm bar}= 0.21 \pm 0.02$), and slow ($\mathcal{R}= 1.8^{+0.5}_{-0.3}$) bar and its pattern speed is amongst the best-constrained ones ever obtained with the TW method. NGC 4277 is the first clear-cut case of a galaxy hosting a slow stellar bar measured with the TW method. A possible interaction with the neighbour galaxy NGC 4273 could have triggered the formation of such a slow bar and/or the bar could be slowed down due to the dynamical friction with a significant amount of DM within the bar region.

3.1 Introduction

The pattern speed is the most important bar structural parameter. It controls the positions of the resonances, affects the stellar and gaseous dynamics, and permits to constrain the DM content. Many indirect methods have been proposed to recover $\Omega_{\rm bar}$ but all of them suffer some limitations. The only model-independent method that can recover $\Omega_{\rm bar}$ is the TW method. To date no 'genuine' slow bar ($\mathcal{R} > 1.4$ at more than 1σ confidence level) has been measured applying the TW method to the stars (see Cuomo et al. 2020 for a review), suggesting that bar formation was not tidally induced by close encounters. The few slow bars that have been found by applying the TW method to a gaseous tracer (Banerjee et al., 2013; Patra & Jog, 2019; Bureau et al., 1999; Chemin & Hernandez, 2009) do no guarantee that the continuity equation holds in the presence of gas phase changes. We report the case of NGC 4277 as the first clear-cut example of a galaxy hosting a slow stellar bar measured with the TW method. We organise the chapter as follows. We report the general properties of NGC 4277 in Sec. 3.2. We present the photometric and kinematic analysis in Sec. 3.3. We discuss the results in Sec. 3.4 and report our conclusions in Sec. 3.5. We adopt as cosmological parameters, $\Omega_{\rm M} = 0.308$, $\Omega_{\Lambda} = 0.692$, and $H_0 = 75$ km s^{-1} Mpc^{-1} (Fixsen et al., 1996).

[§] *Based on Buttitta, C., Corsini, E. M., Cuomo, V., et al. 2022, A&A, 664, L10.*

3.2 General properties of NGC 4277

NGC 4277 is classified as SBa by Binggeli et al. (1985), SAB(rs)0/a by RC3, SB0^0 by Baillard et al. (2011), and SAB(rs)0$^+$ by Buta et al. (2015). It has an apparent magnitude $B_T = 13.38$ mag (RC3), which corresponds to a total absolute corrected magnitude $M^0_{B_T} = -19.27$ mag, obtained adopting a distance $D = 33.9$ Mpc from the systemic velocity with respect to the cosmic microwave background reference frame $V_{\rm CMB} = 2542 \pm 48$ km s^{-1} (Fixsen et al., 1996) and assuming $H_0 = 75$ km s^{-1} Mpc^{-1}. The stellar mass is $M_\star = 8 \cdot 10^9$ M$_\odot$ with a lower limit for the H I mass of $M_{\rm HI} = 7 \cdot 10^8$ M$_\odot$ for the adopted distance (van Driel et al., 2016). The apparent sizes of the galaxy are $D \times d = 1.05 \times 0.87$ arcmin (RC3), that correspond to $D \times d = 10.3 \times 8.6$ kpc, which are the major and minor diameters of the isophote with surface brightness in B band of $\mu_B = 25$ mag arcsec^{-2}. Comerón et al. (2014) found that NGC 4277 hosts an inner pseudoring that extends slightly beyond the bar extension.

The profile of the emission line of H I of NGC 4277 is contaminated by the presence of the nearby spiral galaxy NGC 4273 (van Driel et al., 2000), with which the galaxy possibly forms an interacting pair (Kim et al., 2014). The latter lies at a projected distance of 1.9 arcmin and it is located at a distance $D = 36.3$ Mpc. Its surface brightness radial profile presents a change of slope in the outermost disc regions due to NGC 4277 (Pohlen & Trujillo, 2006). The two galaxies are both classified as possible members of the Virgo cluster (Kim et al., 2014).

NGC 4277 is an ideal target for the application of the TW method to accurately measure $\Omega_{\rm bar}$. It has an intermediate inclination, its bar is oriented at an intermediate angle between the major and minor axes of the disc, and it shows no evidence of spiral arms or patchy dust (Fig. 3.1).

3.3 Data analysis

Broad-band imaging

We retrieved the i-band image of NGC 4277 from the science archive of SDSS Data Release 14 (Abolfathi et al., 2018). The images were already bias subtracted, flatfield-corrected, and flux-calibrated according to the associated calibration information stored in the Data Archive Server (DAS). The choice of i band ensured that we reached a sufficient spatial resolution and depth, and minimised the dust effects with respect to the other SDSS pass-bands to characterise the bar component with an accurate photometric decomposition of the surface brightness distribution. We trimmed the image selecting a FOV centred on the galaxy of 800×800 pixel^2, that corresponds to 5.3×5.3 arcmin^2. We rotated the image in order to orient it with the north up and east left. We fitted elliptical isophotes with the IRAF ELLIPSE task (Jedrzejewski, 1987) to measure the surface brightness radial profile at large distance from the galaxy centre. We estimated the sky contribution fitting the surface brightness profile with a straight line and considering all the radii where the line slope was consistent with being zero within the associated root mean square error. We found a value of the sky surface brightness of $\mu_{i,\rm sky} = 20.46 \pm 0.04$ mag arcsec^{-2}.

Isophotal analysis

We performed an isophotal analysis on the flux-calibrated sky-subtracted i-band image of NGC 4277. First, we masked all the foreground stars, background galaxies, and spurious sources (such as residual cosmic rays and bad pixels) in the image FOV and fitted the galaxy isophotes with ellipses. We allowed the centre, ellipticity, and position angle of the fitting ellipses to vary.

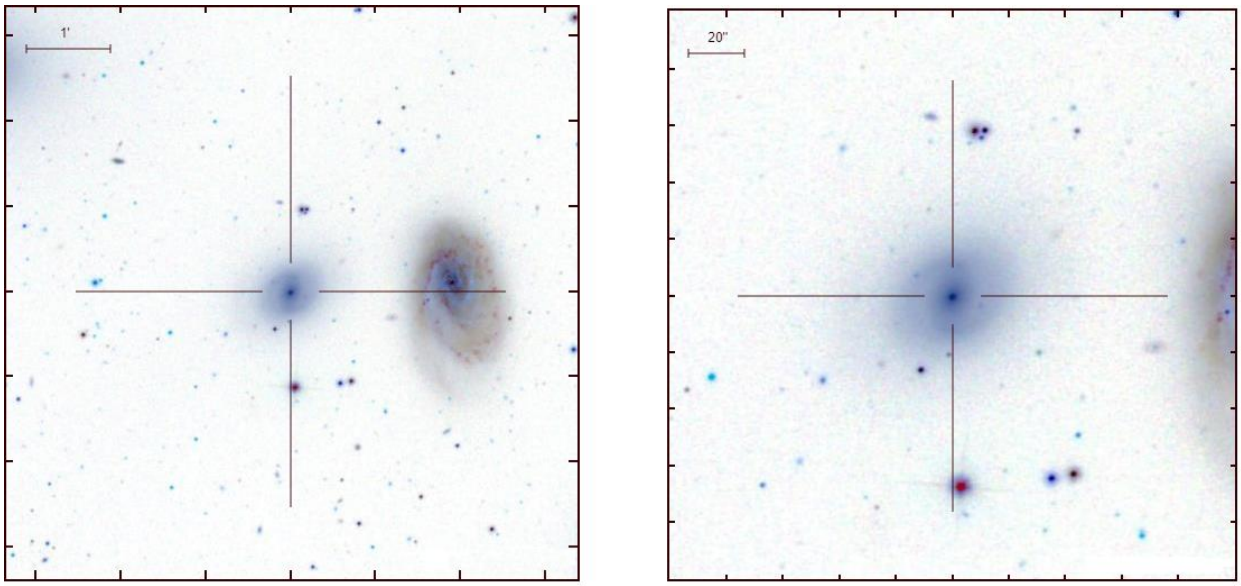

Figure 3.1: SDSS i-band image of NGC 4277 and NGC 4273 (*left panel*) and zoom-in image of NGC 4277 (*right panel*). The scale of the FOV with north up and east left is given in each panel. The cross marks the centre of NGC 4277.

After checking they do not vary within the uncertainties, we fitted again the galaxy isophotes with ellipses fixing the centre coordinates. The radial profiles of the azimuthally averaged surface brightness, μ, position angle, PA, and ellipticity, ϵ, are shown in Fig. 3.2 (left panels) as a function of the semi-major axis of the ellipses, a. These profiles show the typical trends observed in barred galaxies (e.g. Aguerri et al., 2000): ϵ exhibits a local maximum ($\epsilon \sim 0.4$) and the PA is nearly constant in the bar region (PA$\sim 160^{\circ}$), while ϵ and PA are both constant in the disc region. We did not correct the measured surface brightness for cosmological dimming ($z = 0.00730$, NED), Galactic absorption ($A_i = 0.032$ mag, Schlafly & Finkbeiner 2011), or K correction ($K_i = 0.01$ mag, Chilingarian et al. 2010).

We derived the mean values of ϵ and PA of the disc in the radial range $28 \leqslant a \leqslant 48$ arcsec (Fig. 3.2, left panels), which extends outside the bar-dominated region to the farthest fitted isophote. We defined the extension of this radial range by fitting the PA measurements with a straight line and considering all the radii where the line slope was consistent with being zero within the associated root mean square error, as was done by Cuomo et al. (2019a). We obtained a mean value of disc ellipticity of $\langle\epsilon\rangle = 0.242 \pm 0.002$ and of the disc position angle of $\langle\mathrm{PA}\rangle = 123\overset{\circ}{.}27 \pm 0.32$.

Fourier analysis

We performed the Fourier analysis of the deprojected i-band image of NGC 4277. To project the galaxy into the face-on view keeping the flux preserved, the image is stretched along the disc minor axis by a factor of $1/\cos(i)$ where i is disc inclination derived as $i = \arccos(\langle\epsilon\rangle)$. We decomposed the azimuthal profile of the deprojected surface brightness distribution with a Fourier series (see Sec. 1.2 for details). The radial profiles of the relative amplitudes of the even $m = 2, 4, 6$ and odd $m = 1, 3, 5$ Fourier components are shown in Fig. 3.2 (right panels). NGC 4277 presents typical features of barred galaxies (Ohta et al., 1990): since the bar is a bi-symmetric structure, the even components are more prominent respect with the odd ones, the $m = 2$ is the dominant one.

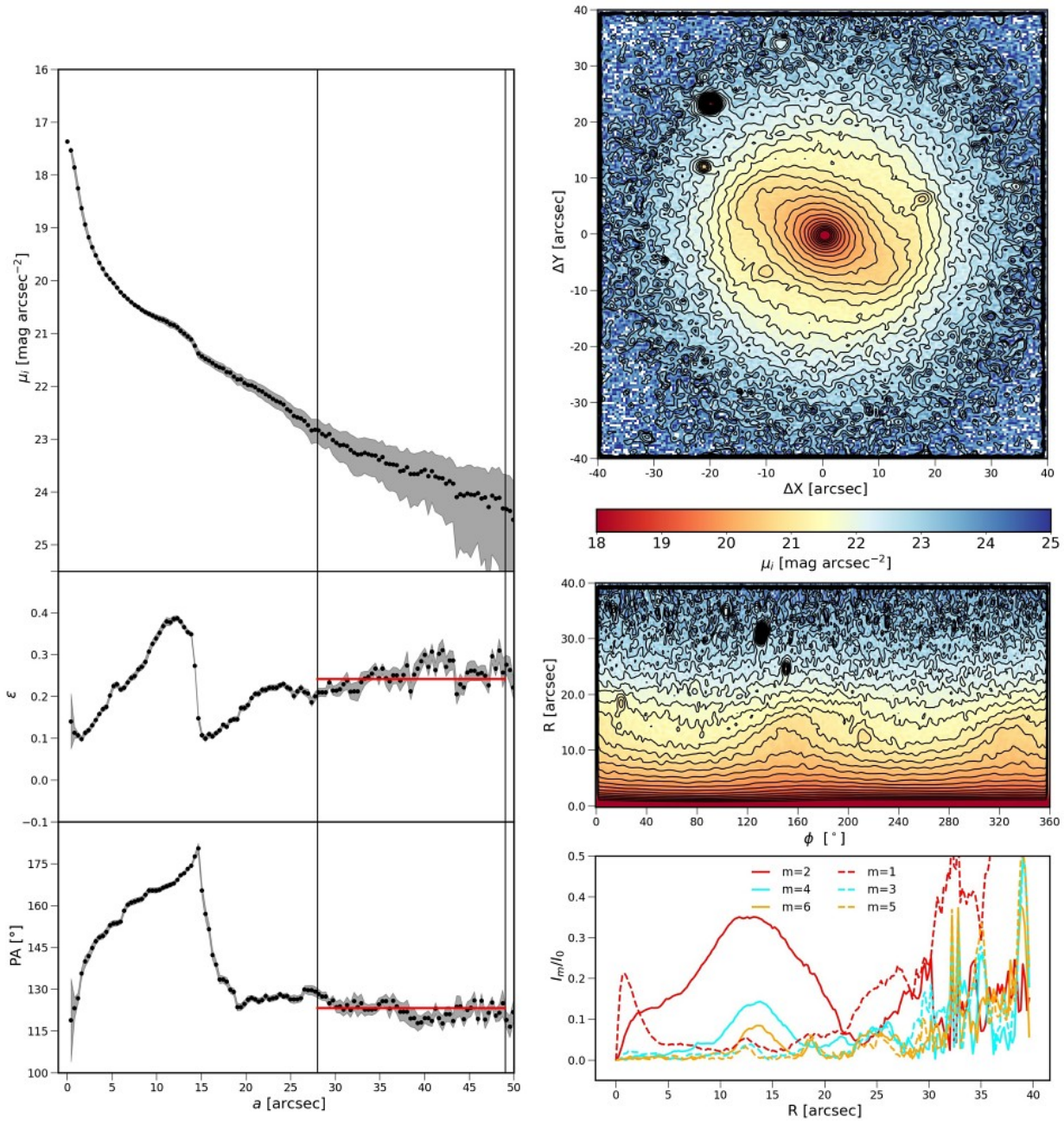

Figure 3.2: *Left panels*: Isophotal analysis of the *i*-band image of NGC 4277. The radial profiles of the surface brightness (*upper panel*), position angle (*central panel*), and ellipticity (*lower panel*) are shown as a function of the semi-major axis of the best-fitting isophotal ellipses. The vertical black lines bracket the radial range adopted to estimate the mean ellipticity $\langle\epsilon\rangle = 0.242 \pm 0.002$ and position angle $\langle \mathrm{PA}\rangle = 123\overset{\circ}{.}27 \pm 0\overset{\circ}{.}32$ of the disc. *Right panels*: Fourier analysis of NGC 4277. Deprojected *i*-band image of NGC 4277 in Cartesian (*top panel*) and polar coordinates (*central panel*), and radial profiles of the relative amplitude of the even $m = 2$ (solid red line), $m = 4$ (solid blue line), and $m = 6$ (solid yellow line), and odd $m = 1$ (dashed red line), $m = 3$ (dashed blue line), and $m = 5$ (dashed yellow line) Fourier components (*bottom panel*).

Photometric decomposition

We derived the structural parameters of NGC 4277 by applying the GASP2D algorithm (Méndez-Abreu et al., 2008, 2017, 2018a) to the flux-calibrated and sky-subtracted i-band image of the galaxy. We modelled the galaxy surface brightness in each pixel of the image to be the sum of the light contribution of a Sérsic bulge, a double-exponential disc, and a Ferrers bar. We did not account for other luminous components, such as rings or spiral arms. We assumed that the isophotes of each component are elliptical and centred on the galaxy centre with constant values for the position angle and axial ratio. We parameterised the bulge surface brightness as:

$$I_{\rm bulge}(x,y) = I_{\rm e} 10^{-b_n[(r_{\rm bulge}/r_{\rm e})^{1/n}-1]},$$

following Sérsic (1968), where (x, y) are the Cartesian coordinates of the image in pixels, $r_{\rm e}$ is the effective radius encompassing half of the bulge light, $I_{\rm e}$ is the surface brightness at $r_{\rm e}$, n is the shape parameter of the surface brightness profile, and $b_n = 0.868n - 0.142$ is a normalisation coefficient (Caon et al., 1993). The radius $r_{\rm bulge}$ is defined as follows:

$$\begin{aligned} r_{\rm bulge} = [(-(x-x_0)\sin{\rm PA}_{\rm bulge} + (y-y_0)\cos{\rm PA}_{\rm bulge})^2 \\ + ((x-x_0)\cos{\rm PA}_{\rm bulge} + (y-y_0)\sin{\rm PA}_{\rm bulge})^2/q^2_{\rm bulge}]^{1/2}, \end{aligned}$$

where (x_0, y_0), ${\rm PA}_{\rm bulge}$, and $q_{\rm bulge}$ are the coordinates of the galaxy centre, bulge position angle, and bulge axial ratio, respectively. We parameterised the disc surface brightness as

$$I_{\rm disc}(x,y) = \begin{cases} I_0 e^{-r_{\rm disc}/h_{\rm in}}, & \text{if } r \leqslant r_{\rm break} \\ I_0 e^{-r_{\rm break}(h_{\rm out}-h_{\rm in})/h_{\rm out}} e^{-r/h_{\rm out}} & \text{if } r > r_{\rm break}, \end{cases}$$

following Méndez-Abreu et al. (2017), where I_0 is the central surface brightness, $r_{\rm break}$ is the break radius at which the surface brightness profile changes slope, and $h_{\rm in}$ and $h_{\rm out}$ are the scalelengths of the inner and outer exponential profile, respectively. The radius $r_{\rm disc}$ is defined as follows:

$$\begin{aligned} r_{\rm disc} = [(-(x-x_0)\sin{\rm PA}_{\rm disc} + (y-y_0)\cos{\rm PA}_{\rm disc})^2 \\ + ((x-x_0)\cos{\rm PA}_{\rm disc} + (y-y_0)\sin{\rm PA}_{\rm disc})^2/q^2_{\rm disc}]^{1/2}, \end{aligned}$$

where ${\rm PA}_{\rm disc}$ and $q_{\rm disc}$ are the disc position angle and axial ratio, respectively. We parameterised the bar surface brightness as follows:

$$I_{\rm bar}(r) = \begin{cases} I_{0,\rm bar}\left[1-(r_{\rm bar}/R_{\rm bar})^2\right]^{2.5} & \text{if } r_{\rm bar} \leqslant R_{\rm bar} \\ 0 & \text{if } r_{\rm bar} > R_{\rm bar}, \end{cases}$$

following Aguerri et al. (2009), where $I_{0,\rm bar}$ and $R_{\rm bar}$ are the bar central surface brightness and bar radius, respectively. The radius $r_{\rm bar}$ is defined as

$$\begin{aligned} r_{\rm bar} = [(-(x-x_0)\sin{\rm PA}_{\rm bar} + (y-y_0)\cos{\rm PA}_{\rm bar})^2 \\ + ((x-x_0)\cos{\rm PA}_{\rm bar} + (y-y_0)\sin{\rm PA}_{\rm bar})^2/q^2_{\rm bar}]^{1/2}, \end{aligned}$$

where ${\rm PA}_{\rm bar}$ and $q_{\rm bar}$ are the bar position angle and axial ratio, respectively. The best-fitting values of the structural parameters of the bulge, disc, and bar are returned by GASP2D by performing a χ^2 minimisation. Fig. 3.3 shows the i-band image, GASP2D best-fitting image, and residual image of NGC 4277.

Table 3.1: Structural parameters of NGC 4277 from the photometric decomposition.

Bulge	
$\mu_{\rm e}$	19.29 ± 0.03 mag arcsec^{-2}
$r_{\rm e}$	1.75 ± 0.03 arcsec
n	2.36 ± 0.03
$q_{\rm bulge}$	0.841 ± 0.004
$\mathrm{PA}_{\rm bulge}$	$135\overset{\circ}{.}09 \pm 0\overset{\circ}{.}05$
$L_{\rm bulge}/L_{\rm T}$	0.11
Disc	
μ_0	20.14 ± 0.01 mag arcsec^{-2}
$h_{\rm in}$	11.82 ± 0.10 arcsec
$h_{\rm out}$	14.81 ± 0.22 arcsec
$r_{\rm break}$	36.16 ± 0.57 arcsec
$q_{\rm disc}$	0.758 ± 0.001
$L_{\rm disc}/L_{\rm T}$	0.82
Bar	
μ_0	21.37 ± 0.01 mag arcsec^{-2}
$a_{\rm bar}$	20.70 ± 0.07 arcsec
$q_{\rm bar}$	0.341 ± 0.001
$\mathrm{PA}_{\rm bar}$	$175\overset{\circ}{.}59 \pm 0\overset{\circ}{.}04$
$\mathrm{PA}_{\rm disc}$	$123\overset{\circ}{.}27 \pm 0\overset{\circ}{.}06$
$L_{\rm bar}/L_{\rm T}$	0.07

Notes: The scalelengths are not deprojected on the galactic plane.

We masked the foreground stars and spurious sources using the same mask adopted for the isophotal analysis. We estimated the PSF applying a Multi-Gaussian Expansion (MGE, Emsellem et al., 1994) algorithm on a bright, isolated. and round star in the FOV. We fixed the disc ellipticity and PA with the values obtained from the previous isophotal analysis, and performed various test to fit the remaining parameters.

We estimated the errors on the best-fitting structural parameters by analysing the images of a sample of mock galaxies generated by Méndez-Abreu et al. (2017) (see also Costantin et al. 2017) with Monte Carlo simulations and mimicking the instrumental setup of the available SDSS image. We adopted the mean and standard deviation of the relative errors of the mock galaxies as the systematic and statistical errors of the parameters of the surface brightness radial profiles of the bulge ($I_{\rm e}$, $r_{\rm e}$, and n), disc ($I_{0,\rm disc}$, $h_{\rm in}$, $h_{\rm out}$, and $r_{\rm break}$), and bar ($I_{0,\rm bar}$ and $a_{\rm bar}$). We adopted the mean and standard deviation of the absolute errors of the mock galaxies as the systematic $\sigma_{\rm syst}$ and statistical $\sigma_{\rm stat}$ errors of the geometric parameters of the bulge ($\mathrm{PA}_{\rm bulge}$ and $q_{\rm bulge}$), disc ($\mathrm{PA}_{\rm disc}$ and $q_{\rm disc}$), and bar ($\mathrm{PA}_{\rm bar}$ and $q_{\rm bar}$). We computed the errors on the best-fitting parameters as $\sigma^2 = \sigma^2_{\rm stat} + \sigma^2_{\rm syst}$, with the systematic errors being negligible compared to the statistical ones. The quoted uncertainties are purely formal and do not take into account the parameter degeneracy and a different parameterisation of the components. The values of the best-fitting structural parameters of NGC 4277 and corresponding errors are reported in Table 3.1.

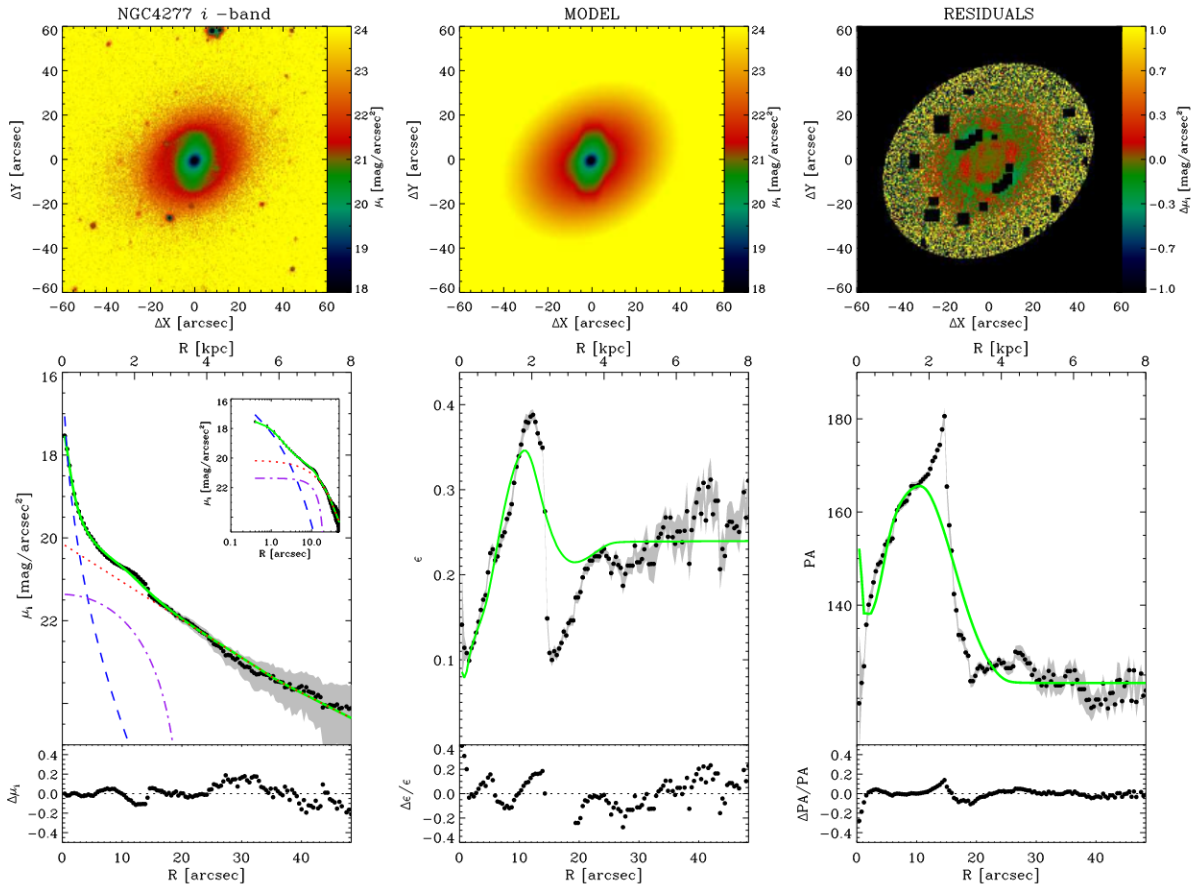

Figure 3.3: *Top panels*: Photometric decomposition of the i-band image of NGC 4277 with the maps of the observed (*left panel*), model (*central panel*), and residual (observed−model) surface brightness distribution (*right panel*). The FOV of the images is oriented with north being up and east to the left. The black areas in the residual image correspond to pixels excluded from the fit. *Bottom panels*: Radial profiles of surface brightness, PA, and ϵ from the isophotal analysis of the observed (black dots) and seeing-convolved modelled image (green solid line) and their corresponding difference. The surface brightness radial profiles of the best-fitting bulge (blue dashed line), bar (purple dot-dashed line), and disc (red dotted line) are also shown in both linear and logarithmic scale for the semi-major axis distance to the centre of the galaxy.

IFU spectroscopy: spectra acquisition and data reduction

We carried out the spectroscopic observations of NGC 4277 in service mode on 20 March 2015 (Prog. Id. 094.B-0241(A); E.M. Corsini) with the Multi Unit Spectroscopic Explorer (MUSE, Bacon et al., 2010) of the European Southern Observatory. We configured MUSE in wide field mode to ensure a nominal FOV of 1×1 arcmin^2 with a spatial sampling of 0.2 arcsec pixel^{-1} and to cover the wavelength range of 4800 – 9300 Å with a spectral sampling of 1.25 Å pixel^{-1} and an average nominal spectral resolution of FWHM = 2.51 Å. We split the observations into two observing blocks (OBs) to map the entire galaxy along its photometric major axis. We organised each OB to perform four pointings. The first pointing was centred on the nucleus, the second one on a blank sky region at a few arcmins from the galaxy, and the third and fourth ones were an eastward and westward offset along the galaxy major axis taken at a distance of 20 arcsec from the galactic nucleus, respectively. The mean value of the seeing during the observations was FWHM $\sim$ 1.1 arcsec.

We performed the standard data reduction with the MUSE pipeline (Weilbacher et al., 2016) under the ESOREFLEX environment (Freudling et al., 2013). The standard steps of the reduction include bias and overscan subtraction, flat-fielding correction, wavelength calibration, determination of the line spread function, flux calibration, and sky subtraction. To deal with the different response of the pixels of the detectors and illumination edge effects between the detectors, a lamp flat-fielding correction was applied to the exposures, while a sky flat-fielding correction was applied to correct the large-scale illumination variation of the detectors. The twilight flat-field exposures were realised in the same observing pattern of the on-target and on-sky exposure, producing a master twilight datacube to determine the effective spectral resolution and its variation across the FOV. The sky contribution was estimated by fitting the sky continuum and emission lines on the on-sky exposures. The resulting sky model spectrum was subtracted from each spaxel of the on-target and on-sky exposures. We aligned the sky-subtracted on-target exposures using the common bright sources in the FOV as a reference in order to produce a combined datacube of the galaxy. The resulting sky-subtracted datacube is characterised by residual sky contamination, which was further cleaned using the Zurich Atmospheric Purge (ZAP) algorithm version 1.1 (Soto et al., 2016) under the ESOREFLEX environment. ZAP evaluates the principal components of the sky residuals by analysing a datacube obtained by the combination of all the individual sky-subtracted on-sky exposures. Then ZAP calculates the eigenvalues of these principal components in each spaxel of the combined sky-subtracted datacube of the galaxy and subtracts from it the best-fitting model of the residual sky lines. Unfortunately, we still have residuals from the sky-line subtraction in the wavelength range centred on the Ca II$\lambda\lambda$8498, 8542, 8662 absorption-line triplet. We found an instrumental FWHM=2.80 Å ($\sigma_{\rm instr}$ = 69 km s^{-1}) with a negligible variation over the FOV and in the wavelength range between 4800 Å and 5600 Å which we choose to measure the stellar kinematics.

Stellar kinematics

We measured the stellar and ionised-gas kinematics of NGC 4277 from the sky-cleaned MUSE datacube using the PPXF (Cappellari & Emsellem, 2004; Cappellari, 2017) and GANDALF (Sarzi et al., 2006) algorithms. We spatially binned the datacube spaxels using the adaptive algorithm of Cappellari & Copin (2003) based on Voronoi tessellation to obtain a target $S/N = 40$ per bin. This ensured us to obtain galaxy spectra with sufficiently high signal to extract a reliable measure of the kinematics. We obtained $\sim$ 800 bins with a variable size that goes from 2 arcsec in the inner region to 50 arcsec in the outermost one, with an associated S/N that varies from $\sim$ 60 to $\sim$ 20.

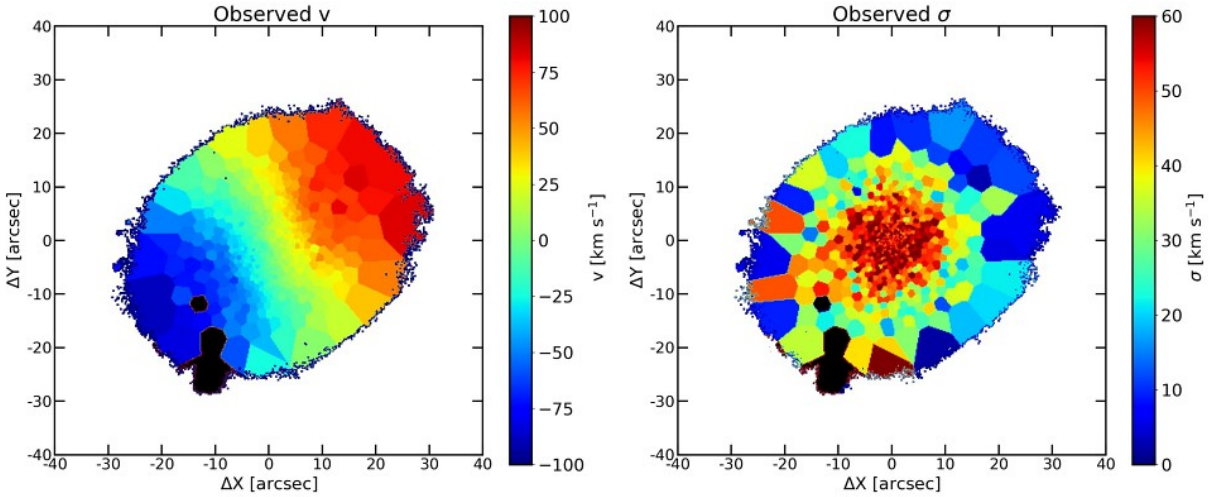

Figure 3.4: Maps of the stellar LOS velocity subtracted of systemic velocity (*left panel*) and velocity dispersion corrected for $\sigma_{\rm inst}$ (*right panel*) of NGC 4277 derived from the $S/N = 40$ Voronoi-binned MUSE data. The FOV is $1.3 \times 1.3\,\mathrm{arcmin}^2$ and is oriented with north up and east to the left. Black regions represent the bins where the fit was not good.

We used the ELODIE library ($\sigma_{\rm instr} = 13$ km s^{-1}, Prugniel & Soubiran 2001) in the wavelength range $4800-5600$ Å centred on the Mg I$\lambda\lambda$5167, 5173, 5184 absorption-line triplet and including the [O III]$\lambda\lambda$4959, 5007 and [N I]$\lambda\lambda$5198, 5200 emission-line doublets. The galaxy spectrum in each bin is modelled convolving a LOS velocity distribution parameterised with a truncated Gauss-Hermite series (Gerhard, 1993; van der Marel & Franx, 1993a) with a combination of stellar templates. After rebinning the stellar spectra to a logarithmic scale along the dispersion direction, we de-reshifted them to the rest frame and cropped their wavelength range to match the redshifted frame of the galaxy spectra. We also added a low-order multiplicative Legendre polynomial (degree = 6) to correct for the different shapes of the continuum of the spectra of the galaxy and optimal template due to reddening and large-scale residuals of flat-fielding and sky subtraction. We applied the PPXF algorithm to obtain the mean LOS velocity v and velocity dispersion σ of the stellar component (Fig. 3.4). We simultaneously fitted the ionised-gas emission lines with Gaussian functions. We did not detect any emission line, except for a few isolated spatial bins in the disc region. In these bins, the signal-to-residual noise of the emission lines is $S/rN > 3$. We estimated the errors on v and σ from formal errors of the PPXF best fit re-scaling the minimum χ^2 to achieve $\chi^2_{\rm min} = N_{\rm dof} = N_{\rm d} - N_{\rm fp}$ as done in Corsini et al. (2018). $N_{\rm dof}$, $N_{\rm d}$, and $N_{\rm fp}$ are the number of the degrees of freedom, data points, and fitting parameters, respectively (Press et al., 1992). The central regions are characterised by an asymmetric S-shape velocity field due to the bar distortion of the isocontours, while in the external regions the velocity field is nearly asymmetric since we are in the disc-dominated region. Stellar velocity rises to $80-90$ km s^{-1} at a radial distance $a \sim 12$ arcsec from the centre along the major axis of the galaxy and becomes nearly constant in the outermost regions. The associated errors in central region ($S/N \sim 45-55$) are about $1-2$ km s^{-1}, while in the external regions ($S/N \sim 30-35$) are $3-5$ km s^{-1}. The velocity dispersion field presents a local minimum at the centre of the value of ~ 50 km s^{-1}, this is a distinctive feature in barred galaxies (Wozniak & Champavert, 2006; Gadotti et al., 2020). It rises to 60 km s^{-1} in external regions and then decreases in the outermost region. Associated errors range from 2-5 km s^{-1} in the central regions, to $5-10$ km s^{-1} in the outermost regions.

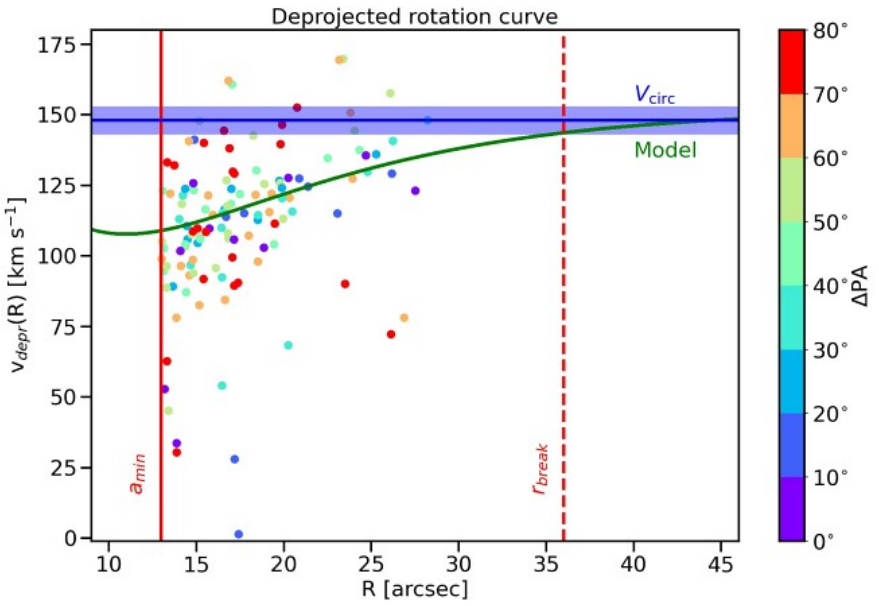

Figure 3.5: Deprojected (solid circles) and model velocities (solid green line) of the stars onto the disc plane. The deprojected velocities are colour-coded according to the bin PA with respect the galaxy major axis. Bins too close to the galaxy minor axis (ΔPA$< 10^{\circ}$) are not shown. The horizontal blue line shows the value of the circular velocity from the asymmetric drift ($V_{\rm circ}$=148$\pm$5 km s^{-1}). The vertical solid and dashed red lines mark the inner edge of the inner disc ($a_{\rm min} = 13$ arcsec) adopted for modelling and the location of the disc break radius ($r_{\rm break} = 36$ arcsec), respectively.

Circular velocity

We derived $V_{\rm circ}$ from the stellar LOS velocity and velocity dispersion in the region of the inner disc using the asymmetric drift equation (Binney & Tremaine, 2008). We selected the spatial bins within an elliptical annulus with semi-major axes $a_{\rm min} = 13$ arcsec and $a_{\rm max} = r_{\rm break} = 36$ arcsec and ellipticity $\epsilon = 0.242$. The minimum semi-axis of the elliptical annulus is set to exclude the bar while the maximum semi-axis of the annulus is chosen to bracket all the available spatial bins of the disc. The choice of a higher S/N ratio and/or narrower annulus results in a sparser data set, which makes it difficult to constrain the circular velocity. We followed the prescriptions of Debattista et al. (2002) and Aguerri et al. (2003) to obtain the following:

$$v(r,\theta) = \sqrt{V^2_{\rm circ}(R) + \sigma^2_R(R)\left[1 - \frac{\sigma^2_\phi(R)}{\sigma^2_R(R)} - R\left(\frac{1}{h} + \frac{2}{a}\right)\right]}\cos\phi\sin i$$

$$\sigma(r,\theta) = \sigma_R(R)\sqrt{\sin^2 i\left[\sin^2\phi + \frac{\sigma^2_\phi(R)}{\sigma^2_R(R)}\cos^2\phi\right] + \frac{\sigma^2_{0,z}}{\sigma^2_{0,R}}\cos^2 i},$$

where r is the galactocentric radius on the sky plane and θ is the anomaly angle measured anticlockwise from the line of nodes. The polar coordinates defined on the galaxy (R, ϕ) and sky plane (r, θ) are related to each other as follows:

$$R\cos\phi = r\cos\theta \quad , \quad \tan\phi\cos i = \tan\theta.$$

We adopted $h = h_{\rm in} = 11.82\,$arcsec and $i = 40.^{\circ}7$ and we assumed the three components of the velocity dispersion to have exponential radial profiles with the same scalelength, but different central values:

$$\sigma_R = \sigma_{0,R}\, e^{-R/a} \quad , \quad \sigma_\phi = \sigma_{0,\phi}\, e^{-R/a} \quad , \quad \sigma_z = \sigma_{0,z}\, e^{-R/a}.$$

This means that we assumed that the shape of the velocity ellipsoid does not change with the galactocentric radius having constant axial ratios $(\sigma_\phi/\sigma_R, \sigma_z/\sigma_R) = (\sigma_{0,\phi}/\sigma_{0,R}, \sigma_{0,z}/\sigma_{0,R})$. Then, we parameterised the circular velocity with the following power law:

$$V_{\rm circ} = V_0\, R^{\alpha}.$$

We have considered different solutions for the asymmetric drift model by either leaving all the dynamical parameters free to vary or fixing some of them to improve the data fitting. For example, we have adopted constant values for the three velocity dispersion components and/or we have chosen $\sigma_{0,z}/\sigma_{0,R} = 0.85$ as found by Aguerri et al. (2015) for a sample SB0/SBa galaxies. The solution given corresponds to the best-fitting result obtained with the largest number of free parameters. Assuming the epicyclic approximation ($\sigma_\phi/\sigma_R = \sqrt{0.5(1+\alpha)}$) and a constant circular velocity ($\alpha = 0$), we found $V_{\rm circ} = 148$ km s^{-1}. The measured and model velocities after being deprojected onto the disc plane and the adopted circular velocity are shown in Fig. 3.5. We performed a set of 100 Monte Carlo simulations by varying the values of $h_{\rm in}$, i, σ_z/σ_R and $V_{\rm syst}$ within their errors and recovering $V_{\rm circ}$ from a Levenberg-Marquardt least-squares fit to the data with the IDL procedure MPCURVEFIT (Press et al., 1992). We adopted the standard deviation of the distribution of circular velocity values as the associated error. We finally obtained $V_{\rm circ} = 148 \pm 5\,$km s^{-1}.

3.4 Characterisation of the bar

Bar radius

The measure of $R_{\rm bar}$ is not a straightforward task. The correct identification of the bar edges is not easy when other components as spiral arms or rings are present in the galaxy too. Several methods have been proposed to derive it, but each of them suffers from some limitations (see Sec. 1.2 for details). The best choice to measure $R_{\rm bar}$ is to adopt different independent methods.

We estimated the bar radius $R_{\rm PA} = 18.2 \pm 0.4\,$arcsec from the isophotal analysis of the deprojected i-band image of NGC 4277. As done in Aguerri et al. (2003), we defined the bar radius $R_{\rm PA}$ as the radius at which we measured $\Delta{\rm PA} = 10^{\circ}$ with respect to the PA of the ellipse with the maximum ϵ (Fig. 3.6, left panel).

A second measure of $R_{\rm bar}$ was obtained from the Fourier analysis of the deprojected i-band image of NGC 4277 (Aguerri et al., 2015). We computed the luminosity of the bar and interbar region calculating $I_{\rm bar} = I_0 + I_2 + I_4 + I_6$, and $I_{\rm interbar} = I_0 - I_2 + I_4 - I_6$, respectively. The bar radius is defined as the radial distance corresponding to the FWHM of the radial profile of the bar-interbar ratio $R_{\rm bar/ibar} = 19.0 \pm 2.2\,$arcsec (Fig. 3.6, central panel).

We also estimated the bar radius from the analysis of the phase angle ϕ_2 of the $m = 2$ Fourier component (Debattista et al., 2002). The bar radius is defined as the radial distance at which the bar phase changes of a angle of $\Delta\phi_2 = 5^{\circ}$ (Fig. 3.6, right panel). We obtained $R_{\phi_2} = 15.8 \pm 4.5\,$arcsec. We finally obtained a fourth estimate of the bar radius ($R_{\rm Ferrers} = 25.0 \pm 0.1\,$arcsec) performing a photometric decomposition of the surface brightness distribution of the deprojected image of NGC 4277 (Méndez-Abreu et al., 2017).

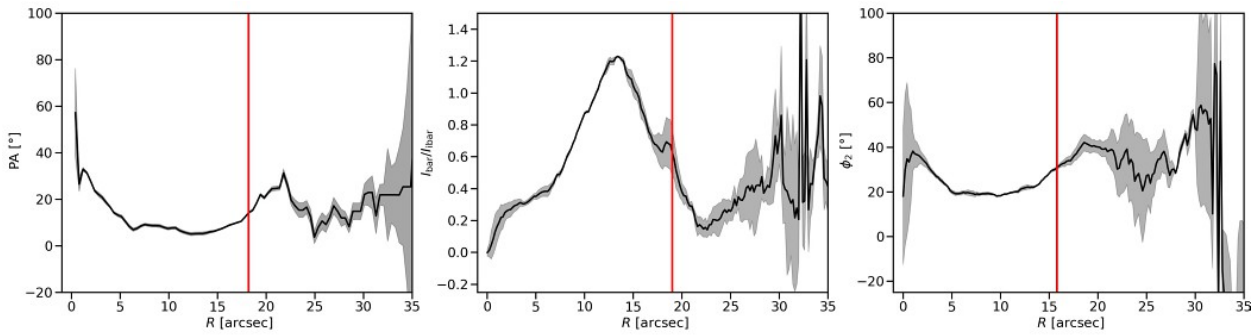

Figure 3.6: Radial profile of PA of deprojected ellipses (*left panel*), of the bar-interbar intensity ratio (*central panel*), and of the bar phase angle ϕ_2 (*right panel*). The red vertical lines represent $R_{\rm PA}$, $R_{\rm bar/ibar}$, and R_{ϕ_2}, respectively.

We adopted the mean of the various measures $R_{\rm PA}$, $R_{\rm bar/ibar}$, R_{ϕ_2}, and $R_{\rm Ferrers}$ as the length $R_{\rm bar}$ of the bar and we calculated its $\pm1\sigma$ error as the difference with respect to highest and lowest measured value. This gives $R_{\rm bar} = 19.5^{+5.5}_{-3.7}$ arcsec, which corresponds to $3.2^{+0.9}_{-0.6}$ kpc at the assumed distance. We compared this value with the typical bar radius of SB0 galaxies measured by Aguerri et al. (2009) and we conclude that NGC 4277 hosts a short bar.

Bar strength

As for $R_{\rm bar}$ we derived $S_{\rm bar}$ by applying different independent methods. We derived $S_{\rm bar}$ using the bar axial ratio $q_{\rm bar}$ as done in Aguerri et al. (2009):

$$S_\epsilon = \frac{2}{\pi}\left[\arctan q_{\rm bar}^{-1/2} - \arctan q_{\rm bar}^{1/2}\right],$$

where $q_{\rm bar} = 1 - \epsilon_{\rm bar}$ can be recovered from the ellipticity of the bar measured at the radial distance $R_{\rm bar}$. We estimated the error with a Monte Carlo simulation by accounting for the error on the ellipticity. We took the standard deviation of the resulting distribution as the statistical error on S_ϵ. We obtained $S_\epsilon = 0.230 \pm 0.003$. We also calculated $S_{\rm bar}$ as the mean value of the I_2/I_0 of $m = 2$ Fourier amplitudes over the bar extension as done in (Aguerri et al., 2000):

$$S_{\rm bar} = \frac{1}{R_{\rm bar}}\int_0^{R_{\rm bar}} \frac{I_2(R)}{I_0(R)} dR.$$

We estimated the error by performing a Monte Carlo simulation and taking the errors on the $m = 0, 2$ Fourier components into account. We generated 100 mock profiles of the I_2/I_0 intensity ratio and we calculated the corresponding bar strength. We took the standard deviation of the resulting distribution as the statistical error on $S_{\rm Fourier}$.

We took the mean value of $S_{\rm Fourier}$ and S_ϵ and their semi-difference as the strength $S_{\rm bar}$ of the bar and its error, respectively. This gives $S_{\rm bar} = 0.21 \pm 0.02$, which means that the bar of NGC 4277 is weak according to the classification of Cuomo et al. (2019b).

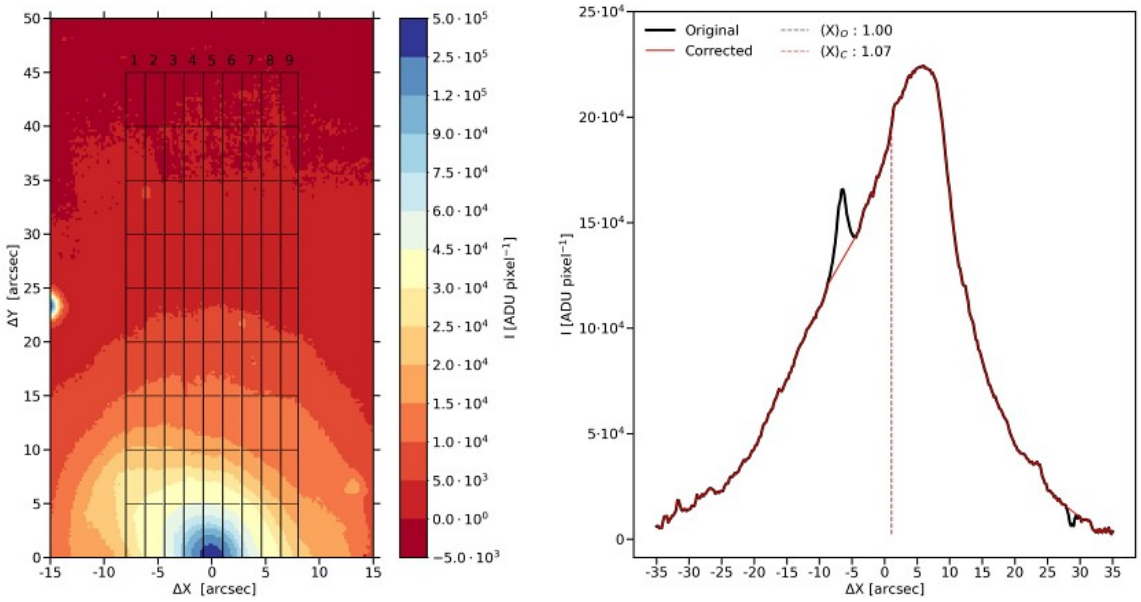

Figure 3.7: *Left panel*: Image of NGC 4277 with pseudo-slits (black lines) with semi-length from 5 arcsec to 45 arcsec. The colour bar gives the flux value of the pixels in ADU. *Right panel*: Surface brightness radial profile along the pseudo-slit 9 crossing NGC 4277 before (black line) and after (red line) subtracting the contribution of foreground stars. The position of the photometric integral before (vertical dashed black line) and after (vertical dashed red line) are shown.

Bar pattern speed

NGC 4277 fully satisfies the requirements for the application of the model-independent TW method. It has an intermediate inclination, its bar is oriented at an intermediate angle between the major and minor axes of the disc, and it shows no evidence of spiral arms or patchy dust. In addition, old stellar population in lenticular galaxies are the most suitable tracer since it rarely presents star-formation activity. Thanks to the integral-field spectroscopic data, the pseudo-slits can be defined *a posteriori* reconstructing from the MUSE datacube the image of NGC 4277, minimising the errors associated with the correct centring with the galaxy.

We defined nine adjacent pseudo-slits crossing the bar and aligned with the disc (Fig. 3.7, left panel). They have a width of nine pixels (1.8 arcsec) to account for seeing smearing effects and a semi-length that ranges from 25 pixels (5 arcsec) to 175 pixels (35 arcsec) to fully cover the extension of the disc, and PA = 123.°27.

We derived the photometric integrals $\langle X \rangle$ from the MUSE reconstructed image, which we obtained by summing the MUSE datacube along the spectral direction in the same wavelength range adopted to measure the stellar kinematics. In each pseudo-slit, we measured the luminosity-weighted position of the stars with respect to the galaxy minor axis as follows:

$$\langle X \rangle = \frac{\sum_{(x,y)} F(x,y)\,\mathrm{dist}(x,y)}{\sum_{(x,y)} F(x,y)},$$

where (x, y) and $F(x, y)$ are the sky-plane coordinates and flux of the pixels in the pseudo-slit, respectively, and $\mathrm{dist}(x, y)$ is the distance of the pixels to the pseudo-slit centre.

We noticed that some of photometric integrals measured for pseudo-slit semi-lengths of 45 arcsec are higher than those measured at 35 arcsec and 40 arcsec. This is due to the presence of many pixels with negative flux values at large radii from the galaxy centre (Fig. 3.7, left panel) probably resulting from a bad subtraction of the sky background at the edges of the MUSE datacube. The number of bad pixels heavily increases if we consider the galaxy image obtained by collapsing the MUSE datacube over the full wavelength range. Therefore, we decided to adopt a semi-length of 35 arcsec as maximum semi-length for the pseudo-slits crossing the bar. Some of the pseudo-slits cover a few foreground stars resulting in spikes in the surface brightness radial profile, which we manually corrected by linearly interpolating over the star light contribution (Fig. 3.7, right panel).

We estimated the errors on $\langle X \rangle$ with a Monte Carlo simulation by generating 100 mock images of the galaxy. To this aim, we processed the convolved and resampled SDSS image using the IRAF task BOXCAR. Then, we added to each image pixel the photon noise due to the contribution of both the galaxy and sky background and the read-out noise of the detector to mimic the actual image of NGC 4277. We measured the photometric integrals in the mock images and adopted the root mean square of the distribution of measured values as the error for the photometric integral in each pseudo-slit (labelled as "MC" in Table 3.2). As a consistency check, we alternatively estimated the errors on $\langle X \rangle$ defining for each slit the radial range in which the value of the photometric integral is constant and adopting the root mean square of the distribution as the error of photometric integrals (labelled as "rms" in Table 3.2).

We derived the kinematic integrals $\langle V \rangle$ in the range 4800-5600Å, the same wavelength range adopted for the stellar kinematics. We summed all the spaxels of each pseudo-slit to obtain a single spectrum from which we measured the luminosity-weighted stellar LOS velocity with PPXF. This is equivalent to calculating the following:

$$\langle V \rangle = \frac{\sum_{(x,y)} V_{\rm LOS}(x,y)\, F(x,y)}{\sum_{(x,y)} F(x,y)},$$

where (x, y) and $V_{\rm LOS}(x, y)$ are the coordinate of the spaxels in the pseudo-slit and their stellar LOS velocity, respectively. We adopted the rescaled formal errors by PPXF as 1σ errors on $\langle V \rangle$.

To define the convergence radial range, we checked the convergence of the kinematic integrals as a function of the pseudo-slit semi-length from 5 arcsec to 45 arcsec (Fig. 3.8, right panel), and we found that in the semi-length range of $20 - 35$ arcsec, the measured values of $\langle V \rangle$ are consistent within the uncertainties.

We choose $\langle X \rangle$ and $\langle V \rangle$ data at semi-length of 35 arcsec for the further analysis. The values of photometric and kinematic integrals lay on a straight line following the equation:

$$\langle V \rangle = \langle X \rangle \Omega_{\rm bar} \sin(i).$$

We derived $\Omega_{\rm bar}$ of NGC 4277 using the FITEXY algorithm (Press et al., 1992), taking into account errors on both $\langle X \rangle$ and $\langle V \rangle$ (Fig. 3.9, left panel). The slope of the best-fit line we obtained is $\Omega_{\rm bar} \sin i = 2.65 \pm 0.37$ km s^{-1} arcsec^{-1}. From the galaxy inclination, we obtained $\Omega_{\rm bar} = 4.06 \pm 0.56$ km s^{-1} arcsec^{-1}, which corresponds to $\Omega_{\rm bar} = 24.7 \pm 3.4$ km s^{-1} kpc^{-1} for the adopted distance.

As a consistent check, we derived the bar pattern speed at different semi-length of the pseudo-slit (Fig. 3.9, right panel). Although at face values $\Omega_{\rm bar}$ is rising, all the estimates in radial range of convergence are fully consistent with each other within their errors. Our adopted value of $\Omega_{\rm bar} = 24.7 \pm 3.4$ km s^{-1} kpc^{-1} is consistent with the mean value $\langle \Omega_{\rm bar} \rangle = 21.4 \pm 1.1$ km s^{-1} kpc^{-1}, which we calculated for all the semi-lengths between 20 arcsec and 35 arcsec.

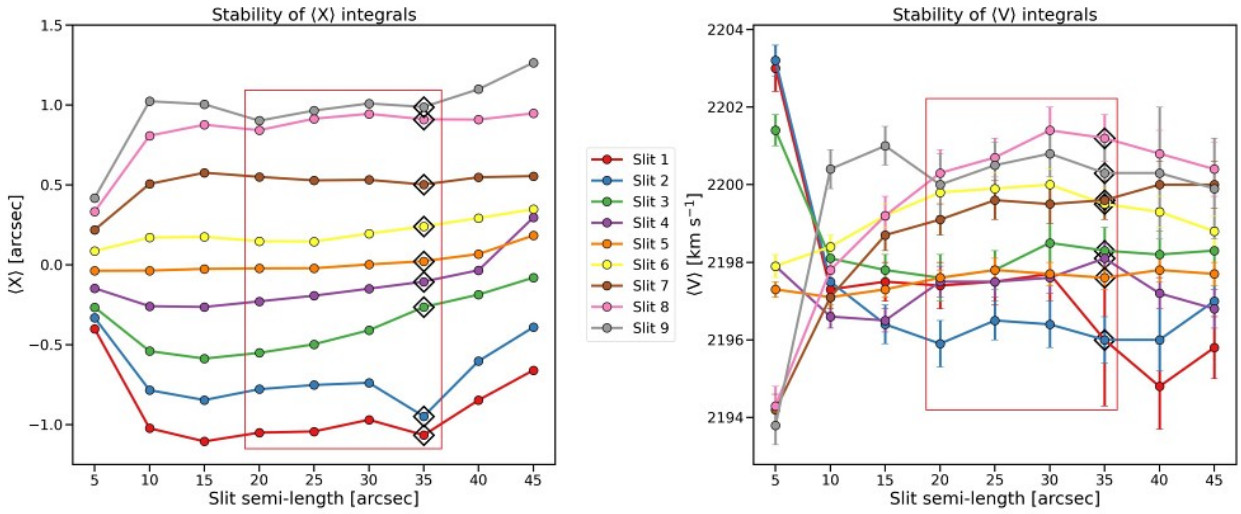

Figure 3.8: Stability of TW integrals. Photometric (*left panel*) and kinematic (*right panel*) integrals as a function of the semi-length of the pseudo-slit. The adopted values for the TW analysis are marked with empty black diamonds. The region enclosed in red box represents the radial range of convergence for photometric and kinematic integrals. Some values of $\langle X \rangle$ at semi-length of 45 arcsec are systematically larger than those measured at 35 arcsec and 40 arcsec (see text for a discussion).

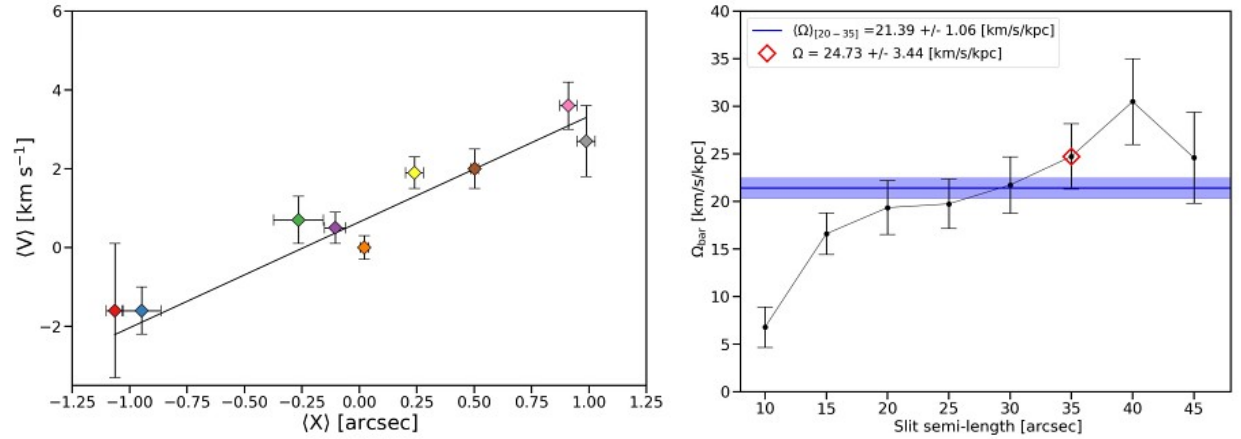

Figure 3.9: *Left panel*: Pattern speed of the bar in NGC 4277. The values of kinematic integrals $\langle V \rangle$ are plotted as a function of their corresponding photometric integrals $\langle X \rangle$. The black solid line represents the best fit to the data, that are colour-coded according to the slit as in Fig. 3.8. *Right panel*: Bar pattern speed as a function of pseudo-slit semi-length. The blue line and shaded region correspond to the mean and rms of $\Omega_{\rm bar}$ between 20 arcsec and 35 arcsec, respectively. The adopted value is marked by empty red diamond.

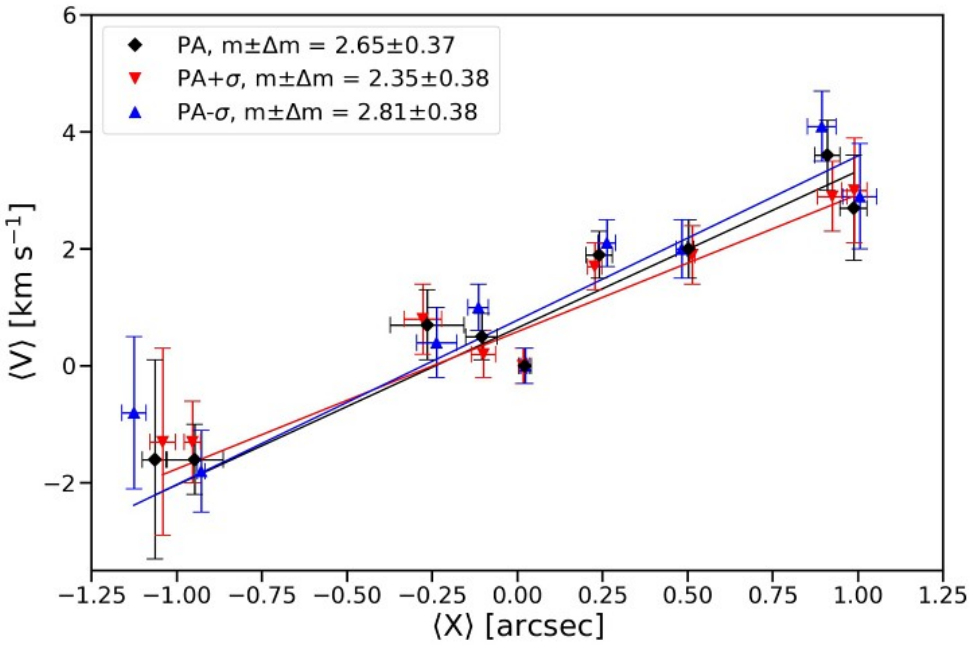

Figure 3.10: Pattern speed of the bar in NGC 4277 for different disc PAs. The values of kinematic integrals $\langle V \rangle$ are plotted as a function of their corresponding photometric integrals $\langle X \rangle$.

We calculated $R_{\rm cor}$ from $\Omega_{\rm bar}$ and $V_{\rm circ}$ as $R_{\rm cor} = V_{\rm circ}/\Omega_{\rm bar} = 36.5 \pm 5.2$ arcsec, which corresponds to $R_{\rm cor} = 6.0 \pm 0.9$ kpc with the 1σ error estimated from the propagation of uncertainty. Finally, we derived the rotation rate $\mathcal{R} = R_{\rm cor}/R_{\rm bar} = 1.8^{+0.5}_{-0.3}$ with the $\pm 1\sigma$ error estimated from a Monte Carlo simulation to account for the errors on $R_{\rm bar}$, $\Omega_{\rm bar}$, i, and $V_{\rm circ}$. We concluded that NGC 4277 hosts a slow bar. We tested the validity of our result with the assumption of a thin disc deriving the inclination of the galaxy in the thick disc assumption with an intrinsic flattening of $q_{\rm int} = 0.3$, which is the median value for a sample of edge-on SDSS S0 galaxies studied by Mosenkov et al. (2015). We derived the new values of $\Omega_{\rm bar}$, $R_{\rm cor}$, and $\mathcal{R}$ with the corresponding errors by performing a Monte Carlo simulation to account for the errors on $R_{\rm bar}$, $\Omega_{\rm bar}$, i, and $V_{\rm circ}$ in the thick disc assumption. The new $\Omega_{\rm bar}$ we derived with the thick disc assumption is equal to $\Omega_{\rm bar} = 3.88 \pm 0.55$ km s^{-1} arcsec^{-1}, which corresponds to $\Omega_{\rm bar} = 23.6 \pm 3.3$ km s^{-1} kpc^{-1}, for the adopted distance. The values of $\Omega_{\rm bar}$ derived with thin and thick disc assumption are compatible within their uncertainties, this means that our conclusions remain unaffected, i. e. the bar hosted in NGC 4277 is slow.

The error on the distance translates into a systematic uncertainty of 0.1 kpc on $R_{\rm bar}$ and $R_{\rm cor}$ but it does not affect our conclusion on the slow classification of the bar since $\mathcal{R}$ is a distance independent parameter.

Even if TW is a model-independent method to recover $\Omega_{\rm bar}$, there are several sources of error which contribute to the resulting accuracy in estimating $\mathcal{R}$ (see Corsini 2011, for a discussion). In particular, the misalignment between the orientation of the pseudo-slits and disc PA translates into a large systematic error (Debattista, 2003). To account for this issue, we repeated the analysis by adopting different PAs for the pseudo-slits ($\langle {\rm PA} \rangle - \sigma = 122\overset{\circ}{.}95$ and $\langle {\rm PA} \rangle + \sigma = 123\overset{\circ}{.}59$) to account for the uncertainty on the PA of the inner disc. We obtained the new reconstructed image and defined nine pseudo-slits crossing the bar with a 1.8 arcsec width and a 35 arcsec semi-length.

Table 3.2: Results of tests on the bar pattern speed and rotation rate of NGC 4277 as a function of the PA of the pseudo-slits.

$\sigma_{\langle X\rangle}$	$\Omega_{\rm bar}\sin i$	$\Omega_{\rm bar}$	$\Delta\Omega_{\rm bar}/\Omega_{\rm bar}$	$\mathcal{R}$	$\Delta\mathcal{R}/\mathcal{R}$
	[km s^{-1} arcsec^{-1}]	[km s^{-1} kpc^{-1}]			
(1)	(2)	(3)	(4)	(5)	(6)
PA $= 123\overset{\circ}{.}27$ ($\equiv\langle$PA$\rangle$)					
MC	2.63± 0.36	24.6±3.4	0.14	$1.77^{+0.45}_{-0.27}$	0.20
rms	2.65± 0.37	24.7±3.4	0.14	$1.76^{+0.46}_{-0.27}$	0.21
PA $= 123\overset{\circ}{.}59$ ($\equiv\langle$PA$\rangle+\sigma$)					
rms	2.35± 0.38	21.9±3.6	0.16	$1.88^{+0.67}_{-0.22}$	0.24
PA $= 122\overset{\circ}{.}95$ ($\equiv\langle$PA$\rangle-\sigma$)					
rms	2.81± 0.38	26.3±3.5	0.13	$1.67^{+0.41}_{-0.26}$	0.20
PA $= 121\overset{\circ}{.}77$ ($\equiv\langle$PA$\rangle-1\overset{\circ}{.}5$)					
rms	3.23± 0.32	30.1±3.0	0.10	$1.41^{+0.36}_{-0.16}$	0.18

Notes: (1) Error on $\langle X\rangle$. (2) Slope of the best-fitting line. (3) Bar pattern speed. (4) Relative error on bar pattern speed. (5) Bar rotation rate. (6) Relative error on bar rotation rate.

We manually corrected the surface brightness radial profile of the pseudo-slit for the light contribution of foreground stars, checked the stability of both photometric and kinematic integrals, and derived the bar pattern speed and rotation rate as was done before. The results for the different PAs are listed in Table 3.2 and are consistent with a slow bar. As a final test, we repeated the analysis, varying the PA of the pseudo-slits in steps of $\pm0\overset{\circ}{.}5$ to look for the PA for which the bar can be classified as fast. This occurs at $\langle$PA$\rangle-1\overset{\circ}{.}5$ (Table 3.2), which corresponds to a misalignment between the pseudo-slits and disc major axis of $\sim 5\sigma$ times the uncertainty on the $\langle$PA$\rangle$. This is not consistent with the results of the photometric analysis (Fig. 3.2) and photometric decomposition (Table 3.1). All the above consistency checks support the finding of a slow bar in NGC 4277.

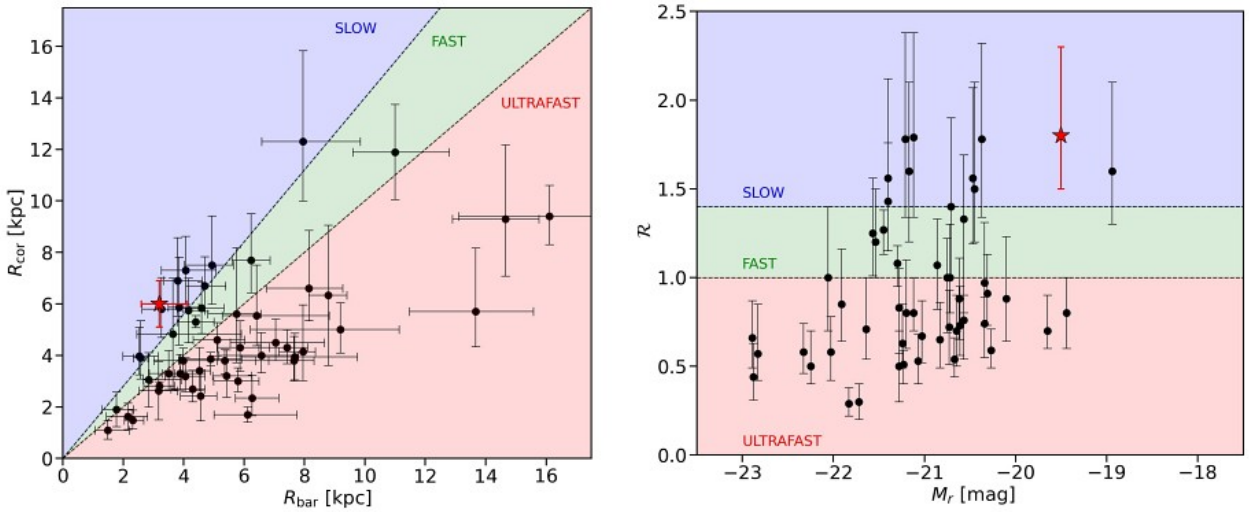

Figure 3.11: Corotation radius as a function of bar radius (*left panel*) and rotation rate as a function of the total r-band absolute magnitude (*right panel*) for barred galaxies for which $\Omega_{\rm bar}$ was measured with the TW method. Only galaxies with $\Delta\mathcal{R}/\mathcal{R} \leqslant 0.5$ are shown and they are taken from the compilation of Cuomo et al. (2020). The red star corresponds to NGC 4277. The coloured regions represent the ultra-fast (red), fast (green), and slow bar (blue) regimes, respectively.

3.5 Conclusions

We measured the broad-band surface photometry and two-dimensional stellar kinematics of NGC 4277, a barred lenticular galaxy located in the region of the Virgo cluster at a distance of 33.9 Mpc, to derive its bar pattern speed ($\Omega_{\rm bar} = 24.7 \pm 3.4$ km s^{-1} kpc^{-1}). We found that NGC 4277 hosts a weak ($S_{\rm bar} = 0.21 \pm 0.02$), short ($R_{\rm bar} = 3.2^{+0.9}_{-0.6}$ kpc), and slow ($\mathcal{R} = 1.8^{+0.5}_{-0.3}$) bar.

The extended spectral range, fine spatial sampling, and large FOV of the MUSE integral-field spectrograph in combination with wide-field SDSS imaging permitted us to carefully deal with the sources of uncertainty in deriving $R_{\rm bar}$, $S_{\rm bar}$, and $\Omega_{\rm bar}$ of NGC 4277. We carefully derived the orientation and inclination of the galaxy disc, to accurately recover the measure of the bar radius. We confidently determined the position and LOS velocity of the galaxy centre, and defined the pseudo-slits crossing the bar minimising the uncertainties related with the correct centring with the galaxy. We maximised the number and S/N of the spectra on the MUSE datacube to accurately measure the stellar kinematics and recover the circular velocity by correcting for asymmetric drift the LOS velocities and velocity dispersions. We quantified the systematic uncertainty due to a possible misalignment of the pseudo-slit with the disc major axis. The bar in NGC 4277 remains slow at face value even if the misalignment between the pseudo-slits and the disc is ΔPA=1.°5. As a consequence, the values of the bar pattern speed ($\Delta\Omega_{\rm bar}/\Omega_{\rm bar} \sim 0.14$) and rotation rate ($\Delta\mathcal{R}/\mathcal{R} \sim 0.21$) of NGC 4277 are amongst the best-constrained ones ever obtained with the TW method applied on a stellar tracer. These results hold even if we adopt the galaxy inclination for a thick rather than infinitesimally-thin stellar disc ($\mathcal{R}=2.0\pm^{+0.6}_{-0.5}$). Indeed, the systematic difference between the inclination-dependent parameters is much smaller than their statistical errors.

We show in Fig. 3.11 all the barred galaxies for which $\Omega_{\rm bar}$ has been measured with the TW method and with a well-constrained rotation rate $\Delta\mathcal{R}/\mathcal{R} < 0.5$ from Cuomo et al. (2020). Most bars are consistent with being fast within errors ($1 \leqslant \mathcal{R} \leqslant 1.4$) with more than 90% of confidence level. The probability of the bar of NGC 4277 to be slow (91%) is ten times higher than that of being fast (9%). The only other galaxy nominally hosting a stellar slow bar was manga 8317-12704 ($\mathcal{R} = 2.4^{+0.8}_{-0.6}$) and measured by Guo et al. (2019), who applied the TW method to the stellar kinematics of a sample of barred galaxies from the MANGA survey (Bundy et al., 2015). However, they adopted a slit semi-length equal to $1.2R_{\rm e}$, which does not guarantee the convergence of TW integrals when the bar radius is longer than the galaxy effective radius. Garma-Oehmichen et al. (2020) show that $\Omega_{\rm bar}$ of manga 8317-12704 was underestimated (and thus $\mathcal{R}$ was overestimated) because $R_{\rm bar} = 10.3\,{\rm arcsec} > 1.2R_{\rm e} = 8.6\,{\rm arcsec}$. They adopted a different PA ($\Delta{\rm PA}\sim 3^{\circ}$) and larger semi-length for the pseudo-slits to obtain stable TW integrals from the MANGA dataset. Garma-Oehmichen et al. (2020) found a new rotation rate for the bar of manga 8317-12704 ($\mathcal{R} = 1.5^{+0.3}_{-0.2}$), which is consistent with the fast regime. The slow bars of NGC 2915 ($\mathcal{R} = 1.7$, Bureau et al. 1999), UGC 628 ($\mathcal{R} = 2.0^{+0.5}_{-0.3}$, Chemin & Hernandez 2009), and DDO 168 ($\mathcal{R} = 2.1$, Patra & Jog 2019) cannot be safely taken into account since a gaseous tracer might not satisfy the continuity equation linking the TW integrals. Indeed, NGC 4277 is the first clear case of a galaxy hosting a slow stellar bar ($\mathcal{R} > 1.4$ at 1.3σ confidence level) measured with the TW method.

Martinez-Valpuesta et al. (2017) studied how the formation scenario produces bar with different properties using N-body simulations. They found that bars formed by the close encounter with a co-planar 1:1 interaction are slower than those formed intrinsically by pure dynamical instabilities in the disc. Bar pattern speed in these bars rapidly evolve to lower values for the following 4 Gyr after the encounter, indeed observations at higher redshift could catch the early evolutionary phases of these bars. Slow bars can eventually be the final result of a fast bar braked by a centrally concentrated DM halo due to the dynamical friction mechanism (Weinberg, 1985; Debattista & Sellwood, 1998). Debattista & Sellwood (2000) showed that a DM halo, either non-rotating or backward-rotating respect with the bar rotation, has a severe effect on the evolution of its bar pattern speed. The effect of the friction is mild when the density of the DM halo is lowered, this permits the bar to remain fast for several bar.

NGC 4273, the galaxy companion of NGC 4277, is a giant and bright spiral galaxy located at a distance of $D = 36.3\,{\rm Mpc}$ (Fig. 3.1, left panel). It lies at a projected distance of 1.9 arcmin with respect to NGC 4277, and presents a disturbed morphology. This feature can be representative of an on-going interaction between the two galaxies. By determining the DM fraction in the bar region, it will be possible to understand whether the uncommonly large $\mathcal{R}$ of NGC 4277 was initially imprinted by a tidal interaction with NGC 4273 triggering the bar formation or whether it is the end result of the bar braking due to the dynamical friction exerted by the DM halo.

Chapter 4

A slow lopsided bar in the interacting dwarf galaxy IC 3167[§]

Abstract

We characterised the properties of the bar hosted in dwarf galaxy IC 3167. We measured $R_{\rm bar}$ and $S_{\rm bar}$ from the surface photometry obtained from the broad-band imaging of the SDSS and we derived $\Omega_{\rm bar}$ from the stellar kinematics obtained from the integral-field spectroscopy performed with the MUSE spectrograph at the VLT. We estimated $V_{\rm circ}$ by correcting the stellar streaming motions for asymmetric drift and we derived the bar rotation rate $\mathcal{R}$. We found that IC 3167 hosts a short ($R_{\rm bar}$=$1.1^{+0.4}_{-0.2}$ kpc), weak ($S_{\rm bar}$=0.27 ± 0.04), and slow ($\mathcal{R}$= $1.7^{+0.5}_{-0.3}$) bar. The probability that the bar is rotating slowly (68%) is twice more likely to be slow (probability of 68%) rather than fast (32%). This allows us to infer that the formation of this bar was triggered by the ongoing interaction rather than to internal processes.

4.1 Introduction

Stellar bars are ubiquitous in nearby disc and irregular galaxies (e.g. Marinova & Jogee, 2007; Aguerri et al., 2009; Buta et al., 2015). They reshape bulges, regulate star formation activity, and drive secular transformation of their host galaxies (e.g. James & Percival, 2016; Lin et al., 2020). They generally cross the galaxy centre and have a bisymmetric boxy shape (e.g., Debattista et al., 2006; Méndez-Abreu et al., 2018a). However, some of them are asymmetric and off-centred with respect to the galaxy disc (e.g., Odewahn, 1994; Kruk et al., 2017). The most iconic example of a lopsided bar is hosted by the Large Magellanic Cloud (LMC, van der Marel, 2001; Jacyszyn-Dobrzeniecka et al., 2016). Off-centred bars are common in low luminosity galaxies with a companion (Odewahn, 1994; Besla et al., 2016). For this reason, their formation was considered as driven by tidal interactions (Buta et al., 2001; Łokas, 2021a). On the other hand, the presence of lopsided bars in non-interacting and isolated galaxies has been thought of as evidence for the gravitational pull of an asymmetric DM halo (Kruk et al., 2017). The effects of cosmological asymmetrical accretion of gas on galaxy discs can create strongly lopsided features, which should correspond to asymmetries in the star formation of the host galaxy (Bournaud et al., 2005).

[§] *Based on Cuomo, V., Corsini, E. M., Morelli, L., et al. 2022, MNRAS, 516, L24.*

Dwarf galaxies outnumber normal and giant galaxies (e.g., McConnachie, 2012; Choque-Challapa et al., 2021) and are very common in dense environments, such as galaxy groups and clusters, which play an important role in shaping their morphology and stellar properties (see Boselli & Gavazzi, 2014, for a review). Some dwarf disc galaxies have bars, lenses, and spiral arms as their giant counterparts and are characterised by a strong asymmetric shape (e.g., Barazza et al., 2002; Lisker et al., 2006; Michea et al., 2021). We consider dwarf barred galaxies as the ideal candidates to host slow-rotating bars because dwarf galaxies are thought to be embedded in massive and quite centrally-concentrated DM haloes (e.g., Adams et al., 2014; Relatores et al., 2019), which may dynamically brake the bar and are prone to interactions with other galaxies and/or cluster triggering the formation of a slow bar. However, $\mathcal{R}$ is poorly known in dwarf galaxies, due to the difficulty of accurately measuring their $\Omega_{\rm bar}$ (Corsini et al., 2007). To start addressing this issue, here we report a detailed photometric and kinematic study of IC 3167, a dwarf barred galaxy located beyond the Virgo cluster. We organise the chapter as follows. We report the general properties of IC 3167 in Sec. 4.2. We present the photometric and kinematic analysis in Sec. 4.3. We discuss the results in Sec. 4.4 and report our conclusions in Sec. 4.5. We adopt as cosmological parameters, $\Omega_{\rm M} = 0.286$, $\Omega_{\Lambda} = 0.714$, and $H_0 = 69.3$ km s^{-1} Mpc^{-1} (Hinshaw et al., 2013).

4.2 General properties of IC 3167

IC 3167 (VCC 407) is a dwarf barred galaxy located in direction of the Virgo cluster (Kim et al., 2014), classified as dSB0(3) by Binggeli et al. (1985) and dS0 by Kim et al. (2014). It has an absolute magnitude of $M_r = -17.62$ mag (Lisker et al., 2006) assuming a distance of 17 Mpc with r-band effective radius $R_{{\rm e},r} = 1.5$ kpc. Its stellar mass is $M_\star = 10^{9.06}$ M$_\odot$ (Bidaran et al., 2020). Despite being initially classified as an early-type dwarf galaxy, IC 3167 presents an inclined disc (Lisker et al., 2006) with a bar (Janz et al., 2014)). The galaxy does not have any bright nearby companion, but it belongs to a bound group of dwarf galaxies recently accreted onto the Virgo cluster and observed at a cluster-centric distance of ~ 1.5 Mpc with a LOS velocity of ~ 700 km s^{-1} with respect to M87 (Lisker et al., 2018).

4.3 Data analysis

Broad-band imaging

We retrieved the flux-calibrated i-band image of IC 3167 from the science archive of the SDSS Data Release 14 (SDSS, Abolfathi et al., 2018) to perform an accurate photometric analysis of the bar properties (Fig. 4.1). We trimmed the image selecting a FOV centred on the galaxy of 700×700 pixel^2, which corresponds to 4.6 ×4.6 arcmin^2, and rotated the image in order to orient it with the north up and east left.

Isophotal analysis

We performed an isophotal analysis on the image of IC 3167 following the prescriptions in Chapter 3. We fitted ellipses to the galaxy isophotes with the IRAF task ELLIPSE to measure the constant residual surface brightness of the sky, which we subtracted as done in Morelli et al. (2016). We derived the radial profiles of the azimuthally-averaged surface brightness, ellipticity ϵ, position angle PA, centre coordinates and third, fourth, and sixth cosine and sine Fourier coefficients (Fig. 4.2).

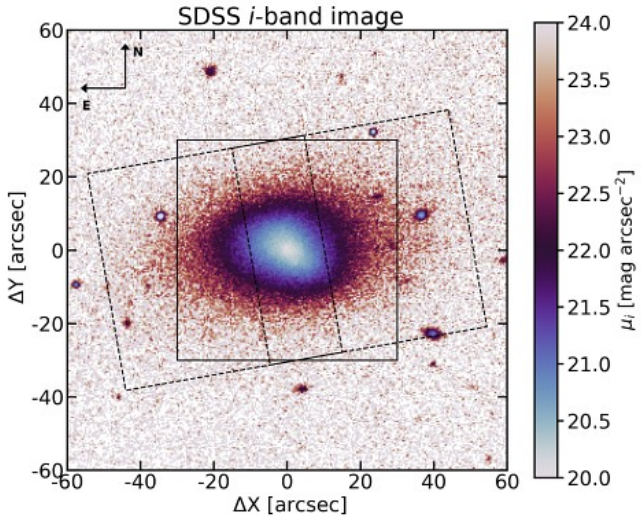

Figure 4.1: SDSS *i*-band image of IC 3167. The three squares mark the MUSE central (solid black lines) and offset (dashed black lines) pointings. The FOV is 2×2 arcmin^2 and is oriented with the north up and east left. The bar and disc extend up to ∼ 15 and ∼ 50 arcsec, respectively.

The higher Fourier coefficients describe the deviation of the isophotal shape from a perfect ellipse (Athanassoula et al., 1990).

Moreover, we fitted the disc-dominated portion of the surface brightness radial profile between $30 \leqslant a \leqslant 45$ arcsec with an exponential law to derive the disc scalelength ($h = 13.4 \pm 1.1$ arcsec) (Fig. 4.2, left panel). The local maximum of ellipticity $\epsilon \sim 0.35$ associated to the nearly constant position angle PA $\sim 55^\circ$ in the inner ∼ 10 arcsec is the isophotal signature of the bar (Fig. 4.2, central panel), which is offset southward by 0.7 arcsec with respect to the disc centre. The bar is remarkably lopsided, as it results from the third sine Fourier coefficient peaking at $B_3 \sim -0.05$. The inner portion of the disc is lopsided too ($B_3 \sim 0.06$, Fig. 4.2, right panel).

We measured the mean disc position angle $\langle \mathrm{PA} \rangle = 96\overset{\circ}{.}5 \pm 1\overset{\circ}{.}4$ and ellipticity $\langle \epsilon \rangle = 0.419 \pm 0.016$ from the constant isophotal profiles in the radial range between 30 and 45 arcsec. We recovered the galaxy inclination from the mean disc ellipticity by calculating $i = \arccos(1 - \langle \epsilon \rangle) = 54\overset{\circ}{.}5 \pm 1\overset{\circ}{.}1$ and assuming an infinitesimally-thin disc.

Fourier analysis

We used disc geometric parameters derived from the isophotal analysis to deproject the galaxy image in face-on view and perform a Fourier analysis, as done in Chapter 3. We derived the radial profiles of the amplitude of the $m = 0, 1, 2, 3, 4$, and 5 Fourier components and phase angle of the $m = 2$ one as in Aguerri et al. (2000) (Fig. 4.3). The even Fourier amplitudes are more prominent with respect to the odd ones, this is the photometric signature of a barred galaxy (Aguerri et al., 2000). In particular, the $m = 2$ component reaches a maximum at $I_2/I_0 \sim 0.3$ and the associated phase angle ϕ_2 remains constant with a value of $\sim 40^\circ$ in the bar region (Fig. 4.5, central top panel). The asymmetric radial profile of the $m = 2, 4$ components shows that the bar does not have a bisymmetric shape. Moreover, the $m = 1, 3, 5$ components have large values within the region of the bar confirming its lopsidedness (Fig. 4.3, right panel).

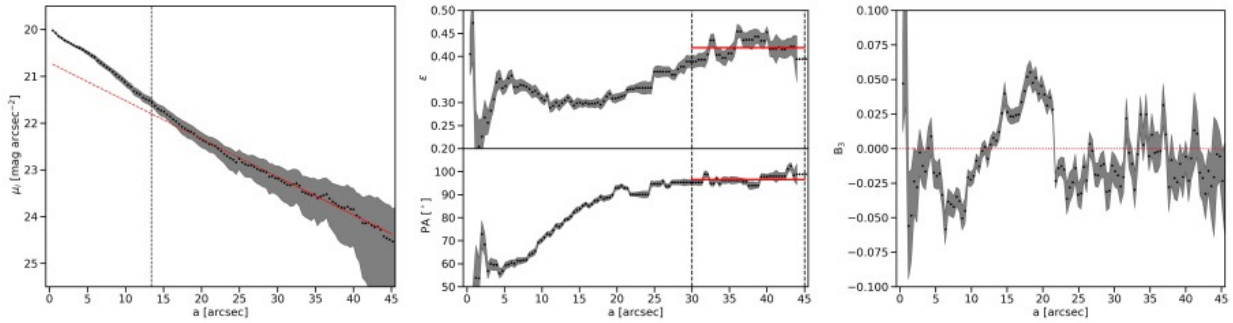

Figure 4.2: Isophotal analysis of the i-band image of IC 3167. Radial profiles of azimuthally-averaged surface brightness (*left panel*), ellipticity ϵ (*central top panel*), position angle PA (*central bottom panel*), and third sine Fourier coefficient (*right panel*). The red dashed line in the left panel marks the best-fitting disc surface brightness with the solid portion corresponding to the region used to fit the disc exponential profile ($30 \leqslant a \leqslant 45$ arcsec). The vertical black dashed line in the left panel corresponds to the disc scalelength ($h = 13.4 \pm 1.1$ arcsec). The vertical black dashed lines in the central panels bracket the radial range adopted to estimate the mean ellipticity $\langle\epsilon\rangle = 0.42 \pm 0.02$ and position angle $\langle\mathrm{PA}\rangle = 96\overset{\circ}{.}5 \pm 1\overset{\circ}{.}4$ of the disc.

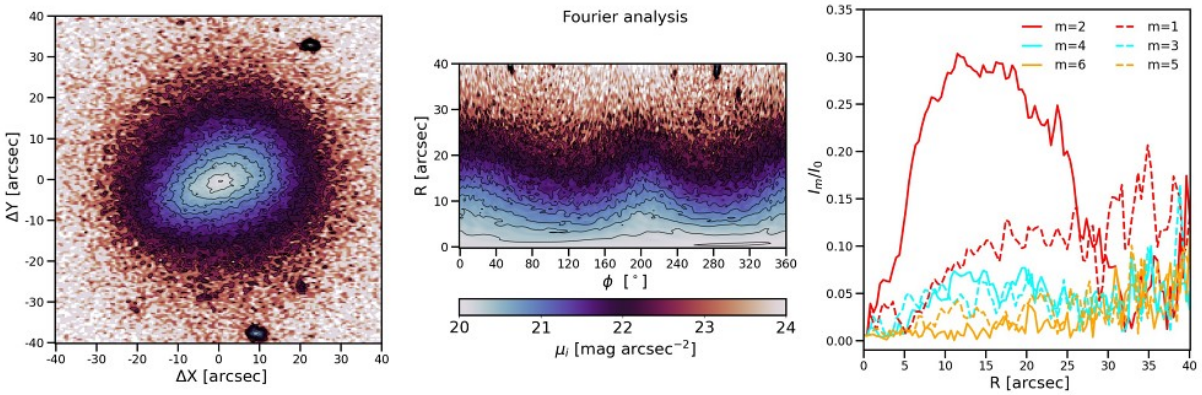

Figure 4.3: Fourier analysis of IC 3167. Deprojected i-band image of IC 3167 in Cartesian (*left panel*) and polar coordinates (*central panel*), and radial profiles of the relative amplitude of the even $m = 2$ (solid red line), $m = 4$ (solid blue line), and $m = 6$ (solid yellow line), and odd $m = 1$ (dashed red line), $m = 3$ (dashed blue line), and $m = 5$ (dashed yellow line) Fourier components (*right panel*).

IFU spectroscopy: spectra acquisition and data reduction

The integral-field spectroscopic observations of IC 3167 were carried out with the MUSE spectrograph of the ESO. MUSE was configured in WFM to ensure a FOV of 1×1 arcmin^2 with a spatial sampling of 0.2 arcsec pixel^{-1} and to cover the wavelength range of $4800 - 9300$ Å with a spectral sampling of 1.25 Å pixel^{-1} and an average nominal spectral resolution of FWHM = 2.51 Å (Bacon et al., 2010). The central pointing was obtained on January 2017 and February 2018 (120 min; Prog. Id. 098.B-0619(A) and 0100.B-0573(A), P.I.: T. Lisker). On April 2021, we took two offset pointings along the galaxy's major axis at a distance of 20 arcsec eastward (20 min) and westward (10 min) from the galaxy nucleus (Prog. Id.: 0106.B-0158(A), P.I.: V. Cuomo). During the nights the seeing reached a mean value of FWHM $\sim$ 1.1 arcsec. In Fig. 4.1, we show the i-band SDSS image of IC 3167 with the MUSE pointings overplotted.

We performed the data reduction using the standard MUSE pipeline (version 2.8.4, Weilbacher et al., 2016) and following the same prescription described in Chapter 3. The procedures of the data reduction include bias and overscan subtraction, flat fielding, wavelength calibration, determination of the line spread function, sky subtraction, and flux calibration. The sky contribution was quantified using an on-sky exposure. Then, we determined the effective spectral resolution and its variation across the FOV, and produced the combined datacube of the galaxy.

Stellar kinematics and circular velocity

We measured the LOS stellar velocity and the velocity dispersion of IC 3167 from the MUSE combined datacube using the Galaxy IFU Spectroscopy Tool pipeline (GIST, Bittner et al., 2019). As done in Chapter 3, we first performed a Voronoi binning with a target $S/N = 60$ per bin to ensure an accurate measure of the stellar kinematics. We adopted the MILES stellar library (FWHM = 2.5 Å, Vazdekis et al., 2010) in the wavelength range $4800-5600$ Å centred on the Mg I$\lambda\lambda$5167, 5173, 5184 Å absorption-line triplet. We estimated the errors on the kinematic parameters using Monte Carlo simulations. In Fig. 4.4 we show the LOS stellar velocity and velocity dispersion maps of IC 3167.

We derived the circular velocity from the LOS stellar velocity and velocity dispersion measured in the disc spatial bins outside the bar-dominated region (i.e., outside the ellipse with semi-major axis of 18.7 arcsec) correcting the stellar streaming motion for asymmetric drift Binney & Tremaine (2008), following the prescriptions described in Chapter 3. We obtained $V_{\rm circ} = 53.8 \pm 1.5$ km s^{-1}.

4.4 Characterisation of the bar

Bar radius

We measured $R_{\rm bar}$ by analysing the i-band image of IC 3167 with four independent methods.

We measured $R_{\rm bar}$ from the luminosity contrast of the bar and interbar region following the prescription in Aguerri et al. (2000) and we obtained $R_{\rm bar/interbar} = 18.3$ arcsec (Fig. 4.5, top left panel). We alternatively estimated $R_{\rm bar}$ from the constant radial profile of $m = 2$ Fourier component (Debattista et al., 2002) and we found $R_{\phi_2} = 15.4$ arcsec (Fig. 4.5, top right panel). We derived a third estimate of $R_{\rm bar}$ from the radial profile of the position angle of deprojected isophotes as done in Aguerri et al. (2009), and we obtained $R_{\rm PA} = 10.2$ arcsec (Fig. 4.5, bottom left panel). We finally recovered a fourth estimate of the bar radius ($R_{Q_{\rm b}} = 11.1$ arcsec) from the location of a peak/plateau in the azimuthally-averaged radial profile of the transverse-to-radial force ratio (Lee et al., 2020) as done in Chapter 2 (Fig. 4.5, bottom right panel).

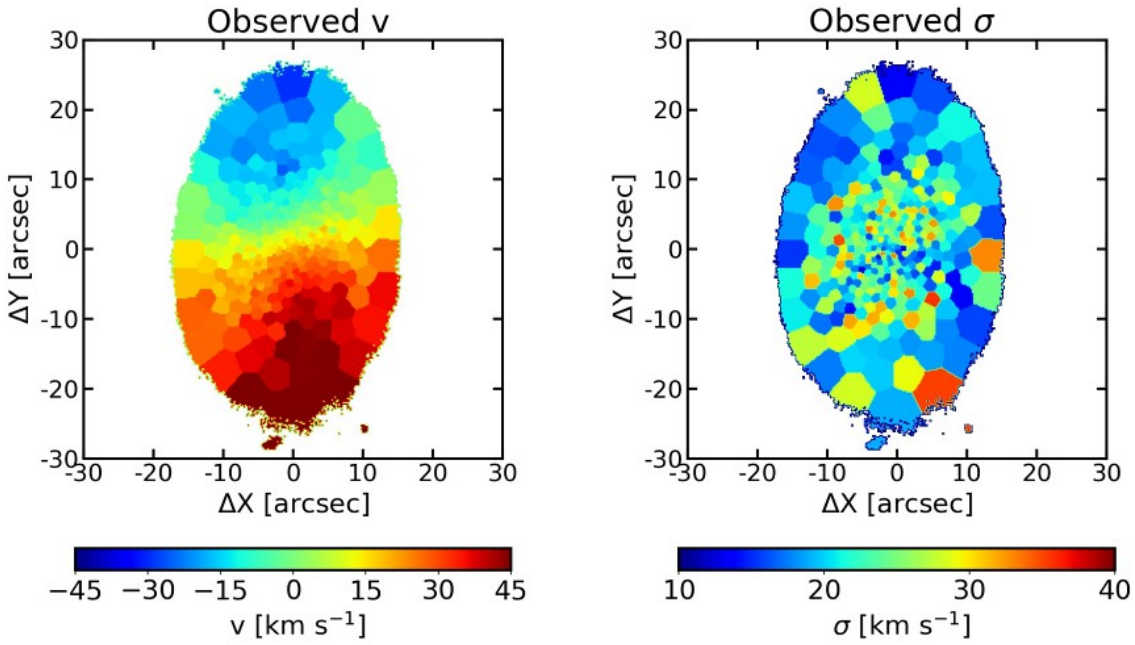

Figure 4.4: Mean stellar LOS velocity map (*left panel*) and velocity dispersion map (*right panel*) of IC 3167. The FOV is 1×1 arcmin^2 and the disc major axis is parallel to the vertical axis.

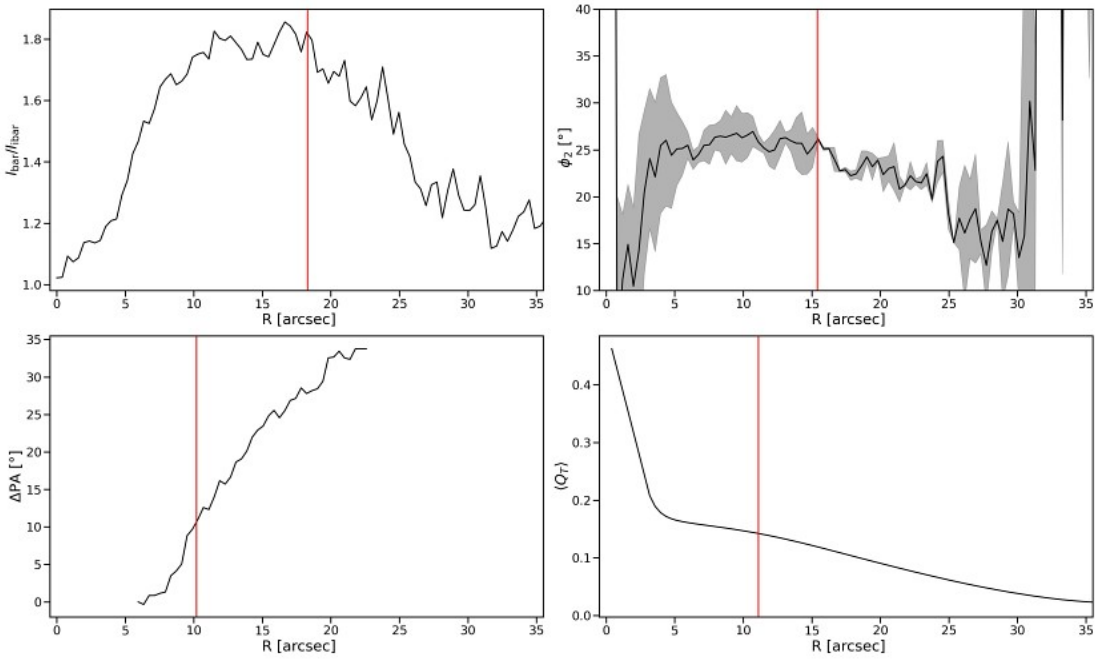

Figure 4.5: Bar radius estimates from the i-band image of IC 3167. Radial profiles of the bar/interbar intensity ratio (*top left panel*), phase angle ϕ_2 (*top right panel*), the difference between PA of the isophotes in the region of the ϵ peak and of the bar (*bottom left panel*), and transverse-to-radial force ratio (*bottom right panel*). In each panel, the vertical red line marks the corresponding $R_{\rm bar}$.

We adopted the mean value of the four measures as the length $R_{\rm bar}$ of the bar and we calculated its $\pm1\sigma$ error as the difference with respect to the highest and lowest measured value. We obtained $R_{\rm bar} = 13.1^{+5.2}_{-2.8}$ arcsec, which corresponds to $R_{\rm bar}= 1.1^{+0.4}_{-0.2}$ kpc at the assumed distance. This value is consistent with the errors with previous results obtained by Janz et al. (2014), which performed a two-dimensional photometric decomposition of the galaxy image ($R_{\rm bar}$=14.5 arcsec).

Bar strength

We measured $S_{\rm bar}$ from the maximum I_2/I_0 ratio between the amplitudes of $m = 2$ and $m = 0$ Fourier components (Athanassoula & Misiriotis 2002) and we obtained $S_{\rm Fourier} = 0.31$, A second estimate of the bar strength was obtained from the transverse-to-radial force ratio map (Lee et al. 2020), and we found $S_{Q_{\rm b}} = 0.23$. We adopt the mean value of the two measures and their semi-difference as strength $S_{\rm bar}$ of the bar and its error, respectively. This gives $S_{\rm bar} = 0.27 \pm 0.04$, which means that the bar of IC 3167 is weak according to the classification by Cuomo et al. (2019b).

Bar pattern speed

We measured $\Omega_{\rm bar}$ applying the TW method to the MUSE combined datacube of IC 3167. We defined 7 adjacent pseudo-slits aligned with the disc PA and crossing the bar (Fig. 4.6, *left panel*). They have a width of 9 pixels (1.8 arcsec, i.e., slightly larger than $\rm FWHM_{seeing}$) to deal with seeing smearing effects and a half-length of 125 pixels (25 arcsec) to reach the disc extension and cover the radial region where the integrals converge to a constant value (Zou et al., 2019). We measured the photometric integrals from the reconstructed image of IC 3167, which we obtained by summing the MUSE combined datacube in the wavelength range $4800 - 5600$ Å, the same wavelength range adopted to derive the stellar kinematics. In each pseudo-slit we derived the radial profile of the total surface brightness and calculated the luminosity-weighted distance $\langle X \rangle$ of the stars from the galaxy minor axis:

$$\langle X \rangle = \frac{\sum_{(x,y)} F(x,y)\, {\rm dist}(x,y)}{\sum_{(x,y)} F(x,y)}.$$

For each pseudo-slit we estimated the errors associated to $\langle X \rangle$ by calculating the root mean square of the distribution of the values measured varying the slit length in the convergence region (Zou et al., 2019). We measured the kinematic integrals from the MUSE combined datacube in the wavelength range $4800 - 5600$ Å. In each pseudo-slit, we collapsed all the spaxels into a single spectrum and derived the luminosity-weighted LOS velocity $\langle V \rangle$ of the stars. We estimated the errors on $\langle V \rangle$ running Monte Carlo simulations on a set of mock spectra.

The photometric and kinematic integrals disposed along a straight line whose slope depends on the galaxy inclination i and $\Omega_{\rm bar}$:

$$\langle V \rangle = \langle X \rangle\, \Omega_{\rm bar} \sin(i).$$

We derived $\Omega_{\rm bar} \sin i = 2.01 \pm 0.38$ km s^{-1} arcsec^{-1} by fitting with a straight line to the $\langle X \rangle$ and $\langle V \rangle$ values and their errors using the FITEXY algorithm (Fig. 4.6, right panel). This corresponds to $\Omega_{\rm bar} = 2.47 \pm 0.45$ km s^{-1} arcsec^{-1}, which is 30.0 ± 5.4 km s^{-1} kpc^{-1}.

The bar in IC 3167 is offset southward by 0.7 arcsec with respect to the disc centre. We took the advantage of the N-body simulations discussed in Chapter 6 to perform some tests to verify that the TW-based bar pattern speeds do not change within errors for the values of offcentring and lopsidedness measured for IC 3167 (see Section 6.4).

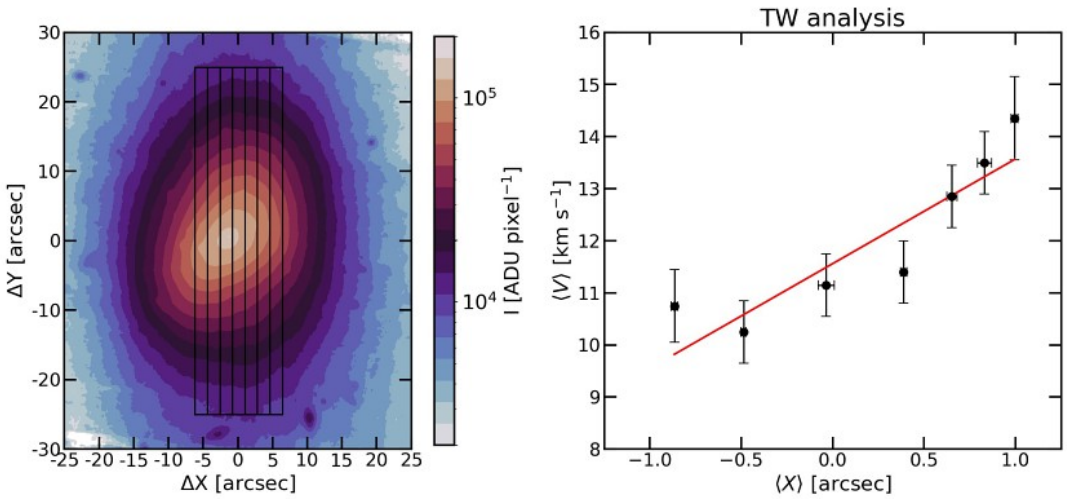

Figure 4.6: MUSE data of IC 3167. *Left panel*: MUSE reconstructed image with pseudo-slits (black lines). The FOV is 50×60 arcsec^2 and the disc major axis is parallel to the vertical axis. *Right panel*: kinematic integrals $\langle V \rangle$ as a function of photometric integrals $\langle X \rangle$. The red solid line represents the best-fitting line to the data.

We derived $R_{\rm cor}$ from the asymmetric-drift corrected $V_{\rm circ}$ of stars $V_{\rm circ}$ and the bar pattern speed, and we obtained $R_{\rm cor}$=$V_{\rm circ}/\Omega_{\rm bar}$=21.8 ± 5.5 arcsec, that corresponds to $R_{\rm cor}$=1.8 ± 0.5 kpc at the assumed distance.

We finally obtained $\mathcal{R}$=$R_{\rm cor}/R_{\rm bar}$=$\mathcal{R}$ = $1.7^{+0.5}_{-0.3}$ with the $\pm 1\sigma$ error estimated from a Monte Carlo simulation to account for the errors on i, $R_{\rm bar}$, $V_{\rm circ}$, and $\Omega_{\rm bar}$. The resulting value of $\mathcal{R}$ lies just above the limit for a bar to be fast. The lopsided bar of IC 3167 is more than twice more likely to be slow (probability of 68%) rather than fast (32%), after excluding the ultrafast regime (2%).

4.5 Conclusions

We present a photometric and kinematic analysis of the lopsided stellar bar hosted in the dwarf lenticular galaxy IC 3167 located behind the Virgo cluster. The galaxy shows an elongated off-centred stellar structure with an uncommon triangular shape embedded in the galaxy disc (see Figs. 4.1 and 4.6).

We confirmed that this peculiar structure is a genuine bar by means of archival i-band SDSS imaging and customised MUSE integral-field spectroscopy. The photometric analysis shows a distinctive bar feature. In particular, the ellipticity and position angle radial profiles obtained from the isophotal analysis present typical behaviours for a barred galaxy: a clear-cut peak and constant behaviour within the bar region, respectively. The triangular shape of the bar leads to the large values of the third sine Fourier coefficient of the isophotal analysis and $m = 3, 5$ components of the Fourier analysis. The Fourier analysis of the deprojected galaxy image highlights strong even components, especially the $m = 2$ component has a strong peak in the bar region. The analysis of the transverse-to-radial force ratio map shows four thick slabs from the corners of the bar, this signature points out the presence of a bar structure (see Chapter 2 for details). Together with a plateau in the radial profile of the azimuthally-averaged force ratio $\langle Q_{\rm T} \rangle$, which typical in the early stage of bar evolution (Lee et al., 2020).

The application of the TW method to the spectroscopic data gave the pattern speed of the bar. It is tumbling as a rigid body with a rotation rate $\mathcal{R} = 1.7^{+0.5}_{-0.3}$ consistent with the slow bar regime. Off-centred bars are common in low-luminosity Magellanic-type galaxies (Odewahn, 1994; Kruk et al., 2017), while lopsided bars are more rare: the LMC hosts the first convincing example of an asymmetric stellar bar (van der Marel, 2001) being as well slightly off-centred with respect to the disc (Jacyszyn-Dobrzeniecka et al., 2016). Another recently found example is the dwarf irregular galaxy DDO 168, which hosts a lopsided gaseous bar (Patra & Jog, 2019).

Bars are typically bisymmetric and elongated structures supported by stars moving in symmetric and elongated periodic orbits belonging to the so-called x_1 family and to the vertically-extended families bifurcating from it (Skokos et al., 2002). Nevertheless, stable regular and stochastic orbits with asymmetric morphologies can also be present (Athanassoula, 1992; Voglis et al., 2007). They could be the backbone of the orbital structure of lopsided bars although it is not yet clear which internal or external process activates this kind of orbits.

Both off-centred and asymmetric bars have been observed in simulated galaxies as the end result of different formation and evolution scenarios. An off-centred bar, one-arm spiral and one-sided star formation can be induced by a short tidal interaction (Yozin & Bekki, 2014). These asymmetries can widely vary in amplitude and can be both short-lived or more persistent, especially in low-mass galaxies. They can occur at the bar formation or later in its evolution. Recently, the presence of lopsided bars has been reported in the Illustris TNG100 simulation (Łokas, 2021b). These asymmetric bars are found in a small fraction ($\sim 5\%$) of barred-like galaxies, where the bulk of the stars typically forms an elongated structure with a little amount of gas (Łokas, 2021a).

Łokas (2021b) investigated two scenarios leading to the formation of a lopsided bar using numerical simulations of galaxy evolution in the cosmological context. First, they considered the interaction between a Milky Way-like barred galaxy and a massive satellite, which is moving onto a radial orbit in the disc plane and perpendicular to the bar at the time of the first flyby. In addition, they analysed the secular evolution of a disc galaxy off-centred with respect to its DM halo. The bars formed in such simulations show some degree of displacement and asymmetry, as it results from their isophotal and Fourier analysis. When the lopsidedness is driven by interaction, the forming bar survives and it becomes stronger and lopsided, because of the asymmetry in the effects of the satellite flybies on the two bar sides. In this case, the $m = 3, 5$ Fourier components present large values within the bar region, while the $m = 1$ component gradually increases in the disc. On the contrary, a lopsided bar formed in an off-centred disc is characterised by smaller values of the $m = 3, 5$ Fourier components. The $m = 1$ component is initially strong for the disc, but then it decreases during the bar formation. The photometric properties of the bar of IC 3167 are consistent with a formation scenario driven by interaction. Indeed, we measured large odd Fourier components within the bar region and a significant increase of the $m = 1$ component in the disc region.

IC 3167 is member of a small group of early-type dwarf galaxies in the initial phase of accretion onto the Virgo Cluster (Lisker et al., 2018). Bidaran et al. (2020) measured the stellar kinematics to derive the specific angular momentum λ_R of IC 3167 to explore the role of the environment in transforming late-type star-forming galaxies into quiescent spheroids. IC 3167 has a steep λ_R radial profile and is a fast-rotating galaxy, which means that both the Virgo environment and processing mechanisms occurred in the host halo before the infall started ~ 2 Gyr ago have been marginal so far. Nevertheless, this does not exclude that the formation of the bar could be triggered by flybies with other galaxies. Fast interactions are indeed predicted to not strongly affect the kinematic properties of the galaxy, except for a small increase of the velocity dispersion in the outer part of the disc. Moreover, bars induced by fast interactions are born slow and stay slow during their evolution.

Finally, they are weaker than bars formed by internal disc instabilities (Martinez-Valpuesta et al., 2016; Łokas, 2018).

Again, our observational findings of a weak and slowly-rotating bar in IC 3167 further support a formation induced by an ongoing interaction within the Virgo cluster. Slow bars are also expected to be the result of efficient dynamical friction exerted by the DM halo, a phenomenon which should be particularly efficient when a large amount of DM is present within the central part of the galaxy as expected for dwarf objects like IC 3167 (Debattista & Sellwood, 2000; Sellwood, 2008; Fragkoudi et al., 2021). Despite the presence of a massive and centrally-concentrated DM halo may have efficiently slowed down the rotation of the bar of IC 3167, its peculiar shape and rotation regime are consistent with a formation scenario driven by interaction.

Galaxies hosting a lopsided bar are quite rare and remain a poorly known class of objects. In fact, IC 3167 is only the third galaxy in which the photometric and kinematic properties of its asymmetric and off-centred bar have been studied in detail. Further efforts to characterise more lopsided bars and to measure the stellar populations of the few lopsided bars known so far could help to understand their evolutionary history giving more constraints to galaxy simulations.

Chapter 5

The bar rotation rate as a diagnostic of dark matter content in the centre of disc galaxies[§]

Abstract

We investigate the link between $\mathcal{R}$ and DM content in barred galaxies by concentrating on the cases of the lenticular galaxies NGC 4264 and NGC 4277. These two gas-poor galaxies have similar morphologies, sizes, and luminosities. But, NGC 4264 hosts a fast bar, which extends to nearly the corotation, while the bar embedded in NGC 4277 is slow and falls short of corotation. We derive the fraction of DM $f_{\rm DM,bar}$ within the bar region from Jeans axisymmetric dynamical models by matching the stellar kinematics obtained with the MUSE integral-field spectrograph and using SDSS images to recover the stellar mass distribution. We build mass-follows-light models as well as mass models with a spherical halo of DM, which is not tied to the stars. We find that the inner regions of NGC 4277 host a larger fraction of DM ($f_{\rm DM,bar} = 0.53 \pm 0.02$) with respect to NGC 4264 ($f_{\rm DM,bar} = 0.33 \pm 0.04$) in agreement with the predictions of theoretical works and the findings of numerical simulations, which have found that fast bars live in baryon-dominated discs, whereas slow bars experienced a strong drag from the dynamical friction due to a dense DM halo. This is the first time that the bar rotation rate is coupled to $f_{\rm DM,bar}$ derived from dynamical modelling.

5.1 Introduction

About two-thirds of disc galaxies, including the Milky Way, have a bar which is tumbling at the centre of the disc (Aguerri et al., 2009; Buta et al., 2015). The bar is an efficient agent for redistributing the stars by exchanging angular momentum, energy, and mass among the different galactic components including the DM halo (Athanassoula et al., 2013; Sellwood, 2014).

The two main mechanisms which trigger the formation of a bar are internal gravitational instabilities of the stellar disc (Sellwood, 1981) and external tidal interactions (Noguchi, 1987). Spontaneously-formed bars are usually thin, long, and fast (Athanassoula et al., 2013), whereas tidally-induced bars are thick, short, and slow (Martinez-Valpuesta et al., 2017). The bar properties evolve with time reshaping the morphology, orbital structure, mass distribution, star formation, and stellar population properties of their host galaxies (Laurikainen et al., 2007; Fragkoudi et al., 2016).

[§] *Based on Buttitta, C., Corsini, E. M., Aguerri, J. A. L., et al. 2022, MNRAS, submitted.*

Once born, the bar becomes longer and stronger and it slows down on timescales, which depend on the DM content in the disc region (Debattista & Sellwood, 1998, 2000; Athanassoula & Misiriotis, 2002; Martinez-Valpuesta et al., 2017; Petersen et al., 2019).

In the last decade, the systematic investigation of the pattern speeds of large samples of barred galaxies with integral-field spectroscopy has shown that almost all bars are fast (Aguerri et al., 2015; Guo et al., 2019; Cuomo et al., 2020; Garma-Oehmichen et al., 2020, 2022) confirming the early findings based on long-slit spectroscopy of few selected objects (Corsini, 2011). This supports the idea that the central regions of lenticular and spiral galaxies host maximal (or nearly maximal) stellar discs with a low content of DM.

These observationally-driven findings are in conflict with the predictions of some hydro-dynamical cosmological simulations, for which galaxies are embedded in centrally-concentrated DM haloes required by the ΛCDM paradigm. Algorry et al. (2017) measured the bar properties in the galaxies extracted from the EAGLE simulation (Schaye et al., 2015) and found a reasonable agreement with the bar radii and strengths measured for real galaxies. However, the simulated bars experienced an intense slowdown due to the dynamical friction of the DM halo and many of them ended up slow at $z \sim 0$. Similarly, Roshan et al. (2021) found that the bars in the TNG50 simulation (Pillepich et al., 2018; Nelson et al., 2018) are much slower ($\mathcal{R} > 1.9$) with respect to the observed ones. More recently, the discrepancy between observations and simulations has been attenuated by the findings of Fragkoudi et al. (2021) and Marioni et al. (2022). Fragkoudi et al. (2021) analysed the barred galaxies in the AURIGA simulation suite (Grand et al., 2017) and showed that they have fast bars because they are more baryon-dominated with respect to those in the TNG simulation. Marioni et al. (2022) investigated the evolution of barred galaxies in the CLUES simulation (Yepes et al., 2009), which have shorter, but not slower, bars with respect to their observed counterparts. A possible explanation for these findings could reside in the different ingredients of the simulations so far analysed, including the resolution of the simulation and the gas fraction, disc thickness, stellar and AGN feedback, and baryonic content of the simulated galaxies.

Dynamical models of barred galaxies with accurate measurements of $\Omega_{\rm bar}$ and $\mathcal{R}$ are needed to rigorously test the predictions of numerical simulations regarding the bar properties as a function of gas content, luminosity and DM distribution. In this paper, we derive the mass distribution of two barred galaxies, NGC 4264 and NGC 4277, for which the values of $\Omega_{\rm bar}$ are amongst the best-constrained ones ever obtained with direct measurements (Tremaine & Weinberg, 1984). This will allow us to investigate the link between $\mathcal{R}$ and the DM content in the bar region because NGC 4264 hosts a fast bar ($\mathcal{R} = 0.9 \pm 0.2$, Cuomo et al. 2019a) while the bar in NGC 4277 is slow ($\mathcal{R} = 1.8^{+0.5}_{-0.3}$, Buttitta et al. 2022). We aim at understanding whether a larger value of $\mathcal{R}$ results from the effective bar braking due to the dynamical friction exerted by the DM halo and therefore is a diagnostic of a large content of DM in the bar region.

We organise the chapter as follows. We report the general properties of the two galaxies and their bars in Sec. 5.2. We discuss the choice and application of the dynamical model in Sec. 5.3. We present the our results in Sec. 5.4 and discuss their implications in Sec. 5.5. We adopt as cosmological parameters, $\Omega_{\rm M} = 0.308$, $\Omega_\Lambda = 0.692$, and $H_0 = 75$ km s^{-1} Mpc^{-1} (Fixsen et al., 1996).

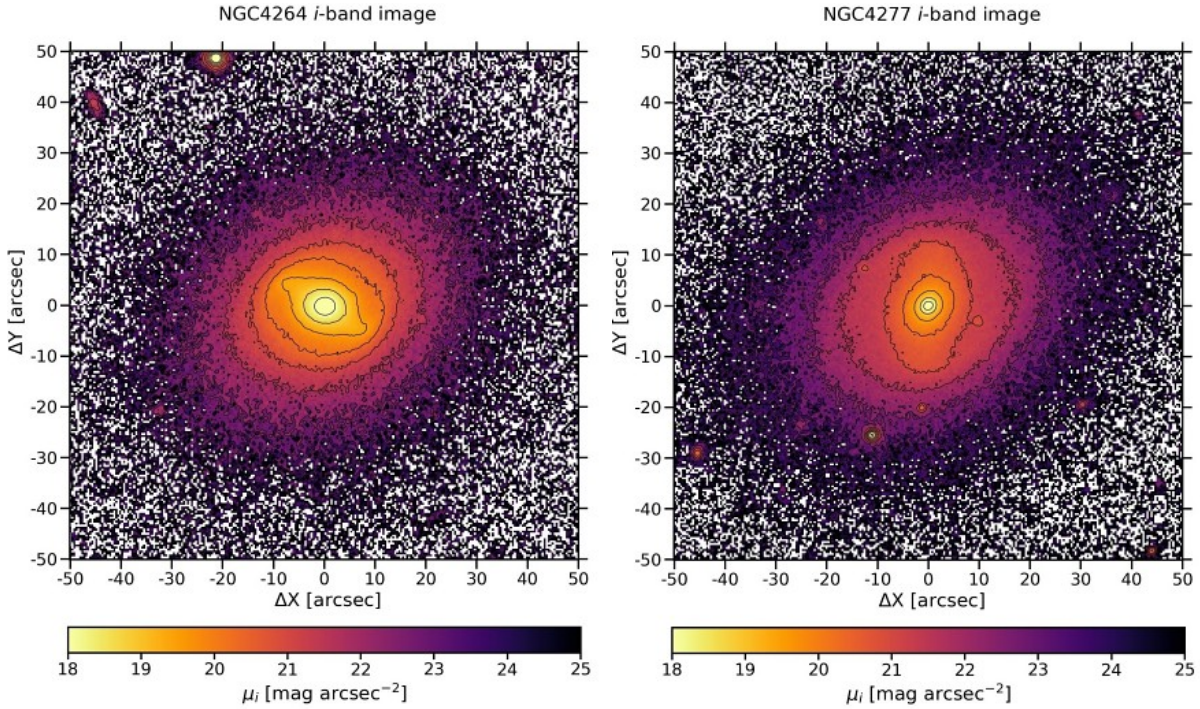

Figure 5.1: SDSS i-band image of NGC 4264 (*left panel*) and NGC 4277 (*right panel*). Some reference isophotes are over-plotted with black lines. The FOV is 1.7×1.7 arcmin^2 and is oriented with north up and east left.

5.2 Main properties of NGC 4264 and NGC 4277

NGC 4264 and NGC 4277 are two early-type disc galaxies classified as SB0$^+$(rs) and SAB(rs)0/a respectively by de Vaucouleurs et al. (1991, hereafter RC3). They have a quite similar morphology (Fig. 5.1) with a well-defined bar surrounded by a pseudo-ring and oriented at an intermediate position angle with respect to the major and minor axes of the disc ($|\mathrm{PA_{bar}} - \mathrm{PA_{disc}| \sim 50^\circ}$). The bar region appears to be mostly free of dust and star formation and the disc has an intermediate inclination ($i_{\mathrm{disc}} \sim 40^\circ$). NGC 4264 and NGC 4277 have similar luminosity and size, as calculated from the apparent corrected magnitude B^0_{T} (RC3) and galaxy diameters D_{25} and d_{25} (RC3) by adopting the distance obtained from the radial velocity with respect to the cosmic microwave background reference frame (Fixsen et al., 1996). NGC 4264 and NGC 4277 are located behind the Virgo cluster. They likely form an interacting couple with the giant elliptical galaxy NGC 4261 (Schmitt, 2001) and with the spiral galaxy NGC 4273 (Kim et al., 2014), respectively. The main properties of both galaxies are given in Table 5.1.

Cuomo et al. (2019a) and Buttitta et al. (2022) analysed the surface photometry and integral-field spectroscopy of NGC 4264 and NGC 4277, respectively, to characterise the properties of their bars. They measured R_{bar} and S_{bar} from the surface photometry obtained from broad-band imaging of the SDSS. They derived the Ω_{bar} from the stellar kinematics obtained from integral-field spectroscopy performed with the MUSE at the VLT. They also estimated R_{cor} from V_{circ} which they constrained by correcting the stellar streaming motions for asymmetric drift. Finally, they derived $\mathcal{R}$. Here, we provide a concise description of the acquisition and analysis of the photometric and kinematic data and a summary of the results. The properties of bars of both galaxies are given in Table 5.1.

Table 5.1: Main and bar properties of NGC 4264 and NGC 4277.

	Property		NGC 4264	NGC 4277
(1)	Morph. Type		$SB0^+$(rs)	SAB(rs)0/a
(2)	$M^0_{B_T}$	[mag]	-19.20	-19.27
(3)	D	[Mpc]	38.0 ± 2.7	33.8 ± 2.4
(4)	$D_{25} \times d_{25}$	[kpc]	10.8×8.8	10.3×8.6
(5)	$\mathrm{PA_{disc}}$	[°]	114.0 ± 1.2	123.3 ± 0.3
(6)	i	[°]	36.7 ± 0.7	40.7 ± 0.7
(7)	$\mathrm{PA_{bar}}$	[°]	56.4 ± 0.1	175.59 ± 0.04
(8)	R_{bar}	[kpc]	3.2 ± 0.5	$3.2^{+0.9}_{-0.6}$
(9)	S_{bar}		0.31 ± 0.04	0.21 ± 0.02
(10)	V_{circ}	[km s^{-1}]	189 ± 10	148 ± 5
(11)	Ω_{bar}	[km s^{-1} kpc^{-1}]	71 ± 4	25 ± 3
(12)	R_{cor}	[kpc]	2.8 ± 0.2	6.0 ± 0.9
(13)	$\mathcal{R}$		0.9 ± 0.2	$1.8^{+0.5}_{-0.3}$

Notes: (1) Morphological type from RC3. (2) Total absolute magnitude from B^0_T in RC3. (3) Distance calculated from the radial velocity with respect to the cosmic microwave background reference frame (Fixsen et al., 1996) (4) Major and minor diameters of the isophote with surface brightness $\mu_B = 25$ mag arcsec^{-2} from RC3. (5) Disc position angle from the isophotal analysis. (6) Disc inclination from the isophotal analysis assuming an infinitesimally thin disc. (7) Bar position angle from the photometric decomposition. (8) Bar radius. (9) Bar strength. (10) Circular velocity from the stellar streaming motion corrected for asymmetric drift. (11) Bar pattern speed. (12) Corotation radius. (13) Bar rotation rate.

Bar radius and strength

Cuomo et al. (2019a) and Buttitta et al. (2022) analysed the flux-calibrated i-band images of both galaxies available in the science archive of the SDSS Data Release 14 (Abolfathi et al., 2018). They were obtained with a spatial sampling of 0.3961 arcsec pixel^{-1}, total exposure time of 53.9 s, and seeing FWHM $\sim$ 1.5 arcsec. The images were sky subtracted and trimmed selecting a FOV of 800×800 pixel^2 centred on the galaxies corresponding to 5.3×5.3 arcmin^2.

The isophotal analysis recovered the geometric parameters $\mathrm{PA_{disc}}$ and i_{disc} of the galaxy disc, which were adopted to deproject the galaxy image. The photometric decomposition was performed to estimate the position angle, $\mathrm{PA_{bar}}$, of the bar and its contribution to the galaxy surface brightness.

For both galaxies, the radius R_{bar} of the bar was derived as the mean of the estimates obtained from the analysis of the radial profile of the position angle of the interpolated isophotes on the deprojected image as in Aguerri et al. (2003), of the intensity contrast between the bar and interbar regions following Aguerri et al. (2000), and of the photometric decomposition adopting a Ferrers bar as in Méndez-Abreu et al. (2017). The strength S_{bar} of the bar was derived as the mean of the values obtained from the Fourier analysis of the deprojected image as in Athanassoula & Misiriotis (2002) and from the bar axial ratio as in Aguerri et al. (2009). The $\pm\sigma$ errors on R_{bar} and S_{bar} were estimated by calculating the difference between the adopted value and the highest/lowest measure. The two bars have lengths consistent with the median value found for SB0 galaxies (Aguerri et al., 2009) and are both weak according to the classification of Cuomo et al. (2019b).

Bar pattern speed and rotation rate

The integral-field spectroscopy was carried out with the wide field mode of MUSE (Prog. Id. 094.B-0241(A); P.I.: E.M. Corsini) mapping a nominal FOV of 1×1 arcmin^2 with a spatial sampling of 0.2 arcsec pixel^{-1} and covering the wavelength range of $4800 - 9300$ Å with a spectral sampling of 1.25 Å pixel^{-1} and a nominal spectral resolution of FWHM = 2.51 Å. The mean value of the seeing during the observations was FWHM $\sim$ 1.1 arcsec. The observations were split into different observing blocks which were mosaiced to fully map the galaxies along their photometric major axis for an actual FOV coverage of 1.0×1.7 arcmin^2.

Cuomo et al. (2019a) and Buttitta et al. (2022) measured the stellar and ionised-gas kinematics of the two galaxies by using the PPXF (Cappellari & Emsellem, 2004) and GANDALF (Sarzi et al., 2006) codes. The spaxels in the datacube were spatially binned with the Voronoi tessellation algorithm (Cappellari & Copin, 2003) to ensure a target $S/N = 40$ per bin. In each bin, the galaxy spectrum was fitted convolving the spectra extracted from the ELODIE stellar library ($\sigma_{\rm instr}$ = 13 km s^{-1}, Prugniel & Soubiran 2001) with a LOSVD modelled with a truncated Gauss-Hermite series (van der Marel & Franx, 1993b; Gerhard, 1993) in the wavelength range $4800 - 5600$ Å. The circular velocity $V_{\rm circ}$ was derived by correcting the stellar streaming motion for asymmetric drift (Binney & Tremaine, 2008).

The pattern speed $\Omega_{\rm bar}$ of both bars was obtained by applying the Tremaine-Weinberg method (Tremaine & Weinberg, 1984) on the reconstructed image and stellar velocity field of the host galaxies. The value of $\Omega_{\rm bar}$ is given by $\langle V \rangle = \langle X \rangle \sin(i_{\rm disc}) \Omega_{\rm bar}$. It depends on the disc inclination and on the luminosity-weighted position $\langle X \rangle$ and LOS velocity $\langle V \rangle$ of the stellar component within apertures parallel to the disc major axis and crossing the bar. Finally, the corotation radius $R_{\rm cor}$ and the rotation rate $\mathcal{R}$ values were estimated calculating $R_{\rm cor}$=$V_{\rm circ}/\Omega_{\rm bar}$ and $\mathcal{R} = R_{\rm cor}/a_{\rm bar}$, respectively. The errors on $R_{\rm cor}$ and $\mathcal{R}$ were estimated by using Monte Carlo simulations. We generated a distribution of $R_{\rm cor}$ and $\mathcal{R}$ by accounting for the errors on $R_{\rm bar}$, $i_{\rm disc}$, and $V_{\rm circ}$. The adopted $\pm\sigma$ errors for $R_{\rm cor}$ and $\mathcal{R}$ are calculated as the 16th and 84th percentiles of the distributions.

The two galaxies have similar properties in terms of $R_{\rm bar}$ and $S_{\rm bar}$, but not in terms of $\Omega_{\rm bar}$: NGC 4264 hosts a fast bar ($\mathcal{R} = 0.9 \pm 0.2$) while the bar in NGC 4277 is slow ($\mathcal{R} = 1.8^{+0.5}_{-0.3}$). The different bar rotation rates could be due to a different bar formation mechanism and/or a different DM content in the bar region. Although NGC 4264 possibly forms an interacting pair with NGC 4261, which is located at a projected distance of 3.5 arcmin (Schmitt, 2001), which corresponds to a quite large physical distance of 4.9 Mpc, it lacks a strong disturbed morphology. According to Cuomo et al. (2019a), this suggests that the interaction is weak and not responsible for have triggered the bar formation in NGC 4264. NGC 4277 is likely paired with NGC 4273, which is located at a projected distance of 1.9 arcmin (van Driel et al., 2000) corresponding to a physical distance of 2.5 Mpc. Buttitta et al. (2022) argued that the bar formation in NGC 4277 could have be triggered by their tidal interaction or alternatively, the bar could have been braked by the dynamical friction of a dense DM halo (Debattista et al., 2006; Athanassoula et al., 2013).

5.3 Stellar dynamical model

Jeans dynamical model

Reconstructing the mass distribution of a disc galaxy using unresolved stars as tracers of the gravitational potential is a challenging task due to the non-uniqueness of the light deprojection (Rybicki, 1987; Gerhard & Binney, 1996).

The bar introduces a further complication since its characterisation requires two additional parameters: the orientation and figure rotation (Lablanche et al., 2012). This increases the degeneracy between the model parameters with different combinations able to reproduce the observed photometric and kinematic properties of the galaxy. Several methods have been developed to recover the dynamical structure of a galaxy from broad-band imaging and long-slit/integral-field spectroscopy, but the dynamical modelling of barred galaxies is still at an early stage. The recently developed orbit-superposition Schwarzschild models by Vasiliev & Valluri (2020) and Tahmasebzadeh et al. (2022), which to date have been applied only to data from N-body simulations, considered the bar pattern speed. Portail et al. (2016) built a dynamical model of the Milky Way to recover its bar pattern speed by using the made-to-measure method as implemented by de Lorenzi et al. (2007).

In general, barred galaxies have been modelled with axisymmetric dynamical models, including the Jeans Anisotropic Modelling (JAM, Cappellari, 2008, 2020), which has been extensively applied to spectroscopic surveys of nearby lenticular and spiral galaxies (e.g., Williams et al., 2009; Cappellari et al., 2013; Guo et al., 2019). It models the LOS second velocity moment for galaxies with an axisymmetric mass distribution, including a DM halo, to be compared with the root-mean-square velocity $V_{\rm rms}$ derived from the observed velocity $V_{\rm los}$ and velocity dispersion $\sigma_{\rm los}$. JAM requires the surface-brightness distribution of the galaxy to be described through a Multi-Gaussian Expansion (MGE, Cappellari, 2002) parameterisation, which simplifies the solution of Jeans equations to recover the galaxy inclination i, mass-to-light ratio $(M/L)_*$ of the matter following the light (which may include DM as well as stars), and anisotropy parameter $\beta_z = 1 - \sigma_z^2/\sigma_R^2$, where σ_R and σ_z are the radial and vertical components of the velocity dispersion, respectively, in a cylindrical coordinate system with the origin in the centre of the galaxy and symmetry axis aligned with its rotation axis.

Cappellari (2008) compared the JAM and orbit-superposition Schwarzschild models of six fast-rotating lenticular galaxies from the SAURON survey (de Zeeuw et al., 2002). They have HST and ground-based photometry and SAURON integral-field spectroscopy. The values of β_z from JAM are consistent within the uncertainties with those obtained with the Schwarzschild modelling. Since fast rotators show a slightly positive value of β_z, the inclination-anisotropy degeneracy was removed, constraining $\beta_z > 0$. Although there is a small dependence on the anisotropy parameter, overall the $(M/L)_*$ values and mass models obtained with the two approaches are also in agreement. This means that the JAM model, with simple and well-motivated assumptions, provides a reasonable description of the mass distribution of lenticular galaxies.

Cappellari et al. (2013) applied the JAM algorithm to 260 nearby early-type galaxies of the ATLAS$^{\rm 3D}$ survey (Cappellari et al., 2011), whose surface-brightness distribution was measured from SDSS and Isaac Newton Telescope imaging and the stellar kinematics were traced out to roughly one effective radius $R_{\rm e}$ with SAURON integral-field spectroscopy. This volume-limited sample was composed of galaxies with a distance $D < 42\,$Mpc, absolute magnitude $M_K < -21.5\,$mag, and stellar mass $M_* \gtrsim 6 \times 10^9\,{\rm M}_\odot$. The stellar kinematics of most of the sample galaxies are reasonably well reproduced by mass-follows-light models, suggesting that early-type galaxies have a simple internal structure within $1R_{\rm e}$, and that the DM halo is not dominant. By adding the contribution of a NFW (Navarro et al., 1995) DM halo, Cappellari et al. (2013) estimated a median DM fraction within the effective radius of $f_{\rm DM}(r < R_{\rm e}) = 0.13$. About one-third of the sample galaxies host a bar and for some of them, the quality of the fit was poor due to the low S/N and/or twisted stellar kinematics or the presence of a strong bar. The recovered values of $(M/L)_*$ for the whole sample have an accuracy of 6 per cent, which raises to 15 per cent for the barred galaxies.

Lablanche et al. (2012) analysed realistic simulations of two lenticular barred galaxies to explore the reliability of the JAM approach in recovering the dynamical parameters of a barred galaxy. The simulated galaxies mimicked NGC 4442 and NGC 4754 and were projected at different disc

inclinations ($i_{\rm disc} = 25^\circ, 45^\circ, 60^\circ$, and 87°) and with different bar orientation ($|{\rm PA_{bar}} - {\rm PA_{disc}}| = 18^\circ, 45^\circ, 60^\circ$, and 87°). In general, $i_{\rm disc}$ can be recovered with JAM although this result is biased by the non-uniqueness of the mass deprojection in nearly face-on or edge-on barred systems (with a maximum error $\Delta i_{\rm disc} \sim 6^\circ$ for edge-on systems). The value of β_z is not well recovered for any disc inclination and bar orientation, because the bar produces a deprojected mass density which is flatter or rounder with respect to the azimuthally averaged one when the bar is viewed side-on or end-on, respectively. This issue is not unique to JAM, but is expected to affect also the axisymmetric dynamical models based on orbit superposition. The recovered M/L depends on the disc inclination and bar orientation. The uncertainty is smaller than 1.5 per cent for systems with $i_{\rm disc} \geqslant 45^\circ$ and $|{\rm PA_{bar}} - {\rm PA_{disc}}| = 60^\circ$ and it never exceeds 3 per cent for the other inclinations. The recovered $(M/L)_*$ is underestimated (overestimated) if ${\rm PA_{disc}} < 45^\circ$ (${\rm PA_{disc}} > 45^\circ$). In their tests, they found that the maximum systematic error of 15 per cent on $(M/L)_*$ occurs when the bar is seen nearly end-on (${\rm PA_{bar}} = 18^\circ$) or side-on (${\rm PA_{bar}} = 87^\circ$). They also investigated how the size of the FOV affects the recovered parameters, and concluded that if the FOV extends out to the bar radius, the systematic uncertainty on $(M/L)_*$ decreases and tends to a limiting value of 10 per cent. However, the mass models of Lablanche et al. (2012) did not include DM haloes.

We adopted the JAM method to recover the mass distribution of NGC 4264 and NGC 4277, since we are confident that applying such an axisymmetric dynamical model gives a reliable estimate of $(M/L)_*$ and DM fraction even in barred galaxies. Both objects are ideal targets according to Lablanche et al. (2012), because they have an intermediate inclination ($i_{\rm disc} \sim 40^\circ$), are not substantially affected by dust, and host a weak bar with an intermediate orientation with respect to the disc major and minor axis ($|{\rm PA_{bar}} - {\rm PA_{disc}}| \sim 50^\circ$). According to Lablanche et al. (2012), in this configuration, we expect to systematically overestimate the $(M/L)_*$ by a factor of 10 per cent. This translates into a larger overestimate of the DM fraction in galaxies with a larger content of luminous matter. In addition, the fine spatial sampling, wide FOV, and high spectral resolution of the MUSE integral-field spectrograph made it possible to accurately map the stellar kinematics throughout the galaxy disc. The kinematic maps do not show strong perturbed features as prescribed to minimise the biases in the estimation of the dynamical parameters. Finally, we notice that NGC 4264 and NGC 4277 have similar luminosities to those of NGC 4442 and NGC 4754. This gives us confidence in extending the findings of Lablanche et al. (2012) to our galaxies.

Multi-Gaussian expansion analysis

To obtain a model for the luminosity volume density of both NGC 4264 and NGC 4277, we started by parameterising the i-band surface brightness of the sky-subtracted image of each galaxy as the sum of a set of Gaussian components by using the MGE Python code, which is based on Cappellari (2002). The MGE method allows for a simple reconstruction of the intrinsic surface brightness distribution provided that the point spread function (PSF) can be approximated as a sum of Gaussian components. The intrinsic surface brightness distribution is then easily deprojected into the luminosity volume density, which is also parameterised as the sum of a set of Gaussian components.

We adopted the centre coordinates derived for the two galaxies by Cuomo et al. (2019a) and Buttitta et al. (2022). We estimated the root mean square of the sky surface brightness by performing a statistical analysis on different regions of the images containing exclusively the sky contribution. These areas were selected in empty regions, which were free of objects and far from the target galaxy to avoid the contamination of the light of field stars and background galaxies, as well as of the galaxy itself. Finally, we modelled the PSF by applying the MGE algorithm on a bright, isolated, and round-shaped field star constraining the best-fitting Gaussians to have a perfect circular shape.

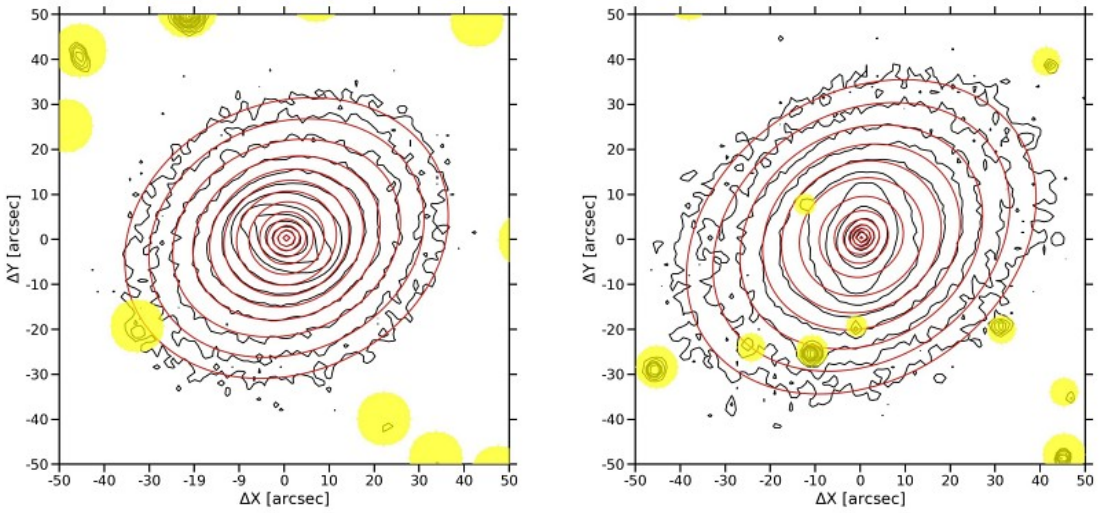

Figure 5.2: Some reference isophotes for the SDSS i-band image (black lines) and MGE model (red lines) of NGC 4264 (*left panel*) and NGC 4277 (*right panel*). The FOV is 1.7×1.7 arcmin^2 and oriented with north up and east left. Flux levels are normalised to the central surface brightness of the image and the contours are spaced by 0.5 mag arcsec^{-2}. While the MGE model was constrained using the original image, the image shown here is binned by 3×3 pixel^2 to reduce the noise for comparison purposes only. The yellow circles correspond to masked regions.

The surface brightness distribution of NGC 4264 is characterised by an isophotal twist in the outermost regions. The internal ($\mathrm{PA_{in}} = 114.^\circ0 \pm 1.^\circ2$) and external ($\mathrm{PA_{out}} = 122.^\circ8 \pm 2.^\circ4$) region of the disc have different orientations but the same shape ($\epsilon = 0.20 \pm 0.02$) as found by Cuomo et al. (2019a). They argued that the isophotal outer twist is not representative of the actual orientation of the disc. We decided to constrain the Gaussians with the geometric parameters of the internal disc which is mapped by the measured stellar kinematics. The radial profiles of PA and ϵ derived by Buttitta et al. (2022) from the surface brightness distribution of NGC 4277 show a clear disc-dominated region with a well-defined orientation ($\mathrm{PA} = 123.^\circ3 \pm 0.^\circ3$) and shape ($\epsilon = 0.24 \pm 0.02$).

We obtained the MGE best-fitting model to the galaxy surface brightness by keeping constant the centre and position angle of the Gaussians derived by Cuomo et al. (2019a) and Buttitta et al. (2022), while further restricting the range of the resulting axial ratios of the Gaussian components to $[q_{\mathrm{min}},\ 1]$ where $q_{\mathrm{min}} = 1 - \epsilon_{\mathrm{disc}}$. This ensured that the permitted galaxy inclinations were not limited to a narrower range than that allowed by the data (e.g., Scott et al., 2013).

We show a few representative isophotes of the i-band images of NGC 4264 and NGC 4277 and compare these to the corresponding MGE best-fitting contours in Fig. 5.2. The MGE algorithm provided the total luminosity in counts, root mean square in pixel, and axial ratio for each best-fitting Gaussian parameterising the intrinsic surface brightness distribution. We converted the output parameters into physical units by using the flux calibration and spatial scale of the images given by Cuomo et al. (2019a) and Buttitta et al. (2022) and correcting for cosmological dimming, K-correction (Chilingarian & Zolotukhin, 2012), and Galactic extinction (Schlafly & Finkbeiner, 2011). We adopted $M_{i,\odot} = 4.53$ mag as the absolute magnitude of the Sun in the SDSS i-band (Willmer, 2018). We list the MGE best-fitting parameters of the intrinsic surface brightness distribution of NGC 4264 and NGC 4277 in Table 5.2.

Table 5.2: Best-fitting parameters of the Gaussian components in the MGE model of the i-band surface brightness distribution of NGC 4264 and NGC 4277.

NGC 4264			NGC 4277		
I_0	σ	q	I_0	σ	q
[$L_\odot$ pc^{-2}]	[kpc]		[$L_\odot$ pc^{-2}]	[kpc]	
(1)	(2)	(3)	(1)	(2)	(3)
15427.0	0.04	0.80	5106.5	0.08	0.88
4309.5	0.13	0.80	1023.8	0.20	0.85
691.4	0.34	0.80	353.5	0.48	0.92
1141.1	0.43	1.00	158.6	1.52	0.91
443.8	1.01	1.00	41.9	3.78	0.76
219.3	1.72	0.80			
64.8	3.86	0.81			

Notes: (1) Central luminosity surface density. (2) Standard deviation. (3) Axial ratio.

Axisymmetric Jeans anisotropic model

With the MGE models at hand, we proceeded to use the JAM Python code based on Cappellari (2008) to build Jeans axisymmetric dynamical models for NGC 4264 and NGC 4277 in order to derive the DM content within the bar region. We selected the best-fitting JAM model by minimising the χ^2 difference between the predicted second moment of the velocity field and MUSE stellar kinematics measured by Cuomo et al. (2019a) and Buttitta et al. (2022). To this aim, we obtained for each spatial bin the observed $V_{\rm rms}$ and its corresponding error:

$$V_{\rm rms} \equiv \sqrt{V_{\rm los}^2 + \sigma_{\rm los}^2} \quad , \quad \epsilon_{V_{\rm rms}} \equiv \frac{1}{V_{\rm rms}} \sqrt{(V_{\rm los}\epsilon_{V_{\rm los}})^2 + (\sigma_{\rm los}\epsilon_{\sigma_{\rm los}})^2}.$$

We discarded the bins with values of $V_{\rm los}$ and $\sigma_{\rm los}$ with relative uncertainties $\epsilon_{V_{\rm los}}/V_{\rm los} > 1$ and $\epsilon_{\sigma_{\rm los}}/\sigma_{\rm los} > 1$. In both galaxies, the maximum uncertainty on $V_{\rm rms}$ never exceeds $\epsilon_{V_{\rm rms}} \sim 8\,{\rm km\ s^{-1}}$. Finally, we symmetrised the resulting values with respect to the disc major axis by means of the Python algorithm PLOTBIN. We show the $V_{\rm rms}$ maps of NGC 4264 and NGC 4277 in the left panels of Fig. 5.3 and 5.5, respectively.

We modelled the total mass distribution of both galaxies as the sum of two components:

$$\rho = \rho_* + \rho_{\rm halo}$$

where ρ_* is the mass volume density of matter (either luminous or dark) that is distributed like the stars and $\rho_{\rm halo}$ is the mass volume density of DM distributed in a spherical halo.

To begin with, we built a set of mass-follows-light models by assuming that the mass volume density ρ_* follows the luminosity volume density $\nu_\star$ derived by deprojecting the intrinsic surface brightness distribution obtained from the MGE fit:

$$\rho_* = (M/L)_* \nu_*$$

These models have three free parameters that are optimised while matching the observed $V_{\rm rms}$. They are i, $(M/L)_*$, and β_z. We adopted radially constant values for both $(M/L)_*$ and β_z.

Then, we included the contribution $\rho_{\rm halo}$ of the DM halo, for which we considered:

1. a quasi-isothermal (QI, Binney & Tremaine, 2008) radial profile of the mass volume density:

$$\rho_{\rm QI}(r) = \frac{\rho_0}{1 + \left(\frac{r}{r_{\rm c}}\right)^2},$$

where ρ_0 and $r_{\rm c}$ are the central mass volume density and core radius, respectively.

2. a NFW radial profile of the mass volume density:

$$\rho_{\rm NFW}(r) = \frac{\rho_{\rm s}}{\frac{r}{r_{\rm s}}\left(1 + \frac{r}{r_{\rm s}}\right)^2},$$

where $\rho_{\rm s}$ and $r_{\rm s}$ are the scale mass volume density and scale radius, respectively. We decided to reduce the number of free parameters by adopting the following parameterization:

$$\rho_{\rm NFW}(r) = \frac{M_{\rm vir}}{4\pi A(c_{\rm vir})} \cdot \frac{1}{r(r_{\rm s} + r)},$$

where the virial mass $M_{\rm vir}$ and coefficient $A_{\rm c_{vir}}$ are respectively given by:

$$M_{\rm vir} = \frac{4\pi}{3} r_{\rm vir}^3 \, \rho_{\rm crit} \Omega_{\rm M} \Delta_{\rm vir} \quad , \quad A(c_{\rm vir}) = \log\left(1 + c_{\rm vir}\right) - \frac{c_{\rm vir}}{1 + c_{\rm vir}},$$

with $\rho_{\rm crit} = 1.37 \cdot 10^{-7}$ $\mathrm{M_\odot\,pc^{-3}}$, $\Omega_{\rm M} = 0.27$ and $\Delta_{\rm vir} = 200$, and $c_{\rm vir} = r_{\rm vir}/r_{\rm s}$ defined as the concentration parameter. We followed the $M_{\rm vir} - c_{\rm vir}$ relation by Klypin et al. (2011) to derive:

$$c_{\rm vir} = 9.6\left(\frac{0.7 M_{\rm vir}}{10^{12}}\right)^{-0.075}.$$

In this way, the mass model has only free parameter $M_{\rm vir}$.

3. a generalised NFW (gNFW, Barnabè et al., 2012) radial profile of the mass volume density:

$$\rho_{\rm gNFW}(r) = \rho_{\rm s}\left(\frac{r}{r_{\rm s}}\right)^{\gamma} \cdot \left(\frac{1}{2} + \frac{1}{2}\frac{r}{r_{\rm s}}\right)^{-(\gamma+3)},$$

where $\rho_{\rm s}$ and $r_{\rm s}$ are the scale mass volume density and scale radius, respectively, while the γ parameter gives the inner slope of the radial profile. We constrained it in the range $-2 < \gamma < 0$, with $\gamma = 0$ corresponding to a cored profile and $\gamma = -1$ to a NFW profile.

For each mass model, we computed the radial profiles of the enclosed mass and circular velocity for the stars, DM in the halo, and their sum. We used Monte Carlo simulations to estimate the 1σ confidence intervals. At each radius, we generated a distribution of enclosed mass and circular velocity taking into account the errors on the best-fitting parameters of the mass model. The adopted $\pm\sigma$ errors of enclosed mass and circular velocity for the stars, DM in the halo, and their sum are calculated as the 16th and 84th percentiles of the distributions.

For the three mass models with a DM halo, we calculated the fraction of DM within the bar region as:

$$f_{\rm DM,bar} = \frac{M_{\rm DM}(r < R_{\rm bar})}{M_{\rm DM}(r < R_{\rm bar}) + M_{\star}(r < R_{\rm bar})}.$$

We calculated the corresponding $\pm\sigma$ errors as the 16th and 84th percentiles of the distribution of $f_{\rm DM,bar}$ that we built from the same Monte Carlo simulations previously generated.

The JAM code allows the inclusion of the contribution of a central supermassive black hole (SMBH), which is modelled through the MGE formalism as a Gaussian having mass $M_{\bullet}$, axial ratio $q = 1$ and $3\sigma \lesssim r_{\rm min}$, with $r_{\rm min}$ defined as the smallest distance from the SMBH that can be chosen $r_{\rm min} \sim \sigma_{\rm PSF}$ (Cappellari, 2008, 2020). Due to the limited spatial resolution of the available ground-based kinematic observations, we can not constrain the mass $M_{\bullet}$ of the central SMBH. Therefore, we decided to adopt the SMBH mass value given by the $M_{\bullet} - \sigma_{\rm e}$ relation (Kormendy, 2013). We estimated the bulge effective velocity dispersion from the MUSE kinematic map and the reconstructed image as the luminosity-weighted average of the observed $V_{\rm rms}$ inside an elliptical region with a semi-major axis equal to half of the bulge effective radius $R_{\rm e,bulge}$ and the same axial ratio $q_{\rm bulge}$ of the bulge. We adopted the values obtained by Cuomo et al. (2019a) and Buttitta et al. (2022) with a parametric photometric decomposition of the SDSS images of NGC 4264 ($R_{\rm eff,bulge} = 1.53$ arcsec, $q_{\rm bulge} = 0.77$) and NGC 4277 ($R_{\rm eff,bulge} = 1.77$ arcsec, $q_{\rm bulge} = 0.84$).

5.4 Results

For both galaxies, we obtained the best-fitting parameters for all the mass models without and with a DM halo. We analysed the mass-follows-light model as well as the models with a QI, NFW, and gNFW DM halo to constrain the DM fraction within the bar region of NGC 4264 and NGC 4277.

NGC 4264

We constructed a starting set of mass models by considering the galaxy inclination as a free parameter. The mass models with a DM halo returned the same value (QI, gNFW) or a value consistent within errors (NFW) with that obtained by Cuomo et al. (2019a) from the isophotal analysis of NGC 4264 ($i = 36.^{\circ}7$), whereas the mass-follows-light model gave a much larger value ($i = 42.^{\circ}9 \pm 1.^{\circ}3$).

We repeated the analysis after masking the kinematic bins within a circular region of radius $r = 8$ arcsec, which corresponds to the bar radius projected onto the sky plane. In this way, we considered only the kinematic data measured in the disc region. But, all the mass models converged to an edge-on solution with $\beta_z \sim -1.45$ as a consequence of the inclination-anisotropy degeneracy (Krajnović et al., 2005; Lablanche et al., 2012). We verified that this result was not driven by the twisted structure of the disc of NGC 4264. The kinematic bins in the external disc ($r > 25$ arcsec) account for less than 1 per cent of the data and the mass models based on a different MGE decomposition of the SDSS image, where we masked the external disc, did not improve the fit. We performed a further sanity check by masking the kinematic bins in the central circular region of radius $r = 2.5$ arcsec to minimise biases due to an uncorrected estimation of the PSF and/or the SMBH mass. Then, we decided to fix the inclination to build the final set of mass models. We adopted $i = 36.^{\circ}5$ which corresponds to the photometric value of Cuomo et al. (2019a). An intrinsic flattening $q_0 = 0.05$ is adopted in JAM modelling to derive i from the observed axial ratio, whereas i is obtained by Cuomo et al. (2019a) assuming an infinitesimally thin disc. The choice of a fixed inclination allowed a straightforward comparison between the best-fitting parameters of the different mass models, which we list in Table 5.3 together with their reduced χ^2.

Model	Parameter		NGC 4264	NGC 4277
mass-follows-light	$(M/L)_{*,i}$	$[\mathrm{M}_\odot\,\mathrm{L}_\odot^{-1}]$	2.55 ± 0.02	2.36 ± 0.05
	i	$[^\circ]$	(36.5)	(40.6)
	β_z		unc.	unc.
	χ^2_ν		5.54	5.81
QI	$(M/L)_{*,i}$	$[\mathrm{M}_\odot\,\mathrm{L}_\odot^{-1}]$	2.18 ± 0.05	1.72 ± 0.02
	$\log_{10}(\rho_0/\mathrm{M}_\odot\,\mathrm{pc}^{-3})$		-0.61 ± 0.13	-1.04 ± 0.04
	r_c	[kpc]	1.33 ± 0.28	2.46 ± 0.24
	i	$[^\circ]$	(36.5)	(40.6)
	β_z		-7.12 ± 1.73	-1.48 ± 0.19
	χ^2_ν		3.99	1.54
	$f_\mathrm{DM,bar}$		0.33 ± 0.04	0.53 ± 0.02
NFW	$(M/L)_{*,i}$	$[\mathrm{M}_\odot\,\mathrm{L}_\odot^{-1}]$	2.14 ± 0.03	1.55 ± 0.03
	$\log_{10}(M_{200}/\mathrm{M}_\odot)$		13.94 ± 0.12	13.33 ± 0.05
	i	$[^\circ]$	(36.5)	(40.6)
	β_z		-7.86 ± 1.99	-1.55 ± 0.20
	χ^2_ν		4.07	1.62
	$f_\mathrm{DM,bar}$		0.35 ± 0.01	0.56 ± 0.01
gNFW	$(M/L)_{*,i}$	$[\mathrm{M}_\odot\,\mathrm{L}_\odot^{-1}]$	2.14 ± 0.05	1.69 ± 0.04
	$\log_{10}(\rho_\mathrm{s}/\mathrm{M}_\odot\,\mathrm{pc}^{-3})$		-1.20 ± 0.15	-2.14 ± 0.36
	r_s	[kpc]	2.25 ± 0.53	11.3 ± 6.6
	γ		(0)	-0.34 ± 0.26
	i	$[^\circ]$	(36.5)	(40.6)
	β_z		-6.86 ± 1.65	-1.49 ± 0.19
	χ^2_ν		3.98	1.55
	$f_\mathrm{DM,bar}$		0.34 ± 0.05	0.53 ± 0.18

Table 5.3: Best-fitting parameters of the mass models of NGC 4264 and NGC 4277. Bracket values refer to fixed parameters, while unconstrained values (having relative errors larger than 1) are labelled.

We found a slightly larger mass-to-light ratio ($(M/L)_{*,i} \sim 2.6\ \mathrm{M}_\odot\,\mathrm{L}_\odot^{-1}$) for the mass-follows-light model with respect to the mass models with a DM halo ($(M/L)_{*,i} \sim 2.1\ \mathrm{M}_\odot\,\mathrm{L}_\odot^{-1}$). This is expected if there is a small amount of DM, which is not distributed like the stars. Since we are interested in recovering the mass distribution of NGC 4264 and not in its orbital structure, we were not concerned by the fact that the mass-follows-light model was not able to constrain β_z and the mass models with the DM halo returned a remarkably negative value of anisotropy ($\beta_z \sim -7.3$).

The observed V_rms is characterised by a central local minimum of $\sim 90\ \mathrm{km\,s^{-1}}$ with a remarkable double-peaked structure with a maximum of $\sim 120\ \mathrm{km\,s^{-1}}$ at $|r| \sim 15$ arcsec along the galaxy major axis followed by a sharp decrease to $\sim 80\ \mathrm{km\,s^{-1}}$ at $|r| \gtrsim 20$ arcsec (Fig. 5.3, left panels). Although the overall shape of the iso-velocity contours is reproduced by the mass-follows-light model, it failed to match the location and amplitude of the double peak of V_rms (Fig. 5.3, left panels). The mass models with a DM halo provided a better fit to the observed V_rms although did not correctly reproduce the decrease measured at large radii along the galaxy major axis (Fig. 5.3, right panels). At face values, the mass model with the QI halo is marginally better than those with the NFW ($\Delta\chi^2_\nu = 0.09$) and gNFW halo ($\Delta\chi^2_\nu = 0.01$).

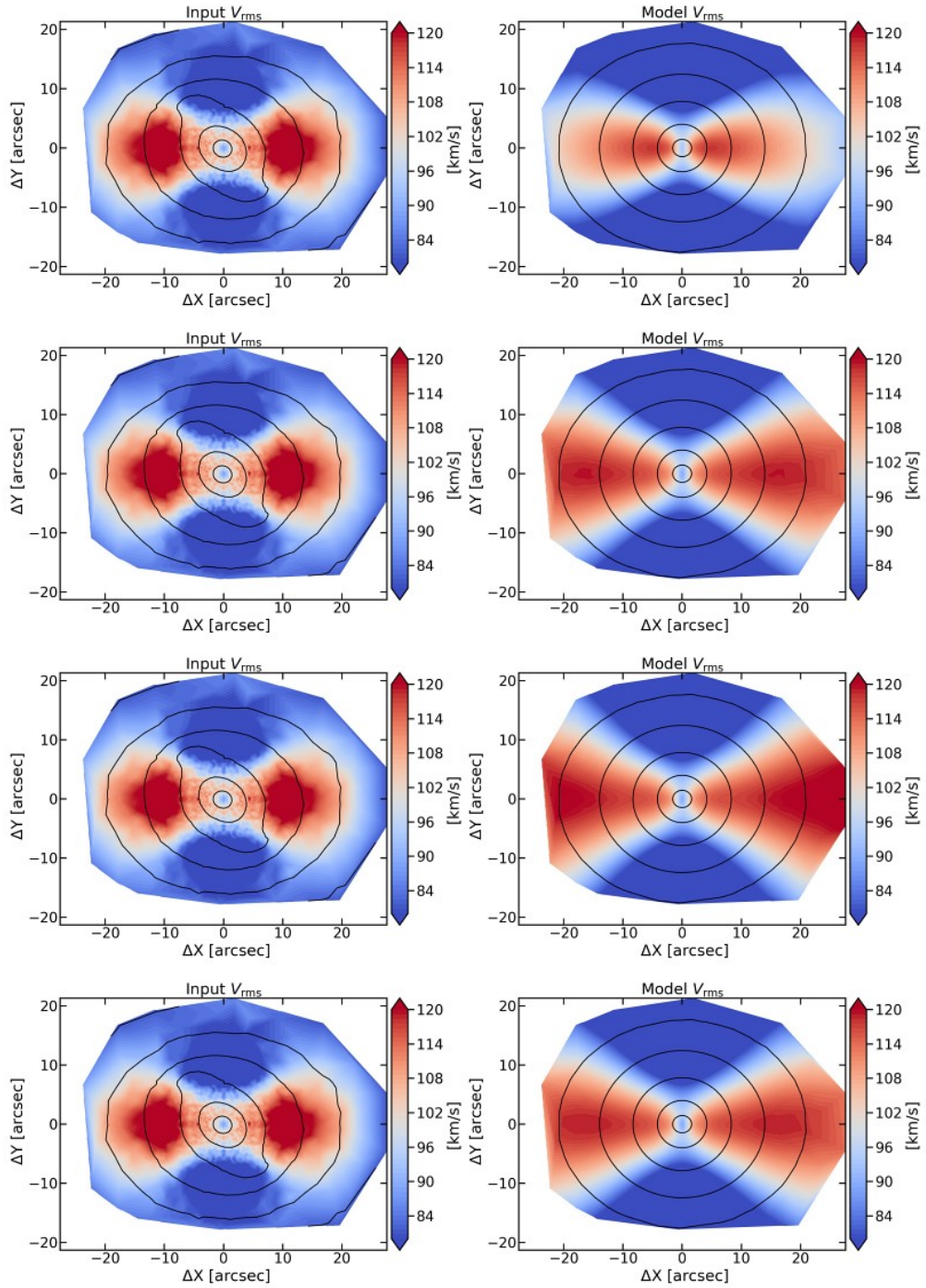

Figure 5.3: Comparison between the symmetrised $V_{\rm rms}$ from the MUSE stellar kinematics of NGC 4264 (*left panels*) and bysimmetric second velocity moment predicted by the mass-follows-light model (*first-row right panel*), by the mass model with a QI halo (*second-row right panel*), with a NFW halo (*third-row right panel*), and with a gNFW halo (*fourth-row right panel*). A few reference isophotes from the SDSS *i*-band image (*left panels*) and MGE model (*right panels*) are also plotted with the galaxy major axis parallel to the horizontal axis.

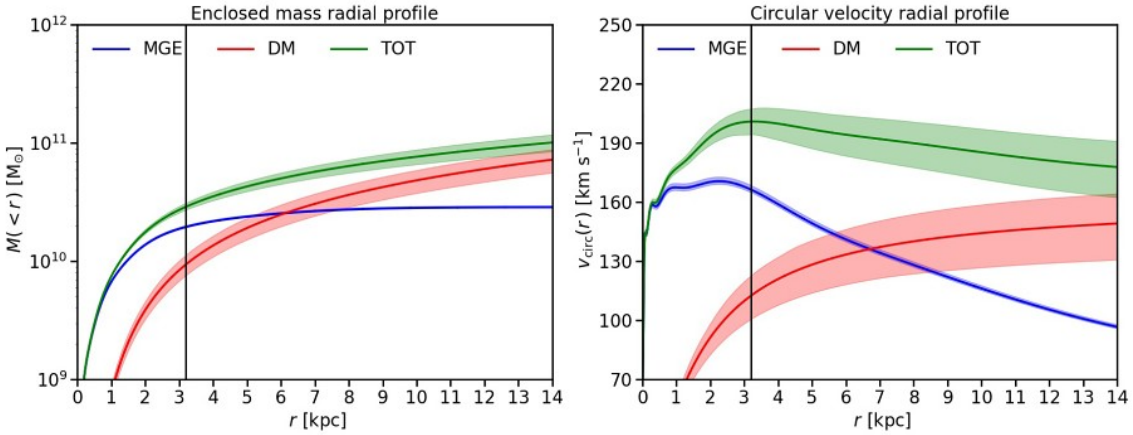

Figure 5.4: Radial profiles of enclosed mass (*left panel*) and circular velocity (*right panel*) of NGC 4264 for the mass model with a QI halo. The contributions of the stars (blue line) and DM (red line) are plotted with their sum (green line). The vertical solid and dashed lines mark the bar radius and the extension of kinematic data, respectively.

The DM fraction within the bar is $f^{\rm QI}_{\rm DM,bar} = 0.33 \pm 0.04$, which is compatible within 1σ errors with that predicted by the mass models with a NFW ($f^{\rm NFW}_{\rm DM,bar} = 0.35 \pm 0.01$) and gNFW halo ($f^{\rm gNFW}_{\rm DM,bar} = 0.34 \pm 0.05$). This suggests that the mass budget of NGC 4264 is a baryon dominated in the radial range mapped by the kinematic data. The corresponding radial profile of the enclosed mass and circular velocity for the stars, DM, and their sum are given in Fig. 5.4 for the best-fitting mass model with the QI halo.

The circular velocity profile in the region between the bar end and the edge of the kinematic data ($3 \geqslant r \geqslant 5\,$kpc) is characterised by a weak decline. This means that, in this radial range, the DM halo does not play a dominant role with respect to the luminous component. This is a local trend which has been commonly observed in galaxies with massive bulges, with more luminous galaxies having on average more strongly declining rotation curves. At large radii, however, all declining rotation curves flatten out, indicating that substantial amounts of DM must be present in these galaxies too (Noordermeer et al., 2007; Kalinova et al., 2017; Frosst et al., 2022).

For the QI model, the contribution of DM starts to dominate the mass budget far beyond the bar region at a galactocentric distance $r > 7$ kpc. As a further check of our dynamical modelling, we derived the mean circular velocity of the inner disc in the radial range ($3.3 \leqslant r \leqslant 4.2\,$kpc) adopted by Cuomo et al. (2019a) to estimate the circular velocity by correcting the stellar streaming motion for asymmetric drift. We found $V^{\rm QI}_{\rm circ} = 200 \pm 7$ km s^{-1} which is consistent within 2σ error with the asymmetric drift estimate $V^{\rm AD}_{\rm circ} = 189 \pm 10$ km s^{-1} by Cuomo et al. (2019a).

We compared our results with those obtained by Cappellari et al. (2013), who modelled using a JAM mass model with a NFW halo. Their NGC 4264 stellar kinematics maps were obtained with the SAURON integral-field spectrograph, covering a smaller FOV (0.55×0.7 arcmin^2) and having a lower angular resolution (FWHM= 1.5 arcsec) with respect to ours. Nevertheless, Cappellari et al. (2013) reported that the DM fraction within the galaxy's effective radius ($R_{\rm e} = 13.4\,$arcsec) is $f_{\rm DM}(r < R_{\rm e}) = 0.31$ with a maximum circular velocity of $V_{\rm circ,max} = 191\,$km s^{-1}. We found a consistent value of $f^{\rm NFW}_{\rm DM}(r < R_{\rm e}) = 0.28 \pm 0.01$, but a larger value of $V^{\rm NFW}_{\rm circ,max} = 260 \pm 4\,$km s^{-1} for the mass model with a NFW halo. The discrepancy between the two values of the circular velocity could reside in the different extension of the adopted data.

NGC 4277

As done for NGC 4264, we constructed a starting set of mass models by considering the galaxy inclination as a free parameter. Considering the intrinsic flattening, the mass models with a DM halo returned a consistent value ($i = 40.^{\circ}6$) with that obtained by Buttitta et al. (2022) from the isophotal analysis of NGC 4277 ($i = 40.^{\circ}7$), whereas the mass-follows-light model gave $i = 46.^{\circ}3 \pm 6.^{\circ}0$. We verified that all the mass models recovered the photometric inclination after masking the kinematic bins belonging to the bar-dominated region ($r < 8$ arcsec). In this way, we relied only on the kinematic bins of the disc. We performed a further check by masking the central kinematic bins ($r < 2.5$ arcsec) to tackle issues related to the wrong PSF and/or the SMBH mass and we found the same model parameters. Finally, we decided to fix the inclination to build the final set of mass models. We adopted the value consistent with the photometric estimate to allow a straightforward comparison between the best-fitting parameters of the different mass models, which are given in Table 5.3 together with the reduced χ^2 of the mass models.

We found a much larger mass-to-light ratio ($(M/L)_{*,i} \sim 2.4$ $\mathrm{M_\odot\,L_\odot^{-1}}$) for the mass-follows-light model with respect to the mass models with a DM halo ($(M/L)_{*,i} \sim 1.7$ $\mathrm{M_\odot\,L_\odot^{-1}}$). This is expected if there is DM in addition to the stars. We were not able to constrain β_z with the mass-follows-light model, whereas all the mass models with a DM halo returned the same negative value within errors for the anisotropy ($\beta_z \sim -1.5$).

We show in Fig. 5.5 the maps of the second velocity moments predicted by the best-fitting mass models of NGC 4277 without and with QI, NFW, and gNFW DM halo to be compared with the map of observed $V_{\rm rms}$. Although more than 60 per cent of the kinematic bins of NGC 4277 are located in the bar-dominated region, where the stars are expected to dominate the galaxy mass (Fig. 5.5, left panels), the predicted second velocity moment of the mass-follows-light model does not match the observed $V_{\rm rms}$ in terms of amplitude ($V_{\rm rms} \sim 80\,\mathrm{km\,s^{-1}}$ for $r \gtrsim 12$ arcsec) and shape of the iso-velocity contours (Fig. 5.5, left panels), contrary to the models with a DM halo. Therefore, we concluded that the best-fitting mass model of NGC 4277 requires a DM halo. As for NGC 4264, the mass model with the QI halo (Fig. 5.5, right panels) is slightly better than those with the NFW ($\Delta\chi^2_\nu = 0.08$) and gNFW halo ($\Delta\chi^2_\nu = 0.01$). The DM fraction within the bar is $f^{\rm QI}_{\rm DM,bar} = 0.53 \pm 0.02$ which is fully consistent with the fractions predicted by the mass models with a NFW ($f^{\rm NFW}_{\rm DM,bar} = 0.56 \pm 0.01$) and gNFW DM halo ($f^{\rm gNFW}_{\rm DM,bar} = 0.53 \pm 0.18$). These findings suggest that NGC 4277 hosts a considerable amount of DM, which is not tied to the stars, within the radial range mapped by the kinematic data. This holds no matter the adopted radial profile of the DM mass volume density.

We argue that the large amount of DM in the inner regions of NGC 4277 is responsible for the slowdown of its bar. The corresponding radial profile of the enclosed mass and circular velocity for the stars, DM, and their sum of the best-fitting mass model with the QI halo are given in Fig. 5.6.

The contribution of the DM starts to dominate the mass budget just outside the bar region ($r > 3$ kpc) and the circular velocity flattens out at a larger galactocentric distance ($r > 5$ kpc) as expected for a DM-dominated region. We derived the mean value $V^{\rm QI}_{\rm circ} = 136 \pm 4$ $\mathrm{km\,s^{-1}}$ of the circular velocity in the same radial range ($2.1 \leqslant r \leqslant 5.9$ kpc) adopted by Buttitta et al. (2022) to estimate the circular velocity by correcting the stellar streaming motion for asymmetric drift. They found $V^{\rm AD}_{\rm circ} = 148 \pm 5$ $\mathrm{km\,s^{-1}}$. The two values are consistent with each other within 2σ errors.

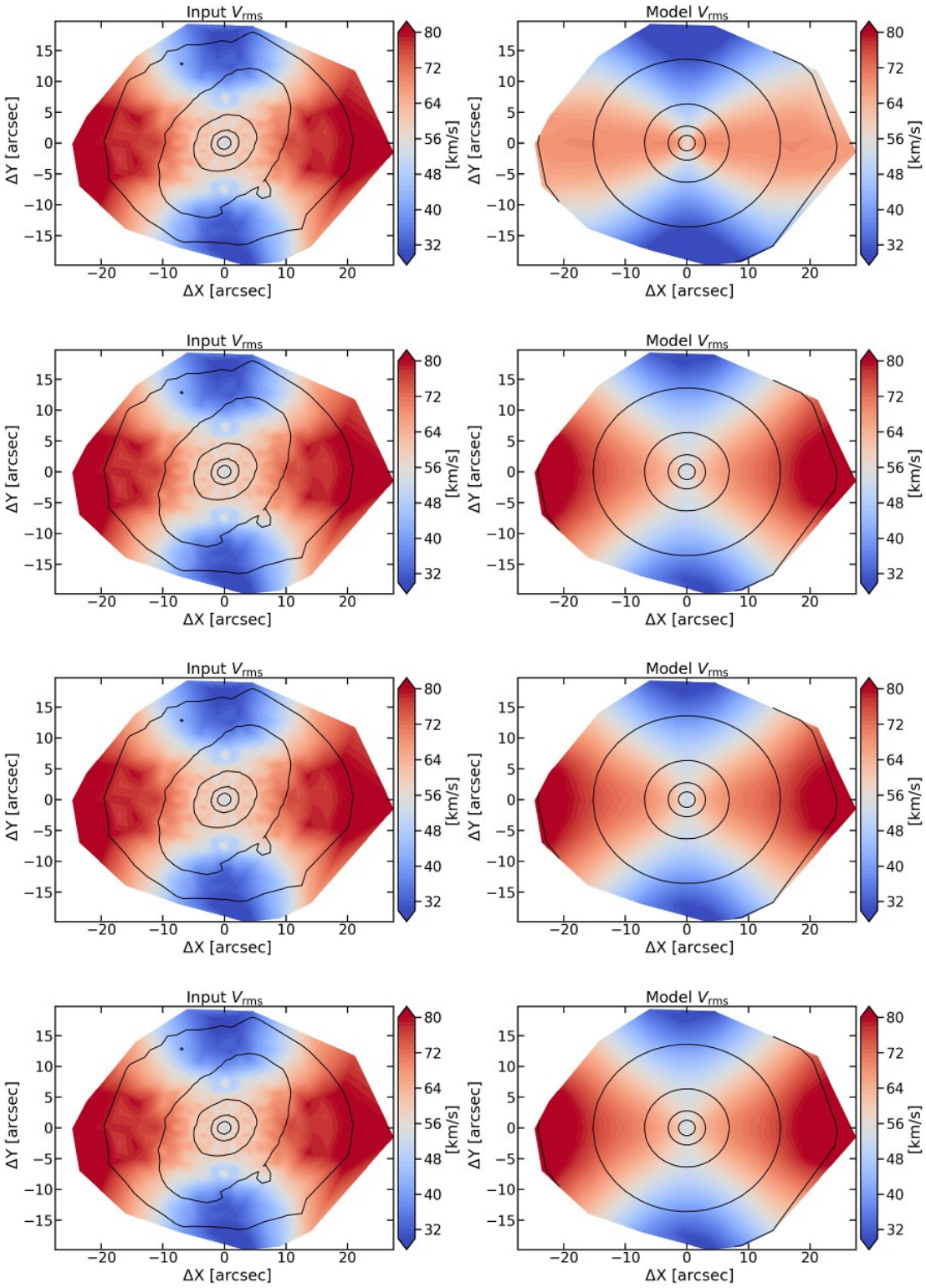

Figure 5.5: Same as in Fig. 5.3, but for NGC 4277.

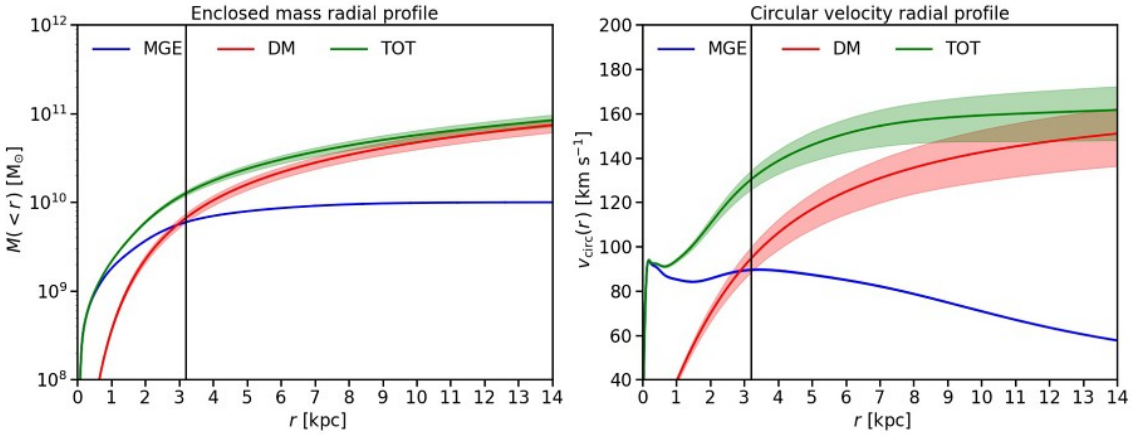

Figure 5.6: Same as in Fig. 5.4, but for NGC 4277.

5.5 Conclusions

We have built Jeans axisymmetric dynamical models for the two barred lenticular galaxies NGC 4264 and NGC 4277. They are very similar in terms of morphology, size, and luminosity. But NGC 4264 hosts a fast bar, which nearly extends out to its corotation ($\mathcal{R} = 0.9 \pm 0.2$, Cuomo et al. 2019a), while the bar embedded in NGC 4277 is slow and falls short of the corotation ($\mathcal{R} = 1.8^{+0.5}_{-0.3}$, Buttitta et al. 2022). We focused on these galaxies because their bar pattern speeds are amongst the best-constrained ones obtained with direct measurements through the Tremaine-Weinberg method (Tremaine & Weinberg, 1984). We considered both mass-follows-light models and mass models with a spherical halo of DM, which is not tied to the stars, by matching the stellar kinematics obtained with the MUSE integral-field spectrograph and using SDSS images to recover the stellar mass distribution.

For both galaxies, the best-fitting mass model has a quasi-isothermal halo for which we derived the fraction of dark matter $f_{\rm DM,bar}$ within the bar region. This is the first time that $\mathcal{R}$ is measured along with $f_{\rm DM,bar}$ obtained from dynamical modelling. We found that the inner regions of NGC 4277 host a larger amount of dark matter ($f_{\rm DM,bar} \sim 0.5$) with respect to NGC 4264 ($f_{\rm DM,bar} \sim 0.3$) in agreement with the predictions of theoretical works and the findings of numerical simulations. Indeed, fast bars are expected to live in baryon-dominated discs, whereas slow bars have experienced a strong drag from the dynamical friction due to a dense halo of dark matter. First, Weinberg (1985) predicted that a DM halo with a significant central mass density exerts a dynamical torque on the bar causing its slowdown. Similar results were later confirmed by several works based on N-body simulations (Debattista & Sellwood, 1998, 2000; Athanassoula & Misiriotis, 2002; Martinez-Valpuesta et al., 2017; Petersen et al., 2019). The bar in a less massive DM halo could require a longer timescale to be slowed down. Tailoring numerical simulations to well-studied galaxies like NGC 4264 and NGC 4277 will make it possible to track the decrease of the bar pattern speed as a function of the DM content and to predict the present value of $\mathcal{R}$ to be compared with observations.

According to the results of numerical simulations, tidally induced bars are typically slower than those spontaneously formed by internal instabilities (Miwa & Noguchi, 1998; Martinez-Valpuesta et al., 2017; Łokas, 2018). Martinez-Valpuesta et al. (2017) found that bars formed after coplanar flybys with massive companions typically have a rotation rate $\mathcal{R} > 1.8$. Similarly, large rotation rates characterise the bars formed in the numerical experiments of Łokas (2018), which explored the

case of retrograde encounters of two galaxies with comparable mass. Buttitta et al. (2022) argued that the formation of the slow bar in NGC 4277 could be induced by the close companion NGC 4273. NGC 4277 does not present strong evidence of tidal interaction with the nearby galaxy, therefore it is not possible to confirm this scenario. However, we can conclude that the large DM fraction in its inner regions influenced the evolution of the bar driving it to an even slower regime. On the other hand, Cuomo et al. (2019a) pointed out that the mild interaction with NGC 4261 favours the spontaneous formation of the fast bar of NGC 4264. We conclude that the low DM fraction in the bar-dominated region was not enough to efficiently slow down the bar to the slow regime.

Following theoretical results (e.g. Athanassoula et al., 2013; Sellwood, 2014) angular momentum is exchanged at resonances, but it is emitted at the inner resonances and absorbed at the outer ones. However, the estimate of the amount of angular momentum exchanged at the resonances would require tracking the temporal evolution of the bar parameters of NGC 4264 and NGC 4277 through tailored N-body simulations. Nevertheless, it is possible to estimate the amount of DM enclosed within the corotation radius. The location of the corotation and bar radius of NGC 4264 are consistent with each other within errors, whereas the corotation radius of NGC 4277 is about twice as large as the bar radius. For NGC 4264, the DM fraction enclosed within the corotation radius ($f_{\rm DM,cor} = 0.29 \pm 0.04$) is the same within errors as that enclosed within the bar radius ($f_{\rm DM,bar} = 0.33 \pm 0.04$). On the contrary, for NGC 4277 the DM fraction enclosed within the corotation radius ($f_{\rm DM,cor} = 0.72 \pm 0.03$) is much larger than that inside the bar radius ($f_{\rm DM,bar} = 0.53 \pm 0.02$) further supporting our conclusions.

A systematic application of the JAM algorithm to simulated barred galaxies with bars of different orientations, lengths, strengths, and pattern speeds is required to extend the parameter space explored by Lablanche et al. (2012). This is needed to understand the uncertainties and biases on the dynamical parameters, including the DM content in the bar-dominated region, for a given galaxy configuration. In particular, the regimes of weakly-barred galaxies and dwarf-barred galaxies, which give a major contribution to the galaxy population, are yet to be explored.

This is a crucial step to extend this dynamical analysis to all the barred galaxies with a measured bar rotation rate from integral-field spectroscopic data, like those targeted by CALIFA (Sánchez et al., 2012; Aguerri et al., 2015; Cuomo et al., 2019b), MANGA (Bundy et al., 2015; Guo et al., 2019; Garma-Oehmichen et al., 2020, 2022), and PHANGS-MUSE (Emsellem et al., 2022; Williams et al., 2021). With a large set of modelled galaxies, it will be possible to look for a quantitative relationship between $\mathcal{R}$ and $f_{\rm DM,bar}$ with the aim of using $\mathcal{R}$ as a diagnostic of the DM content in galaxy disks.

Finally, NGC 4264 and NGC 4277 are amongst the barred galaxies with the best-studied bar properties in terms of surface-brightness distribution, stellar kinematics, and mass modelling. For this reason, they are ideal candidates to be adopted as a test bench in applying the orbit-superposition Schwarzschild dynamical models, which have been recently developed for tumbling bars by Vasiliev & Valluri (2020) and Tahmasebzadeh et al. (2022) but which have been applied to date only to mock galaxies created from N-body simulations.

Chapter 6

Photometric and kinematic comparison of NGC 4277 with N-body simulations[§]

Abstract

We built N-body simulations to mimic the photometric and kinematic properties of the lenticular barred galaxy NGC 4277. Our galaxy models are pure collisionless models comprised of a bulge, a disc, and a DM halo. The models were evolved in isolation, therefore it is not possible to test whether the formation of the slow bar hosted in NGC 4277 was triggered by the tidal interaction with the companion NGC 4273. The galaxy model that best reproduces both the photometry and stellar kinematics of NGC 4277 is characterised by a massive DM halo. Our results agree with the prediction obtained by dynamical modelling, which found a considerable DM fraction in the innermost region of NGC 4277. Thus, we confirmed that the bar hosted in NGC 4277 had experienced a strong drag as a consequence of the interaction with a dense DM halo.

6.1 Introduction

Bars are not rigid and static structures: they form and grow, actively participating in the evolution of the morphological, photometric, and dynamical properties of the host galaxy. Numerical simulations represent a powerful tool to investigate the formation of bars, to track the evolution of bar properties over different time and length scales, and to understand the role of the disc and DM halo (Sellwood, 1981; Athanassoula & Misiriotis, 2002; Athanassoula, 2003; Athanassoula et al., 2013; Martinez-Valpuesta et al., 2006, 2017; Petersen et al., 2019).

The bar lifetime can be roughly divided into three main phases: formation, buckling/thickening phase, and secular evolution. Bars form spontaneously in isolated stellar discs due to an internal instability (Sellwood, 1981; Athanassoula et al., 2013), or can be triggered by the tidal interaction with a companion (Noguchi, 1988; Martinez-Valpuesta et al., 2017). During the initial phase which typically lasts ∼1-2 Gyrs, the bar grows in size and strength and ends up forming a clearly visible non-axisymmetric structure in the galactic disc. During the buckling instability, the bar undergoes a vertical thickening, the bar becomes shorter and thicker and ends up forming a boxy-peanut structure (Raha et al., 1991; Debattista et al., 2005; Martinez-Valpuesta et al., 2006). Subsequently, the bar continues to slowly evolve through secular evolution. The bar strength mildly increases and the bar becomes longer, thinner and slower. This means that the corotation radius shifts toward larger radii and the bar move towards a slower regime ($\mathcal{R} > 1.4$).

[§] *Based on Buttitta, C., Corsini, E. M., Debattista, V. P., et al., in preparation.*

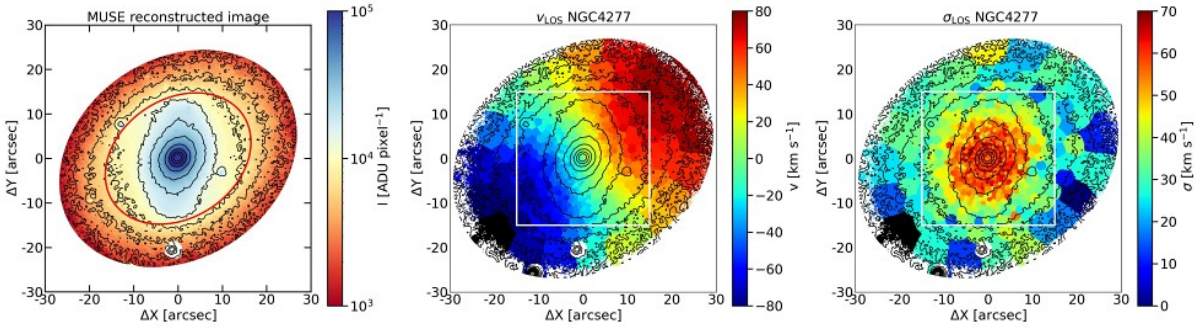

Figure 6.1: *Left panel*: MUSE reconstructed image of NGC 4277. The red ellipse brackets the bar region used for the photometric comparison. *Central panel*: LOS velocity map $V_{\rm LOS}$ of NGC 4277 subtracted of systemic velocity. *Right panel*: LOS velocity dispersion map $\sigma_{\rm LOS}$ of NGC 4277 corrected for $\sigma_{\rm instr}$. Some density contour levels are over-plotted in black in each panel. The white squares in the central and right panel bracket the region used for the kinematic comparison. The FOV is 1×1 arcmin^2 and oriented with the north up and east left.

The evolution of bar properties depends on the efficiency of the exchange of angular momentum, energy, and mass among the bar and the other galactic components, such as the bulge, disc, and DM halo. A spherical component such as a stellar bulge or a DM halo absorbs the angular momentum emitted by the disc at the resonances. A massive spherical component delays bar formation and produces a slow initial growth of the bar amplitudes followed by a strong increase of strength (Athanassoula & Misiriotis, 2002; Athanassoula, 2003). A massive and centrally-concentrated DM halo can slow down the bar due to dynamical friction (Debattista & Sellwood, 1998, 2000; Martinez-Valpuesta et al., 2006; Athanassoula et al., 2013; Petersen et al., 2019).

In this chapter, we use pure stellar models of galaxies to study the photometric and stellar kinematic properties of the lenticular barred galaxy NGC 4277. We organise the chapter as follows. We present the general properties of NGC 4277 in Sec. 6.2. We describe the adopted N-body simulation models, analysis, and comparison between the observations and simulated galaxies in Sec. 6.3. We discuss the results in Sec. 6.4 and we report our conclusions in Sec. 6.5.

6.2 NGC 4277

NGC 4277 is a lenticular barred galaxy located at a distance of $D = 33.9$ Mpc behind the Virgo cluster although it is classified as a possible member (Kim et al., 2014). It possibly forms an interacting pair with the nearby spiral galaxy NGC 4273 that lies at a distance of $\sim$19 kpc and it is located at a distance $D = 36.3$ Mpc. (van Driel et al., 2000). NGC 4277 was already presented in Chapter 3, therefore here we provide a short description of its photometric and kinematic properties useful to understand the subsequent analysis.

NGC 4277 is characterised by a prominent and round bulge, an axisymmetric and unwarped disc, and an elongated bar that lies at an intermediate orientation with respect to the disc major and minor axes (Fig. 6.1, *left panel*). It shows no evidence of spiral arms or patchy dust, and this makes NGC 4277 a suitable candidate for the comparison with pure stellar N-body simulations.

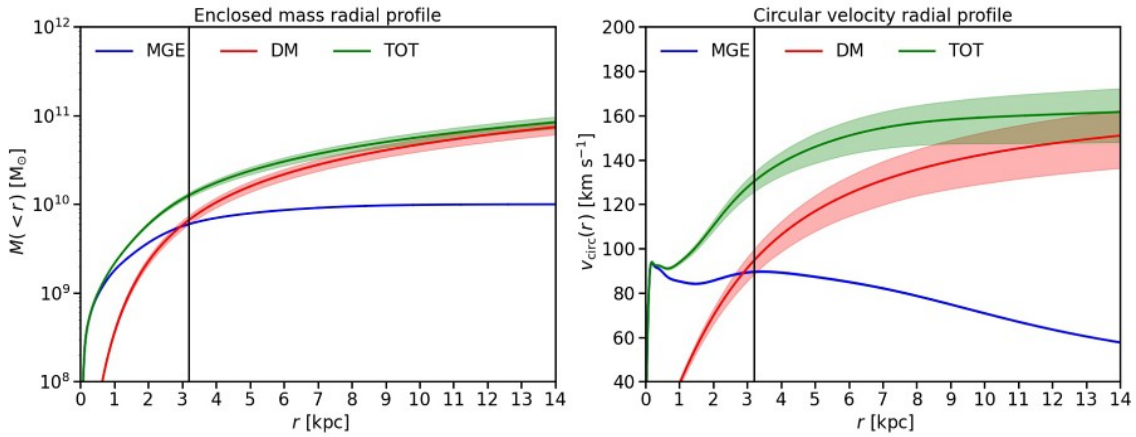

Figure 6.2: Enclosed mass (*left panel*) and circular velocity (*right panel*) radial profiles of NGC 4277 from the best-fitting parameters of JAM model. The blue, red, and green lines represent the stellar, DM, and their sum. The black vertical line marks the extension of the bar radius.

The stellar kinematics of NGC 4277 were derived from the integral-field spectroscopic MUSE data (see Sec. 3.3 for details). We decided to remeasure the stellar kinematics to improve the accuracy of the measurements in a few bins. We measured the stellar kinematic maps of NGC 4277 from the combined MUSE datacube using the GIST pipeline (Bittner et al., 2019). We followed the prescription described in Chapter 3, and performed a Voronoi binning with a target $S/N = 40$ per bin. We adopted the INDOUS stellar library (FWHM=1.1Å, Valdes et al., 2004) in the wavelength range $8300 - 9000$ Å centred on the Ca II$\lambda\lambda$8498, 8542, 8662Å absorption-line triplet. We estimated the errors on the kinematic parameters using Monte Carlo simulations. In the central and right panels of Fig. 6.1 we show the LOS velocity, $V_{\rm LOS}$, subtracted from systemic velocity and the LOS velocity dispersion, $\sigma_{\rm LOS}$, corrected for the instrumental dispersion $\sigma_{\rm instr}$. The innermost region of the velocity field is characterised by an asymmetric S-shape pattern. In contrast, the outer region is nearly symmetric since we are in the disc-dominated region. The velocity dispersion field has a local minimum at the centre, at $\sim 30\,{\rm km\ s^{-1}}$, rising to $\sim 60\,{\rm km\ s^{-1}}$ in external regions before it decreases in the outermost region (Wozniak & Champavert, 2006; Gadotti et al., 2020).

The photometric analysis of NGC 4277 used the SDSS deep broad-band imaging to derive the disc geometrical parameters and bar properties (see Sec. 3.3 for details). To be consistent, we performed a Fourier analysis on the deprojected MUSE reconstructed image of NGC 4277 in the same wavelength range used to derive the stellar kinematics. To project the galaxy into the face-on view keeping the flux preserved, the image was stretched along the disc minor axis by a factor of $1/\cos(i)$ where i is disc inclination derived as $i = \arccos(\langle\epsilon\rangle)$ from the isophotal analysis. The Fourier analysis of NGC 4277 presents the typical features of barred galaxies. The even Fourier components are more prominent with respect to the odd ones, and the $m = 2$ term is the dominant one. The bar phase angle ϕ_2 increases in the very central region and remains nearly constant in the bar region.

We reconstructed the internal structure of NGC 4277 by constructing a Jeans dynamical model (see Chapter 5). In Fig. 6.2 we show the enclosed mass and circular velocity profile of the stellar, DM, and their sum from the best-fitting parameters of the JAM model. At the bar radius, the DM content is almost equal to the stellar content. The global circular velocity curve mildly increases in the central region and becomes flat beyond $r \sim 7\,{\rm kpc}$.

6.3 N-body simulations

Setting the initial conditions

We set up the initial conditions of the N-body simulations with the GalactICS software (Kuijken & Dubinski, 1995; Widrow & Dubinski, 2005; Widrow et al., 2008) to construct axisymmetric and equilibrium models of galaxies. Our models are composed of a bulge, a disc and a DM halo.

- The bulge is parameterised with a Sérsic (1968) mass density profile:

$$\rho_{\rm b}(r) = \rho_{\rm b} \cdot \left(\frac{r}{R_{\rm eff}}\right)^{-p} e^{-b\left(\frac{r}{R_{\rm eff}}\right)^{1/n}},$$

  where ρ_b is the density scale, $R_{\rm eff}$ is the effective radius, n is the Sérsic index, and b is a constant adjusted to have half of the total mass inside $R_{\rm eff}$. We use the depth of the gravitational potential associated with bulge σ_b^2 rather than the density scale $\rho_{0,\rm b}$:

$$\sigma_b \equiv |4\pi n b^{n(p-2)} \Gamma[n(2-p)] R_{\rm eff}^2 \rho_{\rm b}|.$$

  We set $p = -1$ for all the models.

- The disc is exponential along the radial direction and sech^2 along the vertical direction:

$$\Sigma_{\rm d}(R,z) = \Sigma_{0,\rm d}\ e^{(-R/h_R)}\ \mathrm{sech}^2(z/h_z),$$

  where $\Sigma_{0,\rm d}$ is the central surface density, and h_R and h_z are the radial and vertical scale lengths, respectively. The radial velocity dispersion profile of the disc is given by an exponential law:

$$\sigma_R(R) = \sigma_{0,R} e^{(R/R_\sigma)/2},$$

  where $\sigma_{0,R}$ is the central velocity dispersion and R_σ the velocity dispersion scale length. We set $M_{\rm d} = 2\pi\,\Sigma_{0,\rm d}\,h_r^2 = 5.4 \cdot 10^{10}$ M$_\odot$ and $h_r = R_\sigma = 2.6$ kpc for all the models.

- The DM halo is represented by a truncated NFW (Navarro et al., 1995) mass density:

$$\rho_{\rm DM}(r) = \frac{V_0^2\, 2^{(2-\gamma)}}{4\pi a_h^2} \frac{C(r, r_{\rm out}, \delta_r)}{(r/a_h)^\gamma (1 + r/a_h)^{(3-\gamma)}},$$

  where V_0 is the characteristic velocity, a_h is the radial scale length, γ is the slope of the radial profile, and $C(r, r_{\rm out}, \delta_r)$ is a truncation function (Widrow et al., 2008) which goes from 1 to 0 at radius $r = r_{\rm out}$ over a width of δ_r and is defined as:

$$C(r) = \frac{1}{2}\mathrm{erfc}\left(\frac{r - r_{\rm out}}{\sqrt{2}\delta_r}\right).$$

  We set $a_h = 10.5$ kpc, $r_{\rm out} = 100$ kpc, $\gamma = 0.34$, and $\delta_r = 20$ kpc for all the models.

We will explore different bulge ($R_{\rm eff}, \sigma_b$), disc ($h_z, \sigma_{0,R}$), and halo (V_0) parameters. It is important to stress that these quantities can not be directly compared with galaxy observables. Our models have 400000 bulge particles, 10^6 disc particles, $2{\cdot}10^6$ halo particles, with a mass of $M_{\rm b} \simeq 2.1\times10^4\,{\rm M}_\odot$, $M_{\rm d} \simeq 2.8\times10^4\,{\rm M}_\odot$ and $M_{\rm DM} \simeq 1.2\times10^6\,{\rm M}_\odot$, respectively. We evolve the models using the tree code PKDGRAV (Stadel, 2001). The base time-step is $\Delta t = 0.5\,$Gyr and is refined such that the time-step of each particle satisfies $\delta t = \Delta t/2n < \eta\sqrt{\epsilon/a_g}$, where a_g is the acceleration at the particle current position. We use $\eta = 0.2$ and set the opening angle of the tree code gravity calculation $\theta = 0.7$. We evolve the models for 10 Gyr, but in some cases, when the bar formation occurs later, we extend the evolution for 4 Gyr more.

Comparison with the observations

We wrote a dedicated Python code to project the N-body models to the same orientation of NGC 4277 on the sky, rescale the bar size and rotation curve amplitude as NGC 4277, and perform both a photometric and kinematic comparison. We first rescaled and rotated the position of the particles of the model to project the simulation at the same distance and orientation as NGC 4277 on the sky plane. We then convolved the surface mass density of the particles with a Gaussian kernel to mimic the smearing effects of seeing (FWHM $\simeq$ 1 arcsec). We projected the resulting image on face-on view, and decomposed it using Fourier analysis (Aguerri et al., 2009). To be consistent, we applied the same procedure to both the observed and mock images and recovered $R_{\rm bar}$ and $S_{\rm bar}$ with the same approach. We defined the bar radius as the mean value of the measurements obtained by applying two different methods. First, we obtained $R_{\rm bar}$ as the outer radius of the FWHM of the radial profile of I_2/I_0 Fourier amplitude. Then, we estimated $R_{\rm bar}$ from the radial profile of the $m = 2$ phase angle, ϕ_2. We defined the bar radius as the radial distance at which the bar phase angle changes of $\Delta\phi_2 = 10^\circ$ with respect to the phase angle associated with the maximum of the I_2/I_0 Fourier amplitude. For NGC 4277, we obtained a deprojected bar radius of $R_{\rm bar,o}$=17.6 arcsec. In addition, we defined the bar strength $S_{\rm bar}$ as the maximum value of the I_2/I_0 Fourier amplitude. For NGC 4277, we obtained a value for the bar strength of $S_{\rm bar,o} = 0.35$. The positions of the particles were rescaled by multiplying by a factor equal to the ratio between the bar size measured on the observed and mock image $\eta_{\rm pos}$=$R_{\rm bar,o}/R_{\rm bar,m}$. For the photometric comparison, we performed a χ^2 minimisation of the radial profiles of $m = 2, 4, 6$ Fourier amplitudes and $m = 2$ phase angle ϕ_2, excluding the outermost regions to avoid the contribution of the disc.

As for the positions, also the velocities of the particles have to be rescaled. To this aim, we first applied the same Voronoi binned map of the observation to the simulation. We binned the particles in velocity space adopting a velocity bin of $\Delta V = 15\,{\rm km\ s^{-1}}$, that is $\sim 1/3$ of the instrumental resolution of the galaxy spectrum of NGC 4277 ($\sigma_{\rm instr} = 37$ km s^{-1}). In each bin, we fitted the resulting LOSVD of particles with a Gauss-Hermite function (Gerhard, 1993; van der Marel & Franx, 1993a) to recover the LOS velocity $V_{\rm LOS}$ and velocity dispersion $\sigma_{\rm LOS}$ of the particles (Du et al., 2016). We extracted the stellar kinematics in a slice along the disc major axis with a width of 4 arcsec to recover the rotation curve. We scaled the model kinematics by multiplying by a factor equal to the ratio between the amplitudes $\Delta V_{\rm LOS}$ of the observed and modelled rotation curves ($\eta_{\rm vel} = \Delta V_{\rm LOS,o}/\Delta V_{\rm LOS,m}$). For the kinematic comparison, we finally selected a region enclosing the bar and performed a comparison of the $V_{\rm LOS}$ and $\sigma_{\rm LOS}$ maps between observations and model with a χ^2 minimisation. We stress that $\eta_{\rm pos}$ and $\eta_{\rm vel}$ are position and velocity scale factors. If position is rescaled as $L_0 = \eta_{\rm pos}\,L$, and $V_0 = \eta_{\rm vel}\,V$, then the time needs to be rescaled as $T_0 = (\eta_{\rm vel}/\eta_{\rm pos})T$.

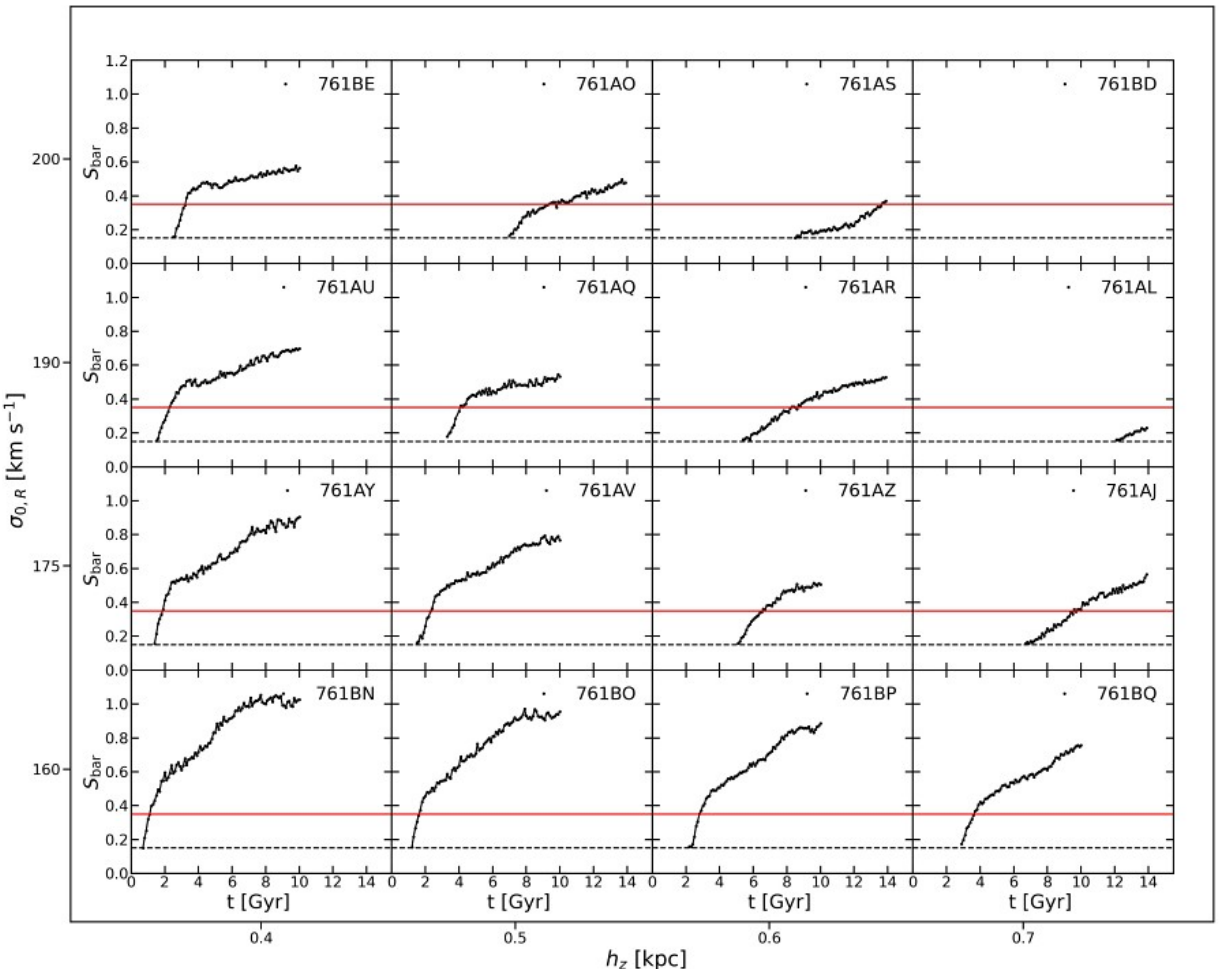

Figure 6.3: Time evolution of the bar strength of 16 galaxy models in the $h_z - \sigma_{0,R}$ plane. The horizontal red solid line marks the bar strength in NGC 4277 ($S_{\rm bar,o} = 0.35$), while the horizontal black dashed line represents the bar strength threshold ($S_{\rm bar} = 0.15$).

Exploring disc parameters

We start by analysing a set of 16 galaxy models fixing the halo ($V_0 = 480\,{\rm km\,s^{-1}}$), and the bulge ($n = 1.409, \sigma_b = 312.6\,{\rm km\,s^{-1}}, R_{\rm eff} = 0.4\,{\rm kpc}$) parameters. The models span a wide range of disc thickness ($h_z \in [0.4, 0.5, 0.6, 0.7]\,{\rm kpc}$) and Toomre Q parameter ($\sigma_{0,R} \in [160, 175, 190, 200]\,{\rm km\ s^{-1}}$). In Fig. 6.3 we show the time evolution of the bar strength in the different galaxy models. We consider a bar to have formed when the strength $S_{\rm bar} \geqslant 0.15$ and the radial profile of the $m = 2$ Fourier amplitude ϕ_2 is constant in the bar region. The bar formation and the evolution of $S_{\rm bar}$ depend on the dynamical properties of the disc. Bar formation occurs early ($\sim 2\,{\rm Gyr}$) in the simulation in models with a thin and cool disc (bottom left corner in Fig. 6.3), whereas the bar formation is delayed or never occurs in thick and hot discs (top right corner in Fig. 6.3). In hotter discs, the bar strength steeply increases for roughly $\sim 1.5\,{\rm Gyr}$ as the bar formation starts, then it remains almost constant or slowly increases until the end of the simulation. In cooler discs, instead, $S_{\rm bar}$ abruptly increases in the early phases and substantially keeps growing for the whole simulation. As the disc becomes thicker, the change of slope becomes smoother.

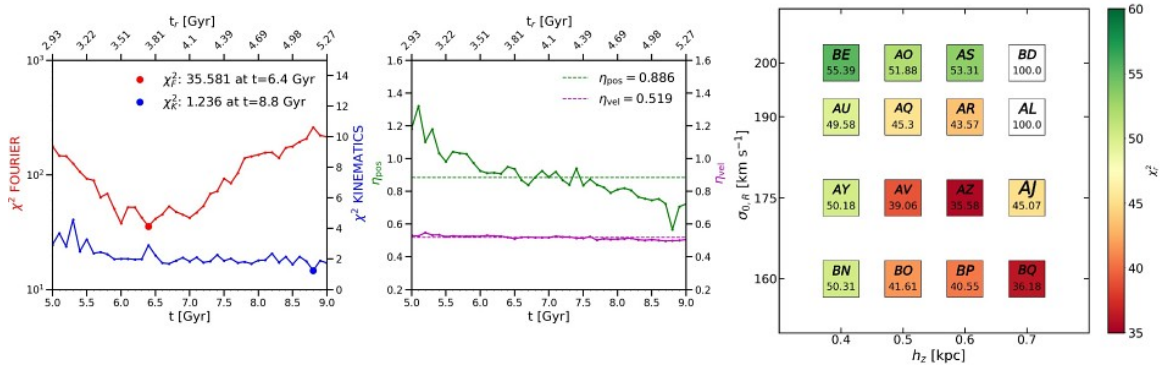

Figure 6.4: *Left panel*: Time evolution of the reduced χ^2 for the Fourier and kinematic comparison (red and blue lines in the left panel), and $\eta_{\rm pos}$ and $\eta_{\rm vel}$ scaling factors (green and purple line in the right panel) for simulation 761AZ. The red and blue circles in the left panel mark the corresponding minima. The top x-axis shows the time after being rescaled with the median values of the rescaling factors marked by the horizontal green and purple dashed lines in the right panel. *Right panel*: Galaxy models in the $h_z - \sigma_{0,R}$ plane. Models are colour coded according to the value of the minimum of the χ^2 from the Fourier analysis.

For each snapshot of each model, we performed a photometric and kinematic comparison with the observations as described in the previous section. We performed a χ^2 minimisation looking for the best combination of scaling factors ($\eta_{\rm pos}, \eta_{\rm vel}$) that minimise both the Fourier analysis and stellar kinematic maps in the bar region. During its evolution, the bar keeps growing in terms of length and strength. This explains the decreasing trend of the scaling factor $\eta_{\rm pos}$. We noticed that the time evolution of the $\eta_{\rm vel}$ is nearly constant (Fig. 6.4, right panel). This means that the bar affects the morphological and photometric properties of the galaxy more than the kinematic ones.

The $\eta_{\rm pos}$ and $\eta_{\rm vel}$ scaling factors act like geometric factors that stretch or shorten the positions and velocities of particles. As a consequence, the profiles of the the Fourier amplitudes are stretched in the radial direction and not in amplitude. We expect to obtain the best match between the observation and simulation as the value of the bar strength in the model approaches the value of $S_{\rm bar,o}$. Indeed, the minimum of the χ^2 for the Fourier comparison occurs nearly at this time (Fig. 6.4, left panel). The time evolution of the χ^2 for the kinematic comparison, instead, remains roughly constant. We analysed the photometric and kinematic properties of the snapshot in which the χ^2 for the Fourier comparison reaches a minimum and the corresponding kinematic maps. In the right panel of Fig. 6.4 we show the different galaxy models in the $h_z - \sigma_{0,R}$ plane, colour coded by the value of the minimum of the χ^2 from the Fourier comparison. We marked in white the simulations that either do not form a bar or do not develop a sufficiently strong bar.

Among the various galaxy models analysed so far, model 761AZ has the lowest χ^2. In Fig. 6.5 we show the Fourier analysis of model 761AZ at the snapshot in which the minimum of χ^2 for the photometric comparison occurs and its corresponding kinematics maps. The radial profile of the $m = 2$ Fourier component of model 761AZ nearly matches the amplitude of that one in NGC 4277 ($\Delta S_{\rm bar} \sim 0.02$), while the $m = 4$ and $m = 6$ Fourier components are less prominent with respect to the observed ones. The radial profile of the bar phase angle ϕ_2 reasonably reproduces the trend in NGC 4277. It increases in the central region, reaches a maximum value of $\phi_2 \sim 26^\circ$ and remains constant in the bar region. In the lower panels of Fig. 6.5 we show the maps of the residuals of the velocity ($V_{\rm LOS,o} - V_{\rm LOS,m}$) and velocity dispersion ($\sigma_{\rm LOS,o} - \sigma_{\rm LOS,m}$).

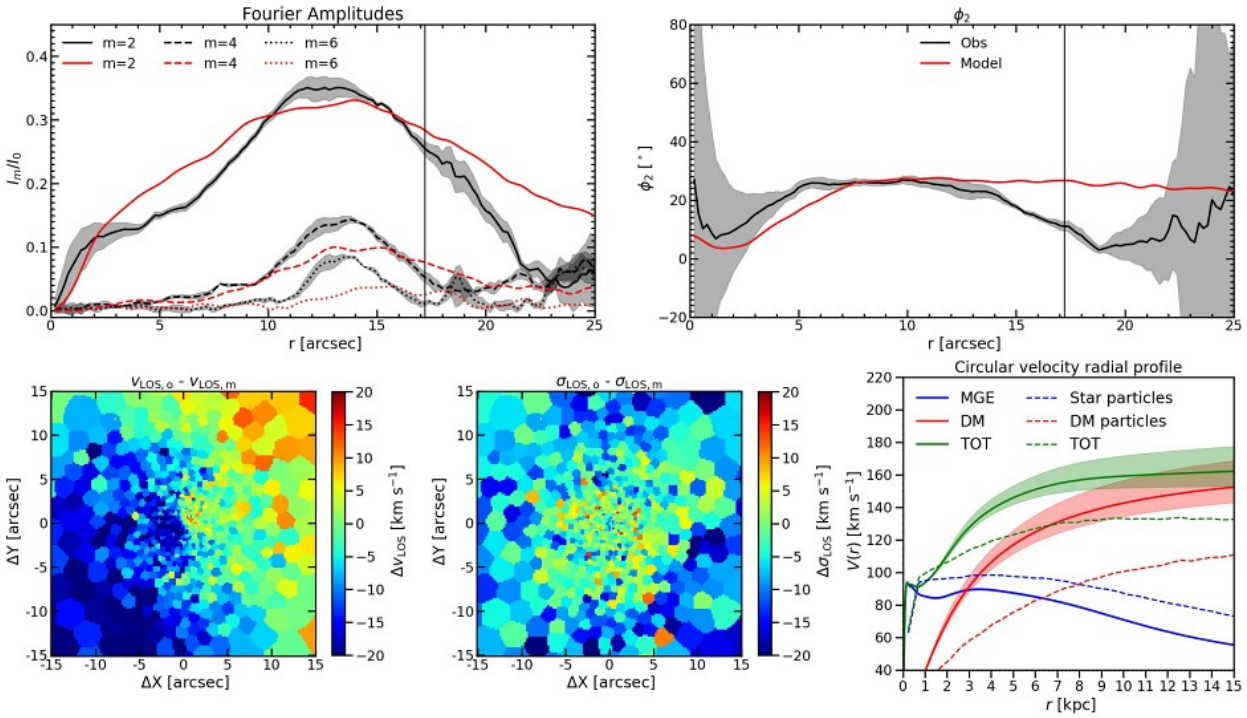

Figure 6.5: Photometric and stellar kinematic comparison between NGC 4277 and model 761AZ. *Top panels*: Radial profiles of $m = 2$ (solid lines), $m = 4$ (dashed lines), $m = 6$ (dotted lines) Fourier amplitudes (*left panel*) and bar phase angle ϕ_2 (*right panel*) for observations (black lines) and model (red lines). The vertical black line marks the radial region used for the comparison. *Bottom panels*: Residuals of LOS velocity (*left panel*) and velocity dispersion (*central panel*) maps. Circular velocity radial profiles of the stellar component (blue lines), DM halo (red lines), and their sum (green lines) for model 761AZ (dashed lines) and the best-fitting JAM model (solid lines).

Positive values in the residual maps (redder colour) mean that the model underestimates the observed data, while negative values (bluer colour) mean that the model overestimates the observed data. The stellar velocity field in NGC 4277 is nearly symmetric (see Fig. 6.1), while the modelled one presents an asymmetry in the outermost region. In fact, the residuals in the top right corner reach a maximum value of $\sim 15\,\mathrm{km\ s^{-1}}$, while in the bottom left corner rise to $\sim 30\,\mathrm{km\ s^{-1}}$. The velocity dispersion is slightly underestimated in the central region and overestimated in the external one.

In addition, we extracted the circular velocity radial profiles of the stellar component, DM halo, and their sum of the particles in simulation 761AZ rescaled with the scaling factors at the minimum of the χ^2 (Fig. 6.5, bottom right panel). We compared them with the predictions obtained from the best-fitting JAM model of NGC 4277. Clearly, the match between the model and JAM fit is not good. The circular velocity profile of the DM component shows the largest deviations from the JAM prediction. At large radial distances, the difference is about $\Delta V_{\mathrm{circ,DM}} \sim 40\,\mathrm{km\ s^{-1}}$. We decided to explore a new set of galaxy models with a more massive DM halo to improve the mock stellar kinematics and circular velocity curve.

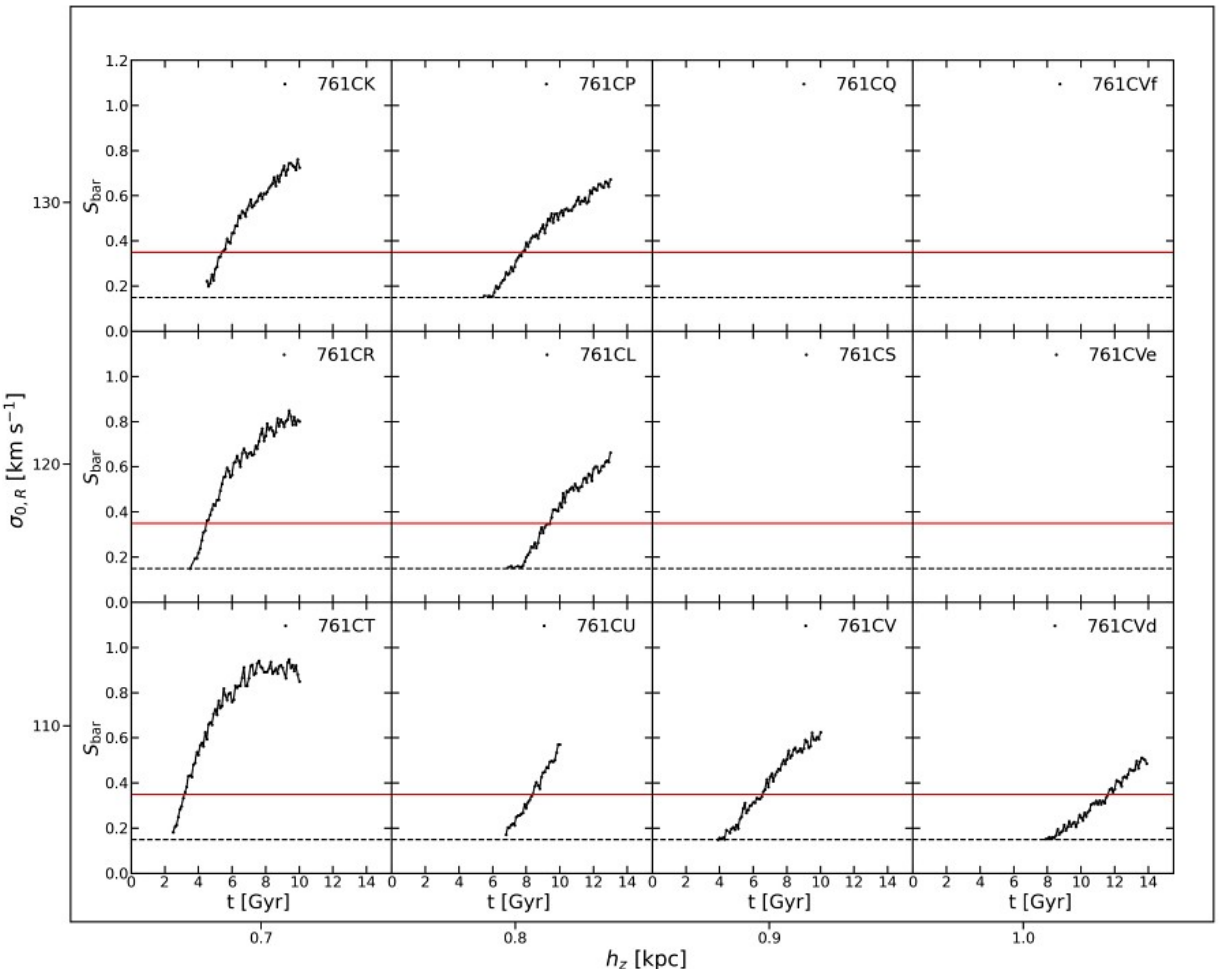

Figure 6.6: Same as in Fig. 6.3, but for galaxy models with a more massive DM halo.

A more massive halo

We analysed a new set of 12 galaxy models with a more massive halo ($V_0 = 600\,\mathrm{km\,s^{-1}}$), fixing again the bulge parameters ($n = 1.409, \sigma_b = 312.6\,\mathrm{km\,s^{-1}}, R_{\mathrm{eff}} = 0.4\,\mathrm{kpc}$). The models span a wide range of disc thickness ($h_z \in [0.7, 0.8, 0.9, 1.0]\,\mathrm{kpc}$) and Toomre Q parameter ($\sigma_{0,r} \in [110, 120, 130]\,\mathrm{km\,s^{-1}}$). In Fig. 6.6 we show the time evolution of the bar strength in the different galaxy models. As already noticed before, the bar formation and the evolution of its strength depend on the dynamical properties of the disc. Thick and hot discs are more robust to bar instabilities (top right corner in Fig. 6.6), while cool and thin discs are unstable to bar instabilities and more prone to bar formation (bottom left corner in Fig. 6.6). In each model, as the bar starts to form, S_{bar} increases for the whole evolution. Model 761CT is the only model in which the evolution of the bar strength shows a phase in which S_{bar} remains nearly constant. The bar strength in various models grows in a smooth way without any abrupt change in slope.

As before, we performed a photometric and stellar kinematic analysis of each snapshot of each galaxy model and we selected model 761CV as the best model among the various analysed so far.

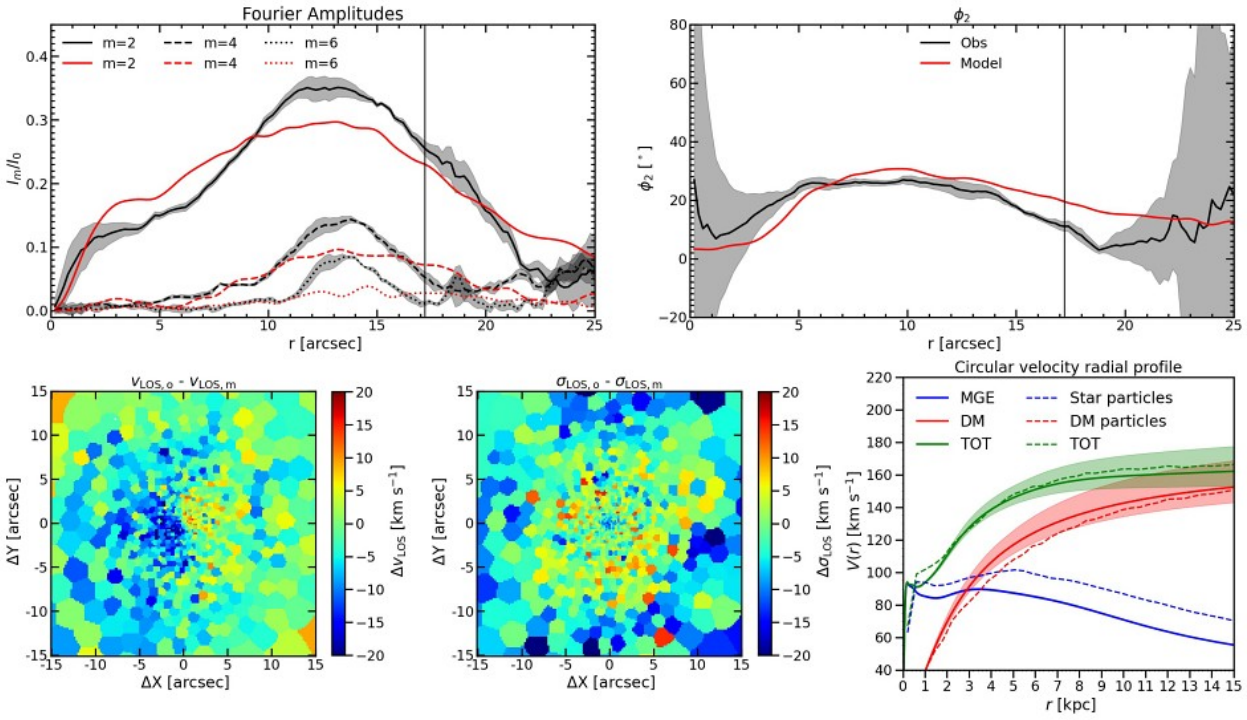

Figure 6.7: Same as Fig. 6.5, but for model 761CV.

In Fig. 6.7 we show the Fourier analysis of model 761CV at the snapshot, where the minimum of χ^2 for the photometric comparison occurs and its corresponding stellar kinematics maps. The radial profile of the $m = 2$ Fourier component marginally reproduces the behaviour observed in NGC 4277. Between the peak associated with the bulge and the one associated with the bar, the profile slightly decreases at $r \sim 5$ arcsec as in the observed profile. However, the peak of the $m = 2$ Fourier amplitude is not well reproduced ($\Delta S_{\rm bar} \sim 0.05$). The trend of the bar phase angle ϕ_2 presents some similarities with the one of NGC 4277.

The kinematic maps of model 761CV reasonably reproduce the velocity fields of NGC 4277. The residuals in the velocity map still show an asymmetry but only in the innermost region $r \lesssim 2.5$ arcsec. In the outermost regions, the difference between the model and observation ranges between $|V_{\rm LOS,o} - V_{\rm LOS,m}| \sim 2 - 15\,{\rm km\ s^{-1}}$. We do not note any significant improvement in the velocity dispersion map of model 761CV with respect to the previous findings.

The radial profiles of the circular velocities show instead a slight improvement. The circular velocity profile of the DM component nearly matches the JAM prediction, indeed, the global contribution of the stellar and DM components is well reproduced too. Although the modelled stellar circular velocity is larger with respect to the observed one ($\Delta V_{\rm circ,\star} \sim 15\,{\rm km\ s^{-1}}$), the shape of the observed profile of the stellar component is well reproduced.

The modelled stellar kinematics maps and circular velocity curves reasonably reproduce the observed ones. The Fourier analysis of NGC 4277 is marginally reproduced by the model, especially in the central region, where the bulge has a large contribution. We decided to explore a new set of galaxy models changing the bulge parameterisation.

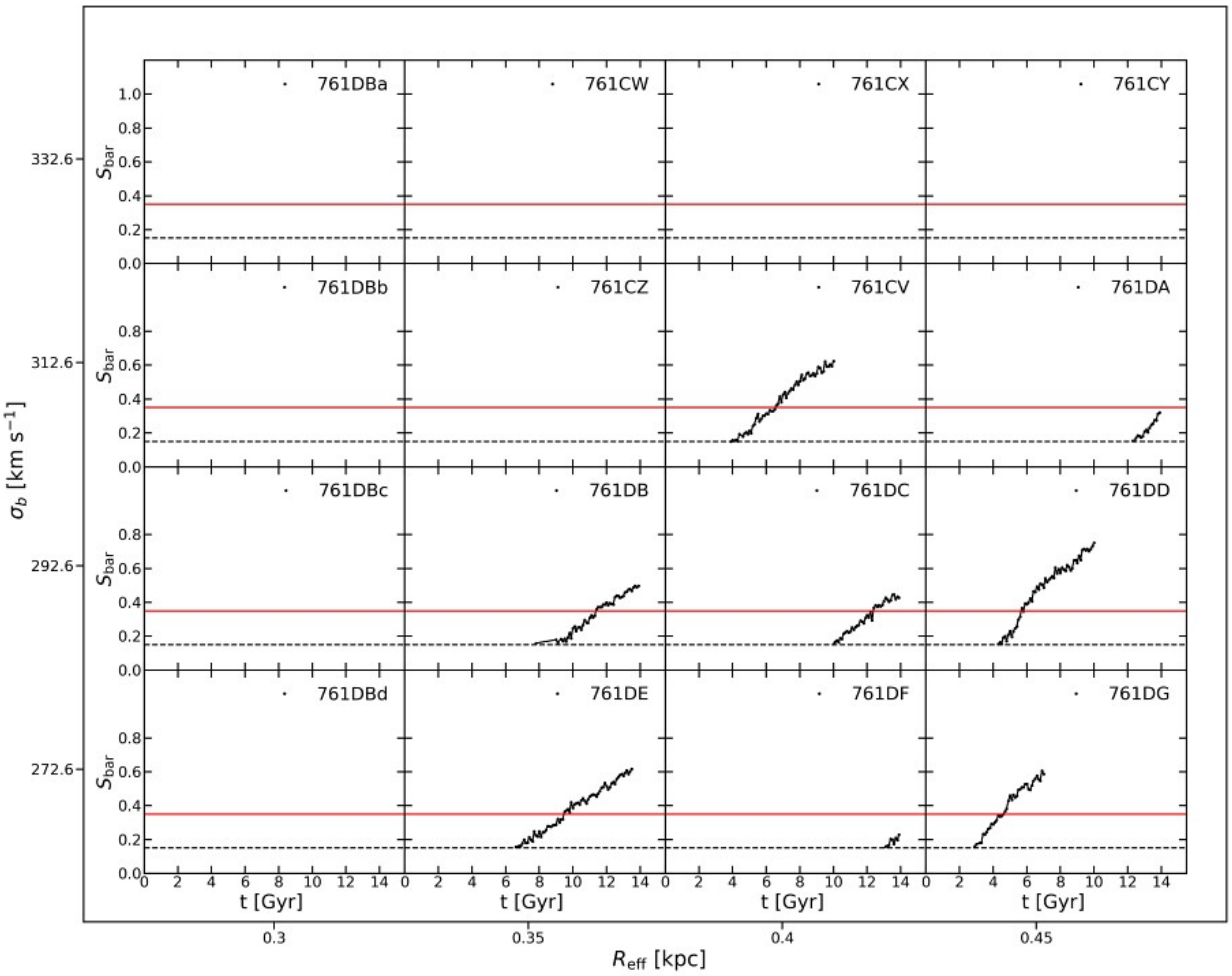

Figure 6.8: Same as in Fig. 6.3, but for galaxy models in the $R_{\rm eff} - \sigma_b$ plane.

Exploring the bulge parameters

We explored a new set of 16 galaxy models, fixing the disc ($h_z = 0.9\,$kpc, $\sigma_{0,R} = 110\,$km s^{-1}) and halo ($V_0 = 600\,$km s^{-1}) parameters and varying the bulge parameters. The models span a wide range of bulge effective radius ($R_{\rm eff} \in [0.3, 0.35, 0.4, 0.45]\,$kpc) and velocity dispersion ($\sigma_b \in [272.6, 292.6, 312.6, 332.6]\,$km s^{-1}). In Fig. 6.8 we show the time evolution of the bar strength in the different galaxy models. There is no clear dependence between the bar formation and the dynamical properties of the bulge since in some cases the bar formation happens at the very end of the simulation or never occurs. We noticed that galaxies with a too compact bulge ($R_{\rm eff} = 0.3\,$kpc) or with a bulge with a too high velocity dispersion ($\sigma_b = 332.6\,$km s^{-1}) do not form a bar. This is in agreement with the results obtained by Athanassoula (2003), which found a delay in the bar formation in galaxy models with a massive central structure. In all the models, the bar strength starts to increase as the bar forms and grows for the whole simulation.

As before, we performed a photometric and stellar kinematic analysis of each snapshot of each galaxy model and we selected model 761DB as the best model among the various analysed so far.

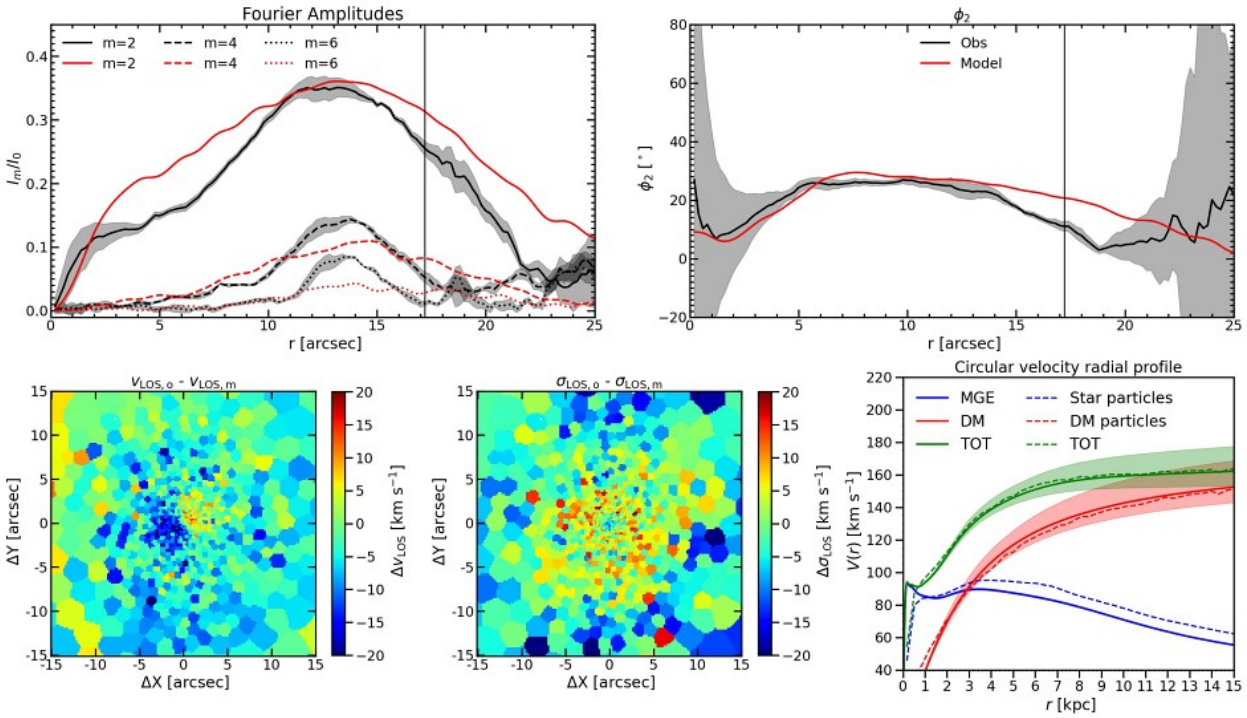

Figure 6.9: Same as in Fig. 6.5, but for model 761DB.

In Fig. 6.9 we show the Fourier analysis of model 761DB at the snapshot, where the minimum of χ^2 for the photometric comparison occurs and its corresponding kinematics maps. The peak of the radial profile of the $m = 2$ Fourier component perfectly matches the bar strength in NGC 4277. The bar phase angle ϕ_2 reasonably reproduces the profile in NGC 4277 too. However, the profile of the $m = 2$ Fourier component is more prominent with respect to the observed one in the radial range $2 \leqslant r \leqslant 10$ arcsec.

The kinematic maps of model 761DB show a significant improvement with respect to the velocity fields of the previous models. The very central region of the residuals map of velocity still shows an asymmetry of about $|V_{\rm LOS,o} - V_{\rm LOS,m}| \sim 15\,{\rm km\ s^{-1}}$. Overall, the model reasonably reproduces the observed velocity field, indeed the difference between the observed and modelled stellar velocity is $|V_{\rm LOS,o} - V_{\rm LOS,m}| \lesssim 5\,{\rm km\ s^{-1}}$. As for the previous models, the velocity dispersion map is slightly underestimated in the central region and overestimated in the external one. In the outermost bins, the difference rises to values of $|\sigma_{\rm LOS,o} - \sigma_{\rm LOS,m}| \sim 17\,{\rm km\ s^{-1}}$, and decreases to $|\sigma_{\rm LOS,o} - \sigma_{\rm LOS,m}| \sim 5\,{\rm km\ s^{-1}}$ in the innermost ones.

The radial profiles of the circular velocities are well reproduced. The total and the DM circular velocities perfectly match those obtained from the JAM predictions. The modelled stellar circular velocity differs from the JAM prediction of $\Delta V_{{\rm circ},\star} \lesssim 8\,{\rm km\ s^{-1}}$ in the very central region ($r \leqslant 1\,{\rm kpc}$) and outer ($r \geqslant 3\,{\rm kpc}$) region.

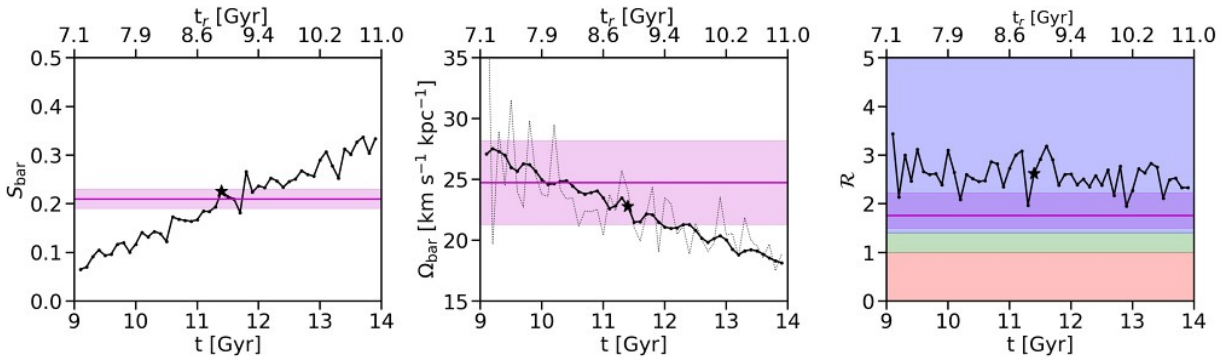

Figure 6.10: Time evolution of the bar strength $S_{\rm bar}$ (*left panel*), pattern speed $\Omega_{\rm bar}$ (*central panel*), and rotation rate $\mathcal{R}$ (*right panel*) of model 761DB. The top x-axis shows the time after being rescaled with the median values of the rescaling factors ($\eta_{\rm pos}$, $\eta_{\rm vel}$). The magenta horizontal line and shaded area in each panel represent the value and associated error of $S_{\rm bar}$, $\Omega_{\rm bar}$, and $\mathcal{R}$ in NGC 4277. The black star in each panel represents the snapshot where the minimum of the χ^2 occurs. The black dotted line in the central panel represents the $\Omega_{\rm bar}$ obtained from the moment of inertia tensor (Wu et al., 2018). The red, green, and blue shaded areas in the right panel represent the ultrafast, fast, and slow regimes, respectively.

Additional simulations

Model 761DB reasonably reproduces the photometry and velocity fields of NGC 4277. However, the central region of the Fourier analysis ($r \lesssim 10$ arcsec) is not well fitted by the model. Moreover, the modelled circular velocity of the stellar component presents a deviation in the same radial range ($r \lesssim 1.6$ kpc). We decided to explore a new set of models varying the Sérsic index n. In addition, we built a set of new simulations composed by a gadolge, a disc, and a DM halo, substituting the Sérsic density profile with an exponential one. As for the previous galaxy models, we performed a photometric and kinematic analysis for each snapshot of each galaxy model, but we did not see any improvement in the Fourier analysis, neither in the stellar kinematics maps. Model 761DB is the best model that reasonably reproduces the photometric and kinematic properties of NGC 4277.

6.4 Results

In Fig. 6.10 we show the evolution of the bar strength $S_{\rm bar}$, the pattern speed $\Omega_{\rm bar}$, and bar rotation rate $\mathcal{R}$ of the best model after being rescaled by the combination of scaling factors ($\eta_{\rm pos}, \eta_{\rm vel}$). To be consistent, we measured the $S_{\rm bar}$ in each snapshot as the mean value of the I_2/I_0 Fourier amplitudes over the bar extension of the surface mass density of the particles (Fig. 6.10, left panel). From the Fourier analysis, we also measured the bar radius $R_{\rm bar}$ and its orientation measuring the phase angle of the $m = 2$ Fourier amplitude ϕ_2. We measured the $\Omega_{\rm bar}$ as the temporal derivative of ϕ_2 $\Omega_{\rm bar}= \Delta\phi_2/\Delta t$, with Δt the unscaled time-step between the snapshots, equal to 0.1 Gyr (Fig. 6.10, central panel). We recovered the circular velocity $V_{\rm circ}$ of the particles calculating the rotation curve from the gravitational potential in the mid-plane using the Python PYNBODY subroutine (Pontzen et al., 2013). We estimated the corotation radius $R_{\rm cor}$ as the radius at which $V_{\rm circ}$ and $\Omega_{\rm bar}$ each other, and we derived the bar rotation (Fig. 6.10, right panel).

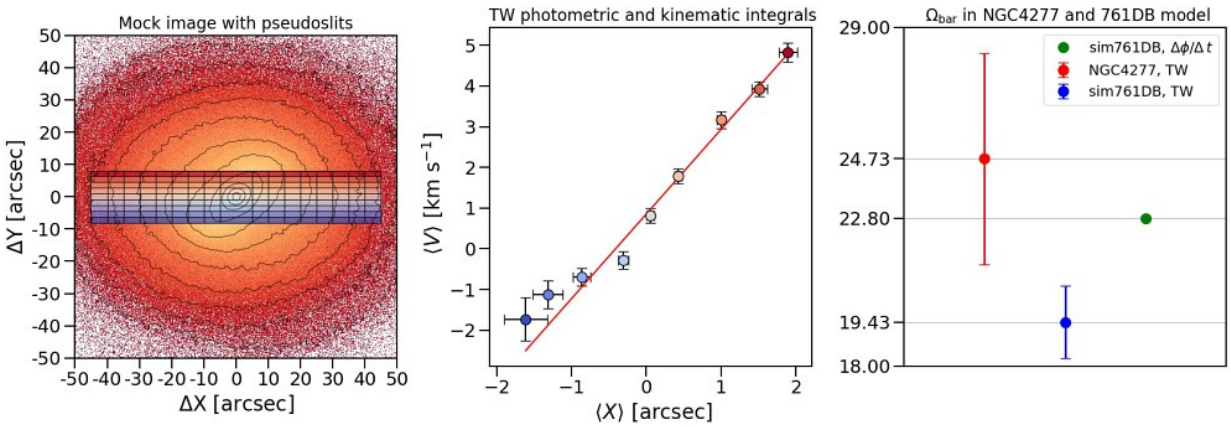

Figure 6.11: *Left panel*: Mock image of model 761DB with pseudoslits. Black lines represent some contour levels. The FOV is $1.7\times1.7\,\mathrm{arcmin}^2$ and is oriented with the north up and the east left. *Central panel*: Kinematic integrals $\langle V\rangle$ as a function of photometric integrals $\langle X\rangle$. The red solid line represents the best fitting-line to the data. *Right panel*: Comparison between the $\Omega_{\rm bar}$ measurements of NGC 4277 (red circle) and model 761DB (blue and green circles).

The bar forms at ∼7.1 Gyr, its strength starts to increase and keeps growing till the end of the simulation. The best match between the observation and model occurs at ∼ 9.1 Gyr. At this time, the value of $S_{\rm bar}$ in model 761DB is nearly equal to the measured value in NGC 4277 ($\Delta S_{\rm bar}$= 0.01). During the whole simulation, $\Omega_{\rm bar}$ decreases. This is a direct consequence of the interaction between the bar and the DM halo (Debattista & Sellwood, 1998; O'Neill & Dubinski, 2003; Athanassoula, 2003). The inner disc loses angular momentum that is acquired by the DM halo at the resonances. The bar brakes due to the dynamical torque exerted by the DM halo, and the slowdown is more efficient for massive DM haloes (Debattista & Sellwood, 1998, 2000). The value of $\Omega_{\rm bar}$ in the best snapshot ($\Omega_{\rm bar}$=22.8 km s^{-1} kpc^{-1}, Fig 6.11) is lower but still consistent within uncertainty to the value we measured in NCG 4277 with the TW method in Chapter 3 ($\Omega_{\rm bar}$=24.7 ± 3.4 km s^{-1} kpc^{-1}, Fig 6.11). We alternatively estimated $\Omega_{\rm bar}$ from the moment of inertia tensor (Wu et al., 2018). The profile presents large oscillations, but the median trend is reasonably in agreement with the other measurement.

In addition, we measured $\Omega_{\rm bar}$ by applying the TW method on the mock image of the model and following the same prescription adopted for NGC 4277. We defined 9 pseudoslits parallel to the disc major axis and crossing the bar region of width equal to 1.8 arcsec and semi-length that ranges from 5 arcsec to 35 arcsec to fully cover the extension of the disc (Fig 6.11, left panel). We measured the luminosity-weighted positions $\langle X\rangle$ and velocities $\langle V\rangle$ of the star particles in each pseudoslits and we verified that the value of $\langle X\rangle$ and $\langle V\rangle$ in pseudo-slits with different lengths remains almost constant. We estimated the errors on $\langle X\rangle$ and $\langle V\rangle$ defining for each slit the radial range in which the value of the photometric and kinematics integrals are constant and adopting the root mean square of the distributions as the error of photometric and kinematic integrals, respectively. As for NGC 4277, we choose the data of pseudoslits with a semi-length of 35 arcsec and we derived $\Omega_{\rm bar}$ by fitting the values of $\langle X\rangle$ and $\langle V\rangle$ with a straight line (Fig 6.11, central panel). We obtained $\Omega_{\rm bar} = 19.4\pm1.2$ km s^{-1} kpc^{-1}, that is consistent within 2σ error with the value measured in NGC 4277 (Fig 6.11, right panel).

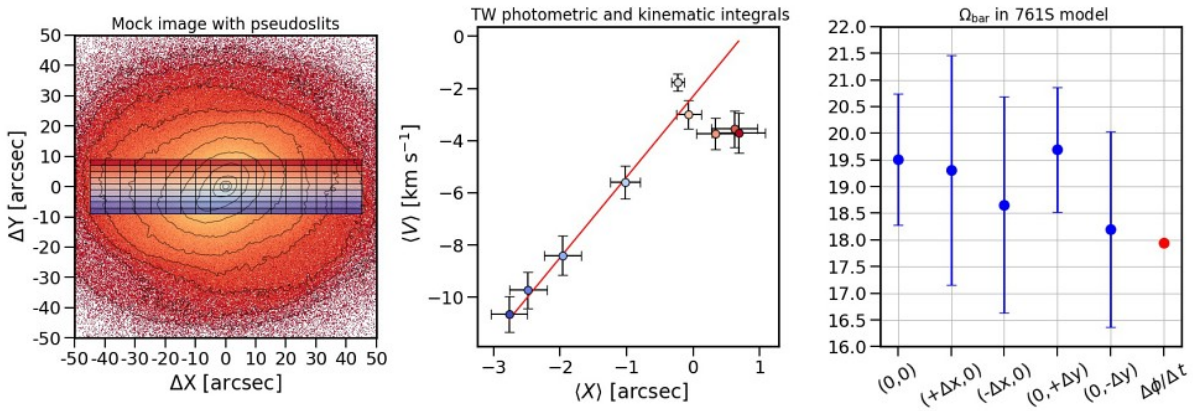

Figure 6.12: *Left panel*: Mock image of model 761S with pseudoslits. Black lines represent some contour levels. The FOV is $1.7\times1.7\,\mathrm{arcmin}^2$ and is oriented with the north up and the east left. *Central panel*: Kinematic integrals $\langle V \rangle$ as a function of photometric integrals $\langle X \rangle$. The red solid line represents the best fitting-line to the data. *Right panel*: Comparison between the $\Omega_{\rm bar}$ measurements obtained with the TW method in different tests (blue circles, ΔX=0.6 arcsec, ΔY=0.6 arcsec) and directly from the simulation (red circle).

We performed additional tests on the application of the TW method to galaxies with a lopsided and offset bar to support our findings about IC 3167 in Chapter 4. We considered the snapshot of model 761S at $t = 1.5$ Gyr since it has a lopsided ($B_{3,\rm max} = 0.045$) and offset (0.6 arcsec) bar, which is quite similar to that of IC 3167. We defined several sets of pseudoslits with different widths, semi-lengths, spatial coverage, and offsets with respect to the disc centre. After checking the radial range where the value of $\langle X \rangle$ and $\langle V \rangle$ were constant, we derived $\Omega_{\rm bar}$ as done before. We found that all the derived values of $\Omega_{\rm bar}$ are consistent with respect to each other and to the value measured from the simulation within 2σ error (Fig. 6.12). Thus, we are confident about pattern speed we measured for IC 3167, although our N-body simulations are not tailored for this dwarf barred galaxy.

The time evolution of $\mathcal{R}$ is very oscillatory, but the mean trend is nearly constant. These variations are due to uncertainties in the measurement of $R_{\rm bar}$ or $R_{\rm cor}$. In fact, in some snapshots, the galaxy model presents a weak evidence of an inner ring or a spiral-like structure that can lead to a wrong estimate of $R_{\rm bar}$. The measure of $R_{\rm cor}$ depends on both $\Omega_{\rm bar}$ and $V_{\rm circ}$. We verified the reliability of the bar phase angle ϕ_2 measuring the orientation of the bar from the moment of inertia tensor, and we found a good agreement between the two measures of ϕ_2. The estimate of $V_{\rm circ}$ should be a robust measure, but we can not exclude possible biases due to a non-axisymmetric distribution of particles on the mid-plane of the disc or other effects.

We noticed that the bar rotation rate in model 761DB is systematically higher compared with the value obtained in the observations ($\mathcal{R}= 1.8^{+0.5}_{-0.3}$). Many works based on cosmological simulations showed that simulated bars are slower (Algorry et al., 2017; Peschken & Łokas, 2019; Roshan et al., 2021) or shorter (Frankel et al., 2022) when compared to observed ones. Although we did not use cosmological simulations, we found a similar trend. At the best snapshot, $R_{\rm bar}$ is lower ($R_{\rm bar} = 2.6$ kpc) with respect to the measured value in NGC 4277 ($R_{\rm bar} = 3.2\pm^{+0.9}_{-0.6}$ kpc), whereas $R_{\rm cor}$ in the model ($R_{\rm cor} = 6.9$ kpc) is longer with respect to the value measured in observations ($R_{\rm cor} = 6.0 \pm 0.9$ kpc). The combination of these two quantities results in an overestimation of the bar rotation rate ($\mathcal{R} = 2.6$). However, the bar properties in model 761DB and in NGC 4277 are consistent with each other within 3σ confidence level.

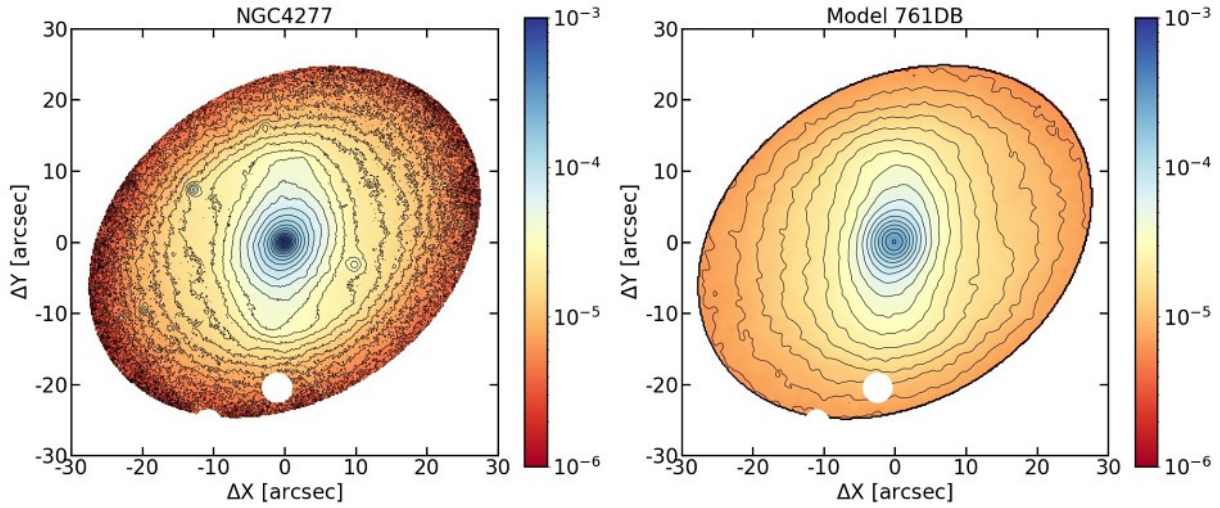

Figure 6.13: Photometric comparison between NGC 4277 and model 761DB. The observed and modelled images are normalised by total flux and total mass, respectively. Black lines represent some contour levels. The FOV is 1×1 arcmin^2 and oriented with the north up and the east left.

In Fig. 6.13 we show the MUSE reconstructed image of NGC 4277 and mass surface density of the particles at the best snapshot of model 761DB rescaled by the best scaling factors ($\eta_{\rm pos}$, $\eta_{\rm vel}$). For better comparison, the observed and modelled images were normalised by the total flux and total mass, respectively. The central region of NGC 4277 is characterised by a prominent and round bulge, that is fainter and less concentrated in model 761DB. In NGC 4277 the isodensity contours in the bar region are weakly bent, suggesting an underlying two-armed spiral structure. In model 761DB, instead, the bar isodensity contours have rounder edges. The disc region in both observations and model is nearly unwarped, elliptical, and symmetric.

In Fig. 6.14 we show the observed and modelled LOS stellar velocity $V_{\rm LOS}$ and velocity dispersion $\sigma_{\rm LOS}$ in the bar region. We overplot some contours to better compare the observed and modelled velocity fields. The kinematics maps of NGC 4277 are well reproduced by the model, except for the very central region ($r \leqslant 2$ arcsec). In the observations, two iso-velocity contours approach each other at the very centre forming an X-shaped structure, whereas they remain nearly parallel in model 761DB instead. The contours of $\sigma_{\rm LOS}$ are scattered in NGC 4277, and nearly circular in model 761DB. Several bins located at $r \lesssim 5$ arcsec reach a value of ~ 65 km s^{-1}, whereas in model 761DB the central peak in the velocity dispersion rises to ~ 60 km s^{-1}. Overall, the stellar kinematics of the observed and modelled galaxy reasonably agree.

To investigate possible hints of secular evolution processes, we performed a further analysis of model 761DB. The buckling instability phase produces a vertical thickening of the bar, whose signature is a characteristic X-shaped structure (Debattista et al., 2006; Martinez-Valpuesta et al., 2006). Therefore, for different snapshots of model 761DB, we performed an unsharp mask on the edge-on particle density distribution (Fig. 6.15). We did not detect any clear evidence of an X-shaped structure in any snapshot and concluded that the model 761DB is characterised by a classical bulge and that its bar did not undergo to the buckling phase.

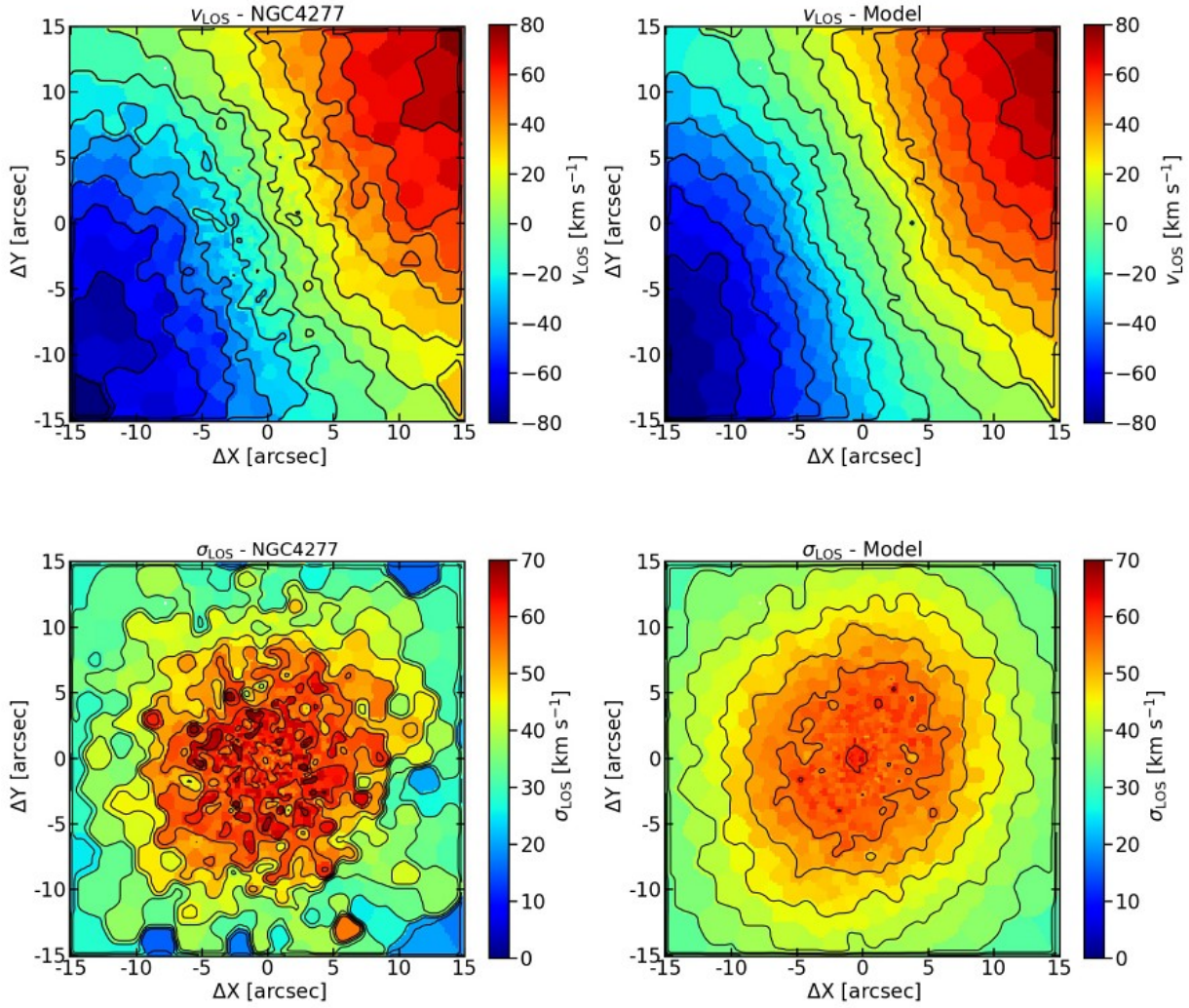

Figure 6.14: Kinematic comparison between NGC 4277 and model 761DB. Observed (*left panels*) and modelled (*right panels*) LOS stellar velocity (*top panels*) and dispersion velocity (*bottom panels*) maps of the bar region. Black lines represent some contour levels. The FOV is 0.5×0.5 arcmin^2 and oriented with the north up and the east left.

To confirm the validity of the approach we adopted in Chapter 5 for the dynamical modelling of NGC 4277, we recovered the mass distribution of the stellar and DM components of the model 761DB with JAM. First, we parameterised the particle surface mass density of model 761DB as the sum of a set of Gaussian components by applying the MGE algorithm on the mock image of the model. We adopted the same prescriptions adopted for modelling the surface brightness of NGC 4277 by keeping constant the centre and position angle of the fitting Gaussians and restricting the range of their axial ratios (Fig. 6.16, left panel). Then, we obtained the map of the second-order velocity moment $V_{\rm rms}$ of the particles of model 716DB. We modelled the total mass distribution of the particles as the sum of a luminous component that follows the star particle distribution and a DM component that is distributed in a spherical halo as done in Chapter 5 for NGC 4277.

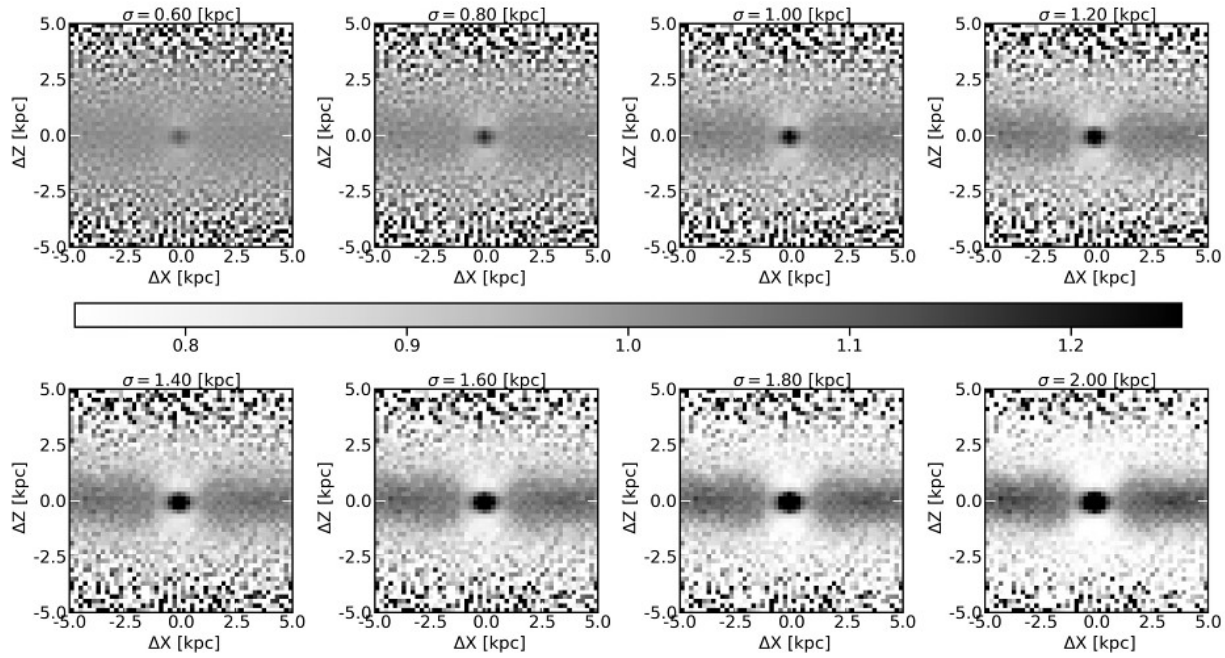

Figure 6.15: Unsharp mask for different sizes of the Gaussian kernel ($\sigma = 0.60, 0.80, ..., 2.00$ kpc) of the edge-on particle density distribution of the best snapshot of model 761DB.

We tested mass models with QI and NFW DM profiles and we performed several tests by varying the extension of the kinematic data, disc inclination, and anisotropy parameter. We found that all the mass models were able to properly fit the disc inclination and decided to fix the inclination to build the final set of mass models. We found that the mass model with a QI DM halo has a lower χ^2_ν than that with a NFW DM halo ($\Delta\chi^2_\nu$=0.6). From the best-fitting parameter of the mass model with the QI DM halo, we derived the corresponding DM fraction enclosed within the bar region $f^{\rm QI}_{\rm DM} = 0.41^{+0.17}_{-0.13}$ and the radial profiles of the circular velocity for the stars, DM, and their sum (Fig. 6.16, right panel), as described in Chapter 5. The value of the DM fraction is consistent within uncertainty with the value recovered from the application of the JAM on NGC 4277 ($f^{\rm QI}_{\rm DM} = 0.53 \pm 0.02$). The radial profile of circular velocity profiles, instead, show some deviations with respect to the true rotation curves of the particles. Due to the small uncertainties of the JAM predictions, the profiles of the stellar components are not consistent within errors with each other and with the true rotation curve of the star particles. The DM and total components, instead, are in agreement and consistent within 1σ error with respect to each other. These preliminary results validate the assumptions that we made when comparing NGC 4277 to the N-body simulation. Moreover, we confirmed the reliability of the application of the JAM model on barred galaxies like NGC 4277. We stress that our aim is not to find the perfect simulation matching a particular galaxy, but show that simple galaxy models may provide a reasonable description of a real barred galaxy in terms of photometry, stellar kinematics, and mass distribution.

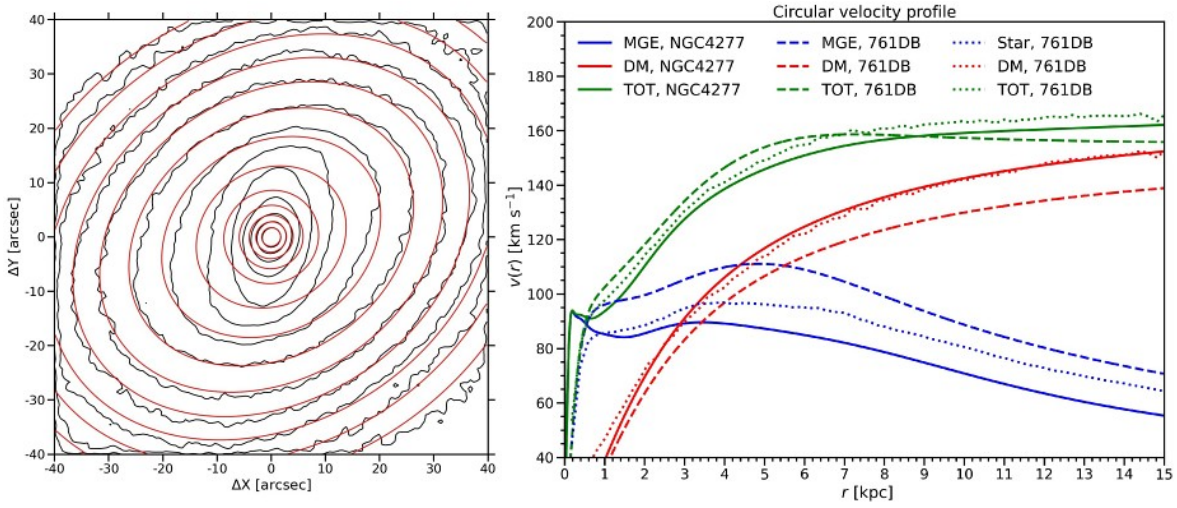

Figure 6.16: *Left panel*: MGE model of 761DB. The black and red lines represent some reference isophotes for the particle surface mass density of 761DB and MGE model, respectively. The FOV is $1.3\times1.3\,\mathrm{arcmin}^2$ and is oriented with north up and east left. *Right panel*: Radial profiles of circular velocity of the best-fitting parameters of the JAM model of NGC 4277 (solid lines) and model 761DB (dashed line), and mid-plane rotation curves of model 761DB (dotted lines) for the stars (blue lines), DM (red lines), and their sum (green lines). We do not show the associated error to improve the clarity of the figure.

6.5 Conclusions

We constructed stellar N-body simulations to mimic the photometric and kinematic properties of the lenticular barred galaxy NGC 4277. This galaxy hosts a short, weak and slow bar and it has a large fraction of DM within the bar region. We set up the initial conditions using the GalactICS (Kuijken & Dubinski, 1995; Widrow & Dubinski, 2005; Widrow et al., 2008) software to construct axisymmetric and equilibrium models of galaxies composed of a Sérsic bulge, an exponential disc, and a truncated NFW DM halo. We used the tree code pkdgrav (Stadel, 2001) to evolve the models up to $t = 14\,\mathrm{Gyr}$, to track the formation of the bar and the time evolution of its parameters.

We wrote a dedicated Python code to project the model at the same orientation of NGC 4277 on the sky, rescale the bar size and rotation curve amplitude, and perform both a photometric and kinematic comparison. We rescaled and rotated the position of the particles of the model to project the simulation at the same distance and orientation of NGC 4277 on the sky plane. We convolved the surface mass density of the particles with a Gaussian kernel to mimic the smearing effects of seeing and we projected the resulting image on the galaxy plane. We performed a Fourier analysis of the image of the galaxy model to measure R_{bar} and S_{bar}. We matched the bar size in NGC 4277 by multiplying the particles of the galaxy model by a factor equal to the ratio between the bar size measured in observations and on the mock image. We also rescaled the velocities of particles to match the same amplitude of the observed rotation curve. We first applied the same Voronoi binned map of the observation to the simulation. We fitted the resulting LOSVD of particles in each bin with a Gauss-Hermite function (Gerhard, 1993; van der Marel & Franx, 1993a) to recover the V_{LOS} and σ_{LOS} of the particles. We extracted the stellar kinematics in a slice along the disc major axis to recover the rotation curve. We scaled the model kinematics by multiplying by a factor equal to the ratio between the amplitudes of the observed and modelled rotation curves.

For each snapshot of each galaxy model, we performed a photometric and stellar kinematic comparison with the observations. We performed a χ^2 minimisation looking for the best combination of scaling factors ($\eta_{\rm pos}$, $\eta_{\rm vel}$) that minimise both the Fourier analysis and stellar kinematic maps in the bar region. For the photometric comparison, we performed a χ^2 minimisation of the radial profiles of $m = 2, 4, 6$ Fourier amplitudes and $m = 2$ phase angle ϕ_2 excluding the outermost regions to avoid the contribution of the disc. For the kinematic comparison, we performed a χ^2 minimisation of the $V_{\rm LOS}$ and $\sigma_{\rm LOS}$ maps between observations and model selecting a region that enclosed only the bar contribution.

We built several galaxy models and explored different combinations of bulge, disc, and halo parameters. We found that the bar formation and the evolution of the bar strength depend on the dynamical properties of the bulge and the disc. Bar formation occurs early in models composed of a thin and cool disc, whereas bar formation is delayed or never occurs in thick and hot discs. This happens because cool and thin discs are unstable to bar instabilities and more prone to bar formation, while thick and hot discs are more robust to bar instabilities (Sellwood & Wilkinson, 1993; Martinez-Valpuesta et al., 2006). In hotter discs, $S_{\rm bar}$ steeply increases for a few Gyr as the bar formation starts, and then it remains almost constant or slowly increases until the end of the simulation. In cooler discs, instead, $S_{\rm bar}$ abruptly increases in the early phases and keeps strongly growing for the whole simulation. As the disc becomes thicker, the change of slope becomes smoother. Galaxies with a too compact or too massive bulge do not form a bar. This is in agreement with the results obtained by Athanassoula (2003), who found a delay in the bar formation in galaxy models with a massive central structure.

We explored and analysed several galaxy models and we found that a galaxy model characterised by a massive DM halo best reproduces both the Fourier analysis and stellar kinematics maps of the observed galaxy. We analysed the evolution of the bar parameters with time. We found that the $S_{\rm bar}$ mildly increases as the bar starts to form to the end of the whole evolution, while $\Omega_{\rm bar}$ always decreases. During the evolution, the bar radius keeps growing too. This means that the bar becomes slower and its $\mathcal{R}$ increases moving towards an even slower regime. Our results agree with the prediction obtained by the JAM dynamical modelling, which found a considerable DM fraction in the innermost region of NGC 4277. Our models evolved in an isolated environment, therefore it is not possible to confirm that the formation of the slow bar hosted in NGC 4277 was triggered by the tidal interaction with the companion NGC 4273. Our results confirmed that the bar hosted in NGC 4277 had experienced a slowdown as a consequence of the interaction with a centrally-concentrated DM halo.

Fux (1997) first used 3D self-consistent barred models to study the spiral structure of the Milky Way and constrain the properties and orientation of its bar by using the COBE K-band photometric data, the radial velocity dispersion profile of M giant stars in the Baade's Window, and H I and CO gas dynamics. Later, Athanassoula & Beaton (2006) attempted to study the properties of the M31 galaxy and its bar orientation by using different N-body simulations and comparing isodensity contours, radial luminosity profiles, and position-velocity diagrams of the gaseous component. Our results showed that by using simple galaxy models it is possible to reasonably match simultaneously both the photometric and stellar kinematic properties of a barred galaxy.

Chapter 7

Conclusions and future perspectives

7.1 Conclusions

In this thesis, we aimed at investigating the nature and dynamics of barred galaxies by studying ultrafast, fast, and slow bars and analysing the internal structure of their host galaxies using dynamical models and N-body simulations. Here we summarised the main results.

Chapter 2: Solving the problem of ultrafast bars

We revisited the case of ultrafast bars, that live in more than 10% of barred galaxies with a direct measurement of $\Omega_{\rm bar}$. These findings are dynamically in disagreement with the theoretical predictions about the stability of stellar orbits supporting the bar (Contopoulos, 1981). We decided to test whether these ultrafast bars are actually an artefact due to an overestimated value of $R_{\rm bar}$ and/or underestimated value of $R_{\rm cor}$ rather than a new class of non-axisymmetric stellar components, whose orbital structure has not been yet understood.

- We selected a sample of 12 barred galaxies from the CALIFA survey that host a bar classified as ultrafast not only if the corresponding bar rotation rate $\mathcal{R}$ is lower than 1 at 95% confidence level, but also if the sum between $\mathcal{R}$ and its upper error is lower than 1. We performed a visual inspection of the colour images of the galaxies and we concluded that most of the galaxies in our sample ($\sim$60%) host inner rings or pseudorings around the bar.

- We remeasured $R_{\rm bar}$ adopting the independent method proposed in Lee et al. (2020) based on the solution of the Poisson equation and using the transverse-to-radial ratio map $Q_{\rm T}(r)$. This method identifies a barred galaxy when the azimuthal profile of the ratio map at the bar radius $Q_{\rm T}(R_{\rm Qb})$ presents four peaks corresponding to the four wings of a typical butterfly-shaped pattern (Buta et al., 2001). This method disentangles the radius corresponding to the maximum strength of the bar from that of the spiral arms and/or of rings by comparing the azimuthal profile of the ratio map at different radial distances and looking for the position of the local maxima of the azimuthal profiles in the image of the galaxy.

- For all the sample galaxies, we found that the bar radius $R_{\rm Qb}$ measured from the analysis of the ratio map is shorter than that obtained with other methods based on ellipse fitting and Fourier analysis of the deprojected galaxy image. These methods turned out to be quite sensitive to the presence of rings, pseudo-rings, and spiral arms and lead to systematically larger values of $R_{\rm bar}$.

- Adopting $R_{\rm Qb}$, the new measure of $\mathcal{R}$ resulted systematically larger with respect to the value obtained by using the previous measure of bar radius. All the galaxies hosting an ultrafast bar turned out to host a fast bar at 95% confidence level, with the only exception represented by NGC 6497. This galaxy was previously discussed in detail by Aguerri et al. (2015) and Garma-Oehmichen et al. (2020). Aguerri et al. (2015) analysed the galaxy extinction map to rule out problems in measuring $R_{\rm bar}$ due to dust and considered the gas kinematics to check the value of $V_{\rm circ}$ and hence $R_{\rm cor}$ obtained from the stellar dynamics. Garma-Oehmichen et al. (2020) reassessed the error budget of $\Omega_{\rm bar}$ by considering a broader set of error sources affecting the TW method. They remeasured $\Omega_{\rm bar}$ and recalculated $R_{\rm cor}$ obtaining a new value of $\mathcal{R} = 1.08^{+0.31}_{-0.25}$ which makes NGC 6497 fully consistent with the fast-bar regime. We can confidently conclude that ultrafast bars are no longer observed when a correct measurement of $R_{\rm bar}$ is adopted.

The results of this chapter are published in Cuomo et al. (2021).

Chapter 3: A slow bar in the lenticular barred galaxy NGC 4277

We fully characterised the properties of the bar hosted in NGC 4277, a lenticular barred galaxy located in the direction of the Virgo cluster at a distance of $D = 33.9$ Mpc. Thanks to the deep SDSS imaging in combination with the extended spectral range, fine spatial sampling, and large FOV of the MUSE spectrograph, we accurately derived the surface photometry, stellar kinematics, and bar properties of the galaxy.

- We retrieved the SDSS i-band image of NGC 4277 to study the photometric properties of the galaxy and to recover $R_{\rm bar}$ and $S_{\rm bar}$. The galaxy presents typical properties of barred galaxies. From the isophotal analysis of the deprojected image of the galaxy, we found that the ellipticity ϵ exhibits a local maximum in the bar region, associated with a nearly constant position angle PA. From the Fourier decomposition of the deprojected image of the galaxy, we found that the $m = 2, 4, 6$ even Fourier amplitudes are prominent in the bar region, especially the $m = 2$, which is the dominant one. We derived $R_{\rm bar}$ and $S_{\rm bar}$ from a combination of different methods and compared their values with the typical values for early-type barred galaxies. We concluded that NGC 4277 hosts a short and weak bar.

- We applied the TW method on the reconstructed MUSE image of NGC 4277 to recover $\Omega_{\rm bar}$. NGC 4277 is an ideal target for the application of the TW method since it has an intermediate inclination, its bar is oriented at an intermediate angle between the major and minor axes of the disc, and it shows no evidence of spiral arms or patchy dust. Thanks to the integral-field spectroscopic data, the pseudo-slits can be defined *a posteriori* reconstructing the image of NGC 4277 from the MUSE datacube. We derived the photometric integrals $\langle X \rangle$ from the MUSE reconstructed image by measuring the luminosity-weighted position of the stars in 9 pseudo-slits of width equal to 1.8 arcsec and semi-length of 35 arcsec. We derived the kinematic integrals $\langle V \rangle$ by summing all the spaxels of each pseudo-slit to obtain a single spectrum from which we measured the luminosity-weighted stellar LOS velocity with PPXF routine in the same wavelength range adopted for the stellar kinematics. We derived $\Omega_{\rm bar}$=24.7±3.4 km s^{-1} kpc^{-1} using the FITEXY algorithm taking into account errors on both $\langle X \rangle$ and $\langle V \rangle$. We finally derived $\mathcal{R}$=$1.8^{+0.5}_{-0.3}$, and we concluded that NGC 4277 hosts a slow bar.

- NGC 4277 is the first bright galaxy known to host a slow bar. The probability of the bar of NGC 4277 being slow (91%) is ten times higher than that of being fast (9%). The bar pattern speed ($\Delta\Omega_{\rm bar}/\Omega_{\rm bar}\sim$ 0.14) and rotation rate ($\Delta\mathcal{R}/\mathcal{R}\sim$ 0.21) are amongst the best-constrained ones ever obtained with the TW method applied on a stellar tracer. We quantified the systematic uncertainty due to a possible misalignment of the pseudo-slit with the disc major axis. The bar in NGC 4277 remains slow at face value even if the misalignment between the pseudo-slits and the disc is ΔPA$= 1\overset{\circ}{.}5$. Moreover, these results hold even if we adopt the galaxy inclination for a thick rather than an infinitesimally-thin stellar disc ($\mathcal{R}$=$2.0^{+0.6}_{-0.5}$).

The results of this chapter are published in Buttitta et al. (2022).

Chapter 4: A slow lopsided bar in the interaction dwarf galaxy IC 3167

We fully characterised the properties of the bar hosted in IC 3167, a dwarf barred galaxy located in the Virgo cluster.

- We retrieved the SDSS i-band image of IC 3167 to study the photometric properties of the galaxy and to recover $R_{\rm bar}$ and $S_{\rm bar}$. The galaxy presents an off-centred bar with a peculiar triangular shape. From the isophotal analysis of the deprojected image of the galaxy, we found that the ellipticity ϵ exhibits a local maximum in the bar region, associated with a nearly constant position angle PA. The bar is remarkably lopsided, as it results from the peak in the third sine Fourier coefficient profile. From the Fourier decomposition of the deprojected image of the galaxy, we found that the $m = 2, 4, 6$ even Fourier amplitudes are prominent in the bar region, especially the $m = 2$, which is the dominant one. The asymmetry in the radial profile of the $m = 2, 4$ components indicates that the bar does not have a bisymmetric shape. Moreover, the $m = 1, 3, 5$ odd components have large values within the bar region. We derived $R_{\rm bar}$ and $S_{\rm bar}$ from a combination of different methods and we concluded that IC 3167 hosts a short and weak bar.

- We applied the TW method on the reconstructed MUSE image of IC 3167 to recover $\Omega_{\rm bar}$. Thanks to the integral-field spectroscopic data, the pseudo-slits can be defined *a posteriori* reconstructing the image of IC 3167 from the MUSE datacube. We derived the photometric integrals $\langle X\rangle$ from the MUSE reconstructed image by measuring the luminosity-weighted position of the stars in 7 pseudo-slits of width equal to 1.8 arcsec and semi-length of 25 arcsec. We derived the kinematic integrals $\langle V\rangle$ by summing all the spaxels of each pseudo-slit to obtain a single spectrum from which we measured the luminosity-weighted stellar LOS velocity with PPXF routine in the same wavelength range adopted for the stellar kinematics. We derived $\Omega_{\rm bar}$=30.0 ± 5.4 km s^{-1} kpc^{-1} using the FITEXY algorithm taking into account errors on both $\langle X\rangle$ and $\langle V\rangle$. We finally derived $\mathcal{R}$=$1.7^{+0.5}_{-0.3}$, and we concluded that IC 3167 hosts a slow bar with a peculiar triangular shape.

- Galaxies hosting a lopsided bar are quite rare and remain a poorly known class of objects. IC 3167 is the third galaxy for which the photometric and kinematic properties of its asymmetric and off-centred bar have been studied in detail to date.

The results of this chapter are published in Cuomo et al. (2022).

Chapter 5: Bar rotation rate as a diagnostic of dark matter content in the centre of disc galaxies

We investigated the link between $\mathcal{R}$ and DM content in barred galaxies by focusing on two lenticular galaxies, NGC 4264 and NGC 4277, that host a fast and slow bar, respectively. We derived the DM fraction $f_{\rm DM,bar}$ within the bar region from Jeans axisymmetric dynamical models by matching the stellar kinematics obtained with MUSE and using SDSS images to recover the stellar mass distribution.

- NGC 4264 and NGC 4277 are two early-type barred galaxies with similar morphology, luminosity, and size. These galaxies are ideal targets for the application of JAM since they have an intermediate inclination, are poorly contaminated by dust, and host a weak bar with an intermediate orientation with respect to the disc major and minor axis. In addition, the fine spatial sampling, wide FOV, and high spectral resolution of MUSE made it possible to accurately map the stellar kinematics all throughout the galaxy disc. For both galaxies, we obtained the best-fitting parameters for all the mass models without and with a DM halo.
- For NGC 4264, the predicted second velocity moment of the mass-follows-light model matches the overall shape of the observed iso-velocity contours, but it fails to match the location and amplitude of the double peak of the observed $V_{\rm rms}$. The mass models with a DM halo provided a better fit to the observed $V_{\rm rms}$, although did not correctly reproduce the decrease measured at large radii. The DM fraction within the bar region is $f_{\rm DM,bar} \sim 0.3$, this suggests that the mass budget of NGC 4264 is baryon dominated in the radial range mapped by the kinematic data.
- For NGC 4277, the predicted second velocity moment of the mass-follows-light model does not match the observed $V_{\rm rms}$ in terms of amplitude and shape of the iso-velocity contours, therefore, we concluded that the best-fitting mass model of NGC 4277 requires a DM halo. The DM fraction within the bar region is $f_{\rm DM,bar} \sim 0.5$, this result suggests that NGC 4277 hosts a consistent DM amount.
- Our results are in agreement with the predictions of theoretical works and findings of numerical simulations: fast bars are expected to live in baryon-dominated discs, whereas slow bars experienced a strong drag from the dynamical friction due to a dense DM halo. This is the first time that $\mathcal{R}$ is coupled to $f_{\rm DM,bar}$ obtained from dynamical modelling.

We present the results of this chapter in Buttitta et al. (2022, submitted).

Chapter 6: Photometric and kinematic comparison with N-body simulations

We constructed stellar N-body simulations to mimic the photometric and kinematic properties of NGC 4277. This galaxy hosts a short, weak, and slow bar and it has a considerable DM fraction within the bar region. NGC 4277 is characterised by a prominent and round bulge, an axisymmetric and unwarped disc, and an elongated bar that lies at an intermediate orientation with respect to the disc major axis. It shows no evidence of spiral arms or patchy dust, and this makes NGC 4277 a suitable candidate for a photometric and kinematic analysis and comparison with pure stellar N-body simulations.

- We used GalactICS software to construct axisymmetric and equilibrium models of galaxies composed of a Sérsic bulge, an exponential disc, and a truncated NFW DM halo. We used the tree code pkdgrav (Stadel, 2001) to evolve the models up to $t = 14$ Gyr, to track the formation of the bar and the time evolution of its parameters. We wrote a dedicated Python code to project the model at the same orientation of NGC 4277 on the sky, rescale the bar size and rotation curve amplitude, and compare both the photometric and kinematic properties by performing a χ^2 minimisation of the Fourier analysis and velocity maps in the bar region.

- We built several galaxy models and explored different combinations of bulge, disc, and DM halo parameters. We found that the bar formation and evolution of the $R_{\rm bar}$, $S_{\rm bar}$, and $\Omega_{\rm bar}$ depend on the dynamical properties of the disc and bulge Debattista & Sellwood (1998); Athanassoula & Misiriotis (2002); Athanassoula (2003). Bar formation occurs early in models composed of a thin and cool disc, while bar formation is delayed or never occurs in thick and hot discs. In hotter discs, $S_{\rm bar}$ steeply increases for a few Gyrs as the bar formation starts, and then it remains almost constant or slowly increases until the end of the simulation. In cooler discs, instead, the bar strength abruptly increases in the early phases and keeps growing strongly for the whole simulation. As the disc becomes thicker, the change of slope becomes smoother. Galaxies with a too compact or too massive bulge do not form a bar. This is in agreement with the results obtained by Athanassoula (2003), who found a delay in the bar formation in galaxy models with a massive central structure.

- The galaxy model that best reproduces both the photometry and the kinematics of NGC 4277 is characterised by a massive DM halo. Our results agree with the prediction obtained by dynamical modelling, which found a large DM fraction in the innermost region of NGC 4277. Thus we confirmed that the bar hosted in NGC 4277 had experienced a strong drag as a consequence of the interaction with a dense DM halo. Moreover, we recovered the same bar pattern speed with the TW method and mass distribution with JAM as NGC 4277. We showed that by using simple galaxy models it is possible to reasonably match simultaneously both the photometric and kinematic properties of a barred galaxy.

We aim at presenting the results of this chapter in Buttitta et al. (in preparation).

7.2 Future perspectives

Dark matter content in dwarf barred galaxies

Dwarf galaxies are commonly considered to host a dense DM halo (Cote et al., 1991). They are the ideal candidates to host slow rotating bars since the exchange of angular momentum with the halo is responsible for the slowdown of the bar (Debattista & Sellwood, 1998, 2000). Dwarf galaxies have a small size and low luminosity, therefore their properties are still poorly known due to the difficulty of identifying and observing them in detail. Characterising the bar properties in dwarf barred galaxies will permit not only to constrain the DM mass distribution in the innermost regions of the galaxy but also to test the bar formation mechanisms.

We aim at constraining the DM content in a small sample of dwarf barred galaxies observed with MUSE (Prog. Id. 0106.B-0158(A); P.I.: V. Cuomo) by characterising the bar properties and deriving $\mathcal{R}$. The galaxies were selected to fully satisfy the requirements for the application of the TW method (Fig. 7.1). They are low inclined systems with a bar oriented at an intermediate angle

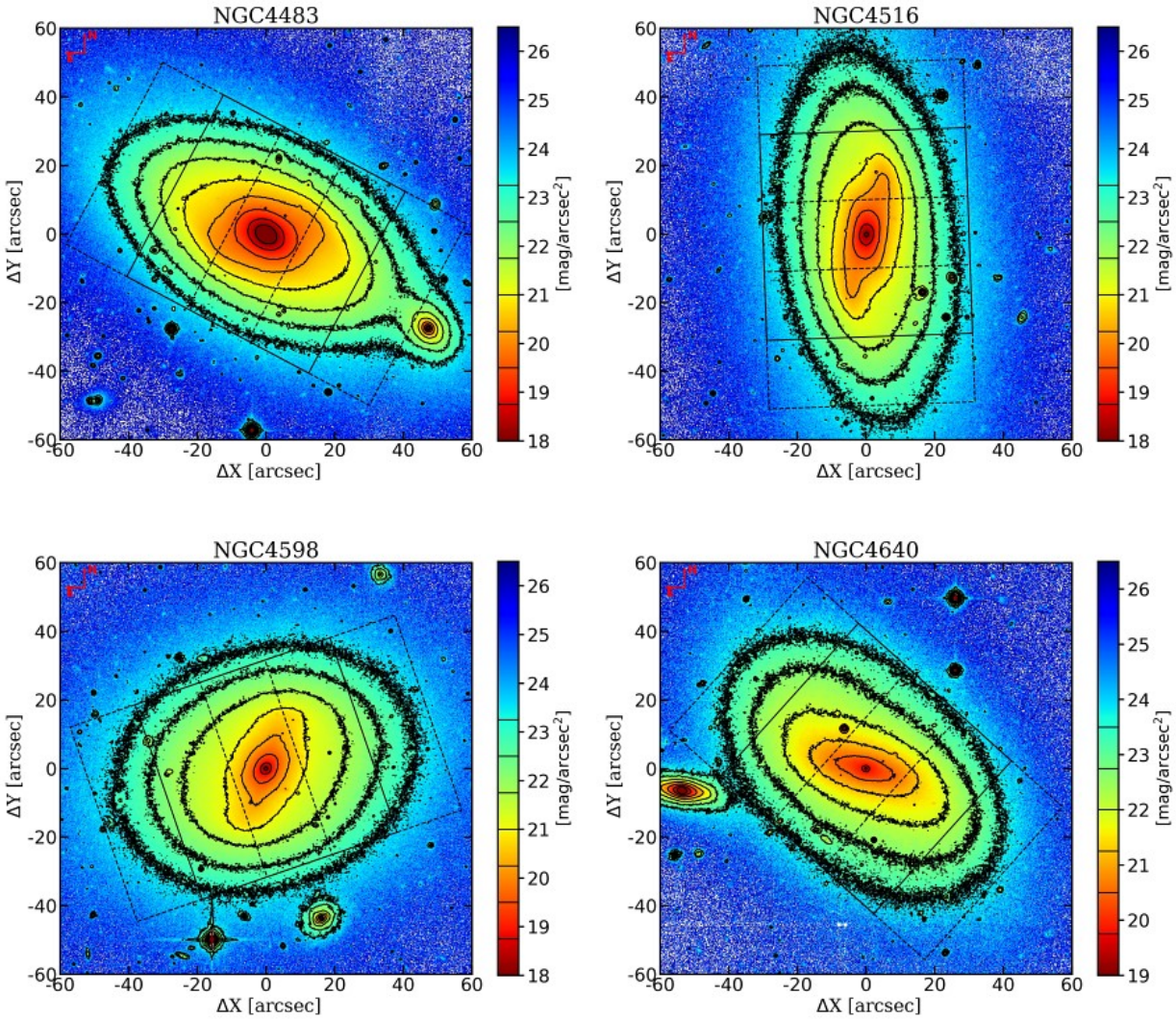

Figure 7.1: Dwarf barred galaxies selected for the TW analysis. The FOV is 2×2 arcmin^2 and is oriented with the north up and east left. Some reference isophotes are over-plotted with black lines. The three squares mark the MUSE central (solid lines) and offset (dashed lines) pointings. The images were taken by the Next Generation Virgo Cluster Survey (NGVS, Ferrarese et al. (2012).

between the disc major and minor axes, there is no dust contamination or ongoing star-forming activity, and the FOV is free from bright foreground stars or nearby galaxies.

We will conduct an accurate analysis of the surface brightness distribution by analysing the archival images and performing an isophotal and Fourier analysis. We will recover the geometrical parameters of the disc, $R_{\rm bar}$, and $S_{\rm bar}$. We will recover $\Omega_{\rm bar}$ by applying the TW method. MUSE data will allow us to carefully address the sources of errors in the TW method, fine-tune the location of the pseudo-slits varying their width and length *a posteriori*, and adjust the extraction of the photometric and kinematic integrals. Finally, we will derive $\mathcal{R}$ to constrain the DM content.

This study will increase the sample of direct measurements of $\Omega_{\rm bar}$ in dwarf barred galaxies.

Application of the JAM code to simulated barred galaxies

Recovering the mass distribution in a barred galaxy is a challenging task since the parameterisation of the bar requires two additional parameters, the orientation PA_{bar} and Ω_{bar} (Lablanche et al., 2012). These quantities, combined with the non-uniqueness of the light deprojection (Rybicki, 1987; Gerhard & Binney, 1996), increase the degeneracy between the model parameters. Indeed, different combinations reproduce the observed photometric and kinematic properties of the galaxy.

In general, barred galaxies are modelled with axisymmetric dynamical models including the JAM model (Cappellari, 2008). This method predicts the LOS second velocity moment for galaxies with an axisymmetric mass distribution, possibly including a DM halo, to be compared with the root-mean-square velocity V_{rms} derived from observed velocity V_{LOS} and velocity dispersion σ_{LOS}. JAM requires the surface-brightness distribution of the galaxy to be described through the MGE parameterization (Cappellari, 2002), which makes straightforward the solution of Jeans equations. Lablanche et al. (2012) already applied this method to realistic simulations of two SB0 galaxies to explore the reliability of the JAM approach in recovering the dynamical parameters. Their results confirmed that recovered dynamical parameters are biased by the non-uniqueness of the mass deprojection, but also depend on the inclination of the disc and bar orientation. Their pilot study focuses on mass models without the contribution of a DM halo, spanning a narrow range of possible inclinations and bar orientations.

We will investigate the reliability of the application of a JAM model to simulated barred galaxies. We want to investigate a wide range of bar shapes, sizes, and strengths, and test different DM halo parameterisations. A systematic application of the JAM code to simulated barred galaxies will provide realistic estimates of the accuracy, uncertainties, and biases on the recovered parameters.

Lopsided bars in simulated barred galaxies

Bars are typical bisymmetric structures with a boxy shape (Debattista et al., 2006; Méndez-Abreu et al., 2018a) but some of them are asymmetric (Odewahn, 1994; Kruk et al., 2017). The presence of lopsided bars in non-interacting and isolated galaxies has been thought of as evidence for the gravitational pull of an asymmetric DM halo (Kruk et al., 2017). Łokas (2021b) explored two scenarios that can lead to the formation of a lopsided bar by using cosmological simulations: the interaction between a Milky Way-like barred galaxy and a massive satellite, and the evolution of an off-centred disc with respect to its DM halo. Both mechanisms are responsible for the formation of a displaced bar with some degree of asymmetry.

We aim at investigating the formation of lopsided bars in simulated galaxies that evolve in an isolated environment. Some of our collisionless stellar galaxy models show short phases along the evolution in which the bar develops a clear asymmetry (Fig. 7.2).

We want to explore if the formation of these lopsided bars depends on the disc, bulge, or DM halo parameterisation, and how the photometric properties of these bars evolve in time and test if these features can be easily observed on real barred galaxies. We propose to quantify the asymmetry of the lopsided bar by performing a Fourier and isophotal analysis on the mass density of particles in different galaxy models at several evolutionary phases. By tracing the time evolution of the photometric signature of lopsided bars it will be possible to test if these bars are short-lived or long-term structures and in which way affect the global morphology of the host galaxy.

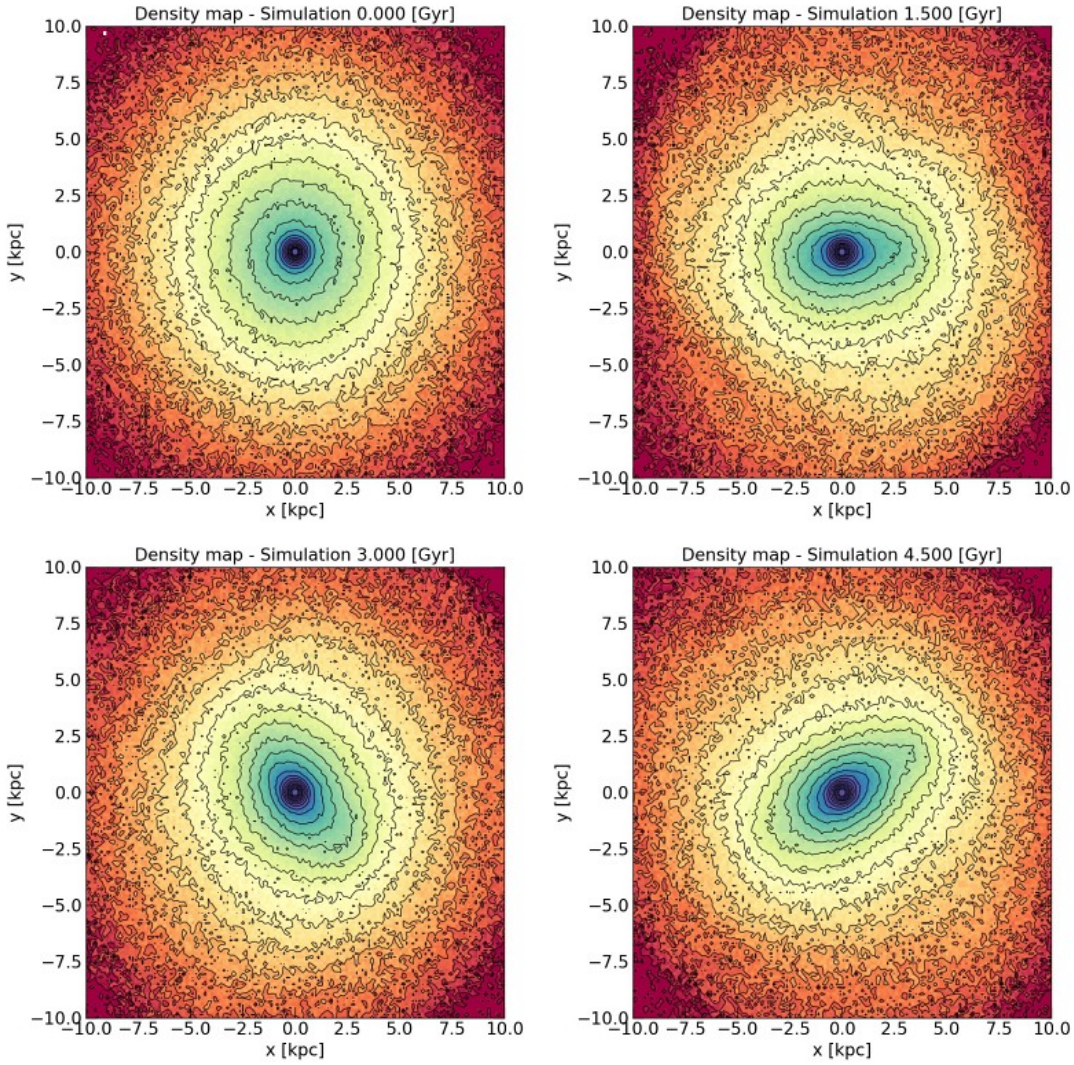

Figure 7.2: Time evolution of the density map of a simulated barred galaxy with an asymmetric bar. Some reference isodensity contours are over-plotted with black lines. From Buttitta et al. (in prep.)

Dynamical models of barred galaxies with the Schwarzschild orbit-superposition method

In Chapter 5, we built a dynamical model of two barred galaxies, NGC 4264 and NGC 4277, by applying the JAM method. We are going to improve the dynamical model of these galaxies by using Schwarzschild orbit-superposition method (Schwarzschild, 1979). This method assumes a galaxy gravitational potential and builds a model by summing the contribution of different families of stellar orbits, whose weights are determined by computing the solution of an optimisation problem that includes the surface brightness distribution of the galaxy and the full knowledge of the LOSVD. It has been recently developed for tumbling bars and applied to mock galaxies with integral-field spectroscopic data extracted from N-body simulations (Vasiliev & Valluri, 2020; Tahmasebzadeh et al., 2022). In Fig. 7.3, we show the stellar kinematics maps of NGC 4264 and NGC 4277, whose properties were extensively studied by Cuomo et al. (2019a) and Buttitta et al. (2022), respectively.

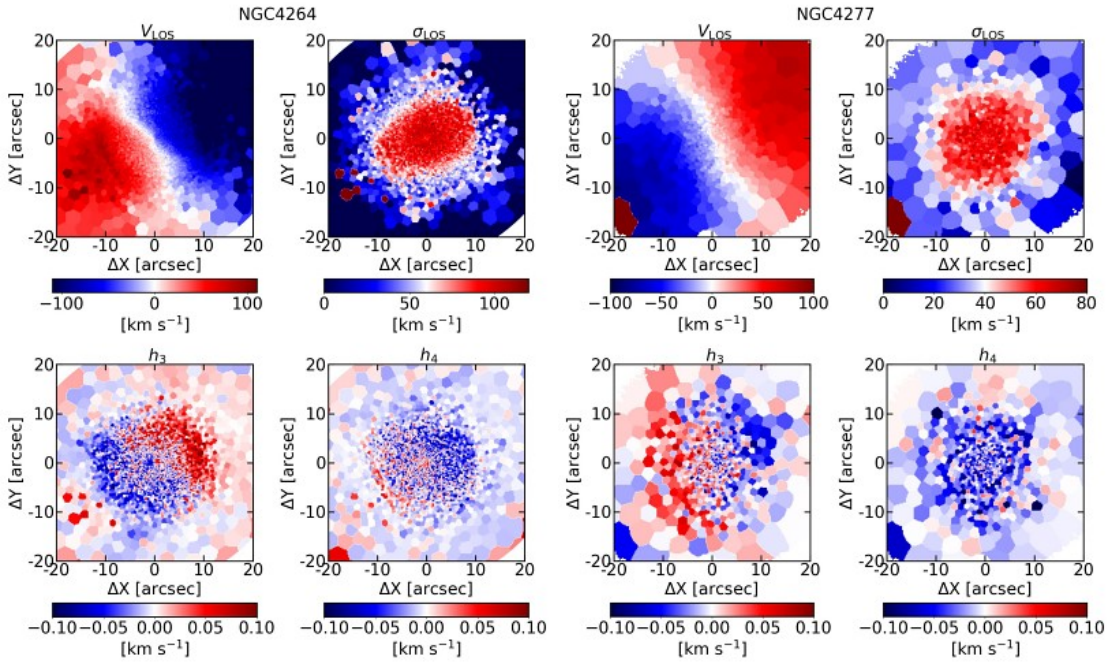

Figure 7.3: Stellar kinematics maps of NGC 4264 (*left panels*) and NGC 4277 (*right panels*). For each galaxy, we show the LOS velocity $V_{\rm LOS}$ subtracted of systemic velocity (*top left*), velocity dispersion $\sigma_{\rm LOS}$ corrected for $\sigma_{\rm inst}$ (*top right*), third-velocity moment h_3 (*bottom left*), and fourth-velocity moment (*bottom right*). The maps were derived from the $S/N = 40$ Voronoi binned MUSE data. The FOV is $40 \times 40\,\mathrm{arcsec}^2$ and is oriented north up and east to the left.

These galaxies have deep SDSS imaging and high-quality MUSE spectroscopy, which we used to derive the galaxy and bar properties and obtain an accurate measurement of the stellar kinematics. We measured the stellar kinematics in both galaxies from the MUSE combined datacube using the GIST pipeline (Bittner et al., 2019). We first performed a Voronoi binning with a target of $S/N = 40$ per bin to ensure an accurate measure of the stellar kinematics. The galaxy spectrum in each bin is modelled convolving a LOSVD, parameterised with a truncated Gauss-Hermite series (Gerhard, 1993; van der Marel & Franx, 1993a), with a combination of stellar templates. We adopted the INDOUS stellar library (FWHM=1.1Å, Valdes et al., 2004) in the wavelength range $8300 - 9000$ Å centred on the Ca II$\lambda\lambda$8498, 8542, 8662Å absorption-line triplet. For each bin, we obtained the mean LOS velocity $V_{\rm LOS}$, velocity dispersion $\sigma_{\rm LOS}$, third-velocity moment h_3 and fourth-velocity moment h_4 of the stellar component. We finally estimated the errors on the kinematic parameters using Monte Carlo simulations. In both galaxies, the stellar kinematics maps clearly show the bar signatures: an asymmetric S-shape velocity field, a broad and flat central velocity dispersion peak, and a $V_{\rm LOS} - h_3$ anti-correlation (Bureau & Athanassoula, 2005; Martinez-Valpuesta et al., 2017). The $V_{\rm LOS} - h_3$ anti-correlation is the signature of the presence of nuclear disc, which is supported by the near-circular orbits of the x_2 family (Gadotti et al., 2020).

NGC 4264 and NGC 4277 are amongst the barred galaxies with the best-studied bar properties in terms of surface-brightness distribution, stellar kinematics, and mass modelling. For this reason, they are ideal candidates to be adopted as a test bench in applying the Schwarzschild orbit-superposition dynamical models. We aim to recover the luminous and DM distributions and reconstruct the three-dimensional stellar orbital structures in barred galaxies.

List of Figures

List of Tables

Bibliography

Abazajian K. N., et al., 2009, ApJS, 182, 543

Abolfathi B., et al., 2018, ApJS, 235, 42

Abraham R. G., Merrifield M. R., 2000, AJ, 120, 2835

Adams J. J., et al., 2014, ApJ, 789, 63

Aguerri J. A. L., Muñoz-Tuñón C., Varela A. M., Prieto M., 2000, A&A, 361, 841

Aguerri J. A. L., Debattista V. P., Corsini E. M., 2003, MNRAS, 338, 465

Aguerri J. A. L., Méndez-Abreu J., Corsini E. M., 2009, A&A, 495, 491

Aguerri J. A. L., et al., 2015, A&A, 576, A102

Algorry D. G., et al., 2017, MNRAS, 469, 1054

Athanassoula E., 1992, MNRAS, 259, 345

Athanassoula E., 2000, Alloin D., Olsen K., Galaz G., eds, ASP Conf. Series Vol. 221, Stars, Gas and Dust in Galaxies: Exploring the Links. (San Francisco: Astronomical Society of the Pacific), p. 243

Athanassoula E., 2003, MNRAS, 341, 1179

Athanassoula E., 2013, Falcón-Barroso J., Knapen J. H., eds, Secular Evolution of Galaxies. Canary Islands Winter School of Astrophysics Lectures. (Cambridge: Cambridge University Press), p. 305

Athanassoula E., 2016, Laurikainen E., Peletier R., Gadotti D., eds, Astrophysics and Space Science Library Vol. 418, Galactic Bulges. (Cham: Springer), p. 391

Athanassoula E., Beaton R. L., 2006, MNRAS, 370, 1499

Athanassoula E., Misiriotis A., 2002, MNRAS, 330, 35

Athanassoula E., Bosma A., Papaioannou S., 1987, A&A, 179, 23

Athanassoula E., Morin S., Wozniak H., Puy D., Pierce M. J., Lombard J., Bosma A., 1990, MNRAS, 245, 130

Athanassoula E., Romero-Gómez M., Bosma A., Masdemont J. J., 2009, MNRAS, 400, 1706

Athanassoula E., Romero-Gómez M., Masdemont J. J., 2011, Mem. Soc. Astron. Ital. Sup., 18, 97

Athanassoula E., Machado R. E. G., Rodionov S. A., 2013, MNRAS, 429, 1949

Bacon R., et al., 2010, McLean I. S., Ramsay S. K., Takami H., eds, Proc. SPIE Vol. 7735, Ground-based and Airborne Instrumentation for Astronomy III. (Bellingham: SPIE), p. 773508

Baillard A., et al., 2011, A&A, 532, A74

Banerjee A., Patra N. N., Chengalur J. N., 2013, MNRAS, 434, 1257

Barazza F. D., Binggeli B., Jerjen H., 2002, A&A, 391, 823

Barazza F. D., Jogee S., Marinova I., 2008, ApJ, 675, 1194

Barnabè M., et al., 2012, MNRAS, 423, 1073

Beckman J. E., Font J., Borlaff A., García-Lorenzo B., 2018, ApJ, 854, 182

Begeman K. G., Broeils A. H., Sanders R. H., 1991, MNRAS, 249, 523

Bertin G., Lin C. C., 1996, Spiral Structure in Galaxies: A Density Wave Theory. (Cambridge: MIT Press)

Besla G., Martínez-Delgado D., van der Marel R. P., Beletsky Y., Seibert M., Schlafly E. F., Grebel E. K., Neyer F., 2016, ApJ, 825, 20

Bidaran B., et al., 2020, MNRAS, 497, 1904

Binggeli B., Sandage A., Tammann G. A., 1985, AJ, 90, 1681

Binney J., Tremaine S., 2008, Galactic Dynamics: 2nd Edition. (Princeton: Princeton University Press)

Bittner A., et al. 2020, Valluri M., Sellwood J. A., eds, IAU Symp. Vol. 353, Galactic Dynamics in the Era of Large Surveys. (Cambridge: Cambridge University Press), p. 140

Bittner A., et al., 2019, A&A, 628, A117

Blais-Ouellette S., Amram P., Carignan C., 2001, AJ, 121, 1952

Boselli A., Gavazzi G., 2014, A&AR, 22, 74

Bournaud F., Combes F., 2002, A&A, 392, 83

Bournaud F., Combes F., Semelin B., 2005, MNRAS, 364, L18

Bundy K., et al., 2015, ApJ, 798, 7

Bureau M., Athanassoula E., 2005, ApJ, 626, 159

Bureau M., Freeman K. C., Pfitzner D. W., Meurer G. R., 1999, AJ, 118, 2158

Buta R., 1996, Buta R., Crocker D. A., Elmegreen B. G., eds, ASP Conf. Series Vol. 91, IAU Colloq. 157: Barred Galaxies. (San Francisco: Astronomical Society of the Pacific), p. 11

Buta R. J., 2017, MNRAS, 470, 3819

Buta R., Combes F., 1996, Fund. Cosm. Phys., 17, 95

Buta R. J., Zhang X., 2009, ApJS, 182, 559

Buta R., Alpert A. J., Cobb M. L., Crocker D. A., Purcell G. B., 1998, AJ, 116, 1142

Buta R., Ryder S. D., Madsen G. J., Wesson K., Crocker D. A., Combes F., 2001, AJ, 121, 225

Buta R., Laurikainen E., Salo H., 2004, AJ, 127, 279

Buta R. J., et al., 2015, ApJS, 217, 32

Buttitta C., et al., 2022, A&A, 664, L10

Caon N., Capaccioli M., D'Onofrio M., 1993, MNRAS, 265, 1013

Cappellari M., 2002, MNRAS, 333, 400

Cappellari M., 2008, MNRAS, 390, 71

Cappellari M., 2017, MNRAS, 466, 798

Cappellari M., 2020, MNRAS, 494, 4819

Cappellari M., Copin Y., 2003, MNRAS, 342, 345

Cappellari M., Emsellem E., 2004, PASP, 116, 138

Cappellari M., et al., 2011, MNRAS, 413, 813

Cappellari M., et al., 2013, MNRAS, 432, 1709

Chemin L., Hernandez O., 2009, A&A, 499, L25

Chilingarian I. V., Zolotukhin I. Y., 2012, MNRAS, 419, 1727

Chilingarian I. V., Melchior A.-L., Zolotukhin I. Y., 2010, MNRAS, 405, 1409

Choque-Challapa N., Aguerri J. A. L., Mancera Piña P. E., Peletier R., Venhola A., Verheijen M., 2021, MNRAS, 507, 6045

Collier A., Shlosman I., Heller C., 2018, MNRAS, 476, 1331

Collier A., Shlosman I., Heller C., 2019, MNRAS, 489, 3102

Combes F., 1991, Combes F., Casoli F., eds, ASP Conf. Series Vol. 146, IAU Colloq. 146: Dynamics of Galaxies and Their Molecular Cloud Distributions. (San Francisco: Astronomical Society of the Pacific), p. 255

Combes F., Sanders R. H., 1981, A&A, 96, 164

Comerón S., et al., 2014, A&A, 562, A121

Contopoulos G., 1981, A&A, 102, 265

Contopoulos G., Grosbol P., 1989, A&AR, 1, 261

Contopoulos G., Papayannopoulos T., 1980, A&A, 92, 33

Corsini E. M., 2011, Mem. Soc. Astron. Ital., 18, 23

Corsini E. M., Debattista V. P., Aguerri J. A. L., 2003, ApJ, 599, L29

Corsini E. M., Aguerri J. A. L., Debattista V. P., Pizzella A., Barazza F. D., Jerjen H., 2007, ApJ, 659, L121

Corsini E. M., et al., 2018, A&A, 618, A172

Costantin L., Méndez-Abreu J., Corsini E. M., Morelli L., Aguerri J. A. L., Dalla Bontà E., Pizzella A., 2017, A&A, 601, A84

Cote S., Carignan C., Sancisi R., 1991, AJ, 102, 904

Cuomo V., et al., 2019a, MNRAS, 488, 4972

Cuomo V., Aguerri J. A., Corsini E. M., Debattista V. P., Méndez-Abreu J., Pizzella A., 2019b, A&A, 632, A51

Cuomo V., Aguerri J. A. L., Corsini E. M., Debattista V. P., 2020, A&A, 641, A111

Cuomo V., Lee Y. H., Buttitta C., Aguerri J. A. L., Corsini E. M., Morelli L., 2021, A&A, 649, A30

Cuomo V., et al., 2022, MNRAS, 516, L24

Curtis H. D., 1918, Pub. Lick Obs., 13, 9

de Blok W. J. G., McGaugh S. S., 1997, MNRAS, 290, 533

de Lorenzi F., Debattista V. P., Gerhard O., Sambhus N., 2007, MNRAS, 376, 71

de Souza R. E., Gadotti D. A., dos Anjos S., 2004, ApJS, 153, 411

de Vaucouleurs G. H., de Vaucouleurs A., Shapley H., 1964, Reference Catalogue of Bright Galaxies. (Austin: University of Texas Press)

de Vaucouleurs G., de Vaucouleurs A., Corwin Jr. H. G., Buta R. J., Paturel G., Fouqué P., 1991, Third Reference Catalogue of Bright Galaxies. (New York: Springer)

de Zeeuw P. T., et al., 2002, MNRAS, 329, 513

Debattista V. P., 2003, MNRAS, 342, 1194

Debattista V. P., Sellwood J. A., 1998, ApJ, 493, L5

Debattista V. P., Sellwood J. A., 2000, ApJ, 543, 704

Debattista V. P., Williams T. B., 2004, ApJ, 605, 714

Debattista V. P., Corsini E. M., Aguerri J. A. L., 2002, MNRAS, 332, 65

Debattista V. P., Carollo C. M., Mayer L., Moore B., 2004, ApJ, 604, L93

Debattista V. P., Carollo C. M., Mayer L., Moore B., 2005, ApJ, 628, 678

Debattista V. P., Mayer L., Carollo C. M., Moore B., Wadsley J., Quinn T., 2006, ApJ, 645, 209

Del Popolo A., Le Delliou M., 2021, Galaxies, 9, 123

Díaz-García S., Salo H., Laurikainen E., 2016, A&A, 596, A84

Diemand J., Zemp M., Moore B., Stadel J., Carollo C. M., 2005, MNRAS, 364, 665

Du M., Debattista V. P., Shen J., Cappellari M., 2016, ApJ, 828, 14

Dubinski J., Berentzen I., Shlosman I., 2009, ApJ, 697, 293

Elmegreen B. G., Elmegreen D. M., 1985, ApJ, 288, 438

Emsellem E., Monnet G., Bacon R., 1994, A&A, 285, 723

Emsellem E., et al., 2022, A&A, 659, A191

Erwin P., 2015, ApJ, 799, 226

Erwin P., 2018, MNRAS, 474, 5372

Erwin P., Debattista V. P., 2013, MNRAS, 431, 3060

Erwin P., Sparke L. S., 2003, ApJS, 146, 299

Eskridge P. B., et al., 2000, AJ, 119, 536

Eskridge P. B., et al., 2002, ApJS, 143, 73

Fanali R., Dotti M., Fiacconi D., Haardt F., 2015, MNRAS, 454, 3641

Fathi K., Beckman J. E., Piñol-Ferrer N., Hernandez O., Martínez-Valpuesta I., Carignan C., 2009, ApJ, 704, 1657

Ferrarese L., et al., 2012, ApJS, 200, 4

Fisher D. B., 2006, ApJ, 642, L17

Fixsen D. J., Cheng E. S., Gales J. M., Mather J. C., Shafer R. A., Wright E. L., 1996, ApJ, 473, 576

Flores R. A., Primack J. R., 1994, ApJ, 427, L1

Font J., Beckman J. E., Epinat B., Fathi K., Gutiérrez L., Hernandez O., 2011, ApJ, 741, L14

Font J., Beckman J. E., Querejeta M., Epinat B., James P. A., Blasco-herrera J., Erroz-Ferrer S., Pérez I., 2014, ApJS, 210, 2

Fragkoudi F., Athanassoula E., Bosma A., 2016, MNRAS, 462, L41

Fragkoudi F., Grand R. J. J., Pakmor R., Springel V., White S. D. M., Marinacci F., Gomez F. A., Navarro J. F., 2021, A&A, 650, L16

Frankel N., et al., 2022, ApJ, 940, 61

Freeman K. C., 1966, MNRAS, 133, 47

Freudling W., Romaniello M., Bramich D. M., Ballester P., Forchi V., García-Dabló C. E., Moehler S., Neeser M. J., 2013, A&A, 559, A96

Friedli D., 1999, Beckman J. E., Mahoney T. J., eds, ASP Conf. Series Vol. 187, The Evolution of Galaxies on Cosmological Timescales. (San Francisco: Astronomical Society of the Pacific), p. 88

Frosst M., Courteau S., Arora N., Stone C., Macciò A. V., Blank M., 2022, MNRAS, 514, 3510

Fujii M. S., Bédorf J., Baba J., Portegies Zwart S., 2018, MNRAS, 477, 1451

Fux R., 1997, A&A, 327, 983

Gadotti D. A., 2008, MNRAS, 384, 420

Gadotti D. A., 2009, MNRAS, 393, 1531

Gadotti D. A., 2011, MNRAS, 415, 3308

Gadotti D. A., Athanassoula E., Carrasco L., Bosma A., de Souza R. E., Recillas E., 2007, MNRAS, 381, 943

Gadotti D. A., et al., 2020, A&A, 643, A14

García-Lorenzo B., et al., 2015, A&A, 573, A59

Gardner J. P., et al., 2006, Space Sci. Rev., 123, 485

Garma-Oehmichen L., Cano-Díaz M., Hernández-Toledo H., Aquino-Ortíz E., Valenzuela O., Aguerri J. A. L., Sánchez S. F., Merrifield M., 2020, MNRAS, 491, 3655

Garma-Oehmichen L., et al., 2022, MNRAS, 517, 5660

Gerhard O. E., 1993, MNRAS, 265, 213

Gerhard O. E., Binney J. J., 1996, MNRAS, 279, 993

Gerssen J., Debattista V. P., 2007, MNRAS, 378, 189

Gerssen J., Kuijken K., Merrifield M. R., 1999, MNRAS, 306, 926

Gerssen J., Kuijken K., Merrifield M. R., 2003, MNRAS, 345, 261

Ghosh S., Saha K., Di Matteo P., Combes F., 2021, MNRAS, 502, 3085

Goldreich P., Lynden-Bell D., 1965, MNRAS, 130, 97

Grand R. J. J., et al., 2017, MNRAS, 467, 179

Gullieuszik M., et al., 2015, A&A, 581, A41

Guo R., Mao S., Athanassoula E., Li H., Ge J., Long R. J., Merrifield M., Masters K., 2019, MNRAS, 482, 1733

Guo Y., et al., 2022, ApJ, in press (arXiv:2210.08658)

Hernquist L., Weinberg M. D., 1992, ApJ, 400, 80

Herrera-Endoqui M., Díaz-García S., Laurikainen E., Salo H., 2015, A&A, 582, A86

Hilmi T., et al., 2020, MNRAS, 497, 933

Hinshaw G., et al., 2013, ApJS, 208, 19

Holley-Bockelmann K., Weinberg M., Katz N., 2005, MNRAS, 363, 991

Hubble E. P., 1926, ApJ, 64, 321

Jacyszyn-Dobrzeniecka A. M., et al., 2016, Acta Astron., 66, 149

James P. A., Percival S. M., 2016, MNRAS, 457, 917

Janz J., et al., 2014, ApJ, 786, 105

Jedrzejewski R. I., 1987, MNRAS, 226, 747

Jeong H., Bureau M., Yi S. K., Krajnović D., Davies R. L., 2007, MNRAS, 376, 1021

Jogee S., et al., 2004, ApJ, 615, L105

Kalinova V., et al., 2017, MNRAS, 469, 2539

Kent S. M., 1987, AJ, 93, 816

Kim S., et al., 2014, ApJS, 215, 22

Kim T., et al., 2015, ApJ, 799, 99

Kim T., Gadotti D. A., Athanassoula E., Bosma A., Sheth K., Lee M. G., 2016, MNRAS, 462, 3430

Kim T., Athanassoula E., Sheth K., Bosma A., Park M.-G., Lee Y. H., Ann H. B., 2021, ApJ, 922, 196

Klypin A. A., Trujillo-Gomez S., Primack J., 2011, ApJ, 740, 102

Koekemoer A. M., et al., 2007, ApjS, 172, 196

Kormendy J., 1979, ApJ, 227, 714

Kormendy J., 2013, Falcón-Barroso J., Knapen J. H., eds, Secular Evolution of Galaxies. Canary Islands Winter School of Astrophysics Lectures. (Cambridge: Cambridge University Press), p. 1

Kormendy J., Kennicutt Robert C. J., 2004, ARA&A, 42, 603

Krajnović D., Cappellari M., Emsellem E., McDermid R. M., de Zeeuw P. T., 2005, MNRAS, 357, 1113

Kruk S. J., et al., 2017, MNRAS, 469, 3363

Kruk S. J., et al., 2018, MNRAS, 473, 4731

Kruk S. J., Erwin P., Debattista V. P., Lintott C., 2019, MNRAS, 490, 4721

Kuijken K., Dubinski J., 1995, MNRAS, 277, 1341

Kumar A., Das M., Kataria S. K., 2022, MNRAS, 509, 1262

Lablanche P.-Y., et al., 2012, MNRAS, 424, 1495

Laurikainen E., Salo H., 2002, MNRAS, 337, 1118

Laurikainen E., Salo H., Buta R., 2005, MNRAS, 362, 1319

Laurikainen E., Salo H., Buta R., Knapen J. H., 2007, MNRAS, 381, 401

Laurikainen E., Salo H., Buta R., Knapen J. H., 2009, ApJ, 692, L34

Lee Y. H., Ann H. B., Park M.-G., 2019, ApJ, 872, 97

Lee Y. H., Park M.-G., Ann H. B., Kim T., Seo W.-Y., 2020, ApJ, 899, 84

Lin L., et al., 2020, MNRAS, 499, 1406

Lisker T., Glatt K., Westera P., Grebel E. K., 2006, AJ, 132, 2432

Lisker T., Vijayaraghavan R., Janz J., Gallagher John S. I., Engler C., Urich L., 2018, ApJ, 865, 40

Łokas E. L., 2018, ApJ, 857, 6

Łokas E. L., 2019, A&A, 629, A52

Łokas E. L., 2021a, A&A, 647, A143

Łokas E. L., 2021b, A&A, 655, A97

Maciejewski W., 2006, MNRAS, 371, 451

Marinacci F., et al., 2018, MNRAS, 480, 5113

Marinova I., Jogee S., 2007, ApJ, 659, 1176

Marioni O. F., Abadi M. G., Gottlöber S., Yepes G., 2022, MNRAS, 511, 2423

Martinez-Valpuesta I., Shlosman I., Heller C., 2006, ApJ, 637, 214

Martinez-Valpuesta I., Knapen J. H., Buta R., 2007, AJ, 134, 1863

Martinez-Valpuesta I., Aguerri J., González-García C., 2016, Galaxies, 4, 7

Martinez-Valpuesta I., Aguerri J. A. L., González-García A. C., Dalla Vecchia C., Stringer M., 2017, MNRAS, 464, 1502

Masters K. L., et al., 2011, MNRAS, 411, 2026

McConnachie A. W., 2012, AJ, 144, 4

Meidt S. E., Rand R. J., Merrifield M. R., Debattista V. P., Shen J., 2008, ApJ, 676, 899

Meidt S. E., Rand R. J., Merrifield M. R., 2009, ApJ, 702, 277

Méndez-Abreu J., Aguerri J. A. L., Corsini E. M., Simonneau E., 2008, A&A, 478, 353

Méndez-Abreu J., Sánchez-Janssen R., Aguerri J. A. L., Corsini E. M., Zarattini S., 2012, ApJ, 761, L6

Méndez-Abreu J., et al., 2017, A&A, 598, A32

Méndez-Abreu J., et al., 2018a, MNRAS, 474, 1307

Méndez-Abreu J., Costantin L., Aguerri J. A. L., de Lorenzo-Cáceres A., Corsini E. M., 2018b, MNRAS, 479, 4172

Menéndez-Delmestre K., Sheth K., Schinnerer E., Jarrett T. H., Scoville N. Z., 2007, ApJ, 657, 790

Merrifield M. R., Kuijken K., 1995, MNRAS, 274, 933

Merrifield M. R., Rand R. J., Meidt S. E., 2006, MNRAS, 366, L17

Michea J., Pasquali A., Smith R., Kraljic K., Grebel E. K., Calderón-Castillo P., Lisker T., 2021, AJ, 161, 268

Michel-Dansac L., Wozniak H., 2006, A&A, 452, 97

Miwa T., Noguchi M., 1998, ApJ, 499, 149

Moore B., Quinn T., Governato F., Stadel J., Lake G., 1999, MNRAS, 310, 1147

Morelli L., Parmiggiani M., Corsini E. M., Costantin L., Dalla Bontà E., Méndez-Abreu J., Pizzella A., 2016, MNRAS, 463, 4396

Morgan W. W., 1958, PASP, 70, 364

Mosenkov A. V., Sotnikova N. Y., Reshetnikov V. P., Bizyaev D. V., Kautsch S. J., 2015, MNRAS, 451, 2376

Navarro J. F., Frenk C. S., White S. D. M., 1995, MNRAS, 275, 56

Navarro J. F., et al., 2004, MNRAS, 349, 1039

Nelson D., et al., 2018, MNRAS, 475, 624

Noguchi M., 1987, MNRAS, 228, 635

Noguchi M., 1988, A&A, 203, 259

Noordermeer E., van der Hulst J. M., Sancisi R., Swaters R. S., van Albada T. S., 2007, MNRAS, 376, 1513

Odewahn S. C., 1994, AJ, 107, 1320

Ohta K., Hamabe M., Wakamatsu K.-I., 1990, ApJ, 357, 71

O'Neill J. K., Dubinski J., 2003, MNRAS, 346, 251

Patra N. N., Jog C. J., 2019, MNRAS, 488, 4942

Peng C. Y., Ho L. C., Impey C. D., Rix H.-W., 2002, AJ, 124, 266

Peschken N., Łokas E. L., 2019, MNRAS, 483, 2721

Petersen M. S., Weinberg M. D., Katz N., 2019, MNRAS, 490, 3616

Pfenniger D., Norman C., 1990, ApJ, 363, 391

Pignatelli E., Fasano G., Cassata P., 2006, A&A, 446, 373

Pillepich A., et al., 2018, MNRAS, 475, 648

Pohlen M., Trujillo I., 2006, A&A, 454, 759

Pontzen A., Roškar R., Stinson G. S., Woods R., Reed D. M., Coles J., Quinn T. R., 2013, Pynbody: Astrophysics Simulation Analysis for Python, Astrophysics Source Code Library, record ascl:1305.002

Portail M., Gerhard O., Wegg C., Ness M., 2016, Monthly Notices of the Royal Astronomical Society, 465, 1621

Press W. H., Teukolsky S. A., Vetterling W. T., Flannery B. P., 1992, Numerical Recipes in FORTRAN. The Art of Scientific Computing. (Cambridge: Cambridge University Press)

Prieto M., Aguerri J. A. L., Varela A. M., Muñoz-Tuñón C., 2001, A&A, 367, 405

Prugniel P., Soubiran C., 2001, A&A, 369, 1048

Puerari I., Dottori H., 1997, ApJ, 476, L73

Quillen A. C., Frogel J. A., Gonzalez R. A., 1994, ApJ, 437, 162

Raha N., Sellwood J. A., James R. A., Kahn F. D., 1991, Nat, 352, 411

Rautiainen P., Salo H., Laurikainen E., 2008, MNRAS, 388, 1803

Relatores N. C., et al., 2019, ApJ, 887, 94

Reyes R., Mandelbaum R., Gunn J. E., Pizagno J., Lackner C. N., 2011, MNRAS, 417, 2347

Ricotti M., 2003, MNRAS, 344, 1237

Rix H.-W., et al., 2004, ApJS, 152, 163

Romero-Gómez M., 2012, A&AT, 27, 303

Romero-Gómez M., Masdemont J. J., Athanassoula E., García-Gómez C., 2006, A&A, 453, 39

Romero-Gómez M., Athanassoula E., Masdemont J. J., García-Gómez C., 2007, A&A, 472, 63

Roshan M., Ghafourian N., Kashfi T., Banik I., Haslbauer M., Cuomo V., Famaey B., Kroupa P., 2021, MNRAS, 508, 926

Rybicki G. B., 1987, de Zeeuw P. T., ed., IAU Symp. 127 Vol. 127, Structure and Dynamics of Elliptical Galaxies. (Dordrecht: Reidel Publishing Co.), p. 397

Sánchez S. F., et al., 2012, A&A, 538, A8

Sánchez-Menguiano L., Pérez I., Zurita A., Martínez-Valpuesta I., Aguerri J. A. L., Sánchez S. F., Comerón S., Díaz-García S., 2015, MNRAS, 450, 2670

Sanders R. H., Huntley J. M., 1976, ApJ, 209, 53

Sanders R. H., Tubbs A. D., 1980, ApJ, 235, 803

Sarkar S., Pandey B., Bhattacharjee S., 2021, MNRAS, 501, 994

Sarzi M., et al., 2006, MNRAS, 366, 1151

Scannapieco C., Athanassoula E., 2012, MNRAS, 425, L10

Schaye J., et al., 2015, MNRAS, 446, 521

Schlafly E. F., Finkbeiner D. P., 2011, ApJ, 737, 103

Schmitt H. R., 2001, AJ, 122, 2243

Schwarzschild M., 1979, ApJ, 232, 236

Scott N., et al., 2013, MNRAS, 432, 1894

Sellwood J. A., 1981, A&A, 99, 362

Sellwood J. A., 2008, ApJ, 679, 379

Sellwood J. A., 2014, RMP, 86, 1

Sellwood J. A., Debattista V. P., 2006, ApJ, 639, 868

Sellwood J. A., Sparke L. S., 1988, MNRAS, 231, 25P

Sellwood J. A., Wilkinson A., 1993, Rep. Prog. Phys., 56, 173

Sérsic J. L., 1968, Atlas de Galaxias Australes. (Cordoba: Observatorio Astronomico de Cordoba)

Shen J., Sellwood J. A., 2004, ApJ, 604, 614

Sheth K., et al., 2008, ApJ, 675, 1141

Sheth K., et al., 2010, PASP, 122, 1397

Skokos C., Patsis P. A., Athanassoula E., 2002, MNRAS, 333, 847

Soto K. T., Lilly S. J., Bacon R., Richard J., Conseil S., 2016, MNRAS, 458, 3210

Sparke L. S., Gallagher John S. I., 2000, Galaxies in the Universe. (Cambridge: Cambridge University Press)

Spinoso D., Bonoli S., Dotti M., Mayer L., Madau P., Bellovary J., 2017, MNRAS, 465, 3729

Stadel J. G., 2001, PhD thesis, University of Washington, Seattle

Tahmasebzadeh B., Zhu L., Shen J., Gerhard O., Ven G. v. d., 2022, ApJ, 941, 109

Tawfeek A. A., et al., 2022, ApJ, 940, 1

Taylor J. E., Navarro J. F., 2001, ApJ, 563, 483

Theureau G., Bottinelli L., Coudreau-Durand N., Gouguenheim L., Hallet N., Loulergue M., Paturel G., Teerikorpi P., 1998, A&AS, 130, 333

Thompson L. A., 1981, ApJ, 244, L43

Toomre A., 1981, Fall S. M., Lynden-Bell D., eds, Structure and Evolution of Normal Galaxies. Proc. Advanced Study. (Cambridge: Cambridge University Press), p. 111

Tremaine S., Weinberg M. D., 1984, ApJ, 282, L5

Tully R. B., Fisher J. R., 1977, A&A, 500, 105

Valdes F., Gupta R., Rose J. A., Singh H. P., Bell D. J., 2004, ApJS, 152, 251

Valenzuela O., Klypin A., 2003, MNRAS, 345, 406

van den Bergh S., 1976, ApJ, 206, 883

van der Marel R. P., 2001, AJ, 122, 1827

van der Marel R. P., Franx M., 1993a, ApJ, 407, 525

van der Marel R. P., Franx M., 1993b, ApJ, 407, 525

van Driel W., Ragaigne D., Boselli A., Donas J., Gavazzi G., 2000, A&AS, 144, 463

van Driel W., et al., 2016, A&A, 595, A118

Varela J., Moles M., Márquez I., Galletta G., Masegosa J., Bettoni D., 2004, A&A, 420, 873

Vasiliev E., Athanassoula E., 2015, MNRAS, 450, 2842

Vasiliev E., Valluri M., 2020, ApJ, 889, 39

Vazdekis A., Sánchez-Blázquez P., Falcón-Barroso J., Cenarro A. J., Beasley M. A., Cardiel N., Gorgas J., Peletier R. F., 2010, MNRAS, 404, 1639

Villa-Vargas J., Shlosman I., Heller C., 2010, ApJ, 719, 1470

Voglis N., Harsoula M., Contopoulos G., 2007, MNRAS, 381, 757

Walcher C. J., et al., 2014, A&A, 569, A1

Weilbacher P. M., Streicher O., Palsa R., 2016, MUSE-DRP: MUSE Data Reduction Pipeline, Astrophysics Source Code Library, record ascl:1610.004

Weinberg M. D., 1985, MNRAS, 213, 451

Weinberg M. D., Katz N., 2002, ApJ, 580, 627

Weiner B. J., Sellwood J. A., Williams T. B., 2001, ApJ, 546, 931

Widrow L. M., Dubinski J., 2005, ApJ, 631, 838

Widrow L. M., Pym B., Dubinski J., 2008, ApJ, 679, 1239

Willett K. W., et al., 2013, MNRAS, 435, 2835

Williams M. J., Bureau M., Cappellari M., 2009, MNRAS, 400, 1665

Williams T. G., et al., 2021, AJ, 161, 185

Willmer C. N. A., 2018, ApJS, 236, 47

Wozniak H., Champavert N., 2006, MNRAS, 369, 853

Wozniak H., Pierce M. J., 1991, A&AS, 88, 325

Wu Y.-T., Pfenniger D., Taam R. E., 2018, ApJ, 860, 152

Yepes G., Martínez-Vaquero L. A., Gottlöber S., Hoffman Y., 2009, Balazs C., Wang F., eds, AIP Conf. Series Vol. 1178, 5th International Workshop on the Dark Side of the Universe. (New York: AIP), p. 64

York D. G., et al., 2000, AJ, 120, 1579

Yozin C., Bekki K., 2014, MNRAS, 439, 1948

Zhang X., Buta R. J., 2007, AJ, 133, 2584

Zou Y., Shen J., Bureau M., Li Z., 2019, ApJ, 884, 23